



University of
Massachusetts
Amherst

The Assembly of Galaxies Over Cosmic Time

Item Type	Dissertation (Open Access)
Authors	Guo, Yicheng
DOI	10.7275/ndgc-f089
Download date	2026-04-23 01:07:08
Link to Item	https://hdl.handle.net/20.500.14394/39087

THE ASSEMBLY OF GALAXIES OVER COSMIC TIME

A Dissertation Presented

by

YICHENG GUO

Submitted to the Graduate School of the
University of Massachusetts Amherst in partial fulfillment
of the requirements for the degree of

DOCTOR OF PHILOSOPHY

September 2012

Astronomy

© Copyright by Yicheng Guo 2012

All Rights Reserved

THE ASSEMBLY OF GALAXIES OVER COSMIC TIME

A Dissertation Presented

by

YICHENG GUO

Approved as to style and content by:

Mauro Giavalisco, Chair

Daniela Calzetti, Member

Min S. Yun, Member

Lorenzo Sorbo, Member

Stephen E. Schneider, Department Chair
Astronomy

To my family.

ACKNOWLEDGMENTS

I would like to express my sincere gratitude to all people who have helped make this thesis possible.

Foremost, I would like to deeply thank my adviser, Prof. Mauro Giavalisco, for his continuous support and guidance during my Ph.D study. His enthusiasm, motivation, knowledge, and patience lead me all the way from a beginner of the high-redshift universe to a qualified Ph.D. Mauro always encouraged me, and even pushed me, to step forward to work with collaborators, helping me build up connections that benefited my Ph.D study and would benefit my career in future. I feel lucky to have Mauro as my Ph.D adviser.

I would like to thank Prof. Houjun Mo and Daniel H. McIntosh for supervising me for my first two research projects. Houjun's door is always open for discussing science, and his insight and knowledge as a theoretician are very helpful during all my Ph.D. study. Dan, a then postdoc in UMASS, supported me in my most difficult time of my graduate study. I cannot forget that he spent hours and hours in his office to teach me how to analyze galaxy images. It was Dan who trained me to become an observer.

I am very lucky to be able to be involved in GOODS and CANDELS, two large HST programs with collaborators and experts in all aspects. My thesis is a result of collaboration with many members of both teams. Therefore, I would like to thank several members of both teams. Prof. Sandra Faber and Dr. Henry Ferguson, both co-PIs of CANDELS, gave me great opportunities to take important tasks in CANDELS. Henry and other members in the GOODS/CANDELS team, Drs. Mark Dickinson,

Anton Koekemoer, Norman Grogan, Kyoung-Soo Lee, Tomas Dahlen, Arjen van del Wel, and Profs. Bahram Mobasher and Casey Papovich, shared their expertise in a variety of ways to help me solve both technical and scientific questions in my thesis.

Discussions with faculties in UMASS helped me considerably improve the quality of my thesis. Especially, I would like to thank my thesis committee members: Profs. Daniela Calzetti, Min S. Yun, and Lorenzo Sorbo for reading it, discussing it, and even grilling me about it. I would also like to thank Prof. William Irvine, our Graduate Program Director, for monitoring me throughout all my study.

I have also learned an enormous amount from my colleagues and friends: Paolo Cassata (for being a very close collaborator), Guilin Liu, Yuxi Chen (for our endless discussion on how to calculate signal-to-noise ratio), Yu Lu, Xiaohu Yang, Li Ji, Hui Dong, Sara Salimbeni, Mark Fardal, Dusan Keres, Yiming Li, Huiyuan Wang, Xiaojie Xu, Christina Williams, Bomee Lee, and all other friends of mine even her/his name is not explicitly remarked here.

This thesis cannot be done without supports from my beloved family, to whom I dedicate this thesis. I am grateful to my parents for their understanding on everything I do and for their selfless helps whenever I was in a difficult time. And finally, my heartfelt thanks go to my wife, Yufeng Zhang, for always being by my side. Her love, understanding, and encouragement are the strongest support for me to pursue my dream of being a scientist.

ABSTRACT

THE ASSEMBLY OF GALAXIES OVER COSMIC TIME

SEPTEMBER 2012

YICHENG GUO

B.Sc., UNIVERSITY OF SCIENCE AND TECHNOLOGY OF CHINA

M.Sc., UNIVERSITY OF MASSACHUSETTS, AMHERST

Ph.D., UNIVERSITY OF MASSACHUSETTS AMHERST

Directed by: Professor Mauro Giavalisco

To Understand how galaxies were assembled across the cosmic time remains one of the most outstanding questions in astronomy. The core of this question is how today's Hubble Sequence, namely the differentiation of galaxy morphology and its correlation to galaxy physical properties, is formed. In this thesis, we investigate the origin of the Hubble Sequence through galaxies at $z \sim 2$, an epoch when the cosmic star formation activity reaches its peak and the properties of galaxies undergo dramatic transitions. Galaxies at $z \sim 2$ have two important features that are distinct from nearby galaxies: much higher frequency of clumpy morphology in star-forming systems, and much compact size. To understand the nature of the two features requires investigations on the sub-structure of galaxies in a multi-wavelength way. In this thesis, we study samples of galaxies that are selected from GOODS and HUDF, where ultra-deep and high-resolution optical and near-infrared images allow us to study the stellar populations of the sub-structures of galaxies at the rest-frame optical bands

for the first time, to answer two questions: (1) the nature of kiloparsec-scale clumps in star-forming galaxies at $z \sim 2$ and (2) the existence of color gradient and stellar population gradient in passively evolving galaxies at $z \sim 2$, which may provide clues to the mechanisms of dramatic size evolution of this type of galaxies. We further design a set of color selection criteria to search for dusty star-forming galaxies and passively evolving galaxies at $z \sim 3$ to explore the question: when today's Hubble Sequence has begun to appear.

TABLE OF CONTENTS

	Page
ACKNOWLEDGMENTS	v
ABSTRACT	vii
LIST OF TABLES	xii
LIST OF FIGURES	xiii
 CHAPTER	
1. INTRODUCTION	1
1.1 Precision Cosmological Framework	2
1.2 Galaxies in the Local Universe	3
1.3 An Transition Era: $1 < z < 4$	5
1.4 Open Questions	8
2. TOOLS	10
2.1 Images	10
2.2 Catalogs	12
2.3 Physical Properties of Galaxies	14
3. KILOPARSEC-SCALE CLUMPS IN STAR-FORMING GALAXIES AT $Z \sim 2$	19
3.1 Introduction	19
3.2 Sample Selection	23
3.3 Clump Detection and Measurement	24
3.3.1 Clump Detection	24
3.3.2 PSF Matched Images	27
3.3.3 Clump Measurement	28
3.4 Physical Properties of Clumps	30

3.4.1	Rest-Frame UV–Optical Color of Clumps	30
3.4.2	SFR–Stellar Mass Relation of Clumps	33
3.4.3	Contribution of Clumps to Host Galaxies	35
3.4.4	Clumps vs. “Disks”	37
3.5	Clumps across Host Galaxies	41
3.5.1	Radial Variation of Color	42
3.5.2	Radial Variations of Physical Properties	44
3.5.3	Effect of Diffuse Background Subtraction	48
3.5.4	Possible Metallicity Variation	54
3.6	Discussion	55
3.6.1	Comparisons with Other Studies	55
3.6.2	Formation of Clumps	60
3.6.3	Fate of Clumps	63
3.6.4	Ongoing Bulge Formation?	67
3.7	Summary and Conclusions	71
4.	COLOR AND STELLAR POPULATION GRADIENTS IN	
	PASSIVELY EVOLVING GALAXIES AT $Z \sim 2$	80
4.1	Introduction	80
4.2	Passively Evolving Galaxies at $z \sim 2$ in HUDF	83
4.3	Annular Photometry of Massive Passively Evolving Galaxies	85
4.3.1	Aperture Size	85
4.3.2	Reliability of Annular Photometry	86
4.4	Color Gradients in Massive Passively Evolving Galaxies	92
4.5	Variation of Single Parameter as the Origin of Color Gradients	97
4.6	Stellar Population Gradients in Massive Passively Evolving Galaxies	101
4.7	Discussion	107
4.7.1	Dust Gradient	107
4.7.2	Metallicity Gradient	112
4.7.2.1	Flat Metallicity Gradient	113
4.7.2.2	Local Metallicity Gradient	114
4.7.2.3	Monolithic metallicity gradient	115
4.7.3	Formation of Passively Evolving Galaxies at $z \sim 2$	117
4.8	Summary and Conclusions	118

5. TOWARDS A COMPLETE CENSUS OF GALAXIES AT	
Z\sim3	124
5.1 Introduction	124
5.2 Color Selection Criteria	128
5.3 Star-forming VJL Galaxies	133
5.3.1 Redshift Distribution	134
5.3.2 Comparison with LBGs	135
5.3.3 Dusty Star-forming Galaxies	139
5.3.4 Contributions of Dusty Star-forming Galaxies	146
5.4 Passively-Evolving VJL Galaxies	150
5.4.1 Clean Sample	151
5.4.2 Passively Evolving Galaxies at $z > 3$?	155
5.4.3 The Evolution of Integrated Stellar Mass Density of Passively-Evolving Galaxies	159
5.4.4 Stellar Mass Locked in Passively-Evolving Galaxies	164
5.4.5 Discussion	166
5.5 Summary and Conclusions	167
6. SUMMARY AND FUTURE DEVELOPMENT	171
6.1 Summary	171
6.2 Future Development	173
BIBLIOGRAPHY	176

LIST OF TABLES

Table	Page
2.1 Sensitivity and Resolution of GOODS Filters	11
2.2 Parameter Space Used for SED-Fitting	17
3.1 Properties of Star-forming Galaxies at $z \sim 2$	75
3.2 Properties of Clumps and “Disks”	75
3.3 Comparison of Derived Properties of Three Galaxies in Our Sample and Elmegreen et al. (2005)	79
4.1 The Physical Properties of massive PEGs in our sample	86
5.1 Passively Evolving Candidates at $z > 3$	153

LIST OF FIGURES

Figure	Page
2.1 Accuracy of our photometric redshift measurement.	15
3.1 Montage of our 10 clumpy star-forming galaxies at $z \sim 2$	25
3.2 Fractional encircled energy of PSFs of 7 bands, before (<i>left</i>) and after (<i>right</i>) our PSF matching.	28
3.3 Color–magnitude diagram of clumps (star), “disks” (triangle), and host galaxies (circle).	31
3.4 SFR–stellar mass relation for clumps (star), “disks” (triangle), and host galaxies (circle).	34
3.5 Fractional contributions of clumps to their host galaxies in terms of rest-frame U-band luminosity (top left), V-band luminosity (top right), stellar mass (bottom left), and SFR (bottom right).	36
3.6 Comparisons between physical properties of clumps and their surrounding “disks”.	39
3.7 Radial variation of the rest-frame U-V color of clumps as a function of their galactocentric distances to the H-band light-weighted centers of their host galaxies.	42
3.8 Radial variation of physical properties of clumps as a function of galactocentric distance.	45
3.9 Radial variation of the rest-frame U-V color of clumps as a function of their galactocentric distances, under different schemes of diffuse background subtraction.	50
3.10 Radial variation of physical properties of clumps as a function of galactocentric distance, under different schemes of diffuse background subtraction.	51

3.11	Age–stellar surface density relation of clumps.	66
4.1	Montage of six massive passively evolving galaxies in our sample.	87
4.2	Effect of PSF–matching in the measure of color gradients.	88
4.3	Probability distribution function of photometric redshift measured (from the <i>HST</i> BVizJH photometry) in concentric annuli around our sample galaxies compared to that of the galaxies as a whole, as well as to their spectroscopic redshift, when available.	91
4.4	Rest-frame B-V (<i>top</i>), U-B (<i>middle</i>) and U-V (<i>bottom</i>) color gradients of the six sample galaxies.	93
4.5	Slope of the (B-V) (<i>bottom row</i>), (U-B) (<i>middle row</i>) and (B-V) (<i>top row</i>) color gradients of the six sample galaxies as a function of redshift, stellar mass M_{star} , $E(\text{B-V})$ as a proxy for dust obscuration, and global rest–frame U-V color.	96
4.6	Predicted rest–frame (B-V), (U-B) and (U-V) color gradients from single stellar population models if the age of the dominant stellar population is the only parameter that varies as a function of radius in the galaxies (thin lines).	98
4.7	<i>HST</i> 7–band photometry (ACS BViz and WFC3/IR YJH) of the sample galaxies in the annular apertures discussed above.	102
4.8	Dust (<i>top row</i>) and age (<i>bottom row</i>) gradients of massive PEGs under three assumptions of metallicity gradients: (1) the flat gradient (<i>left column</i>), (2) the local gradient (<i>middle column</i>), and (3) the monolithic gradient (<i>right column</i>).	104
4.9	Age gradient of the sample galaxies under three different assumptions of dust distribution: (1) no dust; (2) dust as a free parameter in each annulus; (3) dust fixed to the global value from the best–fit of the 12–band GUTFIT photometry to the models.	108
4.10	Similar to Figure 4.8, but showing the results of different extinction laws.	110
5.1	Galaxy models and observed ERS galaxies in the (J-L) vs. (V-J) two-color diagram.	128

5.2	Redshift distributions of star-forming VJL galaxies.	135
5.3	Star-forming VJLs (points) and U-band dropouts (circles: $z < 3.2$; squares: $z > 3.2$) in the (J-L) vs. (V-J) color-color diagram.	137
5.4	E(B-V) distribution as a function of stellar mass for star-forming VJL galaxies (<i>left</i>) and U-band dropouts (<i>right</i>).	140
5.5	<i>Top</i> : Cumulative fraction of number of galaxies as a function of E(B-V) for sVJLs (thick solid for $S/N > 10$ and dotted for $S/N > 20$) and U-band dropouts (thin solid) in two stellar mass ranges. <i>Middle</i> : Cumulative fraction of SFR for sVJLs and U-band dropouts. <i>Bottom</i> : Cumulative fraction of stellar mass for sVJLs and U-band dropouts.	141
5.6	Comparison of MIPS $24\mu\text{m}$ fluxes derived through PSF-fitting and aperture correction for sVJLs with $E(B-V) \geq 0.4$	142
5.7	MIPS $24\mu\text{m}$ fluxes of dusty sVJLs ($S/N > 10$) as a function of stellar mass. Here we only show galaxies with $E(B-V) \geq 0.4$ and $2.3 < z < 3.5$	144
5.8	Comparison of normalized number density (<i>top</i>), SFRD (<i>middle</i>) and stellar mass density (<i>bottom</i>) of U-band dropouts (thin lines) and $S/N > 10$ sVJLs (thick lines), as a function of E(B-V).	148
5.9	Deviation of MIPS $24\mu\text{m}$ fluxes of pVJLs from the predication of pure stellar emission as a function of Kron radius.	153
5.10	Redshift distributions of pVJL selected galaxies. Different panels show cases with different S/N cuts.	154
5.11	Observed and best-fit SEDs for six galaxies at $z > 3$ in our $S/N > 5$ pVJL sample.	157
5.12	Evolution of ISMD for PEGs with $M_{\text{star}} > 10^{10} M_{\odot}$	161
5.13	Fraction of stellar mass locked in PEGs as a function of redshift.	164

CHAPTER 1

INTRODUCTION

Understanding galaxy formation and evolution remains one of the most outstanding questions in astronomy. According to the standard paradigm (White & Rees, 1978), galaxies are initially formed in the center of small cold dark matter halos, gradually assembled with time through hierarchical processes, and eventually evolved into populations with various color, size, morphology, etc., as observed in our local universe (e.g., Blanton & Moustakas, 2009). The behavior of dark matter halos, e.g., growth, interaction, and merger, has been extensively studied and accurately determined through high-resolution N-body simulations (e.g., Navarro et al., 1996, 1997; Wechsler et al., 2002; Springel et al., 2005). However, since dark matter particles only interact through gravity and do not emit or absorb any electromagnetic radiation, the behavior of dark matter halos cannot be directly observed. It can only be inferred from the behaviors of observable baryonic matters. Unfortunately, the relation between dark matter and baryonic matter is complicated. Therefore, the physics of how baryonic matters assemble into stars and galaxies in the potential well of dark matter halos is complex and still poorly understood. In order to fully understand the physics of galaxy formation and evolution, efforts should be made in two sides: theoreticians should provide models to reproduce the observations of galaxies across the cosmic time, while observers should provide complete and detailed observations to constrain and refine theoretical models.

1.1 Precision Cosmological Framework

The cosmological framework is crucial for understanding galaxy formation and evolution in two folds. First, in order to convert the observed apparent quantities, such as flux and angular size, to the intrinsic properties of galaxies, such as luminosity (and therefore stellar mass and star formation rate) and physical size, basic cosmological quantities, such as time, distance, and co-moving volume, at any given redshift should be accurately calculated. Second, the cosmological framework (the cosmological parameters) determines how primordial dark matter density fluctuations evolve under gravity into large-scale structures in the universe, which is the initial condition of all theoretical models.

Thanks to the recent developments of cosmological observations, we have reached to an era of Precision Cosmology. The universe we live in is a so called Λ CDM universe, characterized by three key cosmological parameters: Ω_m (matter density), Ω_Λ (dark energy density), and Ω_k (spatial curvature). Recent observations of the Cosmic Microwave Background Spergel et al. (CMB, 2003); Komatsu et al. (CMB, 2011), the expansion rate of the universe traced by Supernova Type Ia Riess et al. (SN Ia, 1998, 2009) and the baryonic acoustic oscillation Percival et al. (BAO 2007, 2010) have determined these parameters to a high precision: the universe is flat ($\Omega_k = 0$), with total mass/energy density very close to the critical density of closure. About 27% of the total density is in matter ($\Omega_m = 0.27$), and about 73% in dark energy or cosmological constant ($\Omega_\Lambda = 0.73$). If we divide the matter density further into dark matter and baryonic matter, only 4.6% of the total density is in baryonic matter ($\Omega_b = 0.046$), and only about 0.5% in stars that are visible to us. This well established Λ CDM cosmology has so far been very successful in explaining the large-scale structure of the universe, and provides a reliable framework for studying galaxy formation and evolution in a systematic way.

1.2 Galaxies in the Local Universe

Galaxies in the local universe provide a boundary condition to understand galaxy formation and evolution. Thanks to the latest wide-field sky surveys (e.g., SDSS, 2dF, 2MASS, etc.), the physical properties, such as luminosity, mass (both stellar and gas), color, structure, environment, etc., of galaxies in the local universe have been extensively studied to provide detailed and robust criteria to constrain and select theoretical models. Intriguingly, various properties of local galaxies are correlated.

One of the most fundamental observational fact about local galaxies is the Hubble Sequence, a morphological classification of galaxies invented by Edwin Hubble in 1930's. Galaxies are divided into a few classes based on their visual morphology: Ellipticals (E), Lenticulars (S0), Spirals (S), Barred Spirals (SB), and Irregulars (Irr). Although classified by their morphology, galaxies in different classes are also found to have distinguishing physical properties. Most Ellipticals are composed of old stars moving in random orbits and have little recent star formation, while Spirals consist of a flat and rotating disk containing stars, gas, and dust, and have ongoing star formation in their arms. Irregular galaxies are believed to be one product of galaxy merge. Broadly, the Hubble Sequence can be divided into two types: early-type (E and S0) and late-type (S, SB, and Irr).

Another interesting correlation is the color bimodality. Based on their positions in the color–magnitude diagram (CMD), local galaxies can be roughly divided into two populations: blue cloud and red sequence Strateva et al. (e.g., 2001); Blanton et al. (e.g., 2003a); Baldry et al. (e.g., 2004). Galaxies in the blue cloud are very reliably classified as spiral galaxies with ongoing star-formation, and their color is strongly related to the recent star-formation history. However, the red sequence contains a mix of types: dwarf ellipticals, dust-reddened spirals, lenticulars, and giant ellipticals. Generally, red galaxies (except dust-reddened spirals) have little recent star-formation, and their color is weakly related to both mean stellar age and

metallicity. Blue galaxies generally have low Sérsic indices¹, indicating a disk-like morphology, while red galaxies span a wide range of Sérsic indices, from disk-like to spheroid-like morphology. Overall, the divisions of local galaxies based on their morphology (early vs. late), color (red vs. blue), and star-formation activity (passive vs. active) are largely overlapped: early-type galaxies are generally red and passive, while late-types blue and active.

The abundance and stellar mass content of each type of galaxies are well measured through its luminosity function and stellar mass function, namely the number or cosmic density of galaxies in a given luminosity or stellar mass bin. Modern wide-area sky surveys, such as 2dF, SDSS, and 2MASS, have provided data to definitively measure those functions. The measurements of various types of galaxies, divided either by activity (Norberg et al., 2002), color (Blanton et al., 2005b), or morphology (Driver et al., 2006), from different groups have converged (e.g., Bell et al., 2003; Driver et al., 2006): about 60% of stellar mass in today’s universe is contained in early-type galaxies, whose number density, however, only occupies 30% of all local galaxies. Although this result is fundamental, reproducing it from theoretical models is not simple. Early predictions failed to reproduce the color distribution along the luminosity function. The dark matter halo mass function is not simply a re-scaled stellar mass function of galaxies, and predicts too many luminous blue galaxies and too many faint red galaxies, if only the physics of gas falling and cooling is involved. Theoretical models (e.g., Benson et al., 2003; Bower et al., 2006; Croton et al., 2006; De Lucia et al., 2006) require complex ingredients (e.g. feedbacks from stellar wind, AGN, reionization, etc. to quench star formation in galaxies) to reproduce even these basic observations of nearby galaxies: luminosity function (e.g., Blanton et al., 2001;

¹The Sérsic index n is a power index in the Sérsic profile, which is a measurement of the light profile of galaxies and defined as: $I(r) \propto \exp[-(\frac{r}{r_e})^{(1/n)}]$, where r_e is the effective radius (or half-light radius r_{50}) (Sérsic, 1963; Graham & Driver, 2005). The Sérsic index n is widely used to separate disk-like ($n < 2.5$) and spheroid-like ($n > 2.5$) galaxies.

Norberg et al., 2002; Blanton et al., 2003b) and bimodality (e.g., Kauffmann et al., 2003b,a; Bell et al., 2004; Blanton et al., 2005a). Since these ingredients are predicted (or designed) to begin to work since the universe is young, it is essential to test them through observational studies on the physical properties of high-redshift galaxies.

1.3 An Transition Era: $1 < z < 4$

During the 13.7 billion years of the cosmic time, the era of $1 < z < 4$ is of particular interest, in terms of star formation, stellar mass content, and galaxy morphology. First, although the increase of cosmic star formation rate density (SFRD) with redshift is well studied out to $z \sim 1$ (e.g., Hopkins, 2004; Hopkins & Beacom, 2006), the question of whether the SFRD has a broad peak during $1 < z < 4$ is still far from being finally solved (e.g., Hopkins, 2004; Hopkins & Beacom, 2006; Pérez-González et al., 2008; Chary & Pope, 2010). Furthermore, if such a peak exists, what is the mechanism that turns off the bulk of star formation in the universe? Second, being related to the evolution of the SFRD, the assembly history of massive ($> 10^{11} M_{\odot}$) galaxies is still in question. A large number of massive galaxies is found at $z \sim 2$ (e.g., Daddi et al., 2004b; Fontana et al., 2004; Glazebrook et al., 2004; Saracco et al., 2005), but only a few of them are found at $z > 3.5$ (e.g., Mobasher et al., 2005; Dunlop et al., 2007; Rodighiero et al., 2007; Wiklind et al., 2008; Mancini et al., 2009). This dearth of massive galaxies at high-redshift raises the question of when and how these giants were largely assembled in the universe. Last but not the least, the morphology of galaxies also undergoes a transition at $z \sim 3$. Although being studied in detail in the local universe and even being traced back to $z \sim 1.5$ (van den Bergh et al., 2000), the Hubble sequence is believed not yet in place at $z \sim 3$ (Giavalisco et al., 1996; Conselice et al., 2004; Ravindranath et al., 2006), because a large fraction of galaxies in that epoch has irregular shapes (chain-like, clumpy, multiple cores, etc.). Therefore, the origin and emergence of the Hubble sequence remains an open question. To answer

all the above questions requires observational studies on the physical properties (e.g., star formation rate, stellar mass, and morphology) of galaxies at $1 < z < 4$.

Two most fundamental observational descriptions of galaxy formation and evolution across the cosmic time are the star-formation-rate density (SFRD) and stellar mass density (SMD), which are also straightforward quantities provided by theoretical models. The former tells us how many stars were being formed at a give cosmic time, and the later tells how many stars had been formed at a given cosmic time. Hopkins (2004) and Hopkins & Beacom (2006) compiled from literature extensive measurements of SFRD from $z \sim 0$ to $z \sim 6$, using a variety of star-formation rate indicators, including rest-frame UV, far-IR, radio, and X-ray luminosities as well as emission lines ($H\alpha$ and $[OII]$). Bouwens et al. (2007, 2011) extended the measurement to higher redshift, $z \sim 8$, by integrating the rest-frame UV luminosity functions along redshift. Both found that the evolution of the SFRD increases from $z \sim 8$ to $z \sim 4$, then remains roughly constant from $z \sim 4$ to $z \sim 2$, and finally declines by an order-of-magnitude from $z \sim 2$ to $z \sim 0$.

The determination of the SMD across redshift is more difficult, mainly due to the uncertainty in the step of converting light into stellar mass. As shown in Marchesini et al. (2009), the SMDs at $2 < z < 3$ in the literature, when integrated over a fixed range in stellar mass ($10^8 < M_{\text{star}}/M_{\text{sun}} < 10^{13}$), vary by a factor of ~ 3 . At $z \sim 2$, the reported fraction of the local SMD that is in place ranges from $\sim 8 - 25\%$, while that number drops to $\sim 4 - 12\%$ at $z \sim 3.5$. Besides measurement uncertainties, the puzzle of the inconsistency between SFRD and SMD also worries astronomers. Naively, integrating the SFRD over cosmic time and taking into account of stellar mass loss and recycling, one would expect to obtain the SMD at a given redshift. But such effort failed, especially during the redshift range of $1 < z < 4$. The solution, which could be a time-variable initial mass function (IMF) or a steeper faint end of the rest-frame UV luminosity function, is still unknown. Other issues of SMD, such as the flat shape

at low-mass end (overpredicted by theoretical models) and the existence of massive galaxies (marginally underpredicted by theoretical models), all ask for a complete census of galaxies of all types in the redshift range: $1 < z < 4$.

Another feature of local galaxies, the appearance of the Hubble sequence and bimodality, is also a core topic in the observation of high-redshift galaxies. Based on the COMBO-17 survey, Bell et al. (2004) demonstrated that bimodality is detected in the color–magnitude diagram up to $z \sim 1$. Now, using the results from recent near- and mid-IR-selected surveys, other groups have been trying to investigate the existence of galaxy bimodality at even higher redshifts. Using a sample of Spitzer/IRAC $4.5\mu\text{m}$ -selected objects from the GMASS survey with optical through mid-IR SEDs, Cassata et al. (2008) demonstrated the existence of the bimodality up to $z \sim 2$ in the rest-frame U - B color of their galaxies. Brammer et al. (2009) found bimodality in the rest-frame U - V color of a large sample of galaxies selected from the NEWFIRM Medium-Band Survey (NMBS) up to $z \sim 2.5$. Kriek et al. (2008) detected a red sequence in rest-frame U - B colors at $2 < z < 3$. They also found that these high-redshift red-sequence galaxies are characterized by little or no ongoing star formation, with strong Balmer breaks indicating that they are likely in a post-starburst phase. Williams et al. (2009) detected a bimodality in the space of rest-frame U - V vs. V - J color–color space up to $z \sim 2$. Their two-color diagram reveals similar evidence on color bimodality as the color–magnitude (or color–stellar mass) diagram, but is less suffered from the influence of dust reddening. Kriek et al. (2009) studied morphology of spectroscopic sample of massive (both quiescent and emission-line) galaxies at $z \sim 2.3$. Their sample clearly separates into two classes in a color-stellar mass diagram: the large star-forming galaxies that form the blue cloud, and the compact quiescent galaxies on the red sequence. Although their sample is small, the study shows evidence that a Hubble sequence of massive galaxies with strongly correlated galaxy properties is already in place at $z > 2$. The existence of the red sequence and blue cloud as well as

their evolution along redshift provide important constraints on theoretical models of galaxy formation and evolution.

1.4 Open Questions

The core question of galaxy formation and evolution is **when and how today’s Hubble Sequence has been formed**. Since the morphology type, spectral type, and color of local galaxies are broadly correlated, the answer should provide explanations not only on how galaxies are shaped, but also on how their star-formation activity is turned off, and on how their stellar component becomes aged with their morphology changes. The question thus contains the following aspects:

1. When did the passive galaxies appear in the universe?
2. What turned off the star-formation activity in galaxies, making them passive as well as making the cosmic SFRD decline?
3. How were today’s bulges/spheroids formed?
4. What is the role that the environment galaxies reside in playing on their formation and evolution?

In order to answer the above questions, a successful model of galaxy formation and evolution should be able to reproduce, both qualitatively and quantitatively, the observed diversity among galaxy properties — structure, stellar and ISM content, and dynamics — and their evolution along redshift.

Galaxies at $z = 1-4$ provide important criteria and stages “in act” for such tests. Generally, the morphologies of galaxies at $z > 2$ are characterized by two important differences with respect to those of local galaxies. First, the traditional Hubble sequence of regular spirals and elliptical galaxies has not been place by $z \sim 2$, and a much higher frequency of clumpy, irregular morphologies is observed among star-forming

systems (e.g., Lotz et al., 2006; Ravindranath et al., 2006)). Understanding how these clumpy structures formed and eventually vanished in the local universe is crucial for understanding the formation of today’s bulge and disk in spiral galaxies. Second, both star-forming and quiescent galaxies are more compact at fixed stellar mass or rest-frame optical luminosity Buitrago et al. (e.g., 2008). Especially for passive galaxies, recent studies (e.g., Daddi et al., 2005; Trujillo et al., 2006, 2007; van Dokkum et al., 2008) showed that most massive passive galaxies at $z > 1.5$ are, on average, ~ 5 times smaller and ~ 50 times denser than their local counterparts. The physical mechanisms of such a dramatic size evolution is still unknown.

This thesis is motivated by the lack of understanding on the above two unsolved questions in the current study of the formation and evolution of galaxies at $1 < z < 4$. In Chapter 2, I will present the tools that we use to study high-redshift galaxies. The tools include images and catalogs as well as methods of deriving physical properties of galaxies. I will then present a study on the physical properties of giant clumps in a sufficient large sample of star-forming galaxies at $z \sim 2$, using the newly observed images from HST/WFC3, in Chapter 3. To shed a light on the mechanisms of the dramatic size evolution of passive galaxies from high redshift to the local universe, I will study the color gradient of passive galaxies at $z \sim 2$ in Chapter 4. I will then push the boundary to higher redshift in Chapter 5 to search for both passive galaxies and dusty star-forming galaxies at $z \sim 3$ to answer the basic question: when the passive galaxies appeared in the universe. Finally in Chapter 6, the results are summarized and the future developments are discussed. Throughout the paper, we adopt a flat Λ CDM cosmology with $\Omega_m = 0.3$, $\Omega_\Lambda = 0.7$ and use the Hubble constant in terms of $h \equiv H_0/100 \text{ km s}^{-1} \text{ Mpc}^{-1} = 0.70$. All magnitudes in the paper are in AB scale (Oke, 1974) unless otherwise noted.

CHAPTER 2

TOOLS

A few tools are needed to study the high-redshift universe. First, we need large-area sky surveys that are deep enough to image high-redshift galaxies and wide enough to overcome cosmic variance. These surveys are preferred to cover a long wavelength baseline to probe and diagnose emissions from various components of galaxies, such as young stars, old stars, and dust. Second, a catalog should be constructed based on the surveys to record the positions and fluxes of the observed galaxies in different wavelengths, taking into account of the change of resolutions and confusion along wavelength. Last, a method is needed to convert the observed fluxes into physical quantities (SFR, stellar mass, age, etc.) of the galaxies.

2.1 Images

An ideal survey of studying the high-redshift universe is the Great Observatories Origins Deep Survey (GOODS), well balanced between depth and width. GOODS has observed two fields in the southern (GOODS-S) and northern (GOODS-N) sky with various telescopes and instrument combinations, from X-ray to sub-millimeter and radio. Relevant to our study here in GOODS-S (GOODS-S) are imagings of VLT/VIMOS ultra-deep U-band (Nonino et al., 2009), *HST*/ACS BViz (Giavalisco et al., 2004), VLT/ISAAC JHKs (Retzlaff et al., 2010), Spitzer/IRAC 3.6, 4.5, 5.7, 8.0 μm (Dickinson et al. in preparation), and Spitzer/MIPS 24 μm . GOODS-N has the same space-based imagings. Besides, it has the KPNO U-band image and the ground-based near-infrared (NIR) images observed through CFHT WIRCAM J- and

K-band (Lin et al. 2011, in preparation; also see Wang et al., 2010). Table 2.1 summarizes the sensitivity (limiting magnitude of S/N=5 for a point source) and resolution, namely the full-width-half-maximum (FWHM) of point spread function (PSF), of all bands in GOODS that are used in this thesis.

Table 2.1 Sensitivity and Resolution of GOODS Filters

Filter	Sensitivity (limiting magnitude of S/N=5 for point source)	Resolution (FWHM of PSF)
VIMOS U	28.0	0.8''
CTIO U	25.8	~1.5''
KPNO U	27.1	1.15''
ACS F435W (B)	28.7 (GOODS) / 29.4 (HUDF)	0.08''
ACS F606W (V)	28.8 (GOODS) / 29.8 (HUDF)	0.08''
ACS F775W (i)	28.3 (GOODS) / 29.7 (HUDF)	0.08''
ACS F850LP (z)	28.1 (GOODS) / 29.0 (HUDF)	0.09''
WFC3/IR F098M (Y _s)	27.2 (ERS)	0.12''
WFC3/IR F105W (Y)	29.0 (HUDF)	0.12''
WFC3/IR F125W (J)	27.55 (ERS) / 29.0 (HUDF)	0.13''
WFC3/IR F160W (H)	27.25 (ERS) / 29.0 (HUDF)	0.15''
ISAAC J	25.0	~0.5''
ISAAC H	24.5	~0.5''
ISAAC K _s	24.4	~0.5''
CFHT/WIRCAM J	24.6	~0.8''
CFHT/WIRCAM K	24.2	~0.8''
IRAC 3.6 μ m (ch1 or L)	26.1	1.7''
IRAC 4.5 μ m (ch2)	25.5	1.7''
IRAC 5.8 μ m (ch3)	23.5	1.7''
IRAC 8.0 μ m (ch4)	23.4	1.9''
MIPS 24 μ m	20.4	6''

One small patch of GOODS-S is of particular importance and interest for our study: the Hubble Ultra Deep Field (HUDF), which has been observed by to date the deepest and sharpest optical and NIR instrument. The ultra-deep ACS images in the HUDF (Beckwith et al., 2006) cover an area roughly equal to the footprint of the ACS/WFC FOV in the same four filters as the GOODS ACS program, namely F435W (B), F606W (V), F775W (i), and F850LP (z) down to a depth of 29.4, 29.8, 29.7, and 29.0 mag (5σ , 0.35''-diameter aperture), respectively. We use the publicly available

images, which have been rebinned to the same pixels scale as the GOODS/ACS mosaics, namely $0.03''$ per pixel ($0.6\times$ the original ACS pixel scale).

The HUDF WFC3/IR data are taken from the *HST* Cycle 17 program GO-11563 (PI: G. Illingworth), which aims at complementing the HUDF and the two HUDF05 parallel fields (Oesch et al., 2007) with WFC3/IR images in Y (F105W), J (F125W), and H (F160W) of matching sensitivity, ~ 29 mag (Bouwens et al., 2010; Oesch et al., 2010). Here we use only the first epoch of the images, released in September 2009, which includes 18 orbits in Y, 16 orbits in J, and 28 orbits in H. We have carried out our independent reduction of the raw data, and after rejecting images affected by persistence in the J band, our final stacks reach 1σ surface brightness fluctuations of 27.2, 26.6 and 26.3 AB/''² in the three bands, respectively, over an area roughly equal to the footprint of the WFC3/IR camera ($2.1'' \times 2.1''$). We have drizzled the WFC3 images from their original pixel size of $0.121'' \times 0.135''$ to $0.03''$ per pixel to match the scale of the GOODS and HUDF ACS images.

As an early program, the HST/WFC3 Early Release Science (ERS) observation (Windhorst et al., 2010) covers $40\sim 50$ square arcminutes of GOODS-S in 10-bands. The data used in this thesis are its NIR observations, i.e., F098M (Ys), F125W (J) and F160W (H) images. The 50% completeness limit for $5\text{-}\sigma$ detections for typical compact objects (circular aperture with radius of $0.04''$) is 27.2, 27.55 and 27.25 for Ys, J and H. We re-processed the images and drizzled them to a $0.06''$ per pixel scale and registered to the GOODS WCS. ERS NIR imagings are shallower than that of HUDF, but cover a larger sky area.

2.2 Catalogs

A difficulty of constructing multi-wavelength photometry catalog for a survey whose observations cover a long wavelength baseline is to overcome the various resolutions and deblendings in different bands. As can be seen in Table 2.1, the resolution

in GOODS changes from $0.08''$ (ACS) to a few $''$ (IRAC), by a factor of more than twenty. As a result, close companions that are well separated in ACS images could be blended into one source in IRAC images. How to measure the IRAC fluxes for each companion is challenging.

In this thesis, to robustly measure the photometry of objects in all above bands with mixed resolutions, we use a software package with object template-fitting method (TFIT, Laidler et al., 2007). For each object, TFIT uses the spatial position and morphology of the object in a high-resolution image to construct a template. This template is then downgraded to lower resolutions and fit to the images of the object in all other low-resolution bands. During the fitting, the fluxes of the object in low-resolution bands are left as free parameters. The best-fit fluxes are considered as the fluxes of the object in low-resolution bands. These procedures can be simultaneously done for several objects which are close enough to each other in the sky so that the deblending effect of these objects on the flux measurement would be minimized. Experiments on both simulated and real images show that TFIT is able to measure accurate isophotal photometry of objects to the limiting sensitivity of the image (Laidler et al., 2007; Lee et al., 2012).

Catalogs of different fields (ERS, GOODS-S and GOODS-N) are generated based on different detection bands. In the ERS catalog, we use WFC3/IR H-band as the detection band as well as the high-resolution template of TFIT. ACS BViz and WFC3 YJH isophotal photometry is measured in dual-image mode by SExtractor based on H-band detection. U-band, ISAAC Ks-band and IRAC 4 channels' photometry is measured through TFIT. For both GOODS fields, the ACS z-band is chosen as the detection band. ACS isophotal photometry is measured in dual-mode by SExtractor, while other bands' photometry is measured by TFIT with z-band template. All SExtractor isophotal and ground-based TFIT (isophotal) fluxes are converted to total fluxes by multiplying a aperture correction factor, which is the ratio of SExtractor

FLUX_AUTO and FLUX_ISO of the detection band of each field (H-band for ERS and z-band for both GOODS fields).

In addition to the above bands, the GOODS fields are also observed by the Spitzer MIPS $24\mu\text{m}$ channel. Fluxes of sources in MIPS images are measured by fitting PSF to prior positions of objects detected in the Spitzer IRAC $3.6\mu\text{m}$ image. During the fitting, the positions of MIPS sources are allowed to wander by less than $0.6''$ from the IRAC prior position. After the first pass of fitting and subtraction of fitted MIPS sources, a second pass of fitting is run for MIPS sources that do not have IRAC counterparts. Sources detected and fit in both passes are combined together into the final MIPS catalogs. Details about the catalog of $24\mu\text{m}$ photometry can be referred from Magnelli et al. (2011). To combine the TFIT and MIPS catalogs, we match sources in the two catalogs with positions, allowing a maximum matching distance of $1.0''$.

2.3 Physical Properties of Galaxies

We use the method of SED-fitting to derive physical properties of galaxies from their observed multi-wavelength fluxes. This method fits the spectral energy distribution (SED, namely the multi-wavelength fluxes) of the galaxies to stellar population synthesis models. First of all, we should determine the redshift of the galaxies to obtain distance to convert the observed apparent quantities into the absolute ones. In this thesis, models used to measure photometric redshifts (photo-zs) are extracted from the library of PEGASE 2.0 (Fioc & Rocca-Volmerange, 1997). For each model, the fluxes in all bands are pre-computed and stored in a grid database. For each galaxy, we scan the database and calculate χ^2 values for models in all grid-points over the whole parameter space. The χ^2 value is calculated as

$$\chi^2 = \sum_i \frac{(F_{obs,i} - \alpha F_{model,i})^2}{\sigma_i^2}, \quad (2.1)$$

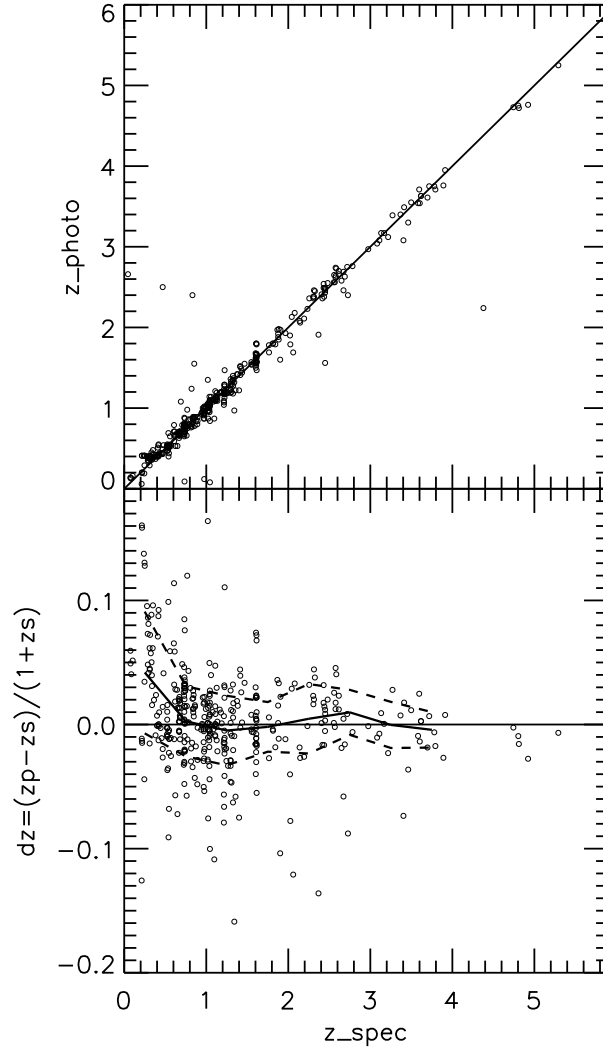


Figure 2.1 Accuracy of our photo-z measurement. *Top*: The comparison of photo-z and spec-z. The solid line shows the 1-to-1 correspondence. *Bottom*: The relative error as a function of redshift. For clarity, the bottom panel zooms into the range of $-0.2 < dz < 0.2$. The solid curve shows the mean of the relative error, while two dashed curves cover the 1σ confidence level.

where $F_{obs,i}$, $F_{model,i}$, and σ_i are the observed flux, model flux, and observational uncertainty in the i th band. α is a normalization factor, which is equal to stellar mass if $F_{model,i}$ is normalized to $1M_{\odot}$ in our pre-computed database. Instead of using the redshift with the least χ^2 , we integrate the probability distribution function of redshift (zPDF) and derive the likelihood-weighted average redshift. When the zPDF has two or more peaks, we only integrate the main peak that has the strongest power.

The accuracy of our photo-z measurement is shown in Figure 2.1, where we compare our photo-zs and spectroscopic redshifts (spec-zs) of galaxies that are spectroscopically observed in the ERS field. The *top* panel shows a very good agreement between photo-zs and spec-zs. The relative error (defined as $(z_{phot} - z_{spec})/(1 + z_{spec})$) has an almost zero mean (0.0005) and a very small deviation (0.037 after 3-sigma clipping). And the fraction of outliers, defined as $|\Delta z|/(1 + z) > 0.15$, is about 3.4%. The *bottom* panel shows the mean and standard deviation (after 3-sigma clipping) of relative errors in each redshift bin with a bin size 0.5. The means of the relative errors have no significant offset from zero at almost all redshift bins, especially for the range of $1 < z < 4$, which is of the most interest in this study. The high accuracy of our photo-z measurement enables us to statistically study the physical properties of our selected galaxies without spectroscopic redshifts.

The physical properties (stellar mass, specific star formation rate [SSFR], and dust reddening) of galaxies are measured through fitting their SEDs to models retrieved from the library of Charlot & Bruzual 2009 (CB09, an updated version of (Bruzual & Charlot, 2003)) with the Salpeter IMF (Salpeter, 1955). The lower and upper cuts on mass in the IMF are $0.1M_{\odot}$ and $100M_{\odot}$, respectively. The models consist of grid-points in a parameter space spanned by redshift, dust extinction $E(B-V)$, SFH (characterized by τ and age), and metallicity. The available values of each parameter are shown in Table 2.2. We apply the Calzetti Law (Calzetti et al., 1997, 2000) and the recipe of Madau (1995) to the models to account for dust extinction and the

opacity of IGM in the universe. The model with the least χ^2 is considered the best-fit model and its parameters are used as the measurements of the properties of the galaxy. During the SED-fitting, the redshift of a galaxy is fixed as its photo-z or its spec-z, if the latter is available.

In this thesis, when deriving the physical properties from the best fit template, we adopt the following definitions. To measure SFR, we average the SFH of the best fit template over the last 100 Myr, which allows a meaningful comparison between SFR derived through SED-fitting and that through rest-frame UV continuum empirically. The age of objects in our paper corresponds to the time from the onset of their star formation to their redshifts. And our stellar mass measurement accounts for the loss of stellar mass over time.

Table 2.2 Parameter Space Used for SED-Fitting

Parameter	Range
redshift	0.0 to 7.0 with a bin size of 0.01
$E(B-V)^1$	0.0 to 1.0, $\Delta E(B - V) = 0.05$
metallicity	0.004, 0.02, 0.08
age (Gyr)	$(1, 2, 3, 5, 8) \times 10^{-3}, 10^{-2}, 10^{-1}, 10^0, 10^1$, up to 13
τ (Gyr)	$(1, 2, 3, 5, 8) \times 10^{-3}, 10^{-2}, 10^{-1}, 10^0, 10^1$, and ∞

We note that in this thesis, the stellar population library used for deriving photo-z (PEGASE) is different from that used to derive physical properties (CB09). This reminds a widely debated question in astrophysics: whether the two different libraries induce inconsistency between the derived photo-z and physical properties? We argue that it is reasonable to use different libraries to derive photo-z and physical properties. First, redshift is not a physical parameter of galaxies. One can actually use an independent method, and hence an independent library, or even an empirical library without physical interpretation, to derive it before measuring the physical properties with another library. The key point is to choose a library that yields statistically the most accurate photo-z measurement. Second, in our method, we use the integrated zPDF, instead of the simple best-fit template, to measure photo-zs. It has largely

reduced the dependence of our results on the individual best-fit template. Therefore, we believe that using two libraries would not bias or induce inconsistency to our later analyses.

CHAPTER 3

KILOPARSEC-SCALE CLUMPS IN STAR-FORMING GALAXIES AT $Z \sim 2$

3.1 Introduction

To understand the physics that drives the formation of the Hubble Sequence, knowledge on the evolution of not only overall galaxies but also their components (e.g., bulges, disks, and super-massive black holes) is required. Thanks to the emergence of facilities with deep sensitivity and high resolution, e.g., HST/ACS, NICMOS and WFC3, galaxy morphology and structure now can be resolved into kpc scale, allowing a study on the properties of sub-structures at redshift of 2 or higher (e.g., Elmegreen & Elmegreen, 2005; Elmegreen et al., 2007, 2009a,b; Gargiulo et al., 2011; Guo et al., 2011; Szomoru et al., 2011). An interesting population of galaxies at $z \sim 2$, the peak of cosmic star formation activity, is the star-forming galaxies (SFGs) that have star formation rate (SFR) of tens to a few hundred $M_{\odot} \text{yr}^{-1}$. This population contributes a large fraction of the cosmic SFR and stellar mass density at the epoch (e.g., Daddi et al., 2007b; Grazian et al., 2007; Reddy et al., 2008; Ly et al., 2011; Rodighiero et al., 2011; Guo et al., 2012). In contrast to passively-evolving galaxies at $z \sim 2$, which have spheroid-like and compact morphology (e.g., Daddi et al., 2005; Trujillo et al., 2006, 2007; van Dokkum et al., 2008, 2010; Cassata et al., 2010), SFGs exhibit a wide diversity on their morphology, from smooth disk-like structure to irregular or merger-like structure (e.g., Conselice et al., 2004, 2008; Lotz et al., 2006; Ravindranath et al., 2006). A common and unique feature of SFGs at $z \sim 2$ is the existence of giant kpc-scale clumps, which are associated with all types of SFGs at $z \sim 2$ (e.g., Elmegreen &

Elmegreen, 2005; Elmegreen et al., 2007, 2009a; Bournaud et al., 2008; Genzel et al., 2008, 2011; Förster Schreiber et al., 2011) but resemble neither the star-burst regions nor bulges of low redshift SFGs.

These giant clumps are mostly identified in high-resolution HST optical ACS images (e.g., Elmegreen & Elmegreen, 2005; Elmegreen et al., 2007), which probe the rest-frame UV region at $z > 1$ at physical spatial resolution of ~ 1 kpc. They are also detected in HST near-infrared (NIR) images of NICMOS (Elmegreen et al., 2009a; Förster Schreiber et al., 2011), which observe the rest-frame optical wavelengths at $z > 1$. Rest-frame optical line emissions from NIR integral field spectroscopy observations of $z \sim 2$ disk galaxies also reveal such giant clumps (Genzel et al., 2008, 2011). Clumps are studied at even higher effective spatial resolution, up to a few ~ 100 pc, in strongly lensed objects at $1 < z < 3$ through rest-optical or CO line emission (e.g., Jones et al., 2010; Swinbank et al., 2010). However, the fraction of galaxies at $z \gtrsim 2$ that show clumpy structures is still uncertain. Lotz et al. (2006); Ravindranath et al. (2006) and Ravindranath et al. (2011, in prep.) concluded that clumpy galaxies are only about 30% of the population at $z \sim 3$, while Elmegreen et al. (2007) argued that the dominant morphology for $z \gtrsim 2$ is clumpy galaxies. Wuyts et al. (2012) measured the fraction of clumpy galaxies in a mass-complete sample of SFGs at $z \sim 2$ by using multi-waveband images and stellar mass maps. They found that the fraction depends sensitively on the light/mass map used to identify the clumps, decreasing from about 75% for clumps selected through rest-frame 2800Å images to about 40% for clumps selected through rest-frame V-band images or stellar mass maps.

The formation and subsequent evolution of these giant clumps, thought to be linked with the formation of bulges and thick disks in today's massive galaxies, are still unknown. In a widely held hypothesis based on theoretical works and numerical simulations, these kpc-scale clumps are formed through gravitational instability in gas-rich turbulent disks (e.g., Noguchi, 1999; Immeli et al., 2004a,b; Elmegreen et al.,

2008; Dekel et al., 2009b; Ceverino et al., 2010, 2012). This scenario is supported by the fact that high-redshift galaxies are gas-rich, with the gas-to-baryonic fraction of 20% to 80% (e.g., Erb et al., 2006; Genzel et al., 2008; Tacconi et al., 2008, 2010; Förster Schreiber et al., 2009; Daddi et al., 2010), possibly as a result of smooth and continuous accretion of cold gas flow (Kereš et al., 2005; Rauch et al., 2008; Dekel et al., 2009a; Cresci et al., 2010; Steidel et al., 2010; Giavalisco et al., 2011). Due to the clump interactions and dynamical friction against the surrounding disks, these clumps would migrate toward the gravitational centers of their host galaxies and eventually coalesce into a young bulge as the progenitor of today’s bulges or be disrupted by either tidal force or stellar feedback to form part of a thick disk (e.g., Bournaud et al., 2009; Dekel et al., 2009b; Murray et al., 2010; Genel et al., 2012).

To confirm or set constraints on the above scenarios, accurate measurements on the physical properties of clumps, such as stellar mass, age, SFR, and star formation history (SFH) as well as their radial variations across the host galaxies, are required. Such measurements, unfortunately, are currently lacking and challenging, because they require spatially resolved multi-band photometry or spatially resolved spectroscopy of each clump. In the work of Förster Schreiber et al. (2011), only two of their six galaxies have marginally enough information to enable a rough measurement on M/L and age for clumps, one with a single ACS/F814W - NIC2/F160W color and the other with H α equivalent width measured by the adaptive optical assisted SINFONI. Their finding of evidence of a systematic trend of older clumps at smaller galactocentric radius is consistent with the above scenarios, but suffers from a small number statistics. Elmegreen et al. (2009a) studied clump clusters and chain galaxies in the HUDF with *HST*/ACS and NICMOS images. They fit stellar population models to the multi-band photometry of clumps and bulges to derive their stellar masses and ages. However, the resolution of their NICMOS images are 3 times poorer than that of the ACS images so that obtaining uniform multi-band photometry for individ-

ual clump is affected by the blend of clumps in the low-resolution images. Recently, Wuyts et al. (2012) performed a detailed analysis on the spatially resolved colors and stellar populations of a large and complete sample of massive SFGs at $0.5 < z < 2.5$ in the ERS and CANDELS-Deep region of GOODS-South. The multi-wavelength images of *HST*/ACS and WFC3 allow them to study light maps in both rest-frame UV and rest-frame optical with similar spatial resolutions. Their results are consistent with an inside-out disk growth scenario with a “Christmas tree” model in which giant star-forming clumps are formed through gravitational instabilities in gas-rich disks, and then are quickly disrupted through feedbacks. Alternatively, the presence of blue and young star-forming clumps superposed on a redder underlying disk in their SFGs is also consistent with the inward migration scenario. However, Wuyts et al. (2012) focused on regions with excess surface brightness and did not identify clumps or subtract the diffuse light of host galaxies from clumps.

In this chapter, we try to measure the physical properties of clumps in SFGs at $z \sim 2$ in a sufficiently large sample, exploiting the advantage of high resolution and deep sensitivity of HST/ACS and WFC3 images in the HUDF. The recently available WFC3 images allow us to measure spatially resolved multi-band photometry across the rest-frame UV and optical regions at this redshift. Especially, the WFC3 F160W image observes light with rest-frame wavelengths longer than the Balmer break, enabling an accurate measurement on the age and stellar mass of clumps. On the other hand, the high resolution of WFC3 images ($0.15''$) enables us to resolve into ~ 1 kpc scale, a typical size of clumps, at $z \sim 2$ to effectively separate the light from clumps and their surrounding disks. We will compare the properties of clumps to those of their surrounding materials (Sec. 3.4) as well as study the radial variations of clump properties across their host galaxies (Sec. 3.5).

3.2 Sample Selection

We use the ultra-deep images of HUDF (Sec. 2.1) and the GOODS-S catalog (Sec. 2.2) to select SFGs with $1.5 < z < 2.5$ in the HUDF to study their clumps. Since we are measuring spatially resolved properties of galaxies through photometry of only seven bands (HST/ACS BViz and WFC3 YJH), in order to reduce the number of free SED-fitting parameters, we restrict our sample to only contain galaxies that have spectroscopic redshifts. The use of spectroscopically observed galaxies reduces a major uncertainty of SED-fitting, namely the uncertainty of (photometric) redshift. However, it also reduces the size of our sample and might bias our sample towards the bright end. In the HUDF, only 15 SFGs ($\text{SSFR} > 0.01 \text{Gyr}^{-1}$) have spectroscopic redshift (spec-z) at $1.5 < z < 2.5$ to enter our sample. We visually inspect the ACS z-band images of these galaxies and exclude 5 galaxies that have no obvious multi-clump morphology. The z-band, H-band, and z-H mosaics of the 10 galaxies in our sample are shown in Figure 3.1. The properties of the galaxies are shown in Table 3.1.

About 67% (10 out of 15 galaxies) of our sample are multi-clump systems in their optical ACS z-band (rest-frame UV) images. This result is quite similar to what Elmegreen et al. (2007) found, namely the majority of SFGs at $z \sim 2$ is clumpy galaxies. It is also consistent with the clumpy fraction that Wuyts et al. (2012) measured through rest-frame UV light. However, we also note that due to the use of spec-z, our sample is small and possibly biased toward UV bright galaxies. The bright UV emission may further suggest that our sample is biased toward bluer (e.g., van Dokkum et al., 2006; Förster Schreiber et al., 2009) and more active galaxies among all SFGs at $z \sim 2$. Moreover, as shown by the recent work of Wuyts et al. (2011), actively star-forming galaxies tend to have the large sizes (see also, e.g., Franx et al., 2008), which presumably introduces a further bias in our sample towards large galaxies. To draw a robust conclusion on the fraction of clumpy galaxies at

$z \sim 2$, a large sample (perhaps with photometric redshift) covering a wide range of both luminosity and stellar mass is needed. The ongoing 902-orbit *HST* Multi-cycle Treasure Program, Cosmic Assembly Near-infrared Deep Extragalactic Legacy Survey (CANDELS Grogin et al., 2011; Koekemoer et al., 2011) has already begun to provide deep images over a large sky area to answer this question as well as to provide robust statistics on clump properties, as demonstrated by Wuyts et al. (2012). We also anticipate that this thesis may lay the groundwork for future studies in the CANDELS survey.

Three galaxies in our sample are studied in Elmegreen & Elmegreen (2005): Galaxy 22284 (with ID 3484 in Elmegreen’s paper), 21739 (Elmegreen ID 3465+), and 27101 (Elmegreen ID 6462+). These galaxies, classified as ”clump-clusters” in the paper, were chosen by Elmegreen et al. because of their large angular size, good resolution into clumps and interclump regions. Elmegreen & Elmegreen (2005) used visual inspection on ACS i-band to identify clumps. They identified more clumps in these galaxies than we find (see Table 3.3). Although the different selection bands may contribute, the different numbers of identified clumps in the two works could be mainly due to different clump identification strategies. We conservatively ask clumps to be 3σ brighter than the diffuse components of the host galaxies (see next section), while Elmegreen & Elmegreen (2005) simply ask clumps to be bright compared to the sky background. We will compare the derived properties of clumps in the two studies in Sec. 3.6.1.

3.3 Clump Detection and Measurement

3.3.1 Clump Detection

We detect clumps from the HUDF HST/ACS z-band images (Sec. 2.1) through a hybrid of automated detection and visual inspection. In the image of each galaxy, a clump is identified if a region contains at least six contiguous pixels that are brighter

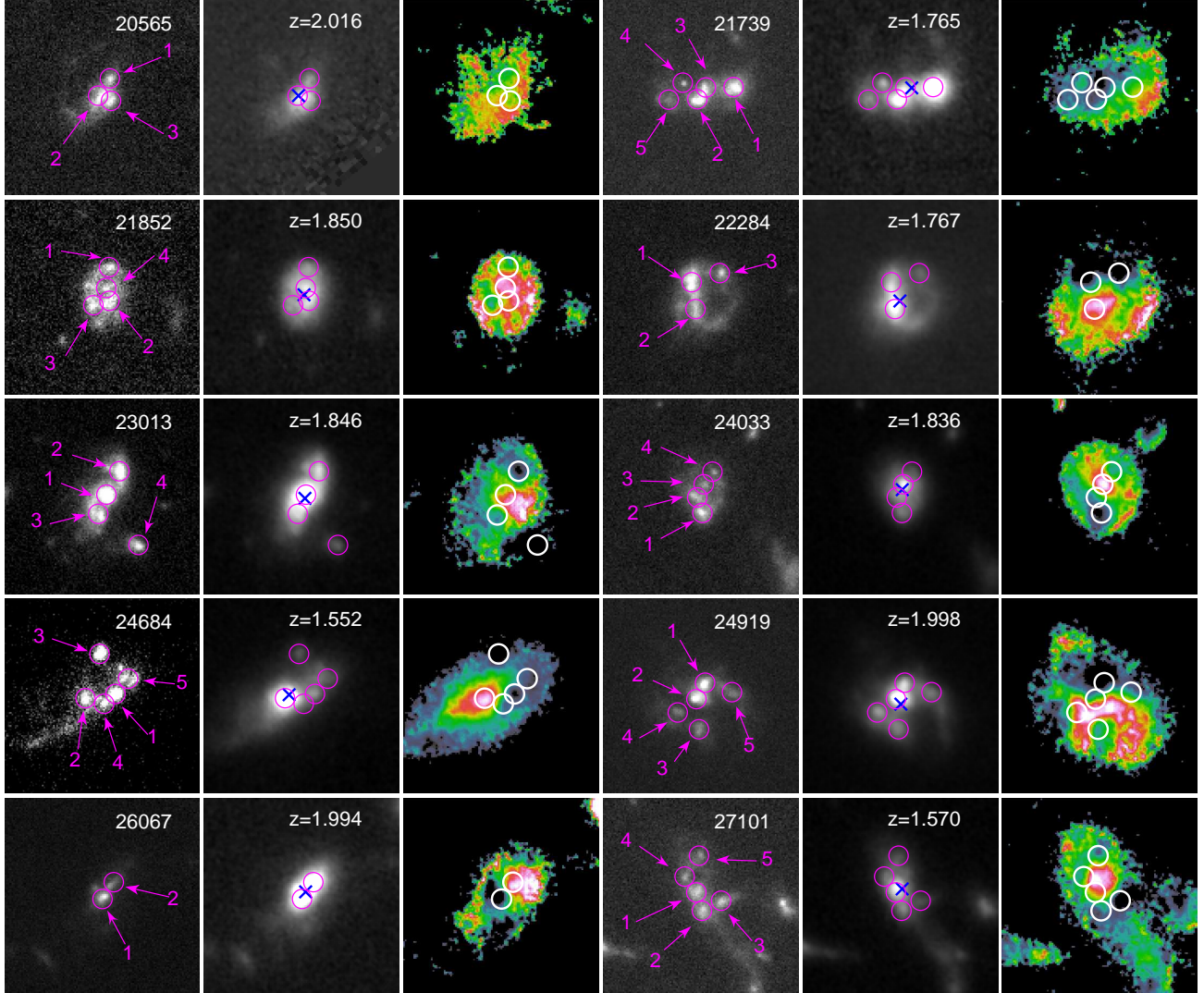


Figure 3.1 Montage of our 10 clumpy star-forming galaxies at $z \sim 2$. Each row shows images of two galaxies. For each galaxy, the panels from left to right show the z-band, H-band, and z-H maps. The GOODS v2.0 ID of each galaxy is shown in their z-band images, while redshift in their H-band images. Small circles (magenta in the z-band and H-band images, and white in the z-H maps) show the identified clumps. Blue “X”es in the H-band images show the light-weighted centers.

than 3σ confidence level of the average surface brightness of the galaxy. If two or more sub-structures above 3σ of the average surface brightness of the galaxy are adjoining, we visually separate them and determine the peak of each clump. The locations of each identified clumps are shown by circles in Figure 3.1.

Our choice of using the ACS z-band as the detection band of clumps raises an issue: how do the number and nature of the identified clumps depend on the choice of the detection band? The issue lies in two folds: (1) the impact of the spatial resolution of detection images on clump identification and (2) the impact of the use of different bands that are dominated by light of different stellar populations on clump identification. This issue was highlighted by Förster Schreiber et al. (2011), who found that, for one galaxy in their sample, clumps identified through WFC3 H-band and ACS i-band images have different physical proprieties. To test the robustness of our clump identification through the rest-frame UV band, we carry on the following two tests.

First, we smooth the ACS z-band images of our galaxies to match the resolution of WFC H-band and repeat our identification procedure. Only one clump (#4 of 24033) is missed, and three pairs of clumps (#2 and #3 of 20565; #2 and #3 of 21739; and #1 and #2 of 26067) are blended in the smoothed images. Given the fact that only 10% (4 out of 40) of our identified clumps are affected, we conclude that the change of resolutions of images (from ACS to WFC3) would not have significant impact on our clump identification and hence on our later results.

The second test is to identify clumps directly from WFC H-band images, which sample the evolved stellar populations at $z\sim 2$. Besides suffering from the impact of resolution, the H-band detection misses a non-negligible fraction, $\sim 20\%$, of clumps that are detected in the z-band. The missed clumps are #5 of 21739; #4 of 23013; #2 and #4 of 24033; #3 and #4 of 24684; #3, #4 and #5 of 27101. These clumps are missed mainly because of lower contrast of clumps against the background diffuse

stellar population in the H-band, and most of them are faint even in the z-band. Two clumps that are bright in the z-band but not detected in the H-band are #4 of 23013 and #3 of 24684. An important result in this test is that we do not find any new detected clumps through using the H-band images. This is different from the case of Förster Schreiber et al. (2011), and can be attributed to the ultra-deep rest-frame UV images used in our study, which allows us to probe even rest-frame UV faint (and hence very red) clumps. Thus, we conclude that our clump identification through ACS z-band images is superior to that through WFC H-band images, as the clumps detected in H-band are just a sub-sample of those detected in z-band. Using the z-band images, we are able to study the nature of clumps in a wide range of physical properties.

3.3.2 PSF Matched Images

For each identified clump, we measure its multi-band photometry from the HUDF HST/ACS BViz and WFC3 YJH images (Sec. 2.1). However, before carrying out the multi-band photometry an additional step was necessary, namely matching the angular resolution of the images in all the filters to that of the H band PSF to eliminate any artificial color gradients introduced by differences in image quality. This varies from FWHM $\sim 0.12''$ in the BViz bands to FWHM $\sim 0.15''$ in the YJH bands.

We measure the PSF in each band from seven well exposed and non-saturated stars whose SExtractor stellarity index in the i-band is larger than 0.98. These stars are used as input to the IRAF DAOPHOT package to generate an average PSF image in each band. DAOPHOT fits an analytical profile to the central region within $\sim 1 \times$ FWHM and adds the averaged outskirts of the stars to the best-fit profile. Once we build the PSF for each of the BVizYJ bands, we use the package IRAF PSFMATCH to calculate a smoothing kernel and convolve each image to match its resolution to that of the H-band.

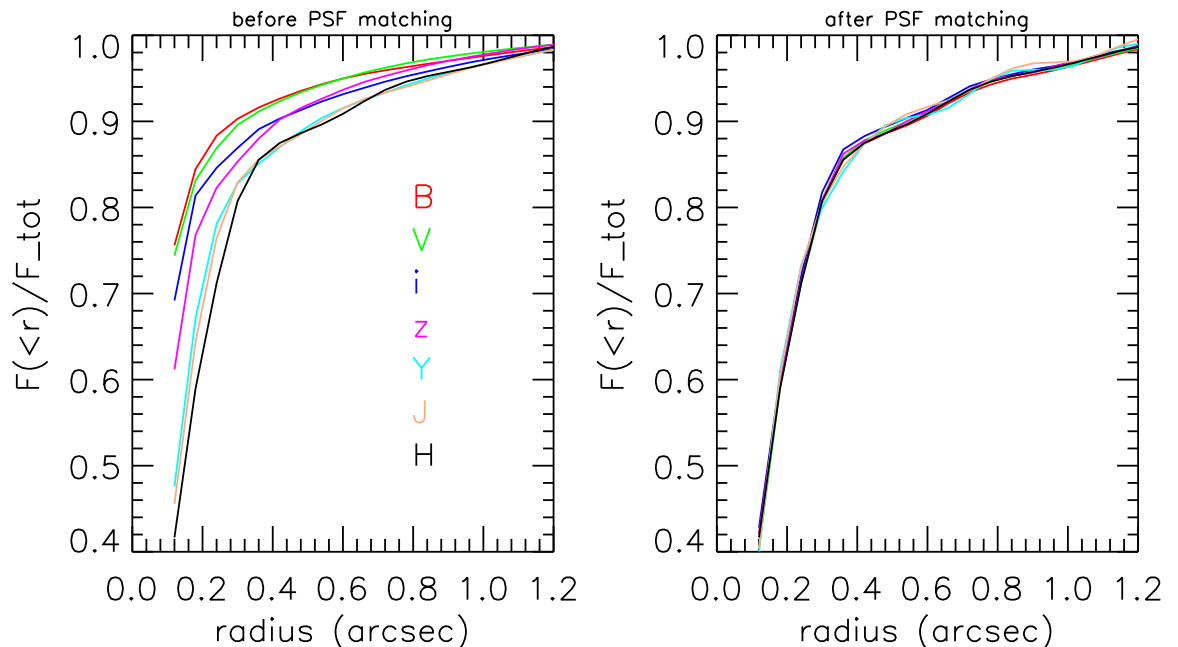


Figure 3.2 Fractional encircled energy of PSFs of 7 bands, before (*left*) and after (*right*) our PSF matching.

We test the effectiveness of PSF matching by comparing the fractional encircled energy of each PSF before and after the procedure. Figure 3.2 shows that after matching, the PSF in all bands have identical profile, especially within the central region (roughly $<0.4''$), where the gradient is steepest. There are some very small fluctuations in the wing ($0.4''$ to $1.0''$) of the Y and J band PSFs, due to differences in the airy rings of the original PSF. These, however, are smaller than 2% and thus we neglect them, since they will not cause any detectable bias in our analysis.

3.3.3 Clump Measurement

The fluxes of clumps in each band are measured within an aperture with size (diameter) of $0.3''$, about two times the FWHM of the H-band images. In order to separate the light of clumps from that of diffuse components of galaxies, we subtract a diffuse background from the flux of each clump. The surface brightness of the background is calculated as the average flux per pixel of the host galaxy, after all

clumps in it (circles with diameter of $0.3''$) are masked out. The product of the surface brightness and area of a clump is then subtracted from the flux of the clump. The diffuse background is subtracted for all clumps in all seven bands.

It is important to note that for all clumps in one galaxy, we subtract a *constant* diffuse background across the whole galaxy. This subtraction might be over-simplified, as the underlying diffuse or “disk” component of a galaxy is likely to have a non-constant profile (e.g., an exponential disk profile). In that case, we would over-subtract background for clumps in outskirts of the galaxy, while under-subtract it for those close to the center. We argue that this over-simplified subtraction would not significantly change our results on the comparison of clump properties and “disk” properties, because on average, only 15% of the raw flux of each clump is subtracted. However, it may induce false signals into our studies on the radial variation of clump properties across the host galaxies. We will discuss its influence later (Sec. 3.5.3). We also notice that the amount of subtraction is comparable to the photometric uncertainty that is caused by our use of the arbitrary $d=0.3''$ aperture. When we enlarge or shrink our aperture size by 2 pixels, the typical change on flux is about 15%~20%. Therefore, we use the difference of the fluxes measured at $d \pm 0.06''$ as the uncertainty of fluxes of clumps.

The physical properties of clumps are measured through fitting seven-band SEDs to stellar population synthetic models, as described in Sec. 2.3. The redshifts of all clumps are fixed at the spec-zs of their host galaxies during the fitting. Since the SFH of galaxies at $z\sim 2$ is controversial (e.g., Lee et al., 2009, 2010; Maraston et al., 2010; Papovich et al., 2011), we fit each clump with three different types of SFHs: exponential declining (τ -model), constant (CSF), and exponential increasing. Among the three fits of each clump, the one with the smallest reduced χ^2 is chosen as the best-fit model and its corresponding parameters are used as the physical properties of the clump. For each fitting parameter, we then use the standard deviation of the

three best-fit values from different SFHs as the uncertainty of the parameter, since we believe that the largest uncertainty of SED-fitting is rooted from the uncertainty of SFHs. We fix the metallicity to the solar value for all clumps. We will discuss the influence of metallicity variation among clumps on our results later (Sec. 3.5.4).

We also measure the fluxes and properties of the diffuse component (called “disk” thereafter) in each galaxy. The flux of a “disk” is measured by subtracting the total fluxes of clumps in its host galaxy from the flux of the galaxy. The physical properties of “disks” are measured with the same method that is used for clumps. We note that whether these diffuse components are real disks or not is still unknown. Actually, it is a key to understand the formation mechanisms of clumps. The existence of underlying disks is a necessary condition for the scenario of fragmentation due to gravitational instability. Kinematic studies, e.g., Förster Schreiber et al. (2009), are essential to understand the nature of the diffuse components. In this thesis, we just call them “disks” for simplicity. The properties of clumps and “disks” are shown in Table 3.2.

3.4 Physical Properties of Clumps

3.4.1 Rest-Frame UV–Optical Color of Clumps

The first straightforward test on the nature of our clumps is to study their positions in color–magnitude diagram (CMD). As introduced in Sec.1.2, present-day galaxies are well separated into two populations: red-sequence and blue cloud in CMD (e.g., Blanton et al., 2003a; Bell et al., 2004). This color bimodality is observed to exist up to $z \sim 2$ (e.g., Bell et al., 2004; Brammer et al., 2009; Mendez et al., 2011). The red-sequence is believed to consist of old and quiescent galaxies, while the blue cloud consists of young and active galaxies. The locations of clumps in CMD, namely among red-sequence or blue cloud, would shed a light on whether they are as quiescent as local red spheroids/bulges or still actively forming stars.

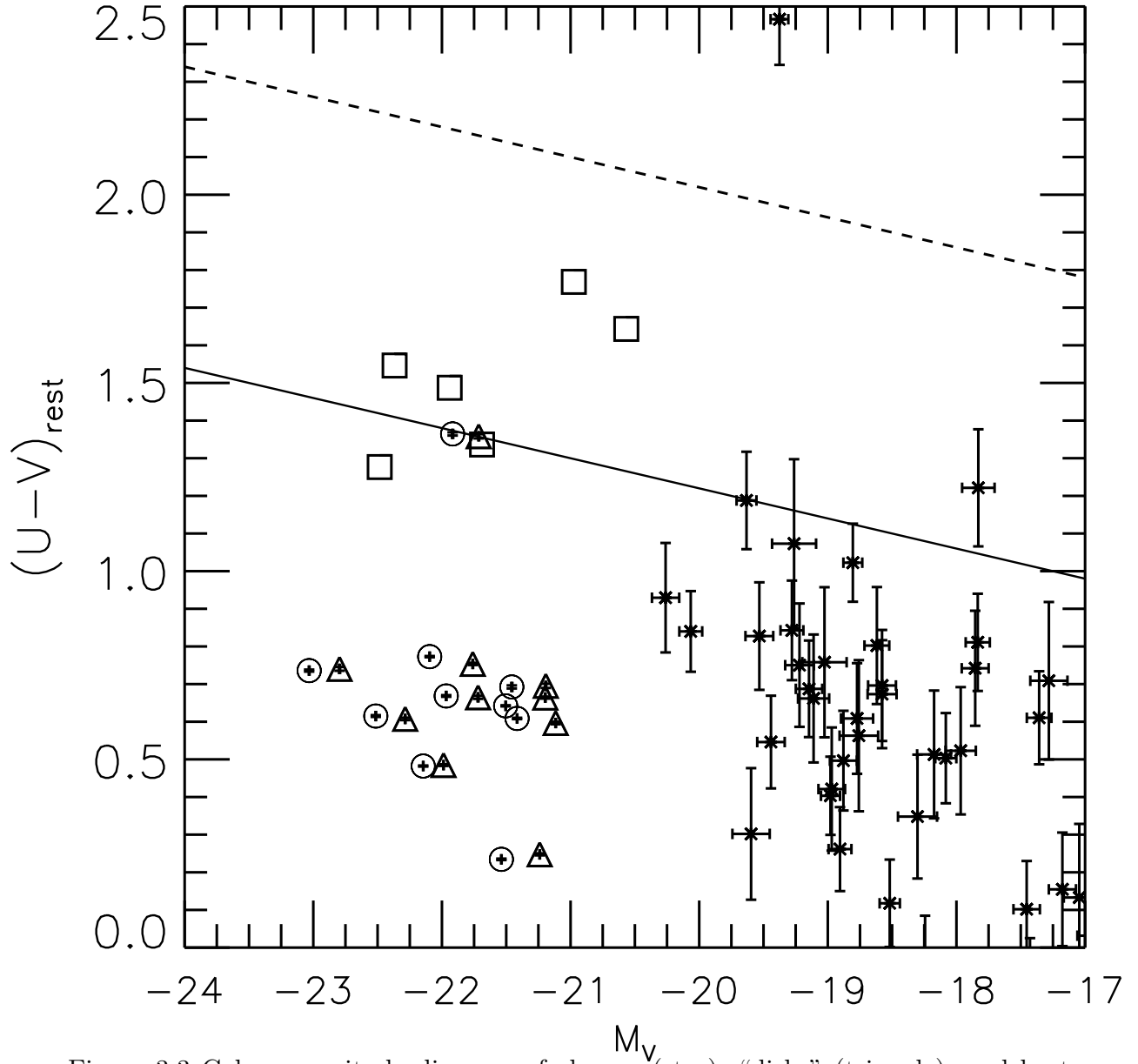


Figure 3.3 Color-magnitude diagram of clumps (star), “disks” (triangle), and host galaxies (circle). Together plotted are six passively-evolving galaxies at $z \sim 2$ (squares) from Guo et al. (2011). We also plot the separation of red-sequence and blue cloud at $z=0$ from Bell et al. (2004) (dashed line). The solid line is the extrapolation of the separation from $z=0$ to $z=2$ by using the formula of evolution of the separation of Bell et al. (2004).

Figure 3.3 shows the diagram of rest-frame (U-V) color vs. absolute rest-frame V-band magnitude for clumps (starred symbols). Rest-frame magnitudes are obtained through interpolating the observed seven-band photometry to corresponding rest-frame wavelengths, based on the redshift of each clump. In the figure, we also plot the “disks” (triangles) and host galaxies as a whole (circles). We also plot the six passively-evolving galaxies from Guo et al. (2011) (squares) in the figure as a passive reference. The separation of red-sequence and blue cloud shifts blueward as the redshift increases, because the cosmic age decreases with redshift. To obtain a red-blue separation line for $z \sim 2$, we extrapolate the separation line at $z=0$ of Bell et al. (2004) to $z=2$ with the empirical evolving formula proposed in their paper: $\langle U - V \rangle = 1.23 - 0.4z - 0.08(M_V - 5\log h + 20)$. The red-blue separation lines at $z=0$ and $z=2$ are shown by dashed and solid lines in the figure.

In general, clumps are as blue as their surrounding “disks” and host galaxies. Only few clumps reach above the red-blue sequence at $z=2$ and might have properties similar to quiescent galaxies at $z \sim 2$. Overall, the blue color indicates that the star formation activity is still strong and has not yet been widely quenched in clumps. We note that our clumps are identified through the excess of the rest-frame UV light in the diffuse background. Therefore, we expect them to have *bluer* color than their surrounding “disks”. However, Figure 3.3 does not support such expectation. What’s more, it shows that, compared with “disks” or host galaxies, clumps seem to have broader color dispersion. This broader scatter suggests that our clumps cover a wide range of physical properties, e.g., age, extinction, star formation histories, evolution stages, etc. This result seems contradictory to the simple “Christmas tree” model, in which clumps are rapidly disrupted once they have formed. In that case, the properties of clumps may concentrate within a narrow range. We will quantify the dispersion of clump colors in Sec. 3.4.4.

3.4.2 SFR–Stellar Mass Relation of Clumps

Figure 3.4 shows the SFR–stellar mass relation of clumps (red stars) as well as that of “disks” (blue triangles) and whole galaxies (black circles). SFR and stellar mass are measured through SED-fitting with various assumed SFHs as described in Sec. 3.3. The best linear fit for the relation of each population is also shown in the plot. In order to evaluate the significance of the SFR–stellar mass relation of both clumps and “disks”, we run bootstrapping 100 times to randomize the pair of SFR and stellar mass of clumps and disks and calculate the correlation coefficients (defined as $\sqrt{\text{COVAR}[X, Y]/(\text{VAR}[X] * \text{VAR}[Y])}$, where COVAR is covariance and VAR is variance of X and Y, and X and Y stand for stellar mass and $\log(\text{SFR})$) for both the observed and randomized relations. By comparing the correlation coefficients of both the observed and randomized relations, we find the relation of both clumps and “disks” are significant at at least 3σ level.

The SFR–stellar mass relation of clumps and “disks” have almost the same slope, although the two populations occupy different ends of the stellar mass range: the stellar masses of clumps spread over the range between $10^8 M_\odot$ and $10^{10} M_\odot$, while those of “disks” between $10^{10} M_\odot$ and $10^{11} M_\odot$. However, the normalization of the relation of clumps is about 5 times higher than that of “disks”, converting to a higher SSFR of clumps. The higher SSFR is consistent with the spectroscopic measures of Genzel et al. (2011).

The reason of the higher SSFR of clumps is important for understanding the nature of clumps, but is unfortunately still unknown. It could be due to the fact that the locations of clumps sample the very high end of the gas density distribution of host galaxies. As a sequence, the gas–to–stellar mass ratio is higher in clumps than in “disks”. This case is likely true, as these clumps are believed to form through gravitational instability in the gas-rich “disks”. Such process indicates a high gas density in their birth locations. However, based on our later analysis, the (projected)

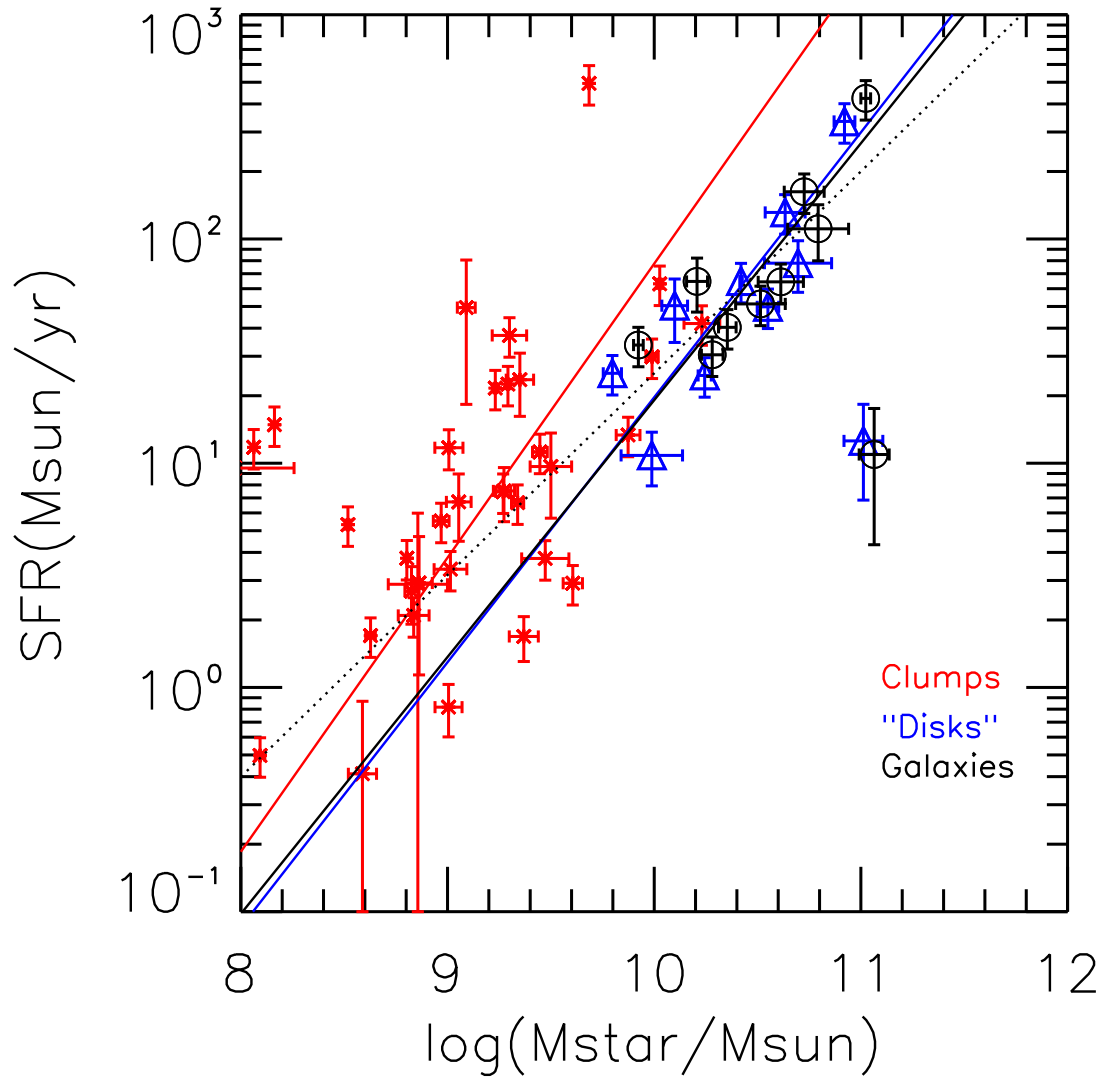


Figure 3.4 SFR–stellar mass relation for clumps (star), “disks” (triangle), and host galaxies (circle). The SFR–stellar mass relation of each population is fitted by a straight line (red, blue, and solid black for clumps, “disks”, and host galaxies, respectively). The dotted line is the relation of Daddi et al. (2007b) for BzK galaxies.

stellar mass density of clumps is also higher than that of "disks". Therefore, it is still uncertain whether the gas-to-stellar mass ratio of clumps is higher than that of "disks". If they turn out to be comparable, clumps would have higher efficiency to convert gas into stars to yield higher SSFR. In this case, other mechanisms, for example a different star-formation law, should be used to explain the higher star formation efficiency of clumps. Further observations on spatially resolved gas density (e.g., through ALMA) are required to investigate the star formation activity in clumps.

Figure 3.4 also shows that the SFR–stellar mass relation (or SSFR) of the galaxies as a whole has almost same slope and normalization as that of "disks". It suggests that "disks" contribute the majority fraction of SFR and stellar mass of the host galaxies. Clumps, on the other side, stand out as regions with enhanced SSFR in the "disks".

3.4.3 Contribution of Clumps to Host Galaxies

Figure 3.5 shows the fractional contributions of clumps to their host galaxies, in terms of rest-frame U-band and V-band luminosity, stellar mass, and SFR. We show the distribution of the contributions of both each individual clump (solid line) and the sum of all clumps in one galaxy (dashed line). For the U-band and V-band luminosity (top left and top right panels), the individual contribution of clumps runs from 1% to 10%, with a median of $\sim 5\%$, while the total contribution of all clumps sharply peaks around 20%. There is no obvious difference between the clump contributions to both luminosities. The clump contribution to stellar mass (bottom left) is similar to that of the light, with a broad distribution of individual contribution running from 1% to more than 10%, and a concentrated total contribution peaking around 20%. We note that the similar contributions to stellar mass and to light of individual clumps do not imply a similar M/L ratio among clumps. Actually, the M/L_V ratio of clumps

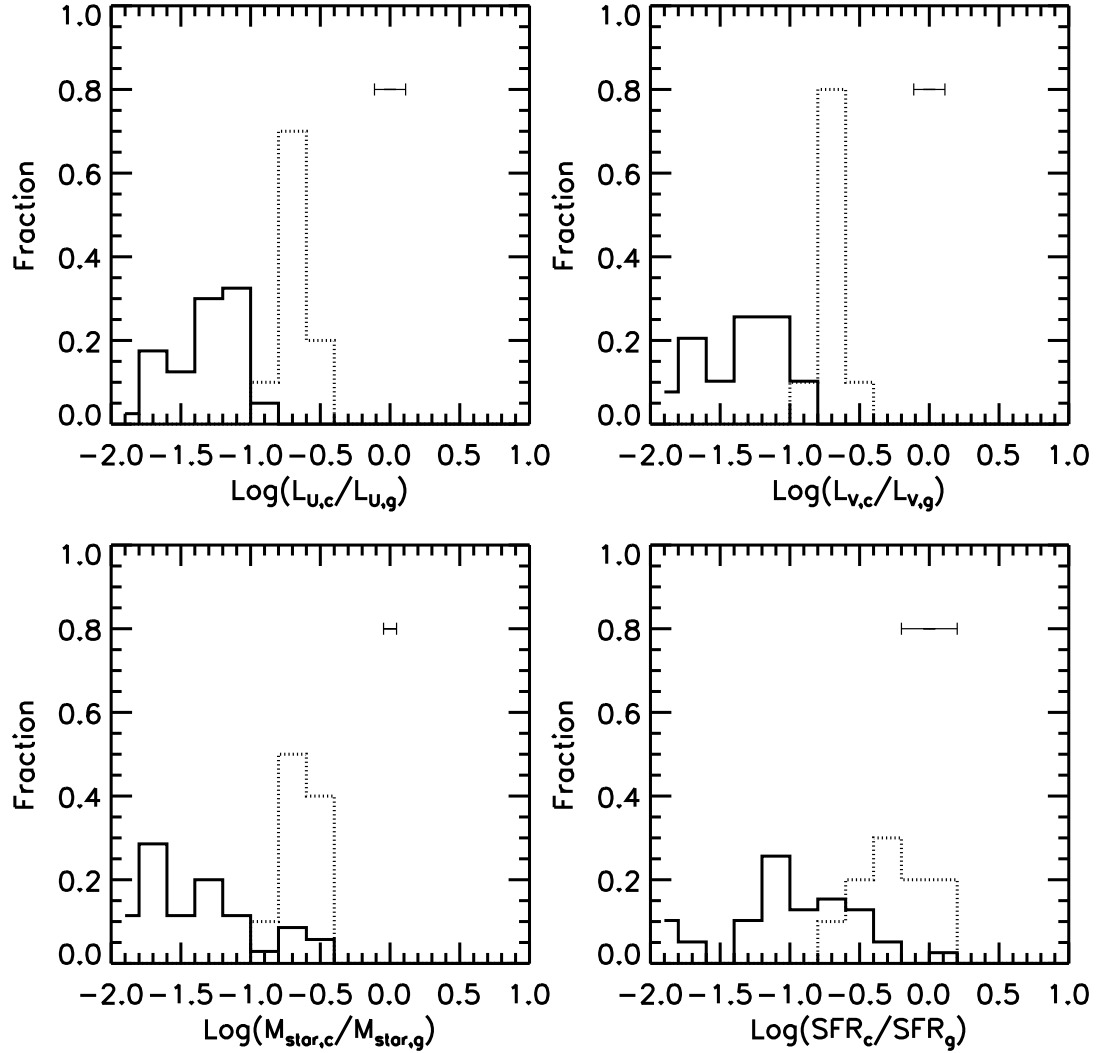


Figure 3.5 Fractional contributions of clumps to their host galaxies in terms of rest-frame U-band luminosity (top left), V-band luminosity (top right), stellar mass (bottom left), and SFR (bottom right). Solid histograms show the distributions of the contribution of each clump, while dotted lines show the distributions of the total contribution of all clumps in each host galaxies. The horizontal error bar in each panel shows the typical error of each measurement.

covers a wide range, from $\sim 0.05 M_{\odot}/L_{\odot,V}$ to several $M_{\odot}/L_{\odot,V}$, with the median of $0.5 M_{\odot}/L_{\odot,V}$ and the standard deviation of 0.5 dex. The widespread M/L ratio of clumps is consistent with our previous argument that clumps are found at different evolutionary stages.

The contribution of clumps to SFR (bottom right) is higher than that to light and stellar mass. The individual contribution peaks around 10%, while the total contribution peaks around 50%. The low contribution to stellar mass and high contribution to SFR are consistent with the fact the clumps have enhanced SSFR relative to “disks” or galaxies as a whole.

3.4.4 Clumps vs. “Disks”

Figure 3.6 shows the difference between clumps (red) and “disks” (blue) in terms of the distributions of UV–optical colors (top left), ages (top right), dust extinction (bottom left) and projected stellar mass densities (bottom right). Each distribution is fitted by a Gaussian function. The top left panel, which quantifies the CMD of Figure 3.3, shows that the mean UV–optical color of clumps are similar to that of disks ($U-V \sim 0.6$). However, the color distribution of clumps is broader than that of disks. The standard deviation of the former is 0.30, while that of the latter is 0.12. Clumps can be as red as $U-V \sim 1.2$ and as blue as $U-V \sim -0.2$, while “disks” are concentrated within $0.2 < U-V < 0.8$, except for one “disk”. The broader color distribution of clumps can be attributed to either different SFHs among clumps or different evolution stages of clumps.

Our SED-fitting method only provides limited information on SFHs, however, the distribution of ages of clumps gives us a hint that the broader color distribution of clumps is more likely associated with the evolution stages. On average, the ages of clumps are only slightly (0.2 dex) younger than that of “disks”. However, the ages of clumps have a broader distribution, covering the range from 0.01 Gyr to a few

Gyr, with the standard deviation of 2.1 dex. In contrast, the ages of “disks” are concentrated within 0.3 to 1 Gyr, with a standard deviation of 1.7 dex. Moreover, in Sec. 3.5, we will show that both color and age of clumps change with the galactocentric distance of clumps. Based on the trend of their radial variations, one can expect a loose correlation between colors and ages of clumps, which would support our speculation that the broader color distribution of clumps is due to the broad age distribution (and hence different evolution stages). However, we note that the age determination in SED-fitting is not robust and strongly depends on the assumed SFHs. As shown by the horizontal error bars in the top right panel, the uncertainty of age in our study, namely the standard deviation of the ages measured by SED-fitting with three different SFHs, is about 0.5 dex and 0.3 dex for clumps and “disks” respectively, comparable to the difference between the mean age of the two populations.

We also argue that other factors, such as extinction and metallicity, are not likely to be the major contributor of the broader color distribution of clumps. The difference of the $E(B-V)$ distributions of clumps and “disks” is not significant (the bottom left panel of Figure 3.6). The mean and standard deviation of the $E(B-V)$ distribution of clumps are 0.31 and 0.11, while those of “disks” 0.27 and 0.10. The differences of both mean and standard deviation of the two components are actually smaller than the typical uncertainty of our $E(B-V)$ measurement (~ 0.05). Although a few clumps do have very high dust extinctions, the insignificant difference between the $E(B-V)$ distributions of clumps and “disks” suggests that extinction is not a major contributor of the broader color distribution of clumps. Another possible reason of the broad color distribution of clumps is the metallicity variation among clumps. Since metallicity is not a free parameter in our SED-fitting, we cannot draw conclusions on the metallicity distribution of clumps. Instead, we will discuss the effect of metallicity variation in Sec. 3.5.4.

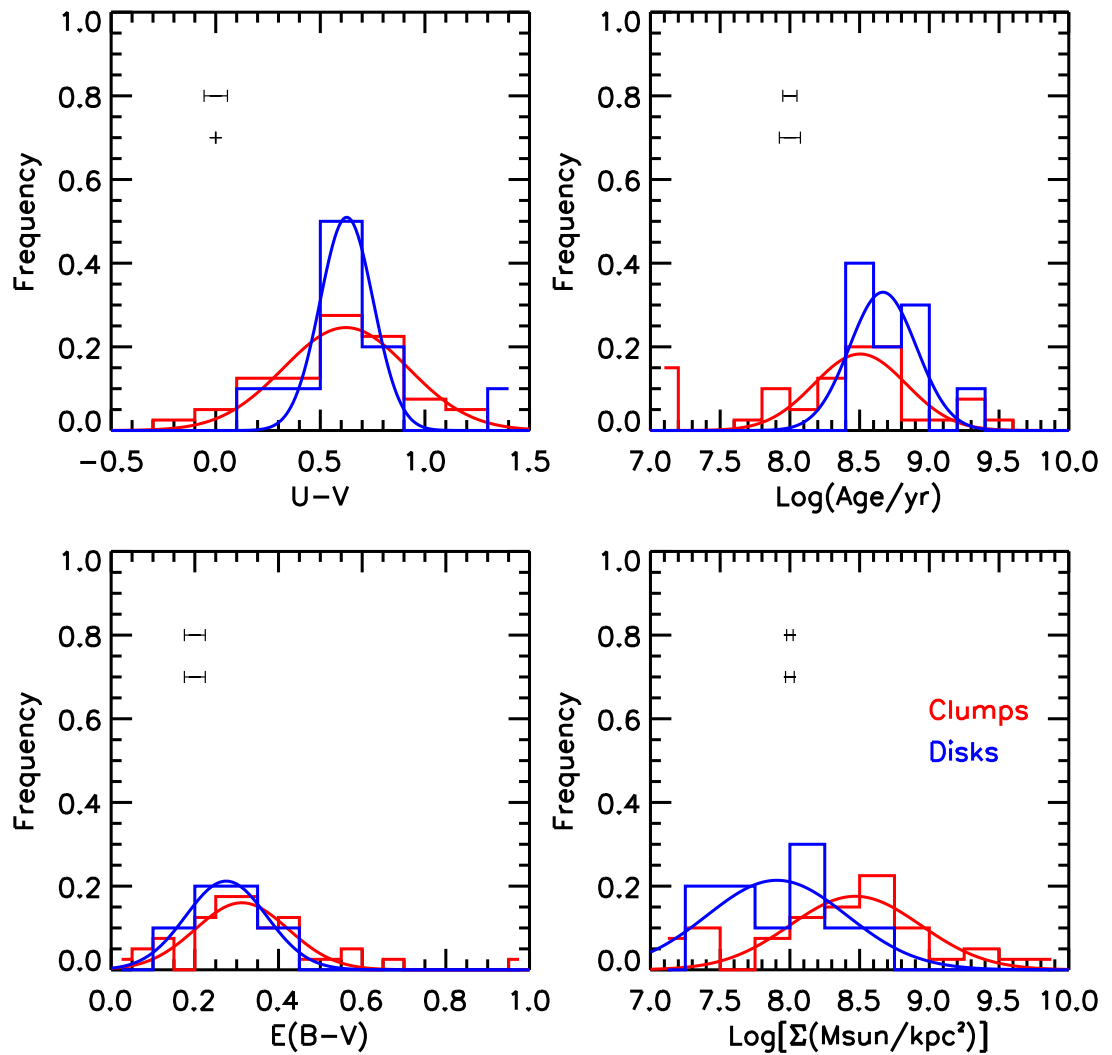


Figure 3.6 Comparisons between physical properties of clumps and their surrounding “disks”. Red histograms show the distributions of properties of clumps, while blue those of “disks”. Red and blue curves show the Gaussian fits to the red and blue histograms. Typical measurement errors are shown as horizontal error bars (upper for clumps and lower for “disks”) in each panel.

A more significant difference between clumps and “disks” comes from the distributions of their projected stellar mass densities. The high resolution of ACS z-band images allow us to resolve each clump and hence measure its projected stellar density. By comparing the FWHM of clumps (after subtracting diffuse background) to that of ACS z-band PSF, we find that all our clumps except one are (marginally) resolved in the ACS z-band image. The fraction of resolved clumps in our sample is higher than that in Förster Schreiber et al. (2011), who found 18 out of 27 of their NIC2 clumps are resolved. The higher fraction of resolved clumps in our study can be explained by the higher resolution of ACS z-band image ($0.12''$), compared to that of NICMOS NIC2 images ($0.15''$). However, we also caution that the measurements of the projected stellar density of clumps in our study may suffer from systematical uncertainty, because the size of clumps is not precisely determined. To do so requires a detailed investigation on the light profiles of clumps and their host galaxies simultaneously. In this work, instead, we simply use the size of the apertures that we use to measure photometry as the size of clumps. The size is about 2 times the FWHM of H-band PSF, equivalent to about 5σ of the PSF, and is believed to be a good representative of clump sizes. The projected stellar density measured with this size can be treated as an average density of a clump.

The bottom right panel of Figure 3.6 shows that clumps are on average 8 times denser than “disks”. This result is non-trivial, because we identify clumps based on z-band images, which, observing the rest-frame UV light, are more sensitive to star formation than to stellar mass. Identified as prominent sub-structures in the z-band images, these clumps are expected to have active star formation but not necessarily to be denser. Using the light from both rest-frame UV and optical bands, our SED-fitting method turns out to show that clumps are regions with not only enhanced SSFRs but also more concentrated stellar distributions.

The higher stellar surface densities of clumps are consistent with the hypothetical scenario that clumps are formed through gravitational instabilities (e.g., Noguchi, 1999; Immeli et al., 2004a,b; Bournaud et al., 2007, 2008; Elmegreen et al., 2008; Dekel et al., 2009b; Ceverino et al., 2010). Genzel et al. (2011) calculated the maps of Toomre Q -parameter for four galaxies in their sample and found that throughout the outer disks and toward the clumps, the Q -parameter is at or even significantly below unity. The small (<1) Q -parameter is evidence of gravitational instability. Since the total Q -parameter is inversely proportional to the sum of the molecular gas and stellar surface densities (see Eq. (2) of Genzel et al. (2011)), the regions with low Q -parameter (namely regions towards clumps) should have higher surface densities of gases and/or stars, as our results show. However, we note that the possibility that the instability is driven by other violent processes, such as interaction or merger, cannot be ruled out simply based on the estimation of Q -parameter.

3.5 Clumps across Host Galaxies

In a widely held view, clumps are expected to migrate towards the gravitational centers of their host galaxies due to dynamical friction against the surrounding disks or clump interactions and eventually coalesce into a young bulge in several dynamical timescales (~ 0.5 Gyr) to form the progenitor of today's bulges. Alternatively, they could also be disrupted by either tidal force or stellar feedback to form part of a thick disk (e.g., Escala & Larson, 2008; Dekel et al., 2009b). If clumps are able to survive the several dynamical timescales of migration, they are expected to exhibit a broad age dispersion, with older clumps generally closer to the galactic centers. Moreover, other physical properties of clumps would also change as the clumps migrate toward the galactic centers. For example, the gas outflows, as observed by Genzel et al. (2011), would be sufficiently strong to expel a large fraction of gas of clumps so that clumps are expected to become less efficient at forming stars when sinking toward

centers. In this section, to understand the evolution of clumps, we study the radial variations of colors and physical properties of clumps along their host galaxies. We also discuss the effect of diffuse background subtraction (see Sec. 3.3) on our results. We will also discuss the possibility of metallicity variation as an explanation of the observed color radial variation.

3.5.1 Radial Variation of Color

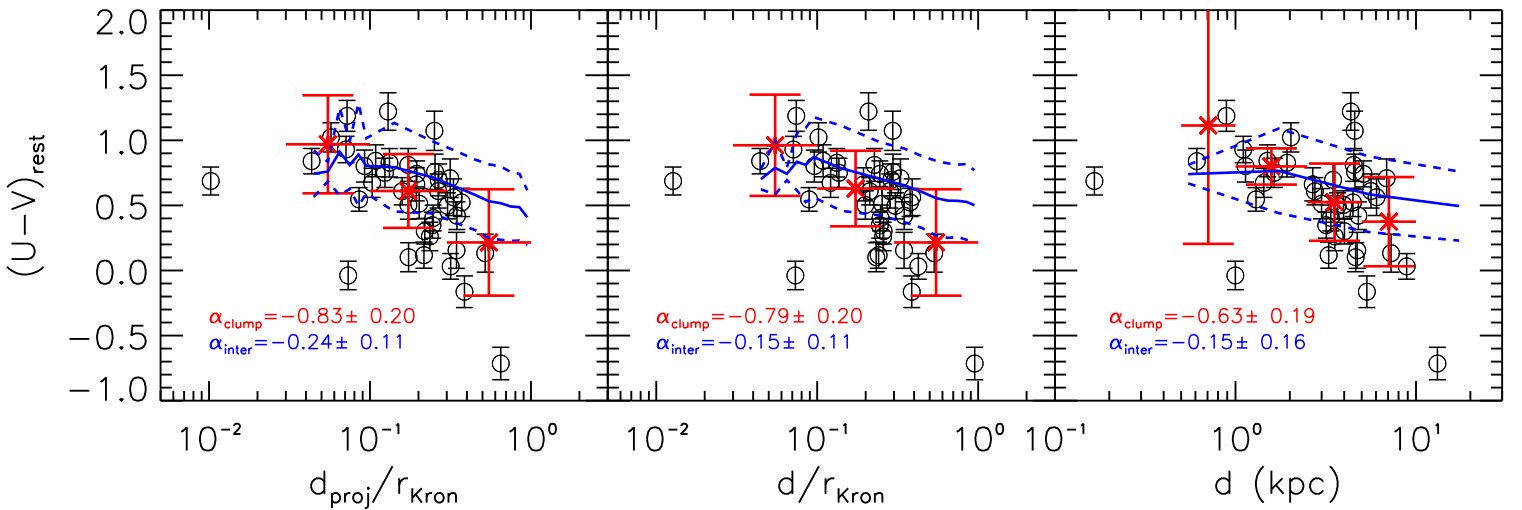


Figure 3.7 Radial variation of the rest-frame U-V color of clumps as a function of their galactocentric distances to the H-band light-weighted centers of their host galaxies. The distance is calculated in different ways in the three panels. *Left:* The distance is the projected distance, scaled by the H-band Kron radius of the host galaxy. *Middle:* It is the deprojected distance, scaled by the H-band Kron radius of the host galaxy. *Right:* It is the deprojected physical distance, in unit of kpc. To calculate the deprojected distance, we assume a circle configuration with the inclination angle equal to the axis ratio for each galaxy. In all panels, each circle with error bar stands for one clump. The red stars and red vertical error bars show the mean and 1σ deviation (after 3σ -clipping) of the clumps in each distance bin, while the bin size is shown by the red horizontal error bar. The solid and dashed blue lines in each panel show the mean and standard deviation of color variation of interclump pixels of all galaxies. The best-fit slope of the color gradients of clumps and interclump pixels are given in each panel.

Figure 3.7 shows the radial variation of the rest-frame U-V color of clumps across the host galaxies. We use the H-band light-weighted centers of host galaxies to

represent the galactic centers, as the H-band is closest to the peak of stellar emission in all available bands. We calculate the galactocentric distance of each clump in the following three ways and study the radial variation in each case, respectively: (1) projected distance, scaled by the H-band Kron radius of its host galaxy (left panel); (2) deprojected distance, scaled by the Kron radius (middle panel); and (3) deprojected physical distance, in unit of kpc (right panel). All panels show a clear trend that clumps close to the centers of their host galaxies have redder rest-frame UV/optical colors than those in the outskirts. Although the slope of the radial color variation (or color gradient), defined as $\alpha = \Delta(U - V)/\Delta\text{Log}(R)$, varies with the definition of the galactocentric distance, it is significant beyond the 3σ confidence level in all cases (the values of the slope can be read from Figure 3.7). Therefore, we conclude that the radial color variation is an intrinsic feature of clumps and not affected by the distance definition. In later analysis, we use the scaled projected distance, as it gives us the strongest signal of radial variation and is independent from the assumption of the circle configuration of galaxies, which is used in our calculation of the deprojected distance, but still very uncertain for our galaxies. With the projected distance, the average colors of clumps become redder by 0.8 mag from radius of $0.7 r_{\text{Kron}}$ to $0.07 r_{\text{Kron}}$. This picture is broadly consistent with the scenario of inward migration of clumps. However, since the color is governed by a few factors: age, dust extinction and metallicity, the radial variation of color itself only provides an indirect comparison with theoretical hypothesis. The radial variations of physical properties are needed to make a direct comparison with models.

There is one more issue that may also complicate the inference of the nature and fate of clumps from color variation and invalidate the inward migration scenario. It is the radial color variation of the diffuse components (“disk”) of our galaxies. If the “disks” exhibit the same radial color variation (or gradient), it is then very likely that clumps are formed and, after that, stay in the locations where they are observed

today. In this case, the radial variation of clumps can be explained by the radial variation of their host “disks”, because thus formed clumps would have same dust extinction and/or metallicity as that of their birthplaces in the host “disks”. In order to examine the possible color gradient of host “disks”, we measure the rest-frame U-V color of all interclump pixels (defined as pixels that are $0.3''$ away from the center of any clumps) and study their radial variation. The mean and standard deviation of the color of interclump pixels are shown as a function of galactocentric distances in Figure 3.7. Interclump pixels show the similar trend of color gradient as clumps: red in center and blue in outskirts. However, the slope of the color gradient of interclump pixels (α_{inter}) is significant at only 2σ level with the rescaled projected galactocentric distance, and decreases to even only 1σ level with the deprojected physical distance, indicating a mild color gradient. More importantly, α_{inter} is significantly, at least at 3σ level, larger (flatter) than α_{clump} , the slope of the color gradient of clumps. The values of α_{inter} and α_{clump} can be read from Figure 3.7. The significant difference between the two slopes suggests that (1) the color gradient of “disks” can only explain a small part of the color gradient of clumps and (2) the formation and evolution of clumps are somehow dynamically separated from those of “disks”. Therefore, a mechanism such like the inward migration is needed to explain the steeper gradient of clumps.

3.5.2 Radial Variations of Physical Properties

Figure 3.8 shows the radial variations of SSFR (top left), age (top right), E(B-V) (bottom left) and stellar surface density (bottom right) of clumps. As same as in Figure 3.7, the galactocentric distances of clumps are scaled by the H-band r_{Kron} of host galaxies. Clumps close to the centers of host galaxies have lower SSFRs, older ages, higher dust extinctions and higher stellar surface densities. On average, clumps located at $d = d_{proj}/r_{Kron} < 0.1$ have 4 or 5 times lower SSFR than those at $d > 0.5$. The average age of clumps at $d > 0.5$ is about 100 Myr, while that of those at $d < 0.1$

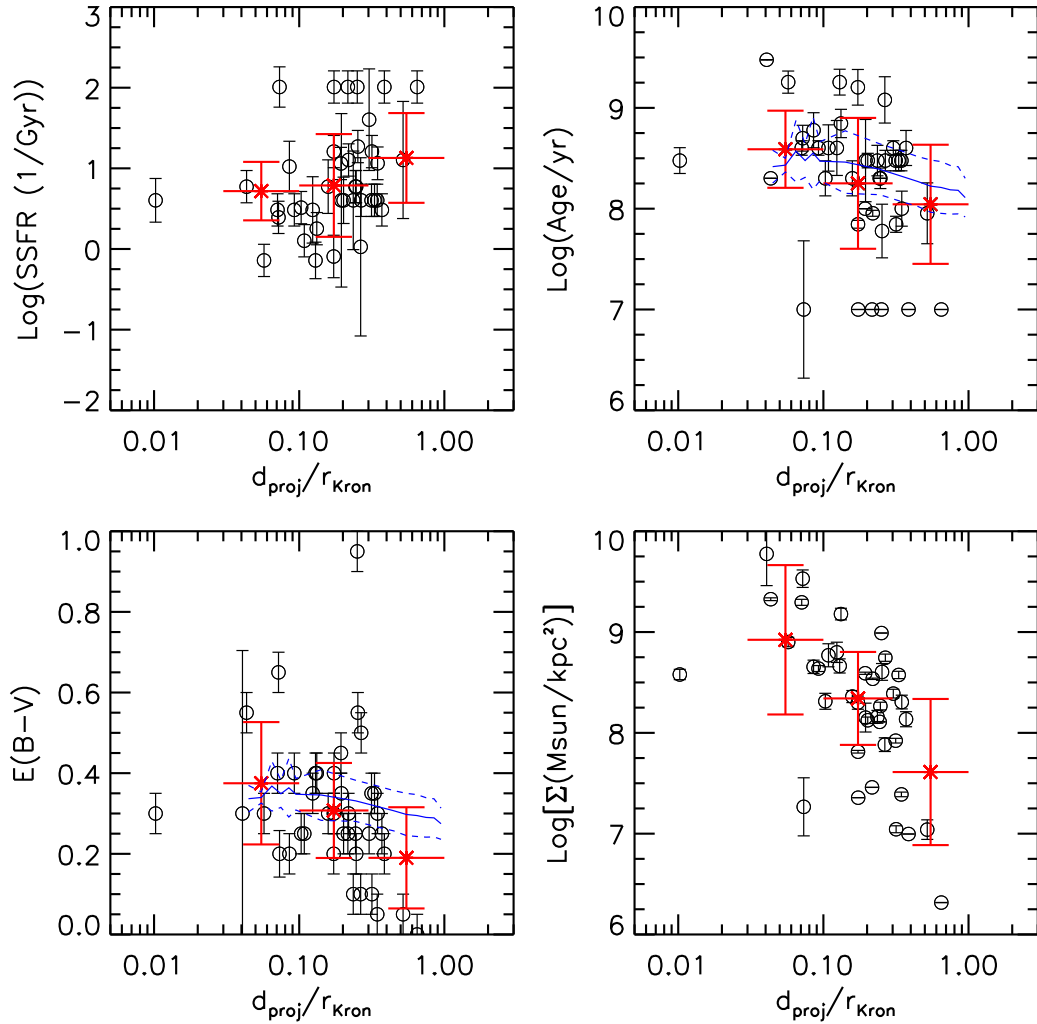


Figure 3.8 Radial variation of physical properties of clumps as a function of galactocentric distance. Symbols and colors are as same as those in Figure 3.7.

is about 700 Myr. The trend of $E(B-V)$ is mild, increasing only 0.2 from $d > 0.5$ to $d < 0.1$. The stellar surface density changes dramatically, increasing about 25 times from $d > 0.5$ to $d < 0.1$.

As we discuss in Sec. 3.5.1, the host “disks” show a mild color gradient, which may contribute a small fraction of the observed radial color variation of clumps. Here we try to examine the implication of this color gradient on the possible gradient of physical properties of “disks”. In order to do so, we have to run SED-fitting in each interclump pixel. However, the large photometric uncertainties of interclump pixels, especially of those in HST/ACS bands due to the relative low rest-frame UV emission of the diffuse components (as one can infer from Figure 3.1), prevent us from getting reliable fitting results for individual interclump pixels. In our study, we take a detour by assuming the (U-V) color–extinction relation and the color–age relation of each interclump pixel follow those of the integrated “disks”. Thus, we extrapolate these relations of “disks” to the color of individual interclump pixels to obtain an estimation of the extinction and age of the pixels. We believe that such extrapolation is valid because the “disks” is the integration of all interclump pixels and hence represents the average color–extinction and color–age relations of the pixels.

The age and extinction gradients of interclump pixels are shown in Figure 3.8. Similar to the case of color gradient, both gradients are mild and cannot fully explain the observed radial variation of clump properties. The age gradient of interclump pixels varies only from ~ 300 Myr at the projected galactocentric distance of $\sim 0.07 r_{\text{Kron}}$ to ~ 100 at $\sim 1 r_{\text{Kron}}$, while a large fraction of clumps are found to have age > 700 Myr at $\sim 0.07 r_{\text{Kron}}$ or to have age < 100 Myr at $\sim 1 r_{\text{Kron}}$. The extinction of interclump pixels varies only by $\Delta E(B - V) \sim 0.1$ throughout the “disks”, while that of clumps varies by $\Delta E(B - V) \sim 0.2$ from galactic centers to outskirts. Although not surprising, these results again demonstrate that the observed radial variations (or gradient) of clump properties are not a simple reflection the gradient of “disks”.

Clumps have their intrinsic radial variations so that their formation and evolution are separated from those of “disks”, as discussed in Sec. 3.5.1.

The trends of these physical properties are consistent with the scenario of clumps migrating toward galactic centers in timescales of $\lesssim 1$ Gyr. The trend of SSFR indicates that if the scenario is true, the intensity of star formation activity in clumps reduces as they migrate toward the gravitational centers. The reason of lower SSFR towards centers could be the gas outflow from massive clumps (Genzel et al., 2011). However, the outflow is not strong enough to fully quench the star formation in clumps, because even for clumps that are closest to galactic centers, their SSFRs are still several tens times higher than the usually quoted value for quiescent galaxies (10^{-2}yr^{-1}).

The trends of age and $E(B-V)$ are actually coupled due to the age–extinction degeneracy. Both high extinction and old age can be used to explain the relative red color of central clumps. To break the degeneracy requires resolved rest-frame NIR images, which unfortunately are not available to date. In our results, both parameters are partly responsible for the relative red color of central clumps. This shared responsibility could be real or just a reflection of the degeneracy. If the latter, using a sole parameter to explain the trend of U-V colors of clumps requires the trend of the parameter being even more prominent than what we see in the figure. That is, central clumps could be even older or more obscured. However, neither of the two situations is likely to be true. First, the stellar feedback would expel gas out of clumps as well as disrupt dust grains. The timescale of disrupting dust grains is much shorter than that of expelling gas and quenching star formation (Draine, 2009). As a result, it is unlikely to find clumps with very high dust extinctions ($E(B-V) > 0.6$) but low SSFRs toward the gravitational centers of host galaxies. Second, the ages of central clumps are already around 1 Gyr in the figure. A more prominent age trend would result in an average age of 2 Gyr or even older. It is hard to explain

why these clumps were formed so early but haven't fully migrated into the centers of galaxies to form bulges. Therefore, we conclude that both age and extinction should be responsible for the relative red color of central clumps.

3.5.3 Effect of Diffuse Background Subtraction

As described in Sec. 3.3, we subtract a *constant* diffuse background for all clumps in each galaxy. The real diffuse or “disk” component of a galaxy, however, is unlikely to have a constant profile, but instead to have a non-constant (e.g., exponential disk) profile. The simplified assumption of *constant* background would result in an over-subtraction for clumps in outskirts and an under-subtraction for central clumps. This problem exists for all bands but is more severe for red bands (e.g., H-band), since the background–clump contrast in the red band images is lower than that in blue band images, as one can infer from the z-band and H-band images in Figure 3.1. Therefore, the imperfect subtraction on diffuse background would redden the color of central clumps and blue the color of clumps in outskirts, inducing a false signal on the trend of radial variation of color in Figure 3.7 and subsequently on the trend of radial variations of physical properties in Figure 3.8.

Accurate subtraction of diffuse background is complicated. It requires knowledge on the light profile of underlying “disk” components of host galaxies. The commonly used method to obtain the light profile is fitting galaxy image with a Sérsic profile. Unfortunately, the image fitting technique has a few shortcomings: model dependent, not suitable for asymmetric source, and affected by the existence of clumps, which make it problematic for determining the underlying components of high redshift irregular-like clumpy galaxies in our sample. Elmegreen et al. (2009a) neglected the contribution of diffuse background when they studied the clumps in HUDF. This seems reasonable for their study, because they only used HST/ACS optical images,

where the background–clump contrast is high so that the flux of clumps is 2–4 times higher than their surroundings.

In another study, Förster Schreiber et al. (2011) subtracted background from their NIC2 H-band images of clumpy galaxies and explored the impact of different background-subtraction schemes, including the one of no subtraction, on their results. They tracked the light profile of clumps until an upturn or a break appears and then used the surface brightness of the upturn or break as the surface brightness of local diffuse background. For clumps without an upturn or break, they measured the background just outside the photometric apertures of clumps. This method is sensible, but somehow subject to the determination of the upturn or break in a smoothly changing light profile, which may vary from person to person. Moreover, subtracting values from the upturns or from pixels just outside the clump photometric apertures would result in an over-subtraction, because (1) the upturn is more likely to be caused by the overlapping of two nearby clumps rather than by the domination of background and (2) there is no reason that the background would immediately dominate the flux just outside the photometric apertures of clumps. This possible over-subtraction could partly explain their findings that the local background light is typically 3–4 times higher than the background-subtracted clump fluxes, while in our study, the background only accounts for on average a few tens percent of the raw clump fluxes, with few of $\gtrsim 50\%$. Förster Schreiber et al. (2011) also estimated the uncertainty on the clump light contributions due to background subtraction by comparing the background-subtracted results with two other measurement methods: directly PSF measurement and raw photometry measurement without subtraction. They found that the clump light contributions are uncertain to a factor of ~ 3 . More importantly, one of their intriguing results, namely the trends of redder colors and of older ages for clumps at smaller galactocentric radii, is not significantly changed by using either background-subtracted or raw photometry.

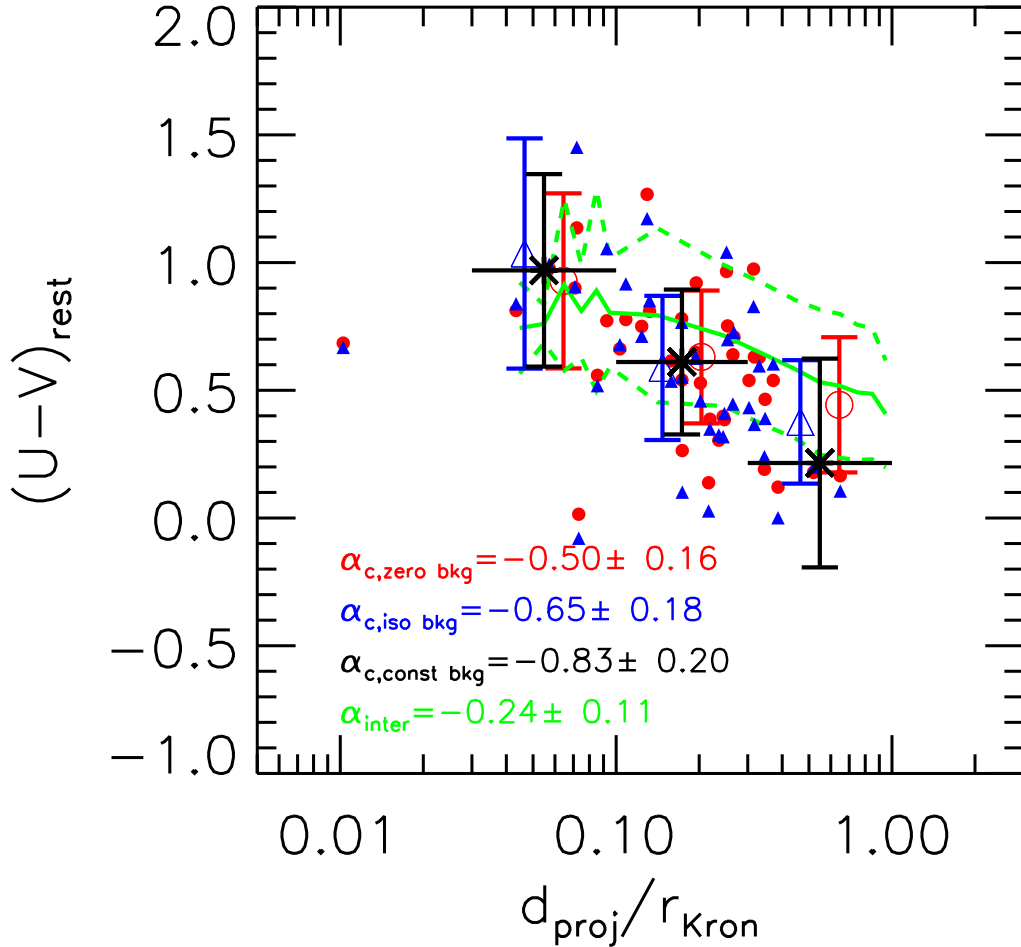


Figure 3.9 Radial variation of the rest-frame U-V color of clumps as a function of their galactocentric distances, under different schemes of diffuse background subtraction. Small filled blue triangles show the case of *local* background subtraction, while red circles show that of *zero* background subtraction. Large empty blue triangles (red circles) with error bars show the mean and 1σ deviation of the small filled blue triangles (red circles). Black “X” with error bars, identical to the red symbols in Figure 3.7, show the mean and 1σ deviation of the case that a global *constant* background is subtracted. Large empty blue triangles (red circles) are shifted along the x-axis for clarity. The typical color uncertainty of each clump is not shown, but can be inferred from the uncertainty of Figure 3.7. Solid and dashed green lines show the mean and standard deviation of color variation of interclump pixels. The best-fit slope of each color gradient is also given in the figure.

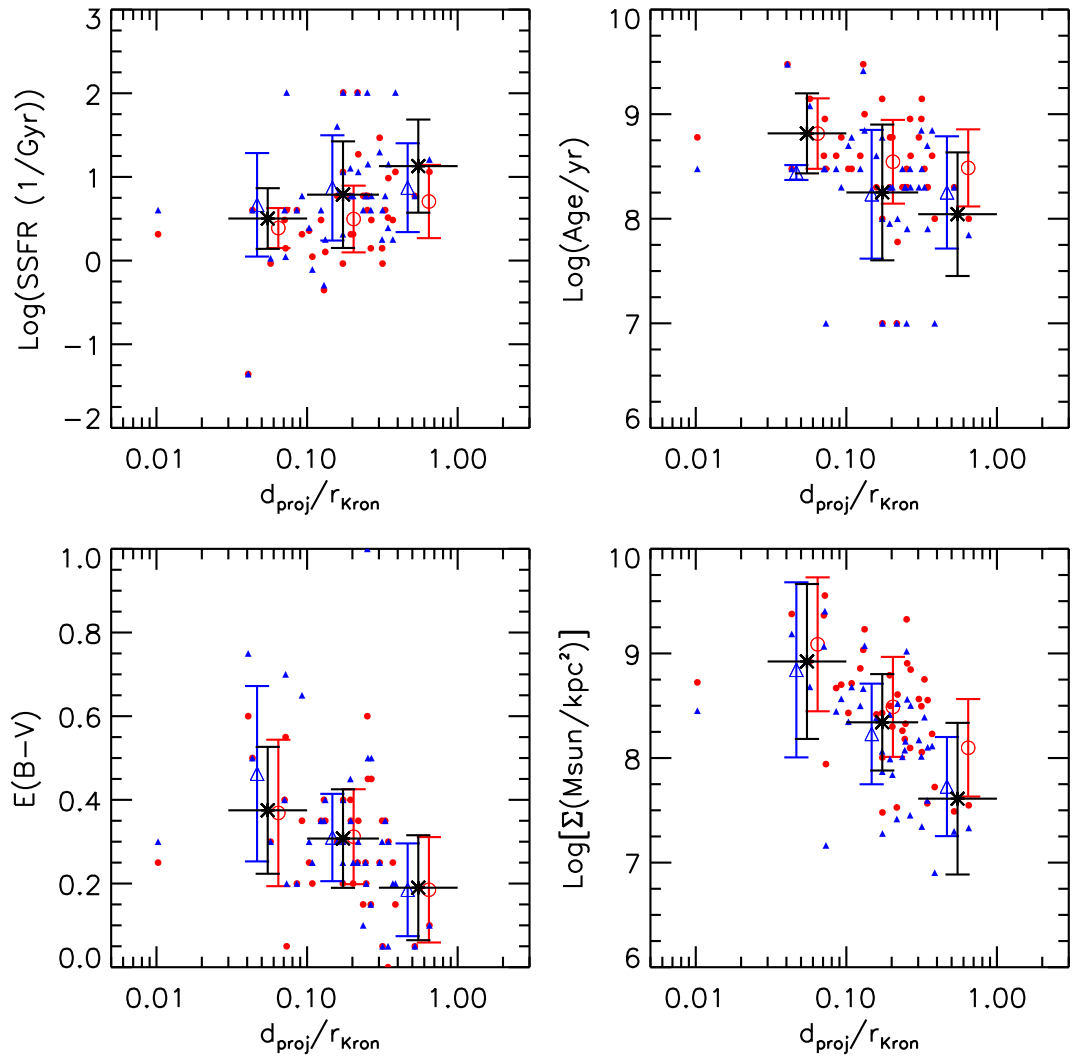


Figure 3.10 Radial variation of physical properties of clumps as a function of galactocentric distance, under different schemes of diffuse background subtraction. Symbols and colors are as same as those in Figure 3.9.

Since the background subtraction scheme would most affect the radial variations of color and physical properties of clumps, we investigate these variations in another two subtraction schemes: local subtraction and no subtraction at all. In the *local* subtraction scheme, for each clump, we measure the background surface brightness in an annulet that is $0.3''$ (two times the radius of our photometry aperture) away from the clump, with all areas within a distance of $0.3''$ of any other clumps masked out. Then, we subtract a corresponding background flux from the raw flux of the clump. In the *zero* scheme, we do not subtract any background from the raw fluxes of the clumps. We re-derive the rest-frame colors and physical properties of the clumps and re-analyze their radial variations. The new results are shown in Figure 3.9 for rest-frame UV/optical color and Figure 3.10 for physical properties and compared with the results of a global *constant* subtraction.

In both new subtraction schemes, the trend of the radial color variation is still present, although being flattened slightly: the difference between the average color of clumps at $d < 0.1$ and $d > 0.5$ becomes from 0.8 mag in the *constant* subtraction (black) to 0.5 mag in the *local* (blue) or the *zero* subtraction (red). As discussed above, the constant background subtraction scheme may over-subtract light, especially red light, from clumps in the outskirts, resulting in a false bluer color for them. However, in the other side, the zero background subtraction leaves the background light in red bands to these outskirts clumps, which would result in a false redder color for them. The real trend of the color radial variation should be the one between the constant subtraction and zero subtraction, most likely the local subtraction. We also note that the color of clumps in $d < 0.1$ is not significantly changed in our zero subtraction scheme, implying that background emission is negligible for central clumps. Overall, the change of the color variation under different subtraction schemes is not statistically significant. Therefore, we conclude that the observed trend of color variation is intrinsic for clumps.

As we discussed in Sec. 3.5.1, the host “disks” exhibit a mild color gradient. It is important to examine whether the radial variation of clumps under different background subtraction is still significantly steeper than that of interclump pixels. Since the background subtraction does not affect the gradient of interclump pixels (as discussed before, we exclude all pixels close to identified clumps), we simply overplot their color gradient obtained in Sec. 3.5.1 in Figure 3.9 (green) and compare its slope with that of clumps under various background subtraction schemes. The slope of clumps in the *zero* background subtraction is only steeper than that of interclump pixels at 2.4σ level. However, as discussed above, this trend, suffering from under-subtraction of diffuse background, can only be treated as the lower limit of the color gradient of clumps. The most likely color gradient of clumps, i.e. the one with *local* background subtraction, is 3.7σ steeper than that of interclump pixels. Thus, we conclude that the subtraction schemes of the diffuse background would not change our previous conclusion that the color gradient of “disks” is significantly flatter/weaker than, and hence only contribute to a small part of, that of clumps.

The radial variations for physical properties under different subtraction schemes are shown in Figure 3.10. The situation here is similar to that of Figure 3.9: all trends are still present, but with strength reduced. The trend of SSFR is reduced the most and only shows a marginal signal that clumps at $d > 0.5$ are only a 1.5–2 times higher than those at $d < 0.1$. The average age of clumps at $d > 0.5$ increases from 100 Myr to 300 Myr so that the age difference between $d < 0.1$ and $d > 0.5$ reduces from >500 Myr of Figure 3.8 to ~ 300 Myr. The trend of dust extinction is almost unchanged, implying that the $E(B-V)$ measurement is statistically robust against background subtraction. The trend of the stellar surface density is also flattened, but still significant, even compared with the trend in Figure 3.8. The stellar surface densities of central clumps are now on average 10 times higher than that of clumps in outskirts.

Similar as for the color, the changes of above trends on physical properties are largely caused by the change of the derived properties of clumps in outskirts. On the other side, properties of central clumps are less (almost not) affected by the employed background subtraction schemes. Compared to the extreme case of over-subtraction due to the assumption of constant background, the zero subtraction is another extreme case for clumps in outskirts. The real diffuse background should be somewhere between these two cases. If the correct background is subtracted for these clumps, we would expect the radial variations of color and physical properties be stronger than those under the zero subtraction, but weaker than those under the constant subtraction. Overall, we can still conclude that central clumps are redder, older, denser, more obscured, and less active in forming stars than clumps in outskirts.

3.5.4 Possible Metallicity Variation

Our above analyses are based on our SED-fitting assumption that all clump have solar metallicity. However, if there is a radial trend in metallicity (rich center and poor outskirts) already in place in the underlying disk, clumps that form closer to the center would tend to be redder, and vice versa. The radial variations due to the underlying metallicity gradient might mimic the color trends expected from the clump migration scenario.

The spatial variation in metallicity is indeed observed in clumpy SFGs at $z \sim 2$. Genzel et al. (2008) found that three out of five their SINS galaxies exhibits a radial gradient of the $[\text{N II}]/\text{H}\alpha$ ratio, which implies a $\sim 20\%$ higher oxygen metallicity in the central region than in the outer disks. Furthermore, Genzel et al. (2011) found clump to clump and center to outer variation in the $[\text{N II}]/\text{H}\alpha$ ratio in another three SFGs at $z \sim 2$. These findings are broadly consistent with the inside-out growth mode predicted by semi-analytic models (e.g., Somerville et al., 2008). However, we note that the metallicity variation in their works is modest though. For example, the

average metallicity among the three galaxies increases from $\sim 0.5 Z_{\odot}$ in outer disks to $\sim 0.8 Z_{\odot}$ in central regions.

Even if the above metallicity variation exists in our galaxies, its contribution to our observed color variation would be small. The rest-frame U-V color of a constant star-forming template with age of 1 Gyr changes only 0.2 mag from $Z = Z_{\odot}$ to $0.2Z_{\odot}$. However, in Figure 3.9, the radial color variation is $\gtrsim 0.6$ mag, requiring other variations to explain it. We acknowledge the existence of metallicity variation, but still conclude that assuming a constant metallicity would not significantly affect our results on the radial variations of the SED-fitting derived properties. Moreover, the modest variation cannot be well constrained by SED-fitting, because the usually employed discrete metallicity distribution: sub-solar, solar, and super-solar, is too broad to describe the variation.

3.6 Discussion

3.6.1 Comparisons with Other Studies

We compare our measurements of the properties of clumps with those of other studies. Due to the differences on a few key ingredients, e.g., sample selection, photometric apertures, background subtraction schemes, and models used to derive physical properties, only order-of-magnitude comparisons can be made. We focus on their stellar masses, SFRs and contributions to host galaxies. We are not able to compare clump sizes with other studies, as we fix a constant photometric apertures for all clumps. In order to compare stellar masses and SFRs that are derived with different IMFs, we apply the relation of Salimbeni et al. (2009b) to convert results with the Chabrier IMF Chabrier (2003) to that with the Salpeter IMF: $\log(M_{\text{Salpeter}}) = \log(M_{\text{Chabrier}}) + 0.24$. Since the normalization of SFR is determined by stellar mass in SED-fitting, we also scale the SED-fitting derived SFRs by a relation deduced from the above one: $\text{SFR}_{\text{Salpeter}} = 1.74 \times \text{SFR}_{\text{Chabrier}}$.

Since three galaxies in our sample (Galaxy 21739, 22284, and 27101) have been studied by Elmegreen & Elmegreen (2005), with ID 3465+, 3483, and 6462+ in their paper, we first compare the derived properties of these galaxies in the two studies in details, and then compare clump properties in sample wise with other studies. Table 3.3 shows the first comparison. As discussed in Sec. 3.2, Elmegreen & Elmegreen (2005) used ACS i-band to select clumpy galaxies and identified more clumps in each galaxy than we do. In order to derive physical parameters, including redshifts, of clumps as well as galaxies, Elmegreen & Elmegreen (2005) compare ACS color pairs of galaxies and clumps to that of stellar population synthesis models with exponentially decline SFH. Although the derived properties of clumps are different between the two studies and we are limited to a very small sample, we do not find systematical difference between the two studies for the following properties: average age of clumps, average stellar mass of clumps, stellar mass of host galaxies, and the fraction of mass in clumps.

The two parameters with obvious offsets between the two studies are the age of disks (called interclump age in Elmegreen & Elmegreen (2005)) and average SFR of clumps. The interclump age in Elmegreen & Elmegreen (2005) is ~ 2 Gyr, while the disk age in our study is 0.3–0.5 Gyr. The difference could be due to the assumption of Elmegreen & Elmegreen (2005) that interclump star formation began at $z=6$. It could also be caused by the degeneracy between age (t) and the characteristic decay time scale (τ) in the SED-fitting of either of the two studies. However, the difference in the disk age would not change the results in both studies. Elmegreen & Elmegreen (2005) found that clumps are bluer than interclump regions, consistent with our conclusion that clumps are spots with enhanced SSFR. The systematical offset in the other parameter, the average SFR of clumps, is likely caused by the use of different SFR indicators in the two studies. Elmegreen & Elmegreen (2005) used the instantaneous SFR at a given time t , while we average the SFR over the last 100 Myr according to

the SFH of the best-fit model. We argue that such average is necessary if one wants to compare the SFR derived from SED-fitting to that empirically derived the rest-frame UV continuum. Since Elmegreen & Elmegreen (2005) used the exponentially declining model, such average will elevate the SFR of clumps from the instantaneous value of $\sim 1 \text{ M}_\odot \text{ yr}^{-1}$ to several $\text{M}_\odot \text{ yr}^{-1}$, consistent with our measurements. Overall, we conclude that the measurements of clump properties and, more importantly, the interpretation of the properties in the two studies are broadly consistent.

Now, we compare clump properties statistically in sample wise with other studies. The stellar masses of our clumps agree very well with those of Förster Schreiber et al. (2011), but are slightly larger those that of Elmegreen & Elmegreen (2005); Elmegreen et al. (2009a). The clumps in the NIC2 sample of Förster Schreiber et al. (2011) span the stellar mass range of 10^8 M_\odot to 10^{10} M_\odot , with a median mass of about $3 \times 10^9 \text{ M}_\odot$. Elmegreen & Elmegreen (2005) found a typical mass of $6 \times 10^8 \text{ M}_\odot$ for clumps in 10 HUDF galaxies. However, a revisit of HUDF by Elmegreen et al. (2009a) with NICMOS images shows clumps are typically in range of 10^7 M_\odot to 10^9 M_\odot . It is possible that the difference of stellar mass is resulted from sample selections. In our sample, we only choose galaxies with spectroscopic observations, which would bias our sample toward UV/optical luminous (and hence massive) end, while Elmegreen et al. (2009a) did not restrict their sample to spec-z and hence were able to detect clumps in fainter galaxies. As discussed in Genzel et al. (2011), the Toomre mass of clumps is proportional to the mass of disks. Clumps detected in our possibly biased massive samples would therefore have higher clump masses.

The SFRs of clumps in our study are broadly consistent with those of Genzel et al. (2011), who measured the SFRs of clumps through extinction corrected $\text{H}\alpha$ luminosity. Their SFRs (after being converted to a Salpeter IMF) run from a few $\text{M}_\odot \text{ yr}^{-1}$ to $\sim 70 \text{ M}_\odot \text{ yr}^{-1}$, with a median (mean) of 24 (28) $\text{M}_\odot \text{ yr}^{-1}$. In our sample, the SFRs of majority clumps cover a similarly wider range, from less than $1 \text{ M}_\odot \text{ yr}^{-1}$

to $\sim 70 \text{ M}_{\odot}\text{yr}^{-1}$, with a median (mean) of ~ 10 (~ 24) $\text{M}_{\odot}\text{yr}^{-1}$. The consistency of SFRs in the two studies is encouraging, because Genzel et al. (2011) and we have used two different physical mechanisms (nebular line emission and stellar color) to measure SFRs. Förster Schreiber et al. (2011) only measured SFR for galaxies as a whole. If we scale the SFRs of their host galaxies by the clump fractional contribution to H-band light in their study, typically 5%, the derived typical SFR of clumps is only a few $\text{M}_{\odot}\text{yr}^{-1}$, smaller than our median value. However, as we discussed in Sec. 3.4.3, as regions with enhanced SSFRs in “disks”, clumps contribute more on SFR than on stellar mass (and hence H-band light) to host galaxies. Therefore, the actual SFRs in clumps of Förster Schreiber et al. (2011) should be higher than the above scaled value, moving them closer to our measurement. In fact, one galaxy (BX 482) in Förster Schreiber et al. (2011) has $\text{H}\alpha$ measurement for each of its clumps. We calculate the $\text{H}\alpha$ derived SFRs for each of its clumps. Since Förster Schreiber et al. (2011) did not report extinctions for individual clumps, we assume that the dust extinction of each clump is equal to the global extinction of BX 482, $A_V = 0.8$, measured through SED-fitting. We find that SFR varies from $5 \text{ M}_{\odot}\text{yr}^{-1}$ to $46 \text{ M}_{\odot}\text{yr}^{-1}$ for clumps in BX 482, with a median (mean) of 9 (14) $\text{M}_{\odot}\text{yr}^{-1}$, broadly consistent with our clump SFRs. Finally, we note that $\text{H}\alpha$ is a measure of instantaneous SFR more than of the averaged SFR over the last 100 Myr, which we derive from our SED-fitting. The difference of the two SFR indicators may induce a bias when we compare the two types of SFRs. However, given the large uncertainties of measuring SFRs in both ways as well as the large scatter of SFRs of clumps, such a bias would not significantly affect our conclusions. SFRs measured through both $\text{H}\alpha$ and SED-fitting on larger samples are needed for carrying out more precise comparisons to better understand the star formation process in clumps.

In terms of fractional contribution of light to host galaxies, we compare our measurement on rest-frame UV/optical light to that on the observed emission of Förster

Schreiber et al. (2011). At $z \sim 2$, the rest-frame U and V band emissions are redshifted to close to the H_{160} and i_{814} bands in the observer’s frame, validating the comparisons between the two studies. In our study, the typical individual clump contribution to the UV/Optical luminosity is $\sim 5\%$ (spreading over a wide range of 1% to 10%) and the total contribution of clumps in a galaxy is $\sim 20\%$. We also find no significant difference between the clump contributions to U-band and V-band light. These results are quite similar to what Förster Schreiber et al. (2011) found with the H_{160} fluxes of their NIC2 clumps as well as i_{814} emission in one of their galaxy. The contribution on ACS i_{775} band emission by clumps in Elmegreen & Elmegreen (2005) and Elmegreen et al. (2009a) is typical 2%, slightly smaller than our average value. However, given that galaxies in Elmegreen & Elmegreen (2005) and Elmegreen et al. (2009a) usually contain 5–10 clumps, about 2 times more than our galaxies, the total contribution of clumps to host galaxies is about 25%, close to our value. Wuyts et al. (2012) found that the fractional contribution of clumps to the total light of their hosts has a mild dependence on the waveband used for identifying clumps, decreasing with the increasing of wavelength. They also found that for a giving identification band, the fractional contribution of clumps slightly decreases with wavelength. In their $z \sim 2$ sample, the fractional contribution of clumps to the total rest-frame U (V) light of their hosts is, on average for detections in 2800Å, U, and V bands, 20% (17%), close to our values. However, we note that besides using a different sample selection criterion (mass-complete), Wuyts et al. (2012) have two other approaches that are different from ours: excluding the central bulge of a galaxy as a clump and not subtracting diffuse background of hosts from clump light, each of which brings an effect to the fractional contribution opposite to the other. These results again highlight the fact that the contribution of clumps to the total light of their host galaxies is small, and the light distributions of galaxies are still dominated by diffuse components.

3.6.2 Formation of Clumps

In the commonly assumed framework that giant clumps are formed through gravitational instability of turbulent gas-rich Toomre-unstable disks (e.g., Noguchi, 1999; Immeli et al., 2004a,b; Bournaud et al., 2007, 2008; Elmegreen et al., 2008; Genzel et al., 2008; Dekel et al., 2009b; Ceverino et al., 2010; Genzel et al., 2011; Förster Schreiber et al., 2011), clumps have a characteristic scale and mass, namely the Toomre length and the Toomre mass. They represent the largest and fastest growing unstable mode that is not stabilized by rotation. Since we use a fix photometric aperture for all clumps, we lose the size information of clumps. However, we can still compare our clump masses with the Toomre mass predicted by the in-situ fragmentation scenario. We use Equation (5) in Genzel et al. (2011) to calculate the Toomre mass of disks:

$$M_{Toomre} \approx 5 \times 10^9 \left(\frac{f_{young}}{0.4} \right)^2 \left(\frac{M_{disk}}{10^{11} M_{\odot}} \right) M_{\odot}, \quad (3.1)$$

where f_{young} is the mass fraction of component of stars, and M_{disk} the total mass of disk, which is close to the baryonic (gas + star) mass in the central ~ 10 kpc of galaxies. The maximum clump mass that can be formed in a uniformly rotationally supported gas disk is actually first derived by Escala & Larson (2008):

$$M_{cl}^{max} = 3 \times 10^7 M_{\odot} \left(\frac{\eta}{0.2} \right)^2 \left(\frac{M_{gas}}{10^9 M_{\odot}} \right), \quad (3.2)$$

where $\eta = M_{gas}/M_{tot}$ is the ratio of the gas mass to the total mass enclosed with a radius R . The maximum clump masses estimated by the two equations are in agreement within a factor of two. ¹

¹We note that the maximum clump mass is not the turbulent Jeans mass, which is often incorrectly interpreted in some of previous studies. The Jeans mass (and Jeans length), beyond which the disk cannot be stabilized purely by thermal pressure, is actually the smallest unstable mode that can be formed in a disk. We refer readers to Escala & Larson (2008) for detailed discussions.

To apply Equation 3.1 to our galaxies, we assume a gas-to-baryonic mass fraction of 0.5, close to the median value of the fraction observed by several authors (e.g., Erb et al., 2006; Genzel et al., 2008; Tacconi et al., 2008, 2010; Förster Schreiber et al., 2009; Daddi et al., 2010). Therefore, we have $f_{young} = 0.5$ and M_{disk} is two times the stellar masses of the disks that are measured through SED-fitting. We compute the Toomre mass for each galaxy and compare the masses of clumps in the galaxy to the Toomre mass. The ratio between clump mass and Toomre mass spans a wide range, from 0.05 to 3.5, with a median of 0.3. This result is encouraging, as it demonstrates that our clump masses is broadly consistent with the characteristic mass predicted by the scenario of disk instability. The statistically smaller masses of clumps is not contradictory with the prediction, as the Toomre mass is the maximum unstable mass. Moreover, Toomre mass is proportional to the third power of gas density and inversely proportional to the forth power of angular rotation speed (see Equation (2) of Escala & Larson, 2008). Since both gas density and angular rotation speed are functions of radius, the Toomre mass also varies with galactocentric distance. In a disk with flat rotation curve and gas density decreasing with radius, the Toomre mass decreases with radius. Our clump mass distribution is also consistent with this argument, as less dense (and hence less massive with given photometric aperture) clumps are found at large galactocentric distances. Overall, the clump masses in our sample are broadly consistent with the prediction of the scenario of gravitational instability.

The in-situ fragmentation due to gravitational instability requires a gas-rich, turbulent and marginally unstable ($Q \sim 1$) disk as the birthplace of clumps. The existence of such disks cannot be directly inferred from our multi-band images; it has to be confirmed through the kinematics of star, gas or ISM. Förster Schreiber et al. (2009) presented the spatially resolved gas kinematics of 62 star-forming galaxies at $z \sim 1-3$, measured through $H\alpha$ and $[N II]$ emission lines observed by the Spectroscopic Imaging survey in the Near-infrared with SINFONI (SINS). They found about one-third of

galaxies in their sample are rotation-dominated yet turbulent disks, another one-third are compact and velocity dispersion-dominated objects, and the remaining one-third are interacting or merging systems. They also found that the fraction of rotation-dominated systems increases towards the massive end of the sample. Since almost all our galaxies have stellar mass larger than $10^{10}M_{\odot}$ and lie on the massive end of the mass spectrum of SINS sample, we expect that the fraction of rotation-dominated turbulent disks in our sample is higher than 40%.

In fact, one galaxy in our sample, 27101, was observed by Bournaud et al. (2008) through H α field spectroscopy using SINFONI on VLT UT4. They found a large-scale velocity gradient throughout the system, with large local kinematic disturbances. They also found a disk-like radial metallicity gradient in the galaxy. These findings can be most likely explained by the scenario of internal disk fragmentation, despite the complex asymmetrical merger-like morphology. However, another galaxy in our sample, 24919, shows an obvious interaction/merger signature. A long (tidal) tail is curving from its lower left part all the way to its upper middle part, as can be seen in its z-band image in Figure 3.1, suggesting an ongoing interaction/merger, which might be responsible for the formation of clumps. To understand to which extension the in-situ fragmentation scenario is valid to explain the formation of giant clumps requires a large survey of kinematics of clumpy galaxies, in addition to their multi-band images.

Another possible interpretation of the clumpy features in our sample galaxies is that these clumps do not actually represent any physical entities, but simply correspond to locations with lower line-of-sight dust obscuration in the host galaxies. This alternative arises from the fact that these clumps are bright in the rest-frame UV images. If this interpretation is true, the properties (e.g., age and SSFR) and observed radial variations of clumps would plausibly reflect those of the underlying galaxy population. Based on our previous results, however, we argue that this al-

ternative interpretation is unlikely true and that clumps are physical entities with properties and formations differing from those of their host “disks”. For clumps in the outskirts (e.g., $r > 0.1r_{Kron}$) of galaxies, it is true that their dust obscuration is lower than that of interclump regions at same galactocentric distance (the bottom left panel of Figure 3.8). However, these clumps also have systematically younger ages than their nearby interclump regions. The very young age ($\lesssim 100$ Myr) of these clumps indicates that they are newly formed, possibly due to the instability induced by the cold accretion, which preferentially occurs in the outskirts of galaxies, in a relatively older (and hence stable) “disks”. For central clumps, if they represented the underlying “disk” stellar populations but had lower dust extinction, their rest-frame colors should be *bluer* than their surrounding areas. However, this expectation is contradictory to our previous result, namely the rest-frame UV color of clumps is redder than that of central interclump regions (Figure 3.7). In fact, the bottom left panel of Figure 3.8 shows that the dust extinction of central clumps is comparable to (or even higher than) that of central “disk” regions, if our SED-fitting technique does not significantly suffer from the age–extinction degeneracy. Overall, it is unlikely that the appearance of the clump features is simply due to lower line-of-sight extinction. As a result, clumps should have origins distinctive from that of “disk” stellar populations.

3.6.3 Fate of Clumps

There are two possible scenarios commonly proposed to explain the fate for giant clumps in $z \sim 2$ SFGs: they would (1) migrate towards the gravitational centers of their host galaxies due to interactions and dynamical friction against the surrounding disks and eventually coalesce into a young bulge as the progenitor of today’s bulges or (2) be rapidly disrupted by stellar feedback, supernova feedback or tidal torques during (or even before the beginning of) their migration towards centers. Dekel et al. (2009b) made a few predictions that observations can test for the possible fate of clumps. If

the migration scenario is true and clumps survive for a migration timescale of ~ 0.5 Gyr, giant clumps would (1) have an age spread of ~ 0.5 Gyr; (2) be gas rich and forming stars at a high rate that is similar to the preceding few hundred Myr; and (3) have a radial age variation in the sense that clumps at large disk radii are younger than ~ 0.5 Gyr, while those at smaller radii are older. In contrast, if clumps are rapidly disrupted, they would (1) have smaller age spread, ~ 100 Myr and (2) have no obvious age gradient with galactocentric radius.

Our findings on the properties of giant clumps are reasonably consistent with the prediction of the inward migration scenario. The top right panel of Figure 3.8 shows that the age distribution of our clumps spans a wide range from < 0.1 Gyr to a few Gyr. The age spread is comparable to the prediction of ~ 0.5 Gyr of the migration scenario, but significantly larger than the prediction (~ 100 Myr) of the disruption scenario. If no background subtraction is applied to our clumps, the age spread (see in Figure 3.10) is even closer to the prediction of the migration scenario. The radial age variation of our clumps is also strongly in favor of the migration scenario. Recently, Ceverino et al. (2012) discussed the internal support of the in-situ giant clumps in gravitationally unstable disks at high redshift, using both an analytic model and high-resolution hydro adaptive mesh refinement simulations. They predicted a steep age gradient of clumps throughout their host disk due to the formation of giant clumps in the outer parts of the disk and their inward migration to form a bulge in the disk center. Our results agree very well with their predictions: clumps at $d > 0.5$ have the mean age of ~ 100 Myr, while those at $d < 0.1 \sim 700$ Myr. Ceverino et al. (2012) even predicted that the age gradient of clumps is steeper than that of interclump stars. Such prediction is similar to our results in Figure 3.8 and hence strengthens our argument on the inward migration scenario. Another piece of evidence, interesting but largely uncertain, is coming from the SFH of clumps. As described in Sec. 3.3, we fit each clump with three types of SFHs: exponentially declining, exponentially

increasing and constant. We then choose the most likely SFH based on the reduced χ^2 of the best-fit of each SFH. About 70%–80% of clumps are thus classified as having constant SFH, agreed with the above prediction of the migration scenario of Dekel et al. (2009b). However, we note that the SFH derived from SED-fitting is approximate and severely model dependent and can only be used as a loose constraint on predictions. Overall, we conclude that the age spread and radial variation indicate that these clumps might eventually migrate into the centers of their host galaxies.

It is also possible, however, that not all clumps can survive long enough to migrate into the gravitational centers. Some of them might still be disrupted, possibly by the stellar feedback (while the effect of supernovae feedback seems unimportant (see Dekel et al. (2009b))). Genzel et al. (2011) observed strong outflows in their clumps, with a rate as large as or even larger than SFRs. They also estimated the gas expulsion time due to outflows, which ranges from 170 to 1600 Myr from clump to clump. A hint of the disruption of clumps can also be inferred from the radial age variation of clumps (the top left panel of Figure 3.8 and Figure 3.10). In this figure, we find no clumps with age $\lesssim 100$ Myr at small galactocentric radius ($d < 0.1$). The reason of the dearth of young central clumps could be either that young clumps are preferentially formed at large radii or that young clumps at small radii are rapidly disrupted due to the somehow stronger outflows or interactions. If the latter is true, the disruption timescale (or lifetime) of clumps should have a relation with their densities, because due to their shallower potential wells and less concentrated structures, low density clumps are easier to be disrupted by either outflows or tidal torques than high density clumps.

Figure 3.11 shows the age of clumps increases with the stellar surface densities of clumps. The upper envelope of the relation provides a rough estimate on the lifetime for clumps with different stellar surface densities. For example, no clumps with density of $10^7 M_\odot/\text{kpc}^2$ are older than 100 Myr, suggesting that the lifetime of

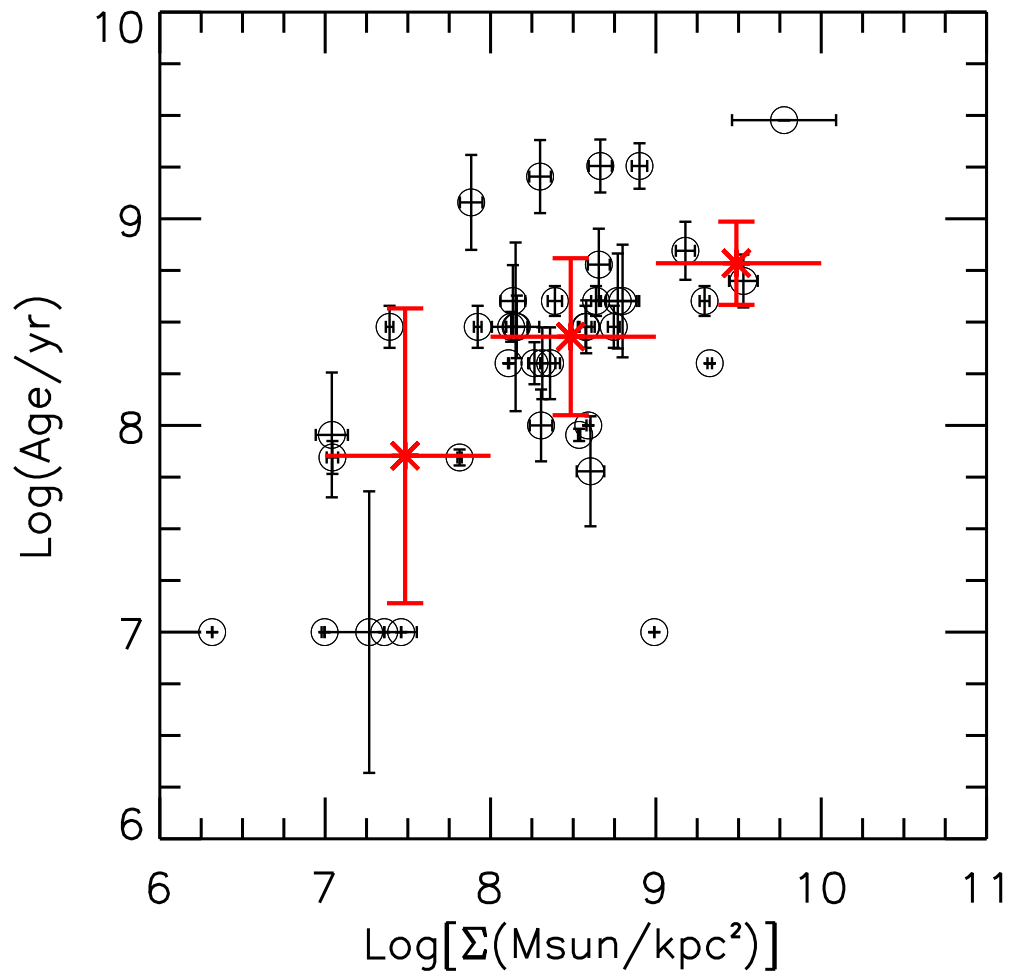


Figure 3.11 Age–stellar surface density relation of clumps. Symbols and colors are as same as in those Figure 3.7. A constant background has been subtracted for clumps in this figure.

this type of clumps is ~ 100 Myr. While for clumps that are one order of magnitude denser, their lifetime could be up to 1 Gyr. However, we note that we cannot rule out an alternative scenario that all clumps are formed at large radii and become old and concentrated when they migrate toward galactic centers.

3.6.4 Ongoing Bulge Formation?

If the inward migration scenario is true, one would expect to find bulges or at least ongoing forming bulges in a fraction of $z \sim 2$ SFGs. Clumps are observed within a wide redshift range, from $z \sim 4$ (Elmegreen et al., 2007) to $z \sim 2$ (e.g., Genzel et al., 2008, 2011; Förster Schreiber et al., 2011) or to even lower redshift. Moreover, very young clumps are observed at $z \sim 2$ in our sample or other studies (e.g., Förster Schreiber et al., 2011). These observations show that the formation of clumps is a continuous process that at least lasts over the cosmic time of ~ 1.7 Gyr from $z \sim 4$ to $z \sim 2$. If we assume a constant clump formation rate over the cosmic time and a bulge formation (due to the coalescent of clumps) timescale of 1 Gyr, a few times the migration timescale of clumps, the fraction of SFGs that contain a young bulge at $z \sim 2$ should be $(1.7-1)/1.7 \times 100\% \sim 40\%$. If the clump formation rate increases with redshift, the bulge fraction would be lower, as the majority of newly formed clumps have insufficient time to coalesce into bulges, and vice versa.

We roughly estimate the bulge fraction in our sample through the following ways:

1. *Morphology and color*: Bulges are believed to have spheroid-like morphology and be redder than other components if they are older. They also tend to reside in the gravitational centers of galaxies. By simply looking at the mosaics of our sample in Figure 3.1, we identify five galaxies (21852, 22284, 24033, 24684, 27101) that contain such a component that satisfies the above conditions. This bulge fraction (50%) is broadly consistent with what we estimated above based on the bulge formation timescale (40%). We note that although

morphology and color are a relative easy way to identify bulges, they suffers from the age–dust degeneracy as well as the problem of subjectivity. A more accurate bulge identification requires other pieces of information, such as the kinematic information of bulges.

2. *Stellar mass*: As we discuss in Sec. 3.6.3, the Toomre mass is the maximum unstable mass that the Jeans-unstable mode not stabilized by rotation can generate. If the mass of a clump is far larger than the Toomre mass in its host disk, the clump may not be a direct result of disk fragmentation. Instead, it could be a coalesced result of a few clumps. In our study, a clump is considered a bulge if its stellar mass is 3 times larger than the Toomre mass. In our sample, four galaxies (23013, 24033, 24684, 27101) contain such super-Toomre mass clumps. Moreover, these super-Toomre mass clumps are all close to the H-band light centers — an approximation of the gravitational centers — of their host galaxies. This sub-sample is largely overlapped with the sub-sample that we identify through morphology and color, with 3/4 of the former being in the latter. The bulge fraction of 40% measured in this way also agree very well with our prediction. However, we note that using stellar and Toomre mass to set constraint on the bulge fraction critically relies on the accuracy and interpretation of the Toomre mass. Therefore, it can only be treated as a rough estimate.

3. *X-ray detection*: It is now widely accepted that super-massive black holes (SMBH) are residing in the center of massive galaxies and co-evolve with bulges. The masses of SMBHs are observed to correlate strongly with both the fourth power of the velocity dispersion of bulges and the first power of the bulge masses. Also, recent theoretical models predict that the internal violent processes, such as clump–clump interaction, tidal force, etc., would feed gas to the center of

galaxies to form bulges as well as SMBHs Bournaud et al. (2011). If bulges have been formed in our sample, we would expect some of our galaxies to be detected as AGN in X-ray due to the energetic feedback released by their accompanying SMBHs. Indeed, four galaxies (23013, 24684, 24919, 27101) in our sample have significant detections in the Chandra 4Ms imaging of CDFS², with three detected in the both soft and hard bands and one (27101) only in the soft band. At such high redshift ($z \sim 2$), all these X-ray sources have high luminosities that can only be generated via AGN ($L_x > 10^{42} \text{ ergs}^{-1}$). This finding is encouraging, since this X-ray detected sub-sample is prominently overlapped with the super-Toomre mass sample that we just discussed above, with 3/4 of the former is found in the latter. The only exception, Galaxy 24919 shows an extraordinary red lane in its z-H color map. Regardless of the component of the lane, i.e., old stars or dust, its existence indicates that the galaxy is undergoing a dramatic violent process, possibly merger, a common way to form bulges. Including that, the bulge fraction inferred from X-ray detection is well agreed with our prediction of 40% as well as that induced from Toomre mass.

4. *Age*: Bulges should contain old stellar populations with ages older than a few times of the migration timescale of clumps ($\sim 0.5 \text{ Gyr}$). In our sample, only two galaxies (24686 and 27101) contain clumps with age older than 1 Gyr. Moreover, these clumps are very close to the centers of host galaxies. These findings indicate that these clumps could be bulges rather than newly formed clumps. The two galaxies also satisfy all above three criteria. Therefore, age provides the most restricted constraint on the bulge fraction and yields the smallest fraction (20%). However, we note that the age measured through SED-fitting is actually a light-weighted average age for both old and young

²<http://cxc.harvard.edu/cda/Contrib/CDFS.html>

population. In our clumps, since their SFRs have not been fully quenched, the new formed population would drag the measured age toward the young side. Therefore, some other clumps with age close but less than 1 Gyr may also contain populations as old as 1 Gyr and hence be candidates of proto-bulges.

Overall, our estimations yields a bulge fraction in our sample of $z\sim 2$ clumpy galaxies from 50% through morphology and color to 20% through age. The most likely fraction of 40%, obtained by the prominent overlapping of super-Toomre mass and X-ray detection, is very close to our prediction based on the migration timescale of clumps. This result suggests that bulges have been likely formed through the coalescence of giant clumps in our sample of $z\sim 2$ clumpy galaxies and this process is still going on.

However, one should be cautionary when generalizing the conclusion to the general bulge formation of SFGs at $z\sim 2$. First, our sample is limited to only ten galaxies selected to be particularly clumpy and is biased toward UV bright, blue, and large galaxies, as discussed in Sec. 3.2. Second, our work cannot fully rule out other processes as the mechanisms of general bulge formation at $z\sim 2$. Genzel et al. (2008, 2011) studied the possible rapid disruption of clumps via vigorous outflows and the kinematic signatures of inward gas streaming motions in clumpy disks. These signatures suggest that the gas inflows that are fed to the centers of galaxies through internal violent processes may play an important role in building bulges along with clump migration, as highlighted in some of the most recent numerical simulations (e.g., Bournaud et al., 2011). Furthermore, given the fact that some objects in our sample may be merging systems, e.g., Galaxy 24919, the role of merger on building bulges cannot be fully excluded. It is very likely that more than one process could be responsible for early bulge building at $z\sim 2$. To understand the contribution of each possible mechanism requires further investigations with larger samples and newer observations.

3.7 Summary and Conclusions

In this chapter, we study the nature and evolution of kpc-scale clumps in $z \sim 2$ SFGs through broad-band multi-wavelength photometry. We identify clumps through a hybrid of auto-detection and visual inspection from 10 galaxies with spec-zs between 1.5 and 2.5 in the HUDF, where the recently available ultra-deep HST/WFC3 and ACS images enable us to resolve into kpc-scale at $z \sim 2$ and to detect clumps toward the faint end. Using the spatially resolved seven-band (BVizYJH) photometry, we measure physical properties of clumps and their “disks” (namely the diffuse components of the host galaxies) through SED-fitting with three types of SFHs: exponentially decreasing, exponentially increasing, and constant. We compare the properties of clumps to those of their surrounding materials and also study the radial variations of clump properties across their host galaxies. The main results of this chapter are summarized as the following:

1. The number of clumps in our galaxies runs from 2 to 5, with a median of 4. The total number of 40 clumps enables us to study the physical properties of clumps with sufficient number statistics.
2. Most of our clumps have blue rest-frame UV–optical colors that are similar to the colors of their surrounding “disks” or their host galaxies as a whole. Only few clumps are as red as quiescent galaxies at $z \sim 2$. The CMD of clumps indicate that they are still actively forming stars.
3. The SFR–stellar mass relation of clumps and “disks” have almost same slopes, but that of clumps has higher normalization, converting to higher SSFR. However, the SFR–stellar mass relation of the host galaxies as a whole is still dominated by “disk”, as both SFR and stellar mass of host galaxies are largely contributed by “disks”. This shows that clumps are regions with enhanced SSFR in “disks”.

4. An individual clump typically contributes a few percent of the rest-frame UV/optical luminosity and stellar mass to its host galaxy. Together, all clumps in one galaxy typically contribute 20% of the luminosity and stellar mass of the host galaxy. The contribution of clumps on SFR is higher, individually about 10% and together 50% of the host galaxies, consistent with the fact that clumps are regions with enhanced SSFR.
5. Clumps differ from their surrounding area in terms of age and stellar surface density. On average, clumps are younger by 0.2 dex and denser by 8 times than their “disks”. There is no obvious difference between the $E(B-V)$ distributions of the two components. In terms of rest-frame U-V color, both components have similar median values, but clumps spread over a broader range, which may indicate the different SFHs or evolutionary stages of clumps.
6. Clumps have obvious radial variations on their properties. Clumps close to the centers of their host galaxies (the Kron radius scaled projected distance $d < 0.1$) are 0.7 mag redder in rest-frame U-V color than those in outskirts ($d > 0.5$). Spatially resolved SED-fitting shows that the color trend can be explained by the combination of radial variations of age and dust extinction. Central clumps ($d < 0.1$) are typically 600 Myr older and more extinguished ($E(B-V)$ larger by 0.2) than those in outskirts, with the latter is typically 100 Myr old and having $E(B-V) \sim 0.2$. The central clumps are also 25 times denser than their outskirts counterparts. However, the trend of SSFR is slightly weak, only increasing by a factor of 5 from the central to outskirts.
7. The radial variations are affected by the scheme of diffuse background subtraction, but our conclusions are unaffected. Besides the above results with a *constant* background subtraction, we also study the radial variations under other two background subtraction schemes: *local* subtraction and *zero* subtraction.

tion. All the trends observed in the *constant* subtraction scheme are reserved in the two new cases of subtractions, but with strength weaken. The change of the strength is largely caused by the redder color of outskirts clumps in new subtraction schemes than in the *constant* subtraction scheme. The central clumps are now only 0.5 mag redder and 300 Myr older than outskirts clumps. The trend of $E(B-V)$ does not significantly changed. And the trend of stellar surface density is still prominent, with the central ones still 10 times denser than the outskirts ones. The SSFR trend is weaken the most, with a difference only a few times between centers and outskirts. Arguing that the real trends would reside between the two extreme cases of background subtraction: *constant* and *zero*, we conclude that central clumps are redder, older, more extincted, denser, and less active on forming stars than outskirts clumps.

8. The host “disks” (interclump regions) exhibit mild gradients of rest-frame UV color, age, and dust extinction. However, these gradients are significantly weaker/flatter than those of clumps. The results suggest that (1) the observed color and property gradients of clumps are not a simple reflection of those of host “disks”; (2) the color and property gradients of “disks” contribute to, if any, only a small part of the gradients of clumps; and (3) the evolution of clumps are dynamically separated from those of “disks”. Thus, we claim that mechanisms such like the inward migration is needed to explain the steeper gradient of clumps. A further test also shows that the use of different background subtraction schemes does not significantly change this result.
9. Our measurements of the properties of clumps are in broadly consistent with those of previous observational studies. They are also consistent the clump formation mechanism that clumps are formed through gravitational instability in gas-rich turbulent disks, proposed by several theoretical work and numerical

simulations. However, we cannot rule out the scenario that clumps are formed through external violent processes, e.g., interactions and mergers, as a couple of galaxies in our sample show merger signatures.

10. The obvious radial variations of clump properties, especially the radial age variation, are consistent with the hypothesis that clumps would migrate toward the centers of their host galaxies, with a timescale of ~ 0.5 Gyr, and eventually coalesce into young bulges. However, the dearth of young clumps in the central regions of galaxies reminds us that not all clumps are able to survive enough to migrate into centers. We argue that the lifetime of clumps are correlated with their stellar surface densities. Only clumps that are dense enough can survive long enough to sink into the centers.
11. We roughly estimate whether some clumps in our sample are actually coalesced bulges or proto-bulges through a few ways: morphology and color of clumps, stellar mass of clumps, X-ray detection of galaxies, and age of clumps. The bulge fraction, namely the fraction of galaxies that contain bulges, in our sample is 20%–50%, depending on the way of constraint. This result is broadly consistent with the prediction based on the migration timescale of clumps. We argue that the process of bulge formation is ongoing in our $z \sim 2$ sample.

We note that our sample only contains 10 galaxies and thus is likely subject to small number statistics incompleteness. Also, our results apply strictly to galaxies with relatively large UV luminosity, since our sample only includes cases with spectroscopic redshifts. In order to obtain a robust statistical characterization of the properties of clumps, including their dependence on radial separation from the center of the galaxies and the fraction of clumpy galaxies at $z \sim 2$, a much larger sample covering a wider range of both luminosity and stellar mass is needed. The ongoing CANDELS (Grogin et al., 2011; Koekemoer et al., 2011) is beginning to provide deep

images over a larger sky area, ≈ 0.5 square degree, to answer these questions. Moreover, the deep NIR observation of CANDELS will significantly improve the accuracy of the photometric redshift measurements at $z \sim 2$, enabling us to construct deeper samples not limited by spec- z . Wuyts et al. (2012) already used part of CANDELS data to study the profiles of color, surface stellar mass density, age, and extinction of a large sample of massive SFGs and to address clump properties. Their approach is different from ours, as we try to identify clumps and separate the light and properties of clumps from those of the diffuse background of host galaxies, while they focused generally on regions with excess surface brightness and did not subtract the diffuse background light from clumps. Both approaches are complementary to each other and needed to obtain a robust view on the nature and fate of clumps. In a future paper we will report on a study similar to the one discussed in this chapter that takes advantage of the CANDELS data set.

Table 3.1 Properties of Star-forming Galaxies at $z \sim 2$

ID	RA J2000	DEC J2000	z	M_{star} $\text{Log}(M^*/M_{\odot})$	SFR M_{\odot}/yr	E(B-V)	U-V	M_V
20565	53.1422430	-27.7954120	2.016	10.28 ± 0.05	30.45 ± 6.09	0.20 ± 0.05	0.64 ± 0.00	-21.50 ± 0.00
21739	53.1485260	-27.7969040	1.765	9.92 ± 0.02	33.64 ± 6.73	0.10 ± 0.05	0.23 ± 0.00	-21.54 ± 0.00
21852	53.1492150	-27.7788090	1.850	10.35 ± 0.04	40.35 ± 8.07	0.25 ± 0.05	0.61 ± 0.00	-21.42 ± 0.00
22284	53.1516190	-27.7964320	1.767	10.51 ± 0.12	51.32 ± 10.26	0.15 ± 0.05	0.48 ± 0.00	-22.15 ± 0.00
23013	53.1556430	-27.7792950	1.846	10.73 ± 0.10	162.39 ± 32.48	0.30 ± 0.05	0.62 ± 0.00	-22.51 ± 0.00
24033	53.1616630	-27.7874320	1.836	10.79 ± 0.15	111.00 ± 31.07	0.35 ± 0.06	0.77 ± 0.00	-22.10 ± 0.00
24684	53.1655460	-27.7697760	1.552	11.06 ± 0.07	10.93 ± 6.60	0.20 ± 0.13	1.36 ± 0.00	-21.92 ± 0.00
24919	53.1668940	-27.7987410	1.998	11.02 ± 0.02	423.67 ± 84.73	0.40 ± 0.05	0.74 ± 0.00	-23.03 ± 0.00
26067	53.1743180	-27.7825190	1.994	10.61 ± 0.11	64.39 ± 12.88	0.25 ± 0.05	0.67 ± 0.00	-21.97 ± 0.00
27101	53.1817060	-27.7830010	1.570	10.21 ± 0.05	64.68 ± 17.49	0.30 ± 0.05	0.69 ± 0.00	-21.46 ± 0.00

Table 3.2: Properties of Clumps and “Disks”

ID 1	ID 2 ¹	d	M_{star} ²	SFR	E(B-V)	age	U-V	M_V
Galaxy	Clump	$\frac{d_{\text{proj}}}{r_{\text{kron}}}$	$\text{log}(M_{\odot})$	$M_{\odot} \text{yr}^{-1}$		Gyr		
20565	1	0.24	8.80 ± 0.00	3.77 ± 0.75	0.25 ± 0.05	0.20 ± 0.00	0.35 ± 0.17	-18.30 ± 0.14
			8.88 ± 0.04	4.45 ± 0.89	0.25 ± 0.05	0.20 ± 0.02	0.40 ± 0.14	-18.52 ± 0.12
			8.77 ± 0.00	3.49 ± 0.70	0.25 ± 0.05	0.20 ± 0.00	0.32 ± 0.15	-18.20 ± 0.13

Table 3.2 – continued

ID 1	ID 2	d	M _{star}	SFR	E(B-V)	age	U-V	M _V
Galaxy	Clump	$\frac{d_{\text{proj}}}{r_{\text{kron}}}$	log(M _⊙)	M _⊙ yr ⁻¹		Gyr		
20565	2	0.01	9.27± 0.05	7.52± 2.04	0.30±0.05	0.30±0.04	0.69±0.14	-19.15± 0.12
			9.42± 0.03	5.40± 2.01	0.25±0.05	0.60±0.05	0.68±0.13	-19.25± 0.10
			9.15± 0.02	5.62± 1.23	0.30±0.05	0.30±0.02	0.67±0.19	-18.80± 0.15
20565	3	0.16	9.05± 0.06	6.72± 2.23	0.30±0.05	0.20±0.03	0.61±0.15	-18.77± 0.12
			9.11± 0.06	7.66± 2.55	0.30±0.05	0.20±0.03	0.62±0.14	-18.92± 0.12
			9.08± 0.09	48.18± 26.62	0.30±0.05	0.40±0.13	0.54±0.20	-18.62± 0.18
20565	D	—	10.24± 0.03	24.62± 4.92	0.20±0.05	0.90±0.07	0.66±0.00	-21.20± 0.00
			10.28± 0.05	30.45± 6.09	0.20±0.05	0.60±0.06	0.64±0.00	-21.50± 0.00
			10.31± 0.05	32.69± 6.54	0.20±0.05	0.60±0.06	0.65±0.00	-21.59± 0.00
21739	1	0.25	8.97± 0.04	5.52± 1.10	0.20±0.05	0.20±0.02	0.40±0.11	-18.98± 0.08
			9.03± 0.03	6.37± 1.42	0.20±0.05	0.20±0.02	0.38±0.10	-19.11± 0.07
			8.86± 0.04	4.33± 0.87	0.20±0.05	0.20±0.02	0.41±0.12	-18.71± 0.10
21739	2	0.22	8.16± 0.00	14.84± 2.97	0.25±0.05	0.01±0.00	0.12±0.11	-18.52± 0.07
			8.23± 0.00	17.36± 3.47	0.25±0.05	0.01±0.00	0.14±0.09	-18.71± 0.07
			8.12± 0.00	13.47± 2.69	0.25±0.05	0.01±0.00	0.03±0.12	-18.35± 0.10
21739	3	0.07	7.97± 0.29	9.51± 2.38	0.20±0.06	0.01±0.01	-0.04±0.13	-18.24± 0.10
			8.65± 0.07	1.77± 0.45	0.05±0.05	0.30±0.08	0.01±0.10	-18.49± 0.08
			7.87± 0.00	7.53± 1.51	0.20±0.05	0.01±0.00	-0.08±0.18	-17.95± 0.14
21739	4	0.34	8.09± 0.02	0.50± 0.10	0.05±0.05	0.30±0.03	0.15±0.17	-17.18± 0.10
			8.27± 0.07	0.61± 0.12	0.00±0.05	0.20±0.03	0.19±0.09	-17.73± 0.07
			8.30± 0.05	0.49± 0.10	0.05±0.05	0.50±0.06	0.24±0.14	-17.31± 0.10
21739	5	0.52	7.74± 0.10	0.70± 0.51	0.05±0.05	0.09±0.03	0.13±0.18	-17.04± 0.13
			8.19± 0.01	0.92± 0.18	0.05±0.05	0.20±0.00	0.18±0.11	-17.65± 0.09
			8.00± 0.01	0.60± 0.12	0.05±0.05	0.20±0.00	0.20±0.15	-17.18± 0.12
21739	D	—	9.80± 0.04	25.18± 5.04	0.10±0.05	0.30±0.05	0.25±0.00	-21.24± 0.00
			9.92± 0.02	33.64± 6.73	0.10±0.05	0.30±0.03	0.23±0.00	-21.54± 0.00
			9.96± 0.02	36.81± 7.36	0.10±0.05	0.30±0.03	0.24±0.00	-21.64± 0.00
21852	1	0.37	8.84± 0.07	2.09± 0.42	0.25±0.05	0.40±0.07	0.52±0.15	-17.97± 0.12
			8.93± 0.08	2.61± 0.52	0.25±0.05	0.40±0.07	0.54±0.12	-18.24± 0.08
			8.82± 0.03	1.17± 0.57	0.20±0.05	0.70±0.03	0.60±0.17	-17.78± 0.14
21852	2	0.10	9.01± 0.08	3.37± 0.67	0.25±0.05	0.20±0.03	0.67±0.13	-18.58± 0.09
			9.13± 0.10	3.09± 0.62	0.25±0.05	0.30±0.07	0.66±0.14	-18.74± 0.10
			9.05± 0.03	2.75± 0.55	0.30±0.05	0.50±0.03	0.68±0.22	-18.15± 0.15
21852	3	0.20	8.83± 0.03	2.69± 0.77	0.25±0.05	0.30±0.02	0.51±0.18	-18.17± 0.12
			9.00± 0.04	2.07± 0.41	0.20±0.05	0.60±0.09	0.53±0.16	-18.40± 0.10
			8.54± 0.03	2.07± 0.41	0.25±0.05	0.20±0.02	0.46±0.29	-17.68± 0.22
21852	4	0.09	9.34± 0.03	6.67± 1.33	0.40±0.05	0.40±0.03	0.80±0.14	-18.62± 0.09
			9.40± 0.03	5.22± 1.04	0.35±0.05	0.60±0.06	0.77±0.14	-18.78± 0.09
			9.27± 0.04	10.98± 2.20	0.65±0.05	0.20±0.02	1.05±0.37	-17.80± 0.25
21852	D	—	9.99± 0.15	10.83± 2.91	0.15±0.06	0.30±0.07	0.60±0.00	-21.12± 0.00
			10.35± 0.04	40.35± 8.07	0.25±0.05	0.70±0.07	0.61±0.00	-21.42± 0.00
			10.41± 0.03	46.11± 9.22	0.25±0.05	0.70±0.06	0.61±0.00	-21.55± 0.00
22284	1	0.24	8.86± 0.06	2.92± 1.79	0.10±0.05	0.30±0.05	0.26±0.14	-18.91± 0.10
			8.96± 0.03	5.47± 1.22	0.15±0.05	0.20±0.02	0.30±0.10	-19.16± 0.08
			8.72± 0.04	2.08± 0.42	0.10±0.05	0.30±0.05	0.33±0.19	-18.57± 0.14
22284	2	0.11	9.47± 0.11	3.76± 0.75	0.25±0.05	0.40±0.09	0.84±0.14	-19.28± 0.10
			9.42± 0.18	2.91± 0.58	0.20±0.05	0.30±0.11	0.78±0.10	-19.47± 0.08

Table 3.2 – continued

ID 1	ID 2	d	M _{star}	SFR	E(B-V)	age	U-V	M _V
Galaxy	Clump	$\frac{d_{\text{proj}}}{r_{\text{kron}}}$	log(M _⊙)	M _⊙ yr ⁻¹		Gyr		
22284	3	0.39	9.38± 0.12	1.89± 0.38	0.25±0.05	0.60±0.13	0.92±0.17	-18.84± 0.13
			7.70± 0.00	5.11± 1.02	0.20±0.05	0.01±0.00	-0.16±0.20	-17.43± 0.15
			8.43± 0.07	3.07± 0.62	0.15±0.05	0.10±0.02	0.12±0.12	-18.21± 0.08
22284	D	—	7.61± 0.00	4.13± 0.83	0.20±0.05	0.01±0.00	0.00±0.26	-17.32± 0.20
			10.42± 0.01	64.88± 12.98	0.20±0.05	0.50±0.02	0.48±0.00	-21.99± 0.00
			10.51± 0.12	51.32± 10.26	0.15±0.05	0.80±0.21	0.48±0.00	-22.15± 0.00
			10.36± 0.11	51.99± 10.40	0.15±0.05	0.30±0.07	0.48±0.00	-22.23± 0.00
23013	1	0.04	10.03± 0.01	63.07± 12.61	0.55±0.05	0.20±0.00	0.84±0.12	-20.07± 0.09
			10.08± 0.04	48.06± 9.61	0.50±0.05	0.30±0.03	0.81±0.11	-20.19± 0.07
23013	2	0.35	9.89± 0.04	30.98± 6.20	0.50±0.05	0.30±0.05	0.84±0.16	-19.76± 0.11
			9.01± 0.07	11.72± 2.38	0.30±0.05	0.10±0.02	0.42±0.15	-18.97± 0.10
			9.25± 0.05	17.40± 3.70	0.30±0.05	0.20±0.05	0.46±0.11	-19.28± 0.09
23013	3	0.19	8.80± 0.02	9.06± 1.81	0.30±0.05	0.08±0.00	0.39±0.18	-18.65± 0.14
			9.29± 0.01	22.52± 4.50	0.45±0.05	0.10±0.00	0.66±0.17	-19.11± 0.11
23013	4	0.65	9.49± 0.01	18.45± 3.69	0.40±0.05	0.20±0.00	0.65±0.13	-19.39± 0.10
			9.12± 0.06	16.62± 7.61	0.45±0.05	0.09±0.02	0.63±0.24	-18.71± 0.17
			7.02± 0.00	1.06± 0.21	0.00±0.05	0.01±0.00	-0.71±0.31	-16.34± 0.29
23013	D	—	8.25± 0.18	2.04± 8.36	0.10±0.05	0.10±0.07	0.17±0.10	-18.03± 0.06
			8.03± 0.02	1.74± 0.35	0.10±0.05	0.07±0.00	0.11±0.13	-17.67± 0.09
			10.63± 0.10	131.35± 26.27	0.30±0.05	0.40±0.08	0.61±0.00	-22.29± 0.00
			10.73± 0.10	162.39± 32.48	0.30±0.05	0.40±0.08	0.62±0.00	-22.51± 0.00
24033	1	0.30	10.76± 0.03	176.46± 35.29	0.30±0.05	0.40±0.02	0.62±0.00	-22.61± 0.00
			9.09± 0.04	49.43± 31.14	0.25±0.05	0.40±0.03	0.50±0.14	-18.88± 0.11
			9.27± 0.10	54.11± 27.27	0.25±0.05	0.60±0.17	0.54±0.12	-19.10± 0.09
24033	2	0.12	8.87± 0.04	14.83± 5.16	0.25±0.05	0.20±0.02	0.43±0.16	-18.65± 0.12
			9.50± 0.10	9.66± 3.97	0.35±0.05	0.40±0.11	0.75±0.16	-19.22± 0.10
			9.56± 0.15	11.05± 7.42	0.35±0.05	0.40±0.16	0.75±0.15	-19.38± 0.09
24033	3	0.07	9.20± 0.03	6.37± 1.27	0.35±0.05	0.30±0.02	0.71±0.21	-18.72± 0.17
			10.23± 0.09	41.96± 8.39	0.65±0.05	0.50±0.06	1.19±0.14	-19.63± 0.09
			10.26± 0.09	25.24± 5.05	0.55±0.05	0.90±0.18	1.14±0.11	-19.75± 0.08
24033	4	0.27	10.11± 0.10	14.20± 5.08	0.70±0.09	0.30±0.02	1.45±0.26	-19.07± 0.15
			9.45± 0.04	11.23± 2.25	0.50±0.05	0.30±0.03	0.70±0.17	-18.58± 0.11
			9.55± 0.08	10.77± 2.15	0.45±0.05	0.40±0.07	0.71±0.14	-18.86± 0.09
24033	D	—	9.20± 0.00	9.48± 1.90	0.50±0.05	0.20±0.00	0.73±0.23	-18.23± 0.15
			10.70± 0.16	78.01± 20.17	0.35±0.06	0.80±0.20	0.75±0.00	-21.76± 0.00
			10.79± 0.15	111.00± 31.07	0.35±0.06	0.70±0.16	0.77±0.00	-22.10± 0.00
24684	1	0.20	10.85± 0.15	125.39± 33.86	0.35±0.06	0.70±0.16	0.78±0.00	-22.23± 0.00
			8.86± 0.14	2.88± 3.10	0.35±0.05	0.30±0.12	0.74±0.12	-17.85± 0.09
			9.20± 0.13	3.30± 3.30	0.35±0.05	0.60±0.24	0.92±0.10	-18.33± 0.07
24684	2	0.04	8.70± 0.06	2.94± 0.59	0.35±0.05	0.20±0.03	0.63±0.16	-17.61± 0.12
			10.48± 0.31	0.00± 0.00	0.30±0.40	3.00±0.00	2.47±0.13	-19.38± 0.06
			10.87± 0.12	3.27± 2.42	0.60±0.20	3.00±0.00	2.26±0.10	-19.51± 0.07
24684	3	0.32	10.93± 0.01	3.78± 2.33	0.75±0.14	3.00±0.00	2.60±0.16	-19.10± 0.07
			7.75± 0.03	0.91± 0.18	0.10±0.05	0.07±0.01	0.03±0.18	-16.91± 0.15
			8.76± 0.04	0.53± 0.11	0.05±0.05	1.40±0.19	0.63±0.08	-17.87± 0.06
24684	4	0.13	8.05± 0.04	0.45± 0.09	0.05±0.05	0.30±0.02	0.37±0.17	-17.21± 0.12
			9.37± 0.07	1.69± 0.38	0.40±0.05	1.80±0.23	1.22±0.17	-17.83± 0.11

Table 3.2 – continued

ID 1	ID 2	d	M _{star}	SFR	E(B-V)	age	U-V	M _V
Galaxy	Clump	$\frac{d_{\text{proj}}}{r_{\text{kron}}}$	log(M _⊙)	M _⊙ yr ⁻¹		Gyr		
24684	5	0.31	9.74± 0.01	2.43± 0.49	0.40±0.05	3.00±0.05	1.27±0.10	-18.31± 0.08
			9.37± 0.01	1.19± 0.24	0.35±0.05	2.60±0.09	1.17±0.19	-17.74± 0.13
			8.63± 0.02	1.70± 0.34	0.35±0.05	0.30±0.03	0.71±0.18	-17.28± 0.13
			9.20± 0.04	2.23± 0.61	0.35±0.05	0.90±0.09	0.97±0.11	-18.00± 0.06
24684	D	—	8.72± 0.04	0.94± 0.49	0.30±0.05	0.70±0.14	0.83±0.24	-17.15± 0.15
			11.01± 0.09	12.58± 5.73	0.25±0.12	2.20±0.17	1.36±0.01	-21.71± 0.00
			11.06± 0.07	10.93± 6.60	0.20±0.13	2.40±0.13	1.36±0.00	-21.92± 0.00
24919	1	0.22	11.10± 0.09	11.86± 6.59	0.20±0.13	2.40±0.13	1.37±0.00	-22.01± 0.00
			9.23± 0.01	21.62± 4.32	0.30±0.05	0.09±0.00	0.30±0.18	-19.60± 0.12
			9.30± 0.10	37.34± 7.47	0.35±0.05	0.06±0.02	0.39±0.15	-19.88± 0.12
24919	2	0.07	9.21± 0.00	18.85± 3.77	0.30±0.05	0.10±0.00	0.35±0.19	-19.50± 0.16
			9.99± 0.03	29.81± 5.96	0.40±0.05	0.40±0.03	0.93±0.15	-20.26± 0.12
			10.06± 0.03	35.04± 7.01	0.40±0.05	0.40±0.03	0.90±0.12	-20.42± 0.10
24919	3	0.25	9.76± 0.00	23.24± 4.65	0.40±0.05	0.30±0.00	0.91±0.20	-19.92± 0.16
			9.30± 0.08	37.13± 7.43	0.55±0.05	0.06±0.02	0.76±0.18	-19.03± 0.15
			9.60± 0.04	23.63± 4.73	0.45±0.05	0.20±0.02	0.75±0.13	-19.47± 0.11
24919	4	0.25	9.26± 0.02	25.65± 5.13	0.50±0.05	0.08±0.00	0.70±0.23	-18.91± 0.17
			9.69± 0.00	494.21± 98.84	0.95±0.05	0.01±0.00	1.07±0.16	-19.26± 0.14
			10.02± 0.02	42.12± 8.42	0.60±0.05	0.30±0.03	0.97±0.13	-19.63± 0.09
24919	5	0.33	9.72± 0.00	530.72±106.14	1.00±0.05	0.01±0.00	1.04±0.23	-19.06± 0.19
			9.27± 0.04	7.46± 1.49	0.35±0.05	0.30±0.03	0.56±0.20	-18.76± 0.17
			9.45± 0.04	11.22± 2.24	0.35±0.05	0.30±0.05	0.63±0.14	-19.30± 0.12
24919	D	—	9.09± 0.00	7.22± 1.44	0.35±0.05	0.20±0.00	0.60±0.30	-18.57± 0.25
			10.92± 0.05	334.27± 66.85	0.40±0.05	0.30±0.05	0.74±0.00	-22.80± 0.00
			11.02± 0.02	423.67± 84.73	0.40±0.05	0.30±0.03	0.74±0.00	-23.03± 0.00
26067	1	0.09	11.06± 0.03	463.33± 92.67	0.40±0.05	0.30±0.02	0.74±0.00	-23.13± 0.00
			9.35± 0.07	23.57± 7.39	0.20±0.05	0.60±0.10	0.55±0.14	-19.44± 0.11
			9.36± 0.04	9.27± 1.85	0.20±0.05	0.40±0.03	0.56±0.14	-19.57± 0.10
26067	2	0.13	9.14± 0.02	5.56± 1.21	0.20±0.05	0.30±0.02	0.52±0.15	-19.18± 0.15
			9.87± 0.06	13.36± 2.67	0.40±0.05	0.70±0.10	0.83±0.12	-19.53± 0.09
			9.93± 0.08	10.71± 2.14	0.35±0.05	1.00±0.20	0.81±0.12	-19.65± 0.10
26067	D	—	9.77± 0.06	10.50± 2.10	0.40±0.05	0.70±0.10	0.85±0.20	-19.28± 0.15
			10.55± 0.05	49.82± 9.96	0.25±0.05	0.90±0.09	0.66±0.00	-21.72± 0.00
			10.61± 0.11	64.39± 12.88	0.25±0.05	0.80±0.20	0.67±0.00	-21.97± 0.00
27101	1	0.06	10.64± 0.11	68.62± 13.72	0.25±0.05	0.80±0.20	0.67±0.00	-22.04± 0.00
			9.61± 0.05	2.91± 0.58	0.30±0.05	1.80±0.20	1.02±0.10	-18.81± 0.07
			9.63± 0.04	3.91± 0.78	0.30±0.05	1.40±0.16	0.98±0.10	-18.95± 0.06
27101	2	0.17	9.39± 0.07	2.58± 2.85	0.30±0.05	1.20±0.28	0.99±0.14	-18.55± 0.10
			8.52± 0.01	5.32± 1.06	0.30±0.05	0.07±0.00	0.50±0.13	-18.08± 0.09
			8.71± 0.64	5.89± 44.74	0.30±0.05	0.10±0.09	0.54±0.09	-18.35± 0.06
27101	3	0.17	8.58± 0.02	4.32± 0.86	0.30±0.05	0.10±0.01	0.55±0.14	-18.01± 0.10
			8.06± 0.00	11.78± 2.36	0.40±0.05	0.01±0.00	0.10±0.12	-17.45± 0.09
			8.18± 0.00	15.62± 3.12	0.40±0.05	0.01±0.00	0.26±0.09	-17.89± 0.06
27101	4	0.17	7.98± 0.00	9.83± 1.97	0.40±0.05	0.01±0.00	0.10±0.17	-17.25± 0.13
			9.00± 0.07	0.82± 0.21	0.20±0.05	1.60±0.28	0.81±0.16	-17.83± 0.10
			9.14± 0.04	1.26± 1.11	0.20±0.05	1.40±0.27	0.78±0.08	-18.16± 0.06
			8.77± 0.16	1.21± 1.16	0.25±0.05	0.60±0.31	0.77±0.17	-17.68± 0.13

Table 3.2 – continued

ID 1	ID 2	d	M _{star}	SFR	E(B-V)	age	U-V	M _V
Galaxy	Clump	$\frac{d_{\text{proj}}}{r_{\text{kron}}}$	log(M _⊙)	M _⊙ yr ⁻¹		Gyr		
27101	5	0.27	8.59± 0.07	0.41± 0.46	0.10±0.05	1.20±0.28	0.61±0.15	-17.36± 0.10
			8.80± 0.06	0.89± 0.18	0.15±0.05	0.90±0.12	0.64±0.10	-17.82± 0.07
			8.16± 0.16	0.58± 1.30	0.15±0.05	0.30±0.18	0.45±0.21	-16.95± 0.15
27101	D	—	10.10± 0.06	50.42± 15.87	0.30±0.05	0.30±0.05	0.70±0.01	-21.19± 0.00
			10.21± 0.05	64.68± 17.49	0.30±0.05	0.30±0.04	0.69±0.00	-21.46± 0.00
			10.25± 0.03	70.69± 14.14	0.30±0.05	0.30±0.02	0.70±0.00	-21.56± 0.00

Table 3.3 Comparison of Derived Properties of Three Galaxies in Our Sample and Elmegreen et al. (2005)

Galaxy	ID	z	N _{clump}	Age _{clump} (Gyr)	Age _{disk} (Gyr)	< M _{clump} > 10 ⁹ M _⊙	f _{mass}	M _{gal} 10 ¹⁰ M _⊙	< SFR _{clump} > M _⊙ yr ⁻¹
1	21739	1.765	5	0.12	0.30	0.27	0.16	0.8	6.2
	3465+	2.4	11	0.22	1.80	0.87	0.28	3.5	4.5
2	22284	1.767	3	0.24	0.50	1.25	0.12	3.2	3.9
	3483	2.2	12	0.26	2.02	1.31	0.32	4.9	1.0
3	27101	1.570	5	0.94	0.30	1.18	0.36	1.6	4.3
	6462+	2.8	8	0.31	2.82	1.57	0.22	5.7	0.9

Note: For each galaxy, the first line shows the data in our work, while the second line shows the data in Elmegreen et al. (2005). In this table, we have applied the relations in Sec. 3.6.1 to convert the Chabrier IMF to the Salpeter IMF.

¹Numbers stand for ID of clumps in the z-band images of Figure 3.1, while “D” stands for the diffuse “disk” component.

²For each clump, properties derived under different background subtraction schemes are listed: global constant background (1st line), zero background (2nd line) and local background (3rd line).

CHAPTER 4

COLOR AND STELLAR POPULATION GRADIENTS IN PASSIVELY EVOLVING GALAXIES AT $Z \sim 2$

4.1 Introduction

The spheroids, namely elliptical galaxies and bulges of spiral galaxies, segregate $\approx 60\%$ of all the stars in the local universe (Hogg et al., 2002; Bell et al., 2003; Driver et al., 2006), and their stellar content mostly consists of old stars that formed at high redshift, e.g. $z > 2$ (Renzini 2006). Therefore, the mechanisms that led to their assembly are key to the evolution of galaxies across the cosmic time in general. But while there is agreement on the age of the stars of the spheroids, how these stars got together and formed the body of ellipticals and bulges remains an open issue.

During the past several years, galaxies at $z > 1$ with stellar mass (M_{star}) and SED similar to those of local early-type galaxies have been identified and studied in relatively large numbers, thanks to the increased availability of deep optical and near-IR photometry from large-area surveys (e.g., Thompson et al., 1999; Franx et al., 2003; Daddi et al., 2004a) as well as spectral data (e.g., Kriek et al., 2006a,b; Cimatti et al., 2008; Onodera et al., 2010). More recently, an increasing number of studies seems to show that the number density of massive galaxies with very low specific star formation rate (SSFR) undergoes rapid evolution between $z \sim 2$ and $z \sim 1$ (e.g., Fontana et al., 2006; Arnouts et al., 2007; Ilbert et al., 2009; Cassata et al., 2011). The physical mechanisms responsible for this apparently rapid assembly of massive passively evolving galaxies (PEGs) remains unknown. Equally unknown is if this is just the assembly of the stellar bodies of the massive galaxies, or if the fraction of stars locked in passively evolving systems is also evolving accordingly. Various formation mechanisms,

for example, merger (e.g., Brinchmann & Ellis, 2000; Le Fèvre et al., 2000; De Lucia et al., 2006; Naab et al., 2007; Naab & Ostriker, 2009) and feedback (e.g., Benson et al., 2003; Croton et al., 2006), have been proposed to explain the rapid emergence of massive PEGs during this redshift range, which is also the cosmic epoch when star formation in the universe reaches at its peak. Such mechanisms would leave distinguishable imprints on the color and stellar population gradients of massive PEGs. For example, a major merger (i.e. mass ratio approximately unitary) of gas-rich galaxies would form a spheroid and trigger a bursts of central star-formation, which would leave a blue core to the spheroid (Menanteau et al., 2001a, 2004; Daddi et al., 2005). Or, if massive PEGs mostly assemble their masses through dry mergers or mergers that do not induce central star-formation, they would generally not have blue cores. Thus, studying color gradients and their implications on the stellar population gradients of massive PEGs is expected to provide important clues on the formation of massive PEGs at $z \sim 2$.

Related to the formation mechanisms is the issue of the subsequent evolution of the massive PEGs. Recent work (e.g., Daddi et al., 2005; Trujillo et al., 2006, 2007; van Dokkum et al., 2008; Cassata et al., 2010) shows that many massive PEGs at $z > 1.5$ are, on average, ~ 5 times smaller and ~ 50 times denser than their local counterparts with similar mass. The physical mechanisms proposed to explain this apparently dramatic evolution of size include major merger (e.g., Hopkins et al., 2009b; van der Wel et al., 2009), minor merger (e.g., Naab et al., 2009), adiabatic expansion (e.g., Fan et al., 2008), and mass-to-light gradients (e.g., Hopkins et al., 2010). Others (e.g., Hopkins et al., 2009a; Mancini et al., 2010) have suggested that the small size of some PEGs at high redshift may be due to an observational bias such that the low surface-brightness halos surrounding these PEGs are not detected by current near-IR observations. They argued that if these missing halos were detected, the derived size of high- z massive PEGs would be similar to that of their local counterparts. In order

to answer the question whether the observed strong size evolution of massive PEGs from $z \sim 2$ to $z \sim 0$ is physical or not, near-IR observations with high sensitivity are required to measure the color and stellar population distributions of massive PEGs to large radius.

Color gradients in early type galaxies have been known for about thirty years (Faber, 1972) and widely studied in local galaxies (e.g., Peletier et al., 1990a; Tamura et al., 2000; La Barbera et al., 2005; La Barbera & de Carvalho, 2009; Gonzalez-Perez et al., 2011), but no information is currently available on color gradients in PEGs at high redshift ($z \sim 2$), because of instrumental limitations on sensitivity and angular resolution, given the compact size of such sources, and the lack of spectral coverage of the rest-frame optical SED. Ground-based observations suffer from poor resolution and/or wavelength-dependent and unstable Strehl ratio. Sensitivity to low-surface brightness regions is also limited due to the high and variable sky background. For example, the typical full-width half-maximum (FWHM) of the point spread function (PSF) of VLT ISAAC Ks-band images is about $0.5''$, corresponding to ~ 4 kpc for a galaxy at $z \sim 2$. This size is almost 4 times of the average effective radius of a PEGs with $M_{\text{star}} = 10^{10} M_{\odot}$ at $z \sim 2$ (Cassata et al., 2010, and reference therein). Even if upcoming adaptive optics systems reach near-*HST* resolution in the K band, performance degrade rapidly at shorter wavelength so that making robust color maps is not yet feasible. To sample the color and stellar population gradients of PEGs at $z \sim 2$ at the \sim kpc scale, a minimum angular resolution of about $\sim 0.1''$ is required at both optical and near-IR wavelength. Although *HST* NICMOS-1 and NICMOS-2 have such required resolution, their small fields of view and low throughput make them inconvenient for surveying large sky area and observing distant and faint galaxies. The detailed study on color gradients of a large sample of high-redshift early-type galaxies is only now available thanks to the WFC3/IR imager on-board of *HST*.

In this chapter we use the HUDF *HST*/ACS images in combination with recent WFC3 near-IR deep images in the same field to measure the color gradients of a sample of massive PEGs at $z \sim 2$ up to about 10 times their effective radius. We measure color gradients for these galaxies in a series of concentric annuli from the ACS and WFC3 images and fit the spatially resolved SED to stellar population synthesis models to derive the corresponding gradients of stellar population parameters (SSFR, age, extinction), looking for trends between the color gradient characteristics and the stellar population properties in an attempt to derive clues on their origins.

4.2 Passively Evolving Galaxies at $z \sim 2$ in HUDF

We select PEGs based on their SSFRs estimated by fitting the GOODS GUTFIT 12-band photometry to stellar population synthesis models (see Sec. 2.2 and 2.3 for details). In our study, PEGs are defined as those galaxies whose specific star-formation rate satisfies the relation

$$\text{SSFR} = \frac{\text{SFR}}{M_{\text{star}}} \leq 10^{-11} \text{ yr}^{-1}. \quad (4.1)$$

We also restrict our samples to only include massive systems, namely those with $M_{\text{star}} > 10^{10} M_{\odot}$. Among 53 galaxies with $M_{\text{star}} > 10^{10} M_{\odot}$ and $1.3 < z < 3.0$ in the HUDF, 11 galaxies have $\text{SSFR} \leq 10^{-11} \text{ yr}^{-1}$. We exclude two of them from our sample, because these systems have irregular morphology and not well-defined centers, possibly implying ongoing merging events, while we are interested in studying color gradients of early-type galaxies. We exclude another two galaxies, because of their extremely faint NIR fluxes. In fact they have negative J, H and IRAC fluxes, which would induce large uncertainties in their photometrically-derived physical properties. Finally, an additional galaxy with an obvious spiral morphology has also been eliminated from the sample. Although the best-fit SSFR of this galaxy is $10^{-11.11} \text{ yr}^{-1}$,

the probability distribution function (PDF) of this SSFR measure has two peaks with similar probability density, one around $10^{-11.11} \text{ yr}^{-1}$ and the other $10^{-10.23} \text{ yr}^{-1}$, implying a substantial probability for this source to be a star-forming galaxy.

After these exclusions, the final sample includes 6 galaxies, whose GOODS ID, coordinates, redshift, SED-fitting parameters and H-band effective radius, measured by Cassata et al. (2010), are shown in Table 4.1. Five out of the six galaxies in the sample satisfy pBzK color-color criterion for PEGs at $1.4 < z < 2.3$ (Daddi et al., 2004a) or the analog VJL criterion for redshift $2 < z < 3$ (VJL Guo et al., 2012). The last galaxy, 24626, resides just below the pBzK selection window in the (B-z) vs.(z-K) color-color plane, most likely because its spectroscopic redshift, $z = 1.31$, is outside of the targeted range of the pBzK criterion. Four galaxies have spectroscopic redshifts: 22704 and 23555 from Cimatti et al. (2008), 24279 from Daddi et al. (2005) and 24626 from Vanzella et al. (2008).

Galaxy 23495 has a counterpart in the Chandra Deep Field South 2-Megasecond catalog (Luo et al., 2008). It has X-ray luminosity $3.8 \times 10^{43} \text{ erg/s}$ and $5.6 \times 10^{43} \text{ erg/s}$ in the soft and hard band, respectively. It is not, however, detected in the VLA map by Kellermann et al. (2008) and Miller et al. (2008). Galaxy 24626 also has a counterpart in the catalog of Luo et al. (2008), but it only has a marginal ($S/N \sim 1.3$) detection in the soft band with X-ray luminosity $2.7 \times 10^{41} \text{ erg/s}$ and none in the hard band. We re-investigate the two sources with the newly released Chandra Deep Field South 4-Megasecond image¹ and find similar results. Other four galaxies have no detection in both bands, either individually or stacked, in the 4-Megasecond image. Finally, all our sample galaxies have no detection at $24 \mu\text{m}$ down to a 1σ limit of $5 \mu\text{Jy}$, consistent with predictions for PEGs at $z \sim 2$ (Fontana et al., 2009).

¹<http://cxc.harvard.edu/cda/Contrib/CDFS.html>

Figure 4.1 shows the images of the sample galaxies in the z- and H-bands, as well as their (z-H) color composites. The z-band images have their original resolution ($\sim 0.12''$), while the resolution of the (z-H) color images is that of the H-band images, after PSF matching (see Sec. 3.3.2). Both the z-band and H-band images show that all the sample galaxies have spheroidal, early-type morphology, while (z-H) color maps reveal both analogies and differences among them. All galaxies have a red center and blue outskirts. Galaxy 24626 has the most well-defined red center and the clearest color gradient. Galaxy 23555 and 24279 also have well-defined red centers, but their outskirts are observed at relatively lower S/Ns and the resulting color gradient is not as clear as that of Galaxy 24626. In the remaining three galaxies, the location of the red stellar populations is slightly off-center, with the distance between the centroid and the red center comparable to the H-band half-light radius of the galaxy. After re-sampling both z-band and H-band images to smaller pixel scale ($0.01''/\text{pixel}$) and re-registering images, we still find such off-center red cores. Therefore, we rule out the sub-pixel image registration issue as the reason of the off-center cores. Instead, we suspect the asymmetry in the cores of our empirical PSFs could be the reason. However, the use of annuli photometry with size of a few FWHM largely reduces the influence of the asymmetry of PSFs so that it would not impact our results, as shown by our later test in §3.3.2. Since we aim at measuring the color gradients up to ~ 10 times of the H-band half-light radius, it is still reasonable to consider that these galaxies, too, have red centers.

4.3 Annular Photometry of Massive Passively Evolving Galaxies

4.3.1 Aperture Size

We measure azimuthally-averaged color gradients for the six galaxies by carrying out aperture-matched, multi-band annular photometry. A problem we face when

Table 4.1 The Physical Properties of massive PEGs in our sample

GOODS ID	RA (J2000)	DEC (J2000)	redshift ^a	M _{star} Log(M _⊙)	SSFR Log(yr ⁻¹)	E(B-V)	Z	R _{eff} kpc
19389	53.1357303	-27.7849320	1.345(p)	10.18 ± 0.11	-11.98 ± 1.19	0.10 ± 0.04	1.0Z _⊙	1.02
22704	53.1537988	-27.7745867	1.384(s)	10.70 ± 0.01	-14.55 ± 1.00	0.15 ± 0.07	0.2Z _⊙	0.50
23495	53.1584550	-27.7739817	2.422(p)	11.07 ± 0.05	-11.98 ± 1.54	0.25 ± 0.06	0.2Z _⊙	<0.38
23555	53.1588102	-27.7971545	1.921(s)	10.82 ± 0.04	-11.98 ± 0.07	0.00 ± 0.01	1.0Z _⊙	0.44
24279	53.1630047	-27.7976545	1.980(s)	10.63 ± 0.07	-12.39 ± 0.34	0.00 ± 0.01	0.2Z _⊙	0.37
24626	53.1651596	-27.7858696	1.317(s)	11.10 ± 0.04	-11.15 ± 0.05	0.10 ± 0.03	0.2Z _⊙	3.69

^aThe number in brackets indicate the quality of redshifts: *p* stands for photometric redshift, *s* for spectroscopic redshift

implementing this procedure is how to properly define the set of concentric apertures for each galaxy in such a way that it optimally samples the color gradient. After some experimentation with automated procedures to determine the annuli based on the effective radius (typically in the H-band), however, we resort to set them manually based on a visual inspection of the (z-H) color images. We test the robustness of our result against the choice of the apertures by perturbing them around the visually determined positions and also by choosing equally-spaced annuli simply based on the (visually established) extent of the color gradient. While variations at the level of 10–15% were observed, in no case these would change our results and conclusions. The chosen annular apertures for each galaxy are shown as white circles in Figure 4.1. Obviously, while with a sample of six galaxies it is relatively simple to manually set the concentric apertures, dealing with large samples will require an automated procedure to be developed. We plan to come back to this problem in a future paper.

4.3.2 Reliability of Annular Photometry

We measure the annular photometry from the PSF matched HUDF HST/ACS and WFC3 images (see Sec. 3.3.2). Here, in addition to the test on the homogeneity of the matched PSFs in Sec. 3.3.2, we carry out one more test to verify the effectiveness of the PSF matching procedure in measuring realistic color gradients by means

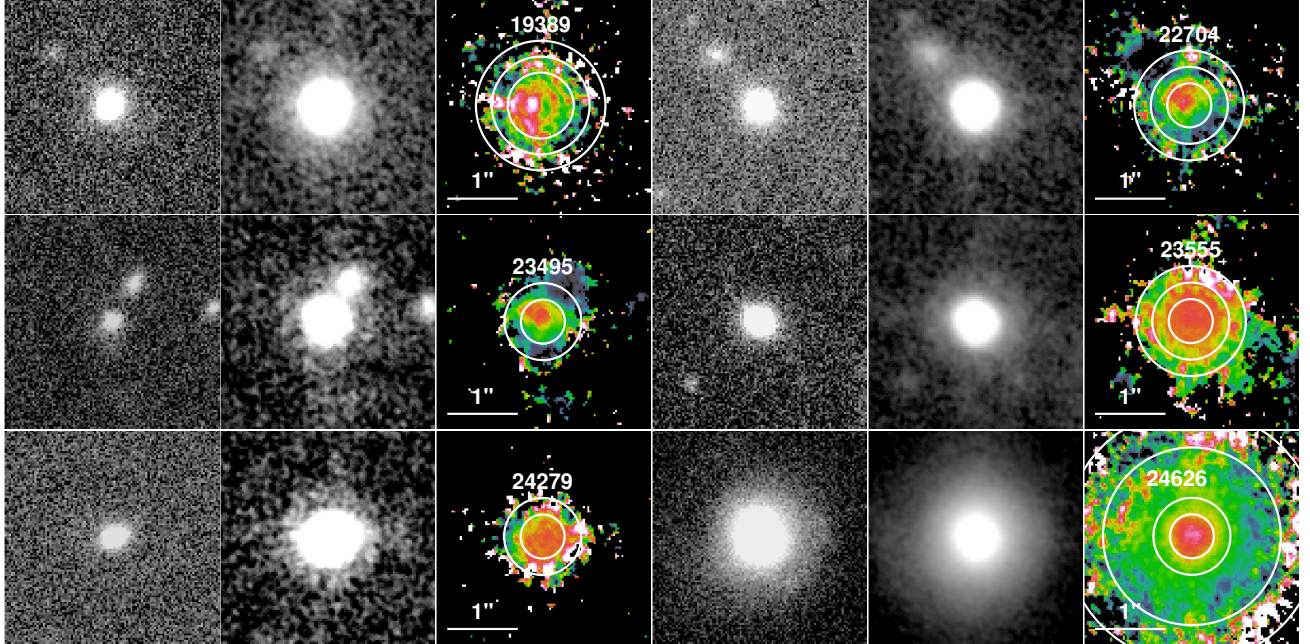


Figure 4.1 Montage of six massive PEGs in our sample. Each row shows two galaxies. For each galaxy, panels from left to right show the HUDF HST/ACS z-band, WFC3/IR F160W, and z-H color images. The GOODDS v2.0 ID of each galaxy is labeled in images. The z-band and H-band images have different resolution (PSF FWHM of $0.12''$ and $0.18''$, respectively), but the z-H color images are generated after matching the z-band PSF to that of H-band (see §3.3.2 for details). The white concentric circles outline the annuli used to measure the multi-band annular photometry. For each galaxy, a white line shows the scale of $1''$.

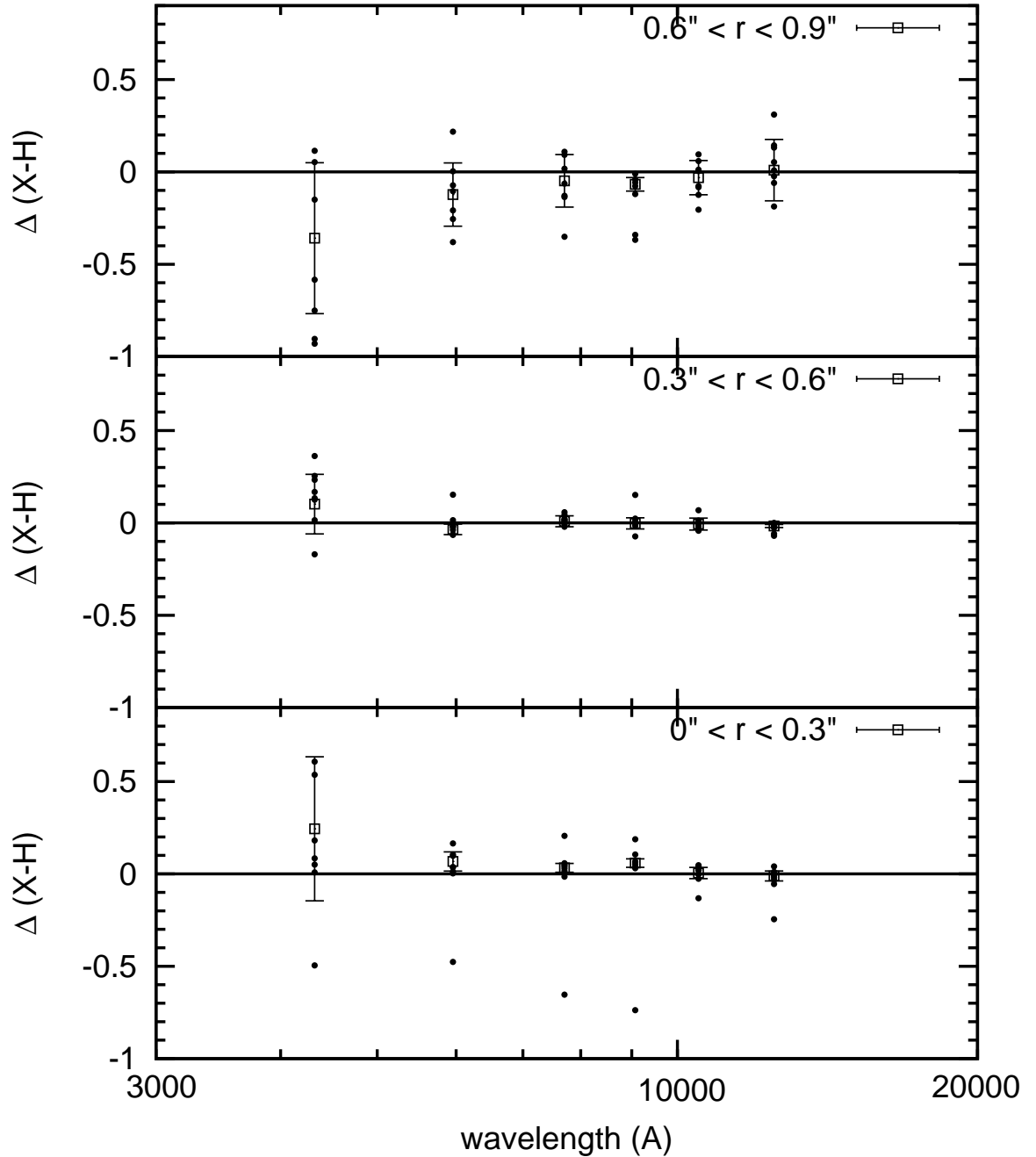


Figure 4.2 Effect of PSF-matching in the measure of color gradients. The figure shows the difference $\Delta(X - H) = \text{output} - \text{input}$, where X is one of BVizYJ, between the input color gradient of a model galaxy and the output one, measured from the real images after convolving the model with the PSF of each image, inserting the result into the image, applying the PSF-matching procedure and measuring the “observed” color gradient. To simulate the effects of a position-dependent PSF, we do not use the average PSF of each band, but rather each of the seven stars (after appropriate normalization) that we use to create the average PSF. Thus, each point represent the color gradient of the same model galaxy observed at different position in the HUDF FOV, while the squares and error bars show the mean and standard deviation of the points in each band.

of simulations that, at the same time, also give us information on the effects of the PSF variations across the field. We generate a model galaxy with given colors and then inserted it into the images in seven different positions. In practice, we use each of the seven stars that went into building the average PSF as position-dependent PSF themselves, after appropriate normalization. For the model galaxy we use a Sérsic spheroid with index $n = 2$ and effective radius $R_{\text{eff}} = 0.5$ kpc in the H-band, and assigned $(X-H)$ color, where X is one of BVizYJ. We convolve the model image with the seven PSFs in each band and inserted the result in the corresponding image in proximity to the star. Then, we apply the PSF-matching procedures to the images and measured the color gradient of the galaxy at its seven different positions as if these were real measures. Figure 4.2 shows the difference $\Delta(X - H) = (X - H)_{\text{out}} - (X - H)_{\text{in}}$ between the “observed” color gradient and the input one in each band at each of the seven positions. As the figure shows, there is no evidence of significant systematic bias introduced by the PSF-matching procedure, with all the deviations consistent with having random nature. The case of the B band is the one with the largest deviations, but while the scatter of $\Delta(B - H)$ is comparatively large, the mean difference between the output and the input colors at radius less than $0.6''$ does not significantly deviate from zero. In the annulus between $0.6''$ and $0.9''$, the simulations suggest that we underestimate the $(B-H)$ color by ~ 0.4 magnitude, although the B-band flux of PEGs in our targeted redshift range is so faint that the background fluctuation, rather than the mismatching of PSFs, likely dominates the uncertainty of the color measurement. In practice, however, this has no direct consequence in our analysis, since we do not use B-band derived color gradients. In conclusion, our test shows that the PSF-matching procedures is effective in recovering the color gradient and introduces no significant bias to our measurements.

We also conduct a further test of the robustness of results derived from the multi-band annular-aperture photometry by comparing the photometric redshift derived

from each annulus to that measured from the integrated photometry. In principle, the redshift of an annulus should be the same as that of the whole galaxy. If large deviations are encountered this flags potential bias in results derived from the annular photometry, especially for the most outer annulus, where the S/N in the bluer bands is significantly lower than the redder ones and, as we have seen for the B band, other systematics can affect the measures.

Figure 4.3 shows the probability distribution function of the photometric redshift measured with the *HST* BVizJH photometry for the annuli and for the whole galaxy for each of our sources. The figure also plots the photometric redshift of the galaxies derived from the integrated GUTFIT photometry, as well as the spectroscopic redshift if available. Generally, there is good agreement between the photometric redshift of the annuli and that of the whole galaxy, with the differences between the peaks of the distribution function of the annuli and the whole galaxy photometric or spectroscopic redshift being typically $\Delta z/(1+z) < 0.05$. Exceptions are two of the annuli of galaxy 24626, which deviate from the spectroscopic redshift by $\Delta z/(1+z) \sim 0.08$, and the outermost annulus of galaxy 23555, which differs from both the spectroscopic and photometric redshifts (which agree very well with each other) by $\Delta z/(1+z) \sim 0.12$.

Overall, the agreement between the annuli’s photometric redshift and the spectroscopic or photometric redshift of the whole galaxies is typical of this types of measures, with no indication that fitting of the observed SED of the annuli to stellar population synthesis models to derive the properties of the stellar populations might be affected by systematics or other problems.

Finally, we wish to point out that the availability of resolved multi-band photometry of sub-structures with more homogeneous color distribution than the whole galaxy provides a powerful means to improve the photometric redshift measurements, as well as to investigate the reason behind catastrophic failures. Although the redshift probability distribution of the individual sub-structure does, in general, deviate

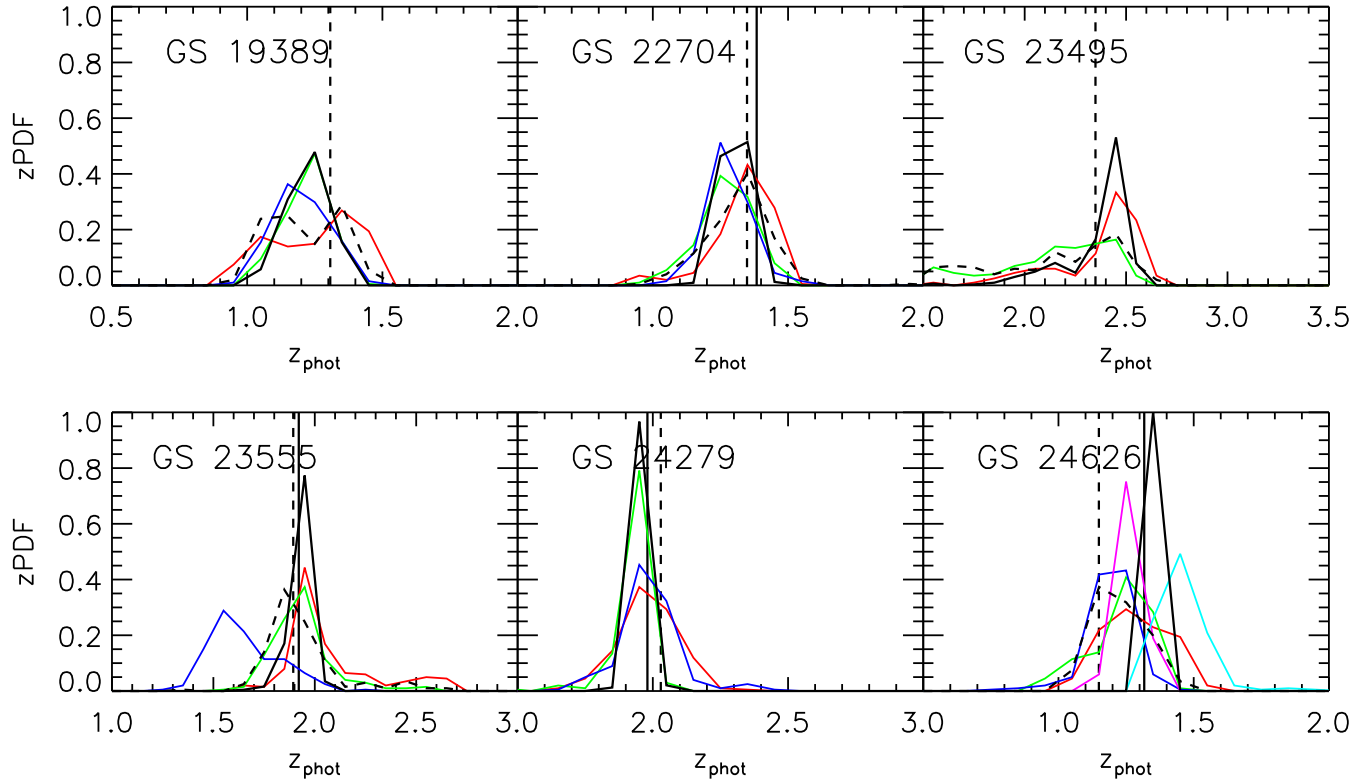


Figure 4.3 Probability distribution function of photometric redshift measured (from the *HST* BVizJH photometry) in concentric annuli around our sample galaxies compared to that of the galaxies as a whole, as well as to their spectroscopic redshift, when available. The concentric annuli, from the center to the outskirts of each galaxy, are plotted with the red, green, blue, violet, cyan, light brown and gray curves. The combined probability, i.e. the product of that of each annulus, is also plotted with a black solid curve. The black dashed curve shows the probability for each galaxy as a whole. The solid vertical line shows the spectroscopic redshift (when available), while the dashed vertical line shows the photometric redshift of the galaxy measured using the 12-band GUTFIT (integrated) photometry.

from the true redshift due to random errors, the combined probability distribution, i.e. their product, is generally closer to the true redshift and more sharply distributed than that of the whole galaxy, because the simpler case of the homogeneous colors of the sub-structures is better described by the stellar population synthesis models than the more complex case of the generally much larger color dispersion inside the whole galaxy. This is illustrated in Figure 4.3, which shows that the peak of the combined redshift probability distribution of each galaxy is closer than the individual ones to the spectroscopic or the (12-band) photometric redshift, with typical deviations $\Delta z/(1+z) < 0.03$. For example, although the annuli redshift probability distribution of galaxy 24626 show relatively large deviations from the spectroscopic redshift, the combined distribution deviates only by $\Delta z/(1+z) \sim 0.02$, a more accurate estimate than that of the 12-band photometric redshift, which has $\Delta z/(1+z) \sim 0.06$.

4.4 Color Gradients in Massive Passively Evolving Galaxies

To investigate possible dependence of the color gradients of the $z \sim 2$ PEGs with other integrated physical properties of the galaxies and also to compare them to those of local early-type galaxies, we interpolate the observed photometry in the annuli to the rest-frame U, B and V band and then obtain the corresponding (U-B), (U-V) and (B-V) colors (e.g. see Dahlen et al. (2005)). Figure 4.4 shows the color gradients of the six massive PEGs, where the rest-frame colors of the annuli are plotted against the annulus radius expressed in unit of the H-band half-light radius ($R_{\text{eff,H}}$). For five galaxies the available angular resolution and sensitivity allow us to measure the color gradients from $\sim 1.5 \times R_{\text{eff,H}}$ to $\sim 8 \times R_{\text{eff,H}}$. For galaxy 24626, due to its much larger size (in the H band we measure $R_{\text{eff,H}} \sim 3$ kpc), we are able to follow the color gradients down to a much smaller radius, $\sim 0.5 \times R_{\text{eff,H}}$.

To the extent that our sample is representative of early-type galaxies at $z \sim 2$, it appears that these systems have negative color gradients in all the three colors that

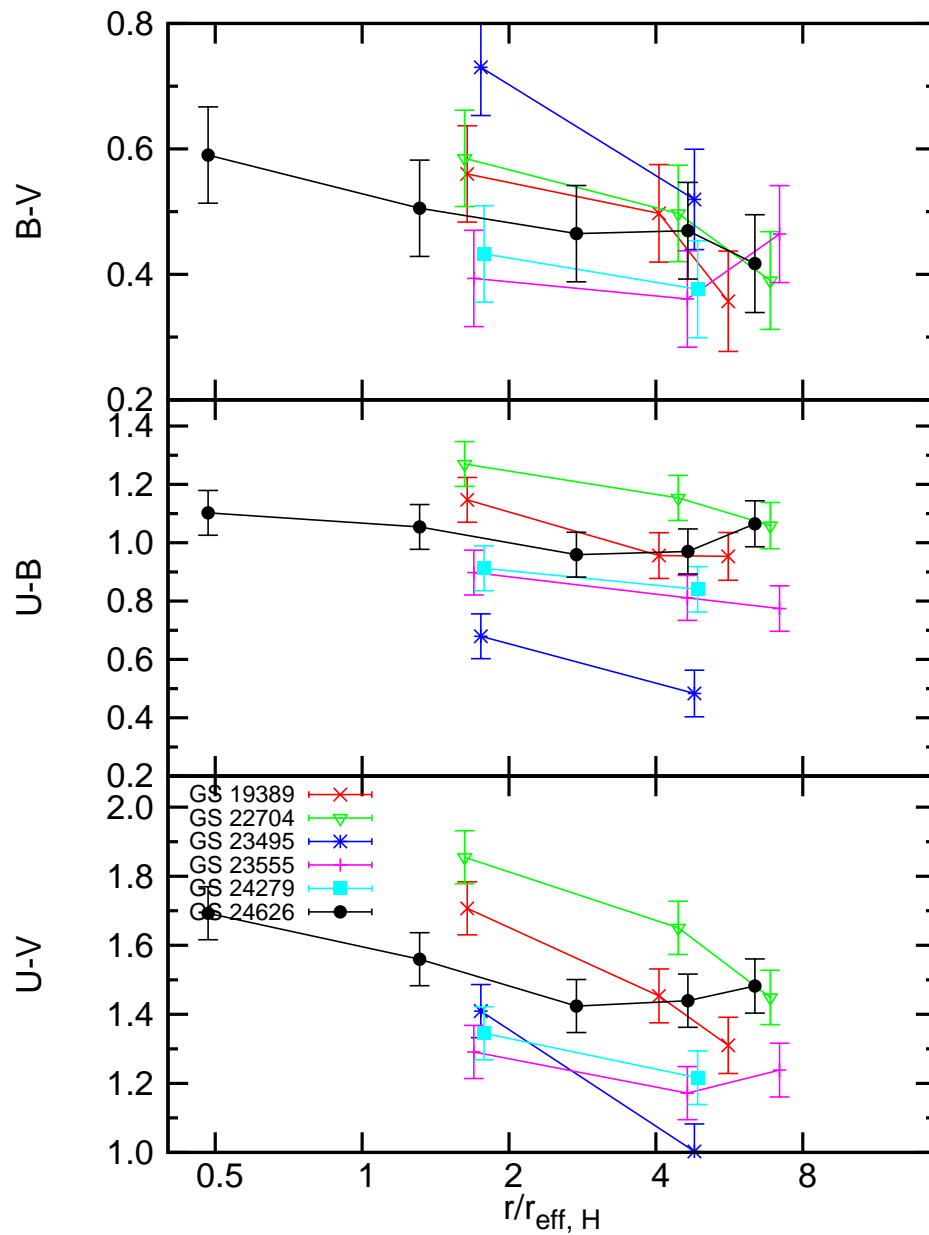


Figure 4.4 Rest-frame B-V (*top*), U-B (*middle*) and U-V (*bottom*) color gradients of the six sample galaxies. Each galaxy gradient is color-coded as labeled in the bottom panel. Also shown are the IDs of the galaxies in the publicly released GOODS v2.0 source catalog.

we consider, in the sense that stellar population in these galaxies becomes bluer with increasing separation from the center. This property can already be inferred from a visual inspection of the (z-H) color images shown in Figure 4.1, where all galaxies exhibit red cores and blue outskirts.

The colors of two of the galaxies appear invert the blueing trend at large radii, i.e. their color gradient shows an upturn to the red at $R/R_{\text{eff,H}} \approx 3-4$. Galaxy 23555 exhibits the red upturn in both the (B-V) and (U-V) color gradients. The photometric redshift probability distribution of the outermost annulus of this galaxy (see §4.3.2) shows a relatively large deviation from its spectroscopic redshift, suggesting that the photometry of this area of the galaxy is subject to some systematics. A visual inspection of the the H-band image reveals that this galaxy resides in a relatively dense environment, with a luminous, large companion and a bright star located nearby. Low-surface brightness H-band light from these sources is very likely contaminating the outermost annulus of the galaxy. Galaxy 24626 has upturns in the (U-B) and (U-V) color gradients. Although there are no large or bright sources nearby, a few faint ones are located close to its outermost annulus. These sources are also more extended in the near-IR bands than at the optical ones, and may significantly contribute red light to the outskirts of the galaxy.

Our findings of red cores and blue outskirts in massive PEGs at $z \sim 2$ are in apparent contradiction of what reported by Menanteau et al. (2001a, 2004), who also find that a large fraction ($\gtrsim 30\%$) of spheroidal galaxies at $z \sim 0.5$ have strong internal color variations, but in most of their cases the cores appear bluer than the surrounding areas, suggesting that blue cores are common in $z \sim 0.5$ elliptical galaxies. Menanteau et al. (2001c) even concluded that most ($\sim 60\%$) of their spheroids formed at $z \lesssim 2$. Regardless of the difference of targeted cosmic epochs between their and our works, different sample selection criteria could be the main reason of the apparent discrepancy. Our galaxies are selected with both early-type morphology and very

low SSFR determined by SED-fitting, while Menanteau et al. (2001a, 2004) only selected galaxies with E/S0 morphology in *HST* I F814W images, independent of their potential star-formation activity. We also note the a recent work by Gargiulo et al. (2011) also reported that 50% of their sample of 20 early-type galaxies at $z\sim 1.5$ has significant radial color variation, with five with red cores and five with blue cores. Their sample was also selected through morphology, mainly based on the visual inspection of *HST*/ACS F850LP images and further cleaned by removing sources with Sérsic index $n < 2$ or clear irregular residuals resulting from light profile fitting Saracco et al. (2010). It is likely that the slope of color gradient (negative or positive) has relation with the star-formation activity of galaxies, even they all have early-type morphology. Besides, both Menanteau et al. (2001a, 2004) and Gargiulo et al. (2011) also found a significant fraction (40%~50%) of their galaxies to have red cores as ours. However, our sample only contains six galaxies and cannot allow to carry our a good statistical analysis to compare with them. The upcoming CANDELS will provide much larger samples to evaluate the fraction of red cores in early-type galaxies at $z\sim 2$.

We investigate the dependence of the color gradients on the integrated properties of the stellar populations of the galaxies. Figure 4.5 shows the slope $\Delta C/\Delta \log(R)$ (C and R are the color and the radius) of the color gradients as a function of redshift, stellar mass M_{star} , color excess $E(B-V)$ as a proxy of dust obscuration, and the global rest-frame (U-V) color of the galaxies. The properties of the stellar populations have been measured from fitting the 12-band GUTFIT photometry of the whole galaxies to spectral population synthesis models, as described in §2.2. We find that the slopes have a mild dependence on the the dust extinction $E(B-V)$, in the sense that galaxies with higher dust obscuration tend to have steeper color gradient (larger slopes). At face value this seems to suggest that the origin of color gradients is somehow related to the dust content of the galaxies. We also find that slopes have a weak dependence on

the global rest-frame (U-V) colors of galaxies, with redder (U-V) colors corresponding to steeper color gradients. No dependence of the slopes on redshift and M_{star} is could be observed.

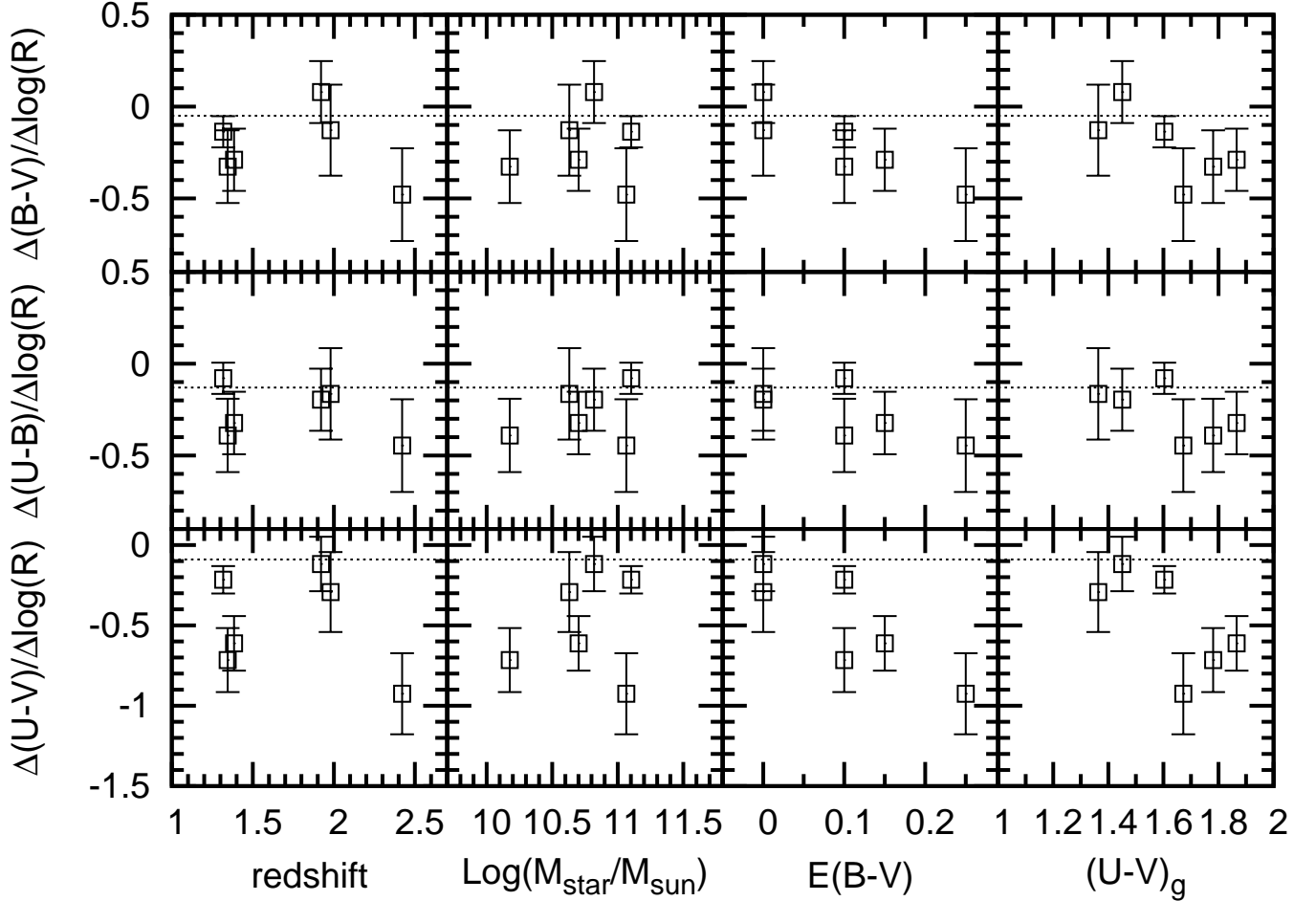


Figure 4.5 Slope of the (B-V) (*bottom row*), (U-B) (*middle row*) and (U-V) (*top row*) color gradients of the six sample galaxies as a function of redshift, stellar mass M_{star} , $E(B-V)$ as a proxy for dust obscuration, and global rest-frame U-V color. The properties of the stellar populations of the galaxies are derived from fitting the 12-band GUTFIT photometry to spectral population synthesis models, as explained in the text. The dotted line in each panel shows the slope of the color gradients of local elliptical galaxies measured by Wu et al. (2005).

We also compare the slopes of the color gradients of the $z \sim 2$ galaxies with that of local ellipticals (dashed lines). The local slopes were measured by Wu et al. (2005), who studied the color gradients of a sample of 36 nearby early-type galaxies

from the Early Data Release of the Sloan Digital Sky Survey and from the Two Micron All Sky Survey. The slopes of the $z \sim 2$ galaxies that have little or no dust extinction are similar to those of the local galaxies, while the $z \sim 2$ galaxies with more pronounced obscuration have steeper color gradients. The color gradients of local elliptical galaxies are generally interpreted as evidence of metallicity gradients (e.g., Tamura et al., 2000; Wu et al., 2005; La Barbera & de Carvalho, 2009). We will investigate the origins of the color gradients in the $z \sim 2$ galaxies in next two sections.

4.5 Variation of Single Parameter as the Origin of Color Gradients

In view of the analysis of the color gradients with SED fitting to spectral population synthesis models to understand their physical origin, in this section we investigate whether it is plausible that the radial variation of one single parameter can be primarily responsible for them. In other words, the observed color gradients can, in general, be explained to the radial variation of age, dust obscuration and metallicity of the stellar populations, either individually or in combination. Here we constrain the radial gradient of any one of these parameters needs to be, while keeping the others constant, for it to be solely responsible for the observed color gradients and discuss the implications. We assume simple parametrization for the dependence of the selected parameter with the radius, and, for simplicity, we only use a single stellar population (SSP) model from CB09 as representative of the SED of our PEGs.

First, we study the possibility that an age gradient is responsible for the observed color gradients, while keeping metallicity and dust obscuration constant with radius. We model the age gradient as

$\alpha_t = \Delta \log(t) / \Delta \log(R/R_{\text{eff}})$, where t_0 is the age at the center, and thus a model is fully described by a set of four values of the parameters t_0 , α_t , Z , $E(B-V)$. Rather than

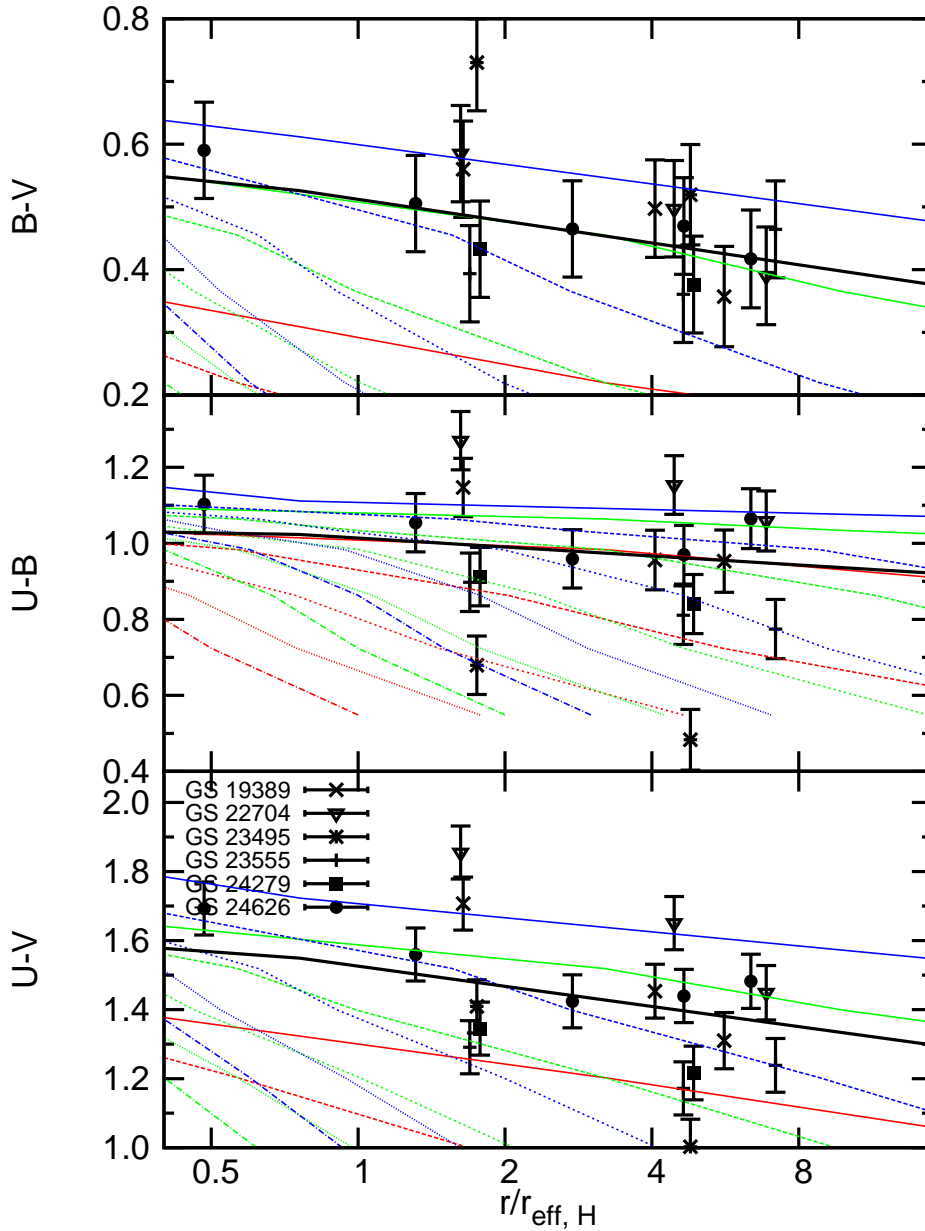


Figure 4.6 Predicted rest-frame (B-V), (U-B) and (U-V) color gradients from single stellar population models if the age of the dominant stellar population is the only parameter that varies as a function of radius in the galaxies (thin lines). The observed colors are plotted as black symbols with error bars. We only plot the predictions for the case of solar metallicity and zero dust extinction in this figure. Blue, green and red lines show the models in which the age at the center has been set at 3, 2 and 1 Gyr, respectively. For each color, different line patterns show different age gradient models, i.e., from top to bottom, $\Delta \log(\text{age})/\Delta \log(R/R_{\text{eff}}) = -0.2$ (solid), -0.4 (long dashed), -0.6 (short dashed), -0.8 (dotted) and -1.0 (dashed-dotted). The thick black line shows the prediction of age gradient that best reproduces the observations. See the text for details.

finding best-fit models we let the parameters vary within a four dimensional (4-D) grid chosen so that the results model predictions for the color gradients bracketed the observed ones. The 4-D grid is defined by $Z = 0.2Z_{\odot}$, Z_{\odot} and $2.5Z_{\odot}$, $E(B-V) = 0.0$, 0.05 , 0.10 and 0.15 , $t_0 = 1, 2$ and 3 Gyr, $\alpha_t = -0.2, -0.4, -0.6, -0.8$ and -1.0 . Given a point in the grid, i.e. the vector $(t_0, \alpha_t, Z, E(B-V))$, we compute the color gradients of (U-B), (U-V) and (B-V) as a function of radius. We also calculate the χ^2 as a metric to characterize the goodness of a model in describing the observations, defined as:

$$\chi^2 = \frac{1}{N_{obs}} \sum_{i=1}^{N_{obs}} \frac{(C_{obs,i} - C_{p,i})^2}{\sigma_{C,obs,i}^2}, \quad (4.2)$$

where $C_{obs,i}$ and $\sigma_{C,obs,i}$ are the observed color and its uncertainty at a given radius, $C_{p,i}$ the predicted color at the radius, and N_{obs} the total number of observed colors at all radii.

Figure 4.6 shows the model color gradients for (B-V), (U-B) and (U-V) compared them with the data. For simplicity, we only show the case of $Z=Z_{\odot}$ and $E(B-V)=0$ in the plot. Blue, green and red lines correspond to $t_0 = 3, 2$ and 1 Gyrs, while the different line patterns show the cases of α_t : -0.2 (solid), -0.4 (long dashed), -0.6 (short dashed), -0.8 (dotted) and -1.0 (dashed-dotted).

The *top* panel shows that the (B-V) color gradient is best approximated by the solid green line, i.e. $t_0 = 2$ Gyr and $\alpha_t=-0.2$ ($\chi^2 = 1.23$). But the *middle* and *bottom* panel show that this set of parameters overestimates the (U-B) ($\chi^2 = 7.73$) and (U-V) ($\chi^2 = 7.12$) color gradients. The (U-B) color gradient is actually best approximated by the green long-dashed line ($t_0 = 2$ Gyr and $\alpha_t=-0.4$, $\chi^2 = 5.42$), while the (U-V) one by the long-dashed blue line ($t_0 = 3$ Gyr and $\alpha_t=-0.4$, $\chi^2 = 5.71$).

Even when we change value of the Z and $E(B-V)$ within the preassigned range we still cannot find a combination of α_t and t_0 that can simultaneously provide a good description for all the three color gradients. The parameter set that best reproduces the (U-B) color gradient is $(t_0, \alpha_t, Z, E(B-V)) = (3.0, -0.6, 0.2Z_{\odot}, 0.15)$ with $\chi^2 = 5.31$,

that of (U-V) by (3.0, -0.4, Z_{\odot} , 0.0) with $\chi^2 = 5.71$, and that of (B-V) by (1.0, -0.2, $2.5Z_{\odot}$, 0.15) with $\chi^2 = 1.10$. We also determine which model minimizes the combined χ^2 , namely $\chi_{U-B}^2 + \chi_{U-V}^2 + \chi_{B-V}^2$. This model, shown by the black lines in the figure correspond to $(t_0, \alpha_t, Z, E(B-V)) = (3.0, -0.2, 0.2Z_{\odot}, 0.0)$, with $\chi_{U-B}^2 = 5.58$, $\chi_{U-V}^2 = 5.89$ and $\chi_{B-V}^2 = 1.19$.

Since there always is a different combination of the model parameters in our chosen 4-D grid that brackets different set of observed colors, we conclude that no combination of α_t and t_0 with constant Z and E(B-V), i.e. age alone, can simultaneously explain the three observed gradients.

We also repeat the same analysis for the case of a metallicity gradient and obscuration gradient to see if either one of these could be responsible for the color gradients, finding similar negative conclusions.

For the case of the metallicity gradient, the parameter sets that best fit the (U-B), (U-V) and (B-V) color gradients are $(Z_0, \alpha_Z = \Delta \log(Z)/\Delta \log(R/R_{eff}), t, E(B-V)) = (2.5Z_{\odot}, -0.4, 1.0, 0.0)$ with $\chi^2 = 5.30$, $(Z_{\odot}, -0.6, 1.0, 0.15)$ with $\chi^2 = 5.44$ and $(2.5Z_{\odot}, -0.8, 1.0, 0.15)$ with $\chi^2 = 1.08$. The corresponding parameter set that results in the minimum combine χ^2 is $(Z_{\odot}, -0.6, 1.0, 0.15)$ with $\chi_{2,U-B} = 5.39, \chi_{2,U-V} = 5.44, \chi_{2,B-V} = 1.18$. For the case of the obscuration gradient, the parameter sets that best reproduce the (U-B), (U-V) and (B-V) color gradients are $(E(B-V)_0, \alpha_{E(B-V)} = \Delta E(B-V)/\Delta \log(R/R_{eff}), t, Z) = (0.15, -0.08, 1.0, 0.2Z_{\odot})$ with $\chi^2 = 5.49$, $(0.15, -0.04, 1.0, 0.2Z_{\odot})$ with $\chi^2 = 6.70$ and $(0.15, -0.08, 1.0, Z_{\odot})$ with $\chi^2 = 1.22$. The one that minimizes the combined χ^2 is $(0.15, -0.06, 1.0, 0.2Z_{\odot})$ with $\chi_{2,U-B} = 5.53, \chi_{2,U-V} = 6.99, \chi_{2,B-V} = 2.12$.

In conclusion, unless the assumption of SSP is grossly inadequate for describing the rest-frame UV/Optical SED of our massive PEGs at $z \sim 2$, it seems unlikely that the radial dependence of only one parameter among age, metallicity or dust obscuration (with the other two being constant) can be responsible for the observed

color gradients. These must originate from the interplay of the gradients of age, extinction and metallicity.

4.6 Stellar Population Gradients in Massive Passively Evolving Galaxies

We investigate the nature of the observed color gradients by fitting the *HST* 7-band photometry (ACS BViz and WFC3/IR YJH) in the annular apertures defined before (see Figure 4.7) to the CB09 spectral population synthesis models to derive the radial dependence of stellar mass, specific star-formation rate, age and dust obscuration of the stellar populations in the annuli. We approximate the star formation history with an exponentially declining model ($e^{-t/\tau}$), where the age of the stellar populations is the time t from the beginning of the star formation to the time of observation. During the fitting, the redshift of each annulus is kept fixed to the spectroscopic redshift or to the photometric redshift of the whole galaxy measured from the GUTFIT 12-band photometry.

While this procedure yields robust estimates of the stellar mass, dust obscuration, age and metallicity suffer from larger uncertainties and degeneracies (e.g., Papovich et al., 2001; Shapley et al., 2001; Lee et al., 2010; Maraston et al., 2010). The degeneracy between age, metallicity and dust obscuration is partially broken if rest-frame infrared photometry is available, as shown by several authors (de Jong, 1996; Cardiel et al., 2003; MacArthur et al., 2004; Wu et al., 2005). Unfortunately, high-angular resolution photometry for our galaxies is limited to rest-frame UV and optical wavelengths, and thus we cannot effectively separate the role that each parameter plays in the observed color gradients. To gain some insight, however, we can make some simplifications and reduce the number of free parameters. Instead of letting the metallicity free to vary in each annulus during the fit, we set it according to one of the following three assumed power-law metallicity gradients: (1) flat, with

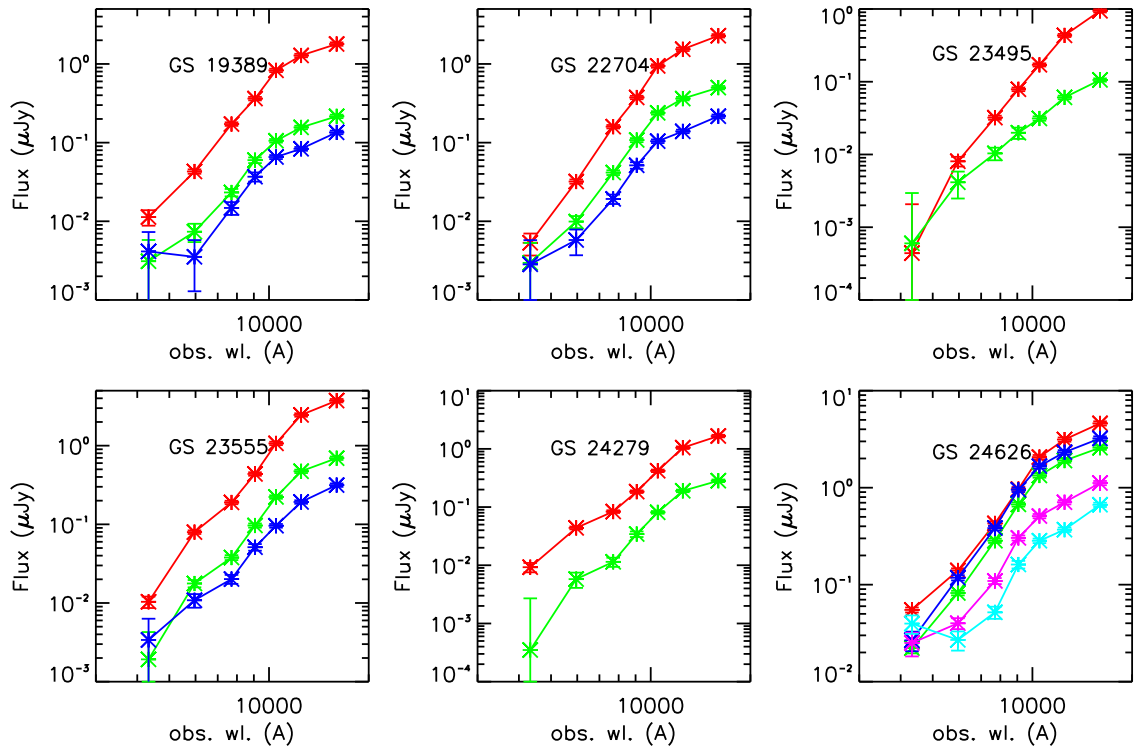


Figure 4.7 *HST* 7-band photometry (ACS BViz and WFC3/IR YJH) of the sample galaxies in the annular apertures discussed above. The curve for each annulus is color-coded as red, green, blue, violet, and cyan in going from the center to the outskirts of each galaxy.

logarithmic slope $\Delta\log(Z)/\Delta\log(R) = 0.0$; (2) the metallicity gradient of local early-type galaxies, with $\Delta\log(Z)/\Delta\log(R) = -0.25$ (Wu et al., 2005); (3) the gradient predicted by the monolithic collapse model, with $\Delta\log(Z)/\Delta\log(R) = -0.5$ (Carlberg, 1984). The latter model is meant to represent the case where the $z \sim 2$ galaxies have formed “in situ” at some epoch prior that of observation through some relatively rapid process.

In the local universe, elliptical galaxies have very little dust obscuration and their stellar populations are essentially coeval in the sense that their age spread is small compared to the mean age (e.g., Tamura & Ohta, 2004; Wu et al., 2005; La Barbera & de Carvalho, 2009). The situation can be very different at $z \sim 2$. The universe is only ≈ 3.5 Gyr old at this time, and thus the approximation of coevality is almost certainly no longer valid, since this time is comparable to that required to make a galaxy develop an early-type SED following the cessation of star formation. Furthermore, we do not understand the mechanisms of dust destruction well enough to make robust predictions on the dust content of early-type galaxies at $z \sim 2$. Dust is expected to disappear on a time-scale of $\sim 10^8$ years after the end of star formation, but this is not observed (e.g., Draine, 2009, and reference therein). Thus, we study the more general case where both dust obscuration and age are left as free parameters. We will discuss the case of no dust in our analysis later.

Figure 4.8 plots, for each galaxy, the gradients of $E(B-V)$ and age from the fits expressed as the ratio between the value at center and that in each annulus for each of the three assumptions on the metallicity gradient. The error bar for each annulus is the standard deviation of the best-fit values from 200 realizations from Monte Carlo bootstrap simulations. The figure also shows the average gradient of each parameter and its best-fit slope $\alpha = \Delta P/\Delta\log(R)$, where P is either $E(B-V)$ or $\log(\text{age})$, R is the radius, and the average includes all sample galaxies but 24626. The best-fit

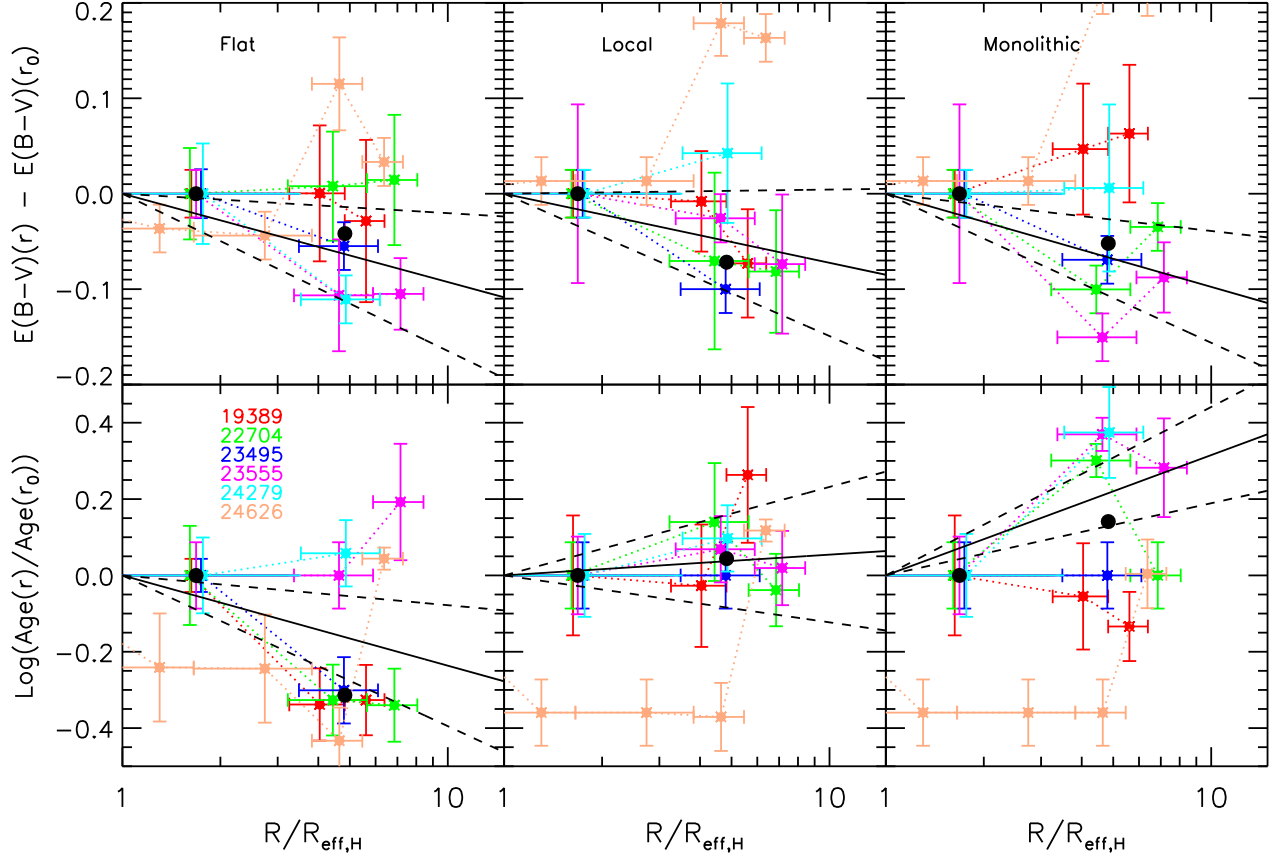


Figure 4.8 Dust (*top* row) and age (*bottom* row) gradients of massive PEGs under three assumptions of metallicity gradients: (1) the flat gradient (*left* column), (2) the local gradient (*middle* column), and (3) the monolithic gradient (*right* column). Galaxies are plotted in different colors, as their IDs show. Horizontal error bars show the size of each annulus, while vertical error bars show the $1\text{-}\sigma$ uncertainty of each parameter, which is measured through fits on 200 times Monte-Carlo sampled SEDs. In each panel, the black solid and black dashed lines show the best-fit value and $1\text{-}\sigma$ uncertainty of the slope of gradient of the parameter. The two black points in each panel show the median values for the bins of $R/R_{\text{eff}} < 3.0$ and $3.0 < R/R_{\text{eff}} < 10.0$.

slope and its 1σ uncertainty are plotted in the figure as black solid and dashed lines, respectively.

Galaxy 24626 is excluded from the average, because, as Figure 4.8 shows, its gradients of dust obscuration and age are very different from those of the other galaxies. Its half-light radius and Sérsic index, $R_{\text{eff}} \sim 3.7$ kpc and Sérsic index $n = 7.4$ (see Cassata et al., 2010), the largest size and most concentrated light profile in the sample, as well as its stellar mass, $\text{Log}(M/M_{\odot}) = 11.1$, are typical of the bright elliptical galaxies in the local universe often observed in groups with estimated total (dark matter) mass $M \sim 10^{13}M_{\odot}$ (Guo et al., 2009). Thus, it is likely that the star-formation and/or stellar-mass assembly history of this galaxy considerably differ from those of the other five sample galaxies, a fact that might reflect in the radial gradients of its stellar population properties. We also note that although the zYJH band images show a regular spheroidal morphology out to $\approx 2.5''$, the B-band image reveals that the galaxy has a close companion at about $1''$ corresponding to 8.4 kpc or $\approx 2.3 \times R_{\text{eff}}$, from its center.

Figure 4.8 also shows that, regardless of the assumptions on the metallicity gradient, the implied average $E(B-V)$ s always has a mild gradient in the sense that the centers ($R/R_{\text{eff}} < 3.0$) of the galaxies have slightly higher dust extinction ($\Delta E(B-V) \sim 0.05$) than the outer regions ($3.0 < R/R_{\text{eff}} < 10.0$). Both the slope and the amplitude of the dust gradient do not depend on the assumed metallicity gradient, implying that a mild negative gradient of dust obscuration is very likely a real feature of massive PEGs at $z \sim 2$, contributing at least in part, to the observed color gradients. This is consistent with the finding, discussed in §4.4, that the slope of color gradient of the individual galaxies correlate with the global $E(B-V)$ value, i.e. the one from the best-fit of each galaxies' GUTFIT 12-band photometry to spectral population synthesis models.

Due to the age–metallicity degeneracy, however, the contribution of an age gradient to the observed color gradient is much harder to determine, since it strongly depends on the assumed gradient of metallicity. As Figure 4.8 shows, a flat metallicity gradient results in the outer regions of the galaxies being $\sim 60\%$ younger than the center, while if the local metallicity gradient were assumed then the galaxies would have a flat age gradient. Finally, in the case of the metallicity gradient predicted by the monolithic collapse model, the stellar populations in the outer regions would be ~ 2 times older than those in the center.

Color gradients and internal color dispersion of intermediate–redshift early–type galaxies have been extensively studied in the past (e.g. Abraham et al., 1999; Menanteau et al., 2001a, 2004). Abraham et al. (1999) studied eleven 11 early-type galaxies at $z \sim 0.5$ in the Hubble Deep Field (HDF), finding that most (7/11) have internal color dispersion consistent with being old and coeval, and implying a small age gradient in the early–type galaxies at higher redshift. Similar properties remain valid at $z \sim 0$ as well (Wu et al., 2005). While this is qualitatively consistent with the null age gradient of our galaxies under the assumption of local metallicity gradient, in practice a quantitative comparison requires an accuracy in measuring the age that we do not have. At $z \sim 2$ the age of the universe is about 3.2 Gyr, while it is 8.4 Gyr at $z \sim 0.5$, and our finding of ~ 1 Gyr age gradient with flat metallicity gradient means that the fractional age differential is $\approx 30\%$. This, however, becomes $\approx 12\%$ (or $\approx 7\%$ at $z \sim 0$) just because the universe has become older. In the next section we will discuss the implications of the assumptions on the metallicity gradients for the evolution of the galaxies from $z \sim 2$ to the present.

4.7 Discussion

4.7.1 Dust Gradient

The mild gradient of dust obscuration, together with its apparent robustness against assumptions on the metallicity gradient, that seems to characterize massive early-type galaxies at $z \sim 2$ is in general agreement with the fact that dust obscuration in early-type galaxies in the local universe is not a dominant effect in determining their rest-frame UV/Optical color and color gradient. Thus, it appears that the lack of a significant presence of dust, or at least of its effects in the UV/Optical rest-frame SED, is a common feature of PEGs, regardless of the cosmic epoch when they are observed. Evidently, whatever physical mechanism is responsible for the destruction of dust in the aftermath of the cessation of star formation in these systems, must act on a significantly shorter time scale than that required to make the galaxy’s SED become typical of a “red and dead” system.

Both the inferred dust gradient and the absolute value of dust obscuration are comparatively small, $\Delta E(B - V)/\Delta \log(R) \sim -0.07$ and $\langle E(B - V) \rangle \sim 0.1$, and, as we have seen, robust against the assumptions on the metallicity gradient. An important question is whether or not the opposite is also true, namely that dust can be neglected when studying the effects of the age and metallicity gradients in the observed color gradients and their implications on the evolution of the galaxies, both prior and subsequent to the epoch of the observations. To answer this question we re-run the fitting procedure in each annulus under the two assumptions: (1) zero dust extinction; (2) dust extinction in each annulus fixed to the integrated value for the whole galaxy from the best-fit of the 12-band GUTFIT photometry to the models, i.e. no $E(B-V)$ gradient. For simplicity, we only consider the case of the local metallicity gradient.

The results are shown in Figure 4.9, where the new derived age gradients (*left* and *right* panels) are compared with the age gradient derived by letting dust as a

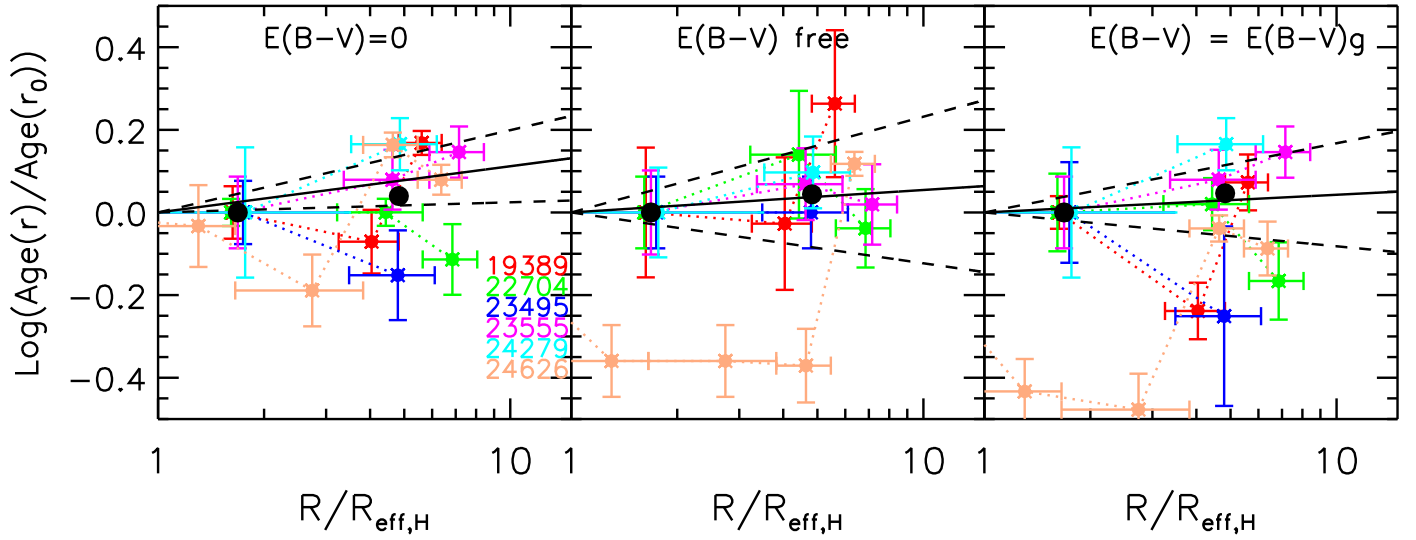


Figure 4.9 Age gradient of the sample galaxies under three different assumptions of dust distribution: (1) no dust; (2) dust as a free parameter in each annulus; (3) dust fixed to the global value from the best-fit of the 12-band GUTFIT photometry to the models. Individual galaxies are color-coded, as labeled. The horizontal error bars represent the width of each annulus, while the vertical ones are the $1\text{-}\sigma$ uncertainty of each parameter measured from 200 bootstrap Monte-Carlo realizations of the observed SEDs. In each panel the black solid and black dashed curves show the best-fit average gradient and $1\text{-}\sigma$ interval. The two black points in each panel are the median in the two bins $R/R_{\text{eff}} < 3.0$ and $3.0 < R/R_{\text{eff}} < 10.0$. The local metallicity gradient is assumed throughout.

free parameter in the fitting (*middle*). While the individual points vary, albeit within their $1 - \sigma$ error bars, the average age gradient remains unchanged in all three cases, regardless of the assumption on dust obscuration.

When the dust obscuration is fixed to zero or to the global 12-band value, the fit yields systematically larger reduced χ^2 than in the case of free dust. This is not just the effect of an extra free parameter in the fit: when we compare the best-fit SED models with the observed photometry, the free dust case obviously yields better agreement, especially in the B band, the most affected by dust obscuration. So, dust does play a role in determining the colors of the galaxies (the dust gradient slope $\Delta E(B - V)/\Delta \log(R) \sim -0.07$ means that the rest-frame B-V color becomes on average bluer by 0.07 mag from R_{eff} to $10 \times R_{eff}$). The absolute value of dust obscuration and its spatial gradient are small enough, however, that uncertainties on both these quantities can be neglected when setting constraints to the age and metallicity gradient from the observed color gradient, which are important to infer the evolutionary history of the galaxies as we are going to discuss in the next section.

Throughout this study we have used the starburst obscuration law (Calzetti et al., 1994, 2000) to model the effects of dust. While this is appropriate in the case of starburst galaxies, it is now known if it remains a good description in the case of the low SSFR, massive galaxies observed at $z \sim 2$, such as our sample. Regardless, however, this choice appears to actually be a conservative one for the implied effects of dust in the color gradients, as we directly verify by repeating our analysis using the Galactic (Cardelli et al., 1989), LMC (Fitzpatrick, 1986) and SMC (Prevot et al., 1984) obscuration laws. For simplicity, we only consider the case of local metallicity gradient. As Figure 4.10 shows, the slope of the dust obscuration gradient is reduced to $\Delta E(B - V)/\Delta \log(R) \lesssim -0.04$ when the Galactic and SMC laws are used, and it is close to zero in the LMC case.

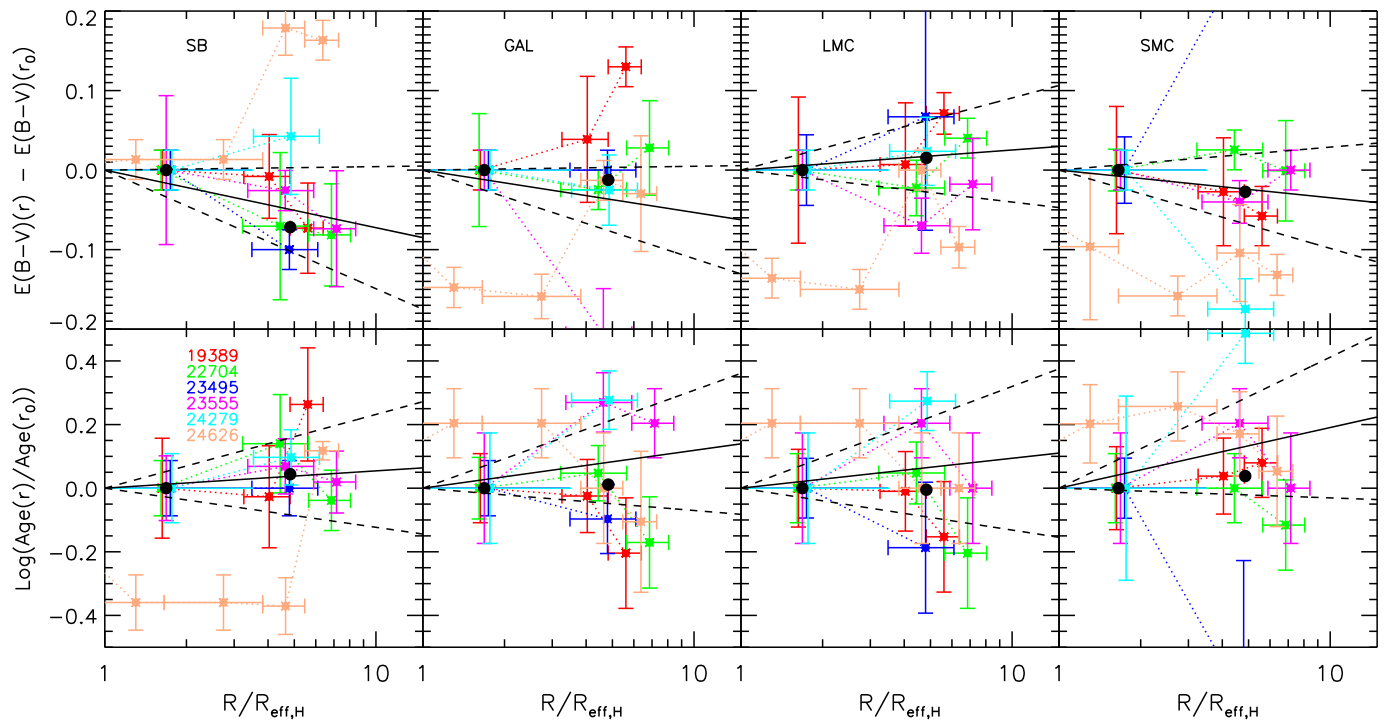


Figure 4.10 Similar to Figure 4.8, but showing the results of different extinction laws. Panels from left to right shows the result of Calzetti Law, Galactic Law, LMC Law and SMC Law. The metallicity gradient is assumed to be the local one.

The color gradient of local early-type galaxies is explained in terms of a metallicity gradient (e.g., Wu et al., 2005). As discussed by Wise & Silva (1996), however, a dust gradient can also reproduce the observed broadband color gradients in many ellipticals. Using *HST* images, van Dokkum & Franx (1995) found that 48% of 64 early-type galaxies show highly concentrated dust absorption at the centers of the galaxies. The sizes of the dust absorption regions are generally smaller than 1 kpc. Rest et al. (2001) and Tran et al. (2001) found dust features in 29 out of 67 galaxies (43%), including 12 with small nuclear dusty disks, while Lauer et al. (2005) found central dust in about half of the 77 galaxies that they observed with the *HST*/WFPC2.

Both an external and internal origin of the dust in the local galaxies have been proposed. The strongest evidence for the external origin, in which galaxies obtain their dust from mergers or accretions, is that the distribution and motions of ionized gas and dust in some local early-type galaxies seem unrelated to the motions of stars (e.g., Goudfrooij & de Jong, 1995; van Dokkum & Franx, 1995; Caon et al., 2000). However, Mathews & Brighenti (2003) and Temi et al. (2007) argued that the dynamical infall time from the edge of a local early-type galaxy (several $\sim 10^8$ yrs) is compatible to the time scale of dust destruction due to the sputtering by hot X-ray gas ($\sim 10^8$ yrs). Therefore, in the external origin, cold gas and dust should be regularly supplied to galaxies in a time scale of $\sim 10^8$ yrs. But observations of local early-type galaxies do not find such evidence. In fact, mergers between early-type galaxies and dusty galaxies are rarely observed in local universe. The lack of effective dust resupplies strongly points to the internal origin, in which dust is produced inside the galaxies by either the mass loss from evolving red giant stars (e.g., Temi et al., 2007) or M-star winds, as discussed in Lauer et al. (2005).

Understanding the origin of dust in massive PEGs at $z \sim 2$ requires spatially resolved stellar and gas kinematics, which are not available. If they have undergone merger or accretions to some extent in their past, dust obtained during these events

should settle to the center with dynamical infall time, a few $\sim 10^8$ yrs. If this dust is responsible for the observed obscuration gradients, then this would argue against the existence of hot X-ray emitting gas, which would otherwise sputter the dust in a shorter time scale ($\sim 10^8$ yrs). If such gas does exist, then a more plausible mechanism to form dust gradients is the episodic settling model proposed by Lauer et al. (2005) to explain the existence and frequency of nuclear dust in local early-type galaxies. The model predicts that dust appears several times throughout the galaxy and then is destroyed as it falls into the center. Therefore, the existence of hot gas in the massive PEGs at $z \sim 2$ is a key to judge the possible formation mechanisms. Unfortunately, although hot gas is commonly observed in many (or most) local massive elliptical galaxies (see the review of Mathews & Brighenti, 2003), no study on hot gas has been done for galaxies at $z \sim 2$, limited by the sensitivity of our current X-ray detectors.

4.7.2 Metallicity Gradient

In the previous sections we have seen that, because of the age-metallicity degeneracy, different assumptions for the metallicity gradient result in different age gradients, given the observed color gradients. We have also seen that uncertainties on the dust obscuration (both the total amount and its gradient) do not affect the quantitative details of the relationship between age and metallicity, given the current uncertainty. Thus, an interesting question to ask is: given a realistic assumption for the metallicity gradient at $z \sim 2$, namely one that is consistent with the metallicity gradient seen in early-type galaxies $z \sim 0$ and with our current ideas on how metallicity gradients evolve, what is the implied gradient of stellar population age? What would such an age gradient tell us about the way $z \sim 2$ PEGs assembled and their subsequent evolution, if they really are the progenitors of the local early-type galaxies?

4.7.2.1 Flat Metallicity Gradient

Under the assumption of a flat metallicity gradient, i.e. metallicity is constant as a function of radius, the observed color gradients of the galaxies imply a negative age gradient, namely the age of the stellar populations is younger as the radial distance from the center increases, with average gradient $\Delta\log(t)/\Delta\log(R) \sim -0.1$. Stars located at $\approx 10 \times R_{\text{eff}}$ from those in the center are, on average, ~ 1 Gyr younger. The SSFR is also higher in the outer regions. For example, the external rings in three of the galaxies, 19389, 22704 and 24626 have $\text{SSFR} > 10^{-11}/\text{yrs}$, larger than the global value we use to classify the galaxies as passive. The younger stellar populations and larger specific star formation rate in the outskirts of the galaxies could mean a later cessation of star formation relative to the center, newer episodes of star formation or accretion of younger stellar populations.

It is interesting, at this purpose, to explore whether the residual star formation in the outskirts can explain the apparent size evolution of massive PEGs from $z \sim 2$ to $z \sim 0$, as discussed by recent studies (e.g., Daddi et al., 2005; Trujillo et al., 2006, 2007; van Dokkum et al., 2008; Cassata et al., 2010). To do so, we simulate a galaxy with Sérsic index $n = 2.0$ and effective radius $R_{\text{eff}} = 0.5$ kpc (typical values for massive PEGs at $z \sim 2$, see by Cassata et al. (2010)), central $\text{SSFR} 10^{-11}\text{yr}^{-1}$ and the same SSFR gradient as the one in Figure 4.8. If this galaxy evolves from $z = 2$ to $z = 0$ only through in-situ star formation, i.e. with no significant accretion of external stars, our calculation shows that it cannot evolve into today's typical massive early-type galaxies, which have $n = 4$ and $R_{\text{eff}} \sim 2.5\text{kpc}$, since that would require the SSFR in the outskirts to be > 1.5 dex higher than the central one SSFR, a much steeper gradient than our observations seem to find. This implies that external mechanisms, such as merger and accretion, are necessary to build the extended halos of massive PEGs from $z \sim 2$ to $z \sim 0$. We also note that the assumption of flat metallicity results in the steepest positive SSFR gradient compared to the local metallicity gradient and

the monolithic-collapse gradient that we will discuss next. Thus, these two cases, too, would imply external mechanisms if the $z \sim 2$ massive PEG are to evolve into the local early types.

If merger and accretion do drive the evolution, they must be able to do so in a way that makes the flat metallicity gradient evolve into the one observed in local early-type galaxies, $\Delta\log(Z)/\Delta\log(R) \sim -0.3$, while at the same time cancel the negative age gradient, since the age the stellar populations in local galaxies has very little but positive radial dependence (e.g., Tamura & Ohta, 2004; Wu et al., 2005; La Barbera & de Carvalho, 2009). While secular orbit mixing could help explain today’s flat age gradient, it seems hard to understand how a flat metallicity gradient at $z \sim 2$ can evolve into the local one if major merger drives the evolution, since major merger is believed to flatten, not steepen the metallicity gradient (Kobayashi, 2004).

4.7.2.2 Local Metallicity Gradient

If we assume that the $z \sim 2$ PEGs have the same metallicity gradient as their local counterparts, the observed color gradients imply no age gradient, as shown in the *middle* panel of Figure 4.8. In other words, the radial dependence of metallicity and age of the the stellar populations of the $z \sim 2$ galaxies is already similar to that of their local counterparts. Furthermore, the implied gradient of SSFR is also flat. Thus, if merger or accretion drive the evolution to $z \sim 0$, this must happen in a way that maintains the gradients of metallicity and age roughly constant in time. Since major merger appears to flatten the metallicity gradient (Kobayashi, 2004), the assumption of the local metallicity gradient would also imply a more gradual accretion process as the one responsible for the apparent growth in size of PEG from $z \sim 2$ to the present (e.g. van Dokkum et al., 2010).

4.7.2.3 Monolithic metallicity gradient

The monolithic collapse is an idealized model in which a whole worth of stars of a massive galaxy form during ~ 1 dynamical time scale. Although a recent monolithic collapse model by Pipino et al. (2010) that allows certain scatter for the star formation efficiency would produce the metallicity gradient that agrees with the observation of local elliptical galaxies, earlier models by Larson (1974) and Carlberg (1984) define a maximum steepness boundary in the metallicity gradient slope–mass plane. We discuss models by Larson (1974) and Carlberg (1984) here simply as the limiting case of a class of assembly mechanisms capable to produce the steepest metallicity gradient across the galaxy.

During the monolithic collapse, stars begin to form everywhere in the collapsing cloud and, once formed, remain in their orbits with little net inward motion, while the gas keeps sinking to the center of the galaxy due to dissipation. While getting closer to the center, the gas become more and more enriched by the rapidly evolving massive stars. Consequently, stars formed in the central regions are more metal rich than those formed in the outskirts. Stellar feedback tends to reduce the inflow of gas and hence reduce the metallicity gradient. But gas outflows occur earlier and more effectively at large galactocentric distance than in the center due to lower escape velocity, lowering the star–formation rate at larger distance and contribute to create a strong negative metallicity gradient and a positive age one.

Under the assumption of the monolithic collapse metallicity gradient, the observed color gradients of our sample galaxies indeed imply a positive age gradient such that the stars at $R \approx 10 \times R_{\text{eff}}$ in are ~ 0.5 Gyr older than those in the central regions. We could directly test this prediction of the monolithic collapse (or equivalent scenarios), if we were able to independently measure the age gradient, something that is not possible with the present data. The monolithic collapse metallicity gradient also implies a weak SSFR gradient for our galaxies such that the outer regions at $R \sim 10 \times R_{\text{eff}}$

have SSFR ~ 0.5 dex lower than in the center. This is qualitative consistent with the general feature of the model that stellar feedback is more effective at larger radii than at the center at reducing the star formation activity²

If the PEGs observed at $z \sim 2$ formed through mechanisms similar to monolithic collapse, their subsequent evolution must be such to significantly reduce the magnitude of their metallicity gradient and to a minor extent the age gradient, since the monolithic-collapse gradient is much steeper (Larson, 1974; Carlberg, 1984) than that observed in local ellipticals (e.g., Peletier et al., 1990b; Idiart et al., 2003; Tamura & Ohta, 2003). Major merger provides such a mechanism Kobayashi (2004), although the effectiveness of minor merger or gas accretion and subsequent star formation in diminishing the steep metallicity gradient is not known.

The monolithic collapse model also predicts that the slope of the metallicity gradient, and hence the color gradient, depends on the mass of the galaxies, because a deeper potential well is more effective at retaining metals in the center than a shallower one and thus make more metal-rich stars (e.g., Tortora et al., 2010). As shown in Figure 4.4, the color gradient of our galaxies does not show any obvious dependence on the stellar mass, to the extent that this quantity is a good proxy for the galaxies' total mass. The relative high scatter in our small sample and the limited stellar mass dynamic range that it probes, however, might hide such signal. We will return to the correlation of the color gradient with the galaxies' properties using a much larger and significantly deeper sample extracted from the new WFC3 CANDELS survey.

Independent measures of the age gradient of the stellar populations would also test if mechanisms similar to the monolithic collapse play a role in assembling the $z \sim 2$ PEG, since in this case the stars in the central regions would be younger than

²We note that according to Martinelli et al. (1998) constant star formation efficiency with galactocentric distance can also explain the observed metallicity gradient and the correlation between colors/metallicity and escape velocity in early-type galaxies.

those in the outskirts. In fact, such an inverted age gradient is requested by our data in order to reproduce the observed color gradients if the metallicity gradient of the monolithic collapse is assumed, since this would result in significantly steeper color gradients, as we have directly verified.

4.7.3 Formation of Passively Evolving Galaxies at $z \sim 2$

It is more likely, however, that massive PEGs at $z \sim 2$ are formed through gas-rich major mergers rather than a single collapse process. Recently, Wuyts et al. (2010) analyzed SPH simulations of gas-rich mergers and their remnants that are treated with radiative transfer. They predicted that quiescent compact galaxies at $z \sim 2$ should typically show red cores and their color gradients should be a superposition of age, dust, and metallicity gradients. They found that in the gas-rich merger scenario, stars in the galactic center are formed during final coalescence out of more obscured and enriched gas. The dust and metallicity gradients compensate the positive age gradient (young center and old outskirts) so that their cores are typical when these galaxies are classified as passive systems. They also predicted that the strength of the color gradient to be correlated with galaxy's integrated color. All these predictions agree well with our observations and serve as important evidence of the validity of gas-rich major mergers.

Even if gas-rich major merger is considered as the formation mechanism of massive PEGs at $z \sim 2$, their subsequent evolution is still ambiguous. Kobayashi (2004) predicts that gas-rich merger can effectively flatten the metallicity gradient to the one of local early-types. Therefore, mechanisms that can significantly flatten the metallicity gradient, such as major merger, are not required in the subsequent evolution. Wuyts et al. (2010), however, find that the typical metallicity gradient in the simulated $z \sim 2$ gas-rich merger remnants is steeper than the typical metallicity gradient of local early-types. This requires major mergers in the subsequent evolution to flatten

the metallicity gradient, unless other mechanisms (accretion and minor merger) are proved to be capable to flatten the metallicity gradient too.

Overall, with the current data it is not possible to conclusively rule out or validate any of the three cases of metallicity gradients possible formation mechanism of massive PEGs at $z \sim 2$ that we have discussed. Passively evolving galaxies appear to undergo substantial structural evolution from $z \sim 2$ to $z \sim 0$ that reduces their compactness and stellar density (e.g., Daddi et al., 2005; Trujillo et al., 2006, 2007; van Dokkum et al., 2008; Cassata et al., 2010) If major merging events are the driver of this evolution, to the extent that we understand how merger rearranges gradients of metallicity and age, it seems unlikely that the $z \sim 2$ PEG have flat metallicity gradients, since subsequent merger can only keep it flatter, not steepen it to an extent required to match the observed one in local ellipticals. Of course, the size evolution can be driven by less dramatic minor merging events or continuous accretion, as some have suggested (van Dokkum et al., 2010). We do not know what these mechanisms would imply for the evolution of the metallicity and age gradients compatible with the color gradients observed at $z \sim 2$ if they have to evolve into those observed at $z \sim 0$. Finally, we remind that our discussion is based on resolved photometry that only covers the UV/Optical rest frame. Future high-resolution observations with JWST extending the wavelength baseline to the near and mid-IR will allow us to considerably reduce the extent of the age-metallicity degeneracy, and help us constraint a self-consistent evolutionary scenario for the assembly of the $z \sim 2$ PEG, as well as their subsequent evolution.

4.8 Summary and Conclusions

In this chapter, we have discussed the detection and implications of color gradients in early-type galaxies at $z \sim 2$ from deep high-angular resolution images at optical and near-IR wavelengths obtained with *HST* and the ACS and WFC3 cameras.

In particular, we have measured spatially resolved rest-frame UV-optical colors of a sample of six massive ($> 10^{10}M_{\odot}$) and passively evolving ($SSFR < 10^{-11}\text{yr}^{-1}$) galaxies at $1.3 < z < 2.5$. After defining for each galaxy a set of concentric apertures that optimally sample the observed gradient of colors, we have carried out fits to spectral population synthesis models using the available seven-band (BVIZYJH) photometry to determine how dust obscuration ($E(B-V)$), mean age, specific star formation rate (SSFR), and stellar mass (M_{star}) vary with the galactocentric distance. We have then used above information to discuss possible evolutionary scenarios for these galaxies in light of recent results on the apparent evolution of their morphological evolution and on theoretical expectations on how merger modifies existing gradients of metallicity and stellar age. This chapter can be summarized as follows:

1. Color gradients could be measured over scales that typically go up to $\approx 10 \times R_{\text{eff}}$, where R_{eff} is the effective radius of the Sérsic profile. The *HST* images show that the inner regions of these galaxies have redder rest-frame UV-optical colors (U-V, U-B and B-V) than their outer parts.
2. The slopes of the color gradients have no dependence on the redshift and stellar mass of the galaxies. However, they have a mild dependence on the global dust extinction and rest-frame U-V color of the galaxies. Galaxies with larger $E(B-V)$ or redder U-V color tend to have steeper color gradients.
3. The slopes of the color gradients of these galaxies are generally steeper than that of local early-type galaxies.
4. We investigate whether the variation of a single parameter (age, extinction, or metallicity) along radius can be used to explain the observed color gradients. Using the single stellar population model, we find that the variation of any single parameter cannot simultaneously fit the three observed color gradients (U-B, U-V and B-V) with the maximum likelihood. We conclude that the observed color

gradients of massive PEGs at $z \sim 2$ cannot be explained by a single gradient of age, extinction or metallicity and should be originated from an interplay of gradients of the three parameters.

5. The fits of spatially resolved stellar populations to the spectral population synthesis models are run under three assumptions of metallicity gradients: (1) a flat metallicity gradient ($\Delta\log(Z)/\Delta\log(R) = 0$), (2) the metallicity gradient of local early-type galaxies ($\Delta\log(Z)/\Delta\log(R) = 0.25$), and (3) the gradient predicted by the monolithic collapse ($\Delta\log(Z)/\Delta\log(R) = 0.5$).
6. Regardless of the assumptions on metallicity, a modest gradient of dust obscuration is always implied from the fits in the sense that the central regions of the galaxies have slightly higher dust obscuration than the outer parts, with an average gradient of $\Delta E(B - V)/\Delta\log(R) \sim -0.07$, if the starburst obscuration law by Calzetti et al. (1994, 2000) is used. Other extinction laws that we have tested (MW, SMC, LMC) result in smaller obscuration gradients. Overall, both the absolute value of dust obscuration and its gradient are small, however, consistently with the present-day early-type galaxies, where dust generally has small, if any effects on the observed colors. It appears that once a galaxy has become passive, for whatever physical mechanisms, dust obscuration ceases to play a significant role in the determining the UV/Optical SED.
7. While dust obscuration contributes in small measure to the observed color gradients of the $z \sim 2$ galaxies, its presence does not seem to affect the general age-metallicity degeneracy in the sense that the implied gradient of age derived from a given assumption for the gradient of metallicity does not depend on how dust is treated, i.e. if forced to a fixed value or left as a free parameter in each annulus, or on the adopted extinction law. Whatever inference on the age or

on the metallicity gradient is made, after assuming one or the other parameter, does not seem to appreciably depend on the assumption on dust obscuration.

8. Due to the age–metallicity degeneracy, the derived age gradients are strongly coupled with the assumed metallicity gradients: (1) assuming a flat metallicity gradient, the outer regions of the galaxies are younger than the inner regions with a age gradient of $\Delta\log(t)/\Delta\log(R) \sim -0.1$; (2) assuming the metallicity gradient observed in local early–type galaxies, the stellar populations in the outer regions have same age as those in the inner regions; and (3) for the metallicity gradients predicted by the monolithic collapse, the outer regions are older than the inner regions, with the average age gradient $\Delta\log(t)/\Delta\log(R) \sim 0.15$. Their specific star–formation rate is also ~ 0.5 dex lower than that in the inner regions.
9. The mass–size (or equivalently mass–stellar density) relationship of the $z \sim 2$ galaxies cannot evolve into the local one only through in–situ star formation driven by the small observed star–formation activity ($\text{SSFR} < 10^{-11} \text{ yr}^{-1}$ or less). This implies the accretion of stellar mass from outside (van Dokkum et al., 2010).
10. Overall, with the current data it is not possible to conclusively rule out or validate any of the three cases of metallicity gradients that we have considered. A major source of uncertainty is the fact that major merger rearranges the gradients of metallicity and age on a short time scale, while less dramatic events such as minor merger or a more continuous accretion might induce a more “secular” evolution of these properties. Passively evolving galaxies appear to undergo substantial structural evolution from $z \sim 2$ to $z \sim 0$ that reduces their compactness by a factor of 3–5 and their stellar density by ~ 2 orders of magnitude (e.g., Daddi et al., 2005; Trujillo et al., 2006, 2007; van Dokkum

et al., 2008; Cassata et al., 2010) If major merging events are the driver of this evolution, then, to the extent that we understand how merger rearranges gradients of metallicity and age, it seems unlikely that the $z \sim 2$ PEG have flat metallicity gradients, since subsequent merger can only keep it flatter, not steepen it to an extent required to match the observed one in local ellipticals. Of course, the size evolution can be driven by minor merger/accretion, as some have suggested (van Dokkum et al., 2010). In this case, we have much less guidance in inferring which metallicity and age gradients are compatible with the color gradients observed at $z \sim 2$ if they have to evolve into those observed at $z \sim 0$.

11. While it is possible that the subsequent evolution reconciles the metallicity and age gradient emerging from the monolithic collapse to those observed at $z \sim 0$, the observations do not seem to show any correlation between the strength of the color gradient and the stellar mass, which is predicted if the $z \sim 2$ PEG formed through such a mechanism. The inherent statistical noise in a sample as small as ours, and the fact that the sample itself only covers a small dynamic range in mass, can very well hide any such correlation. We do observe, however, a correlation between the color gradient and the dust obscuration ($E(B-V)$), even if such parameter is generally much less accurately estimated with broad-band SED fitting than the stellar mass, which is the most accurate one. This seems to support the lack of a correlation between the color gradient and the stellar mass, and thus argue against the monolithic collapse, or any formation mechanism capable to produce an equally steep metallicity gradient, as responsible for the formation of the $z \sim 2$ PEG. We will return on this subject using substantially large samples of such sources from the CANDELS project.

12. The metallicity gradient of the galaxies could be either close to that of the local early-type galaxies or flat. In the first case, the subsequent evolution must be such to preserve the metallicity gradient, which would seem to rule out major merger. In the second case, the evolution must create the gradient. This also seems to rule out major merger, since it can only flatten, not steepen, the gradient.

CHAPTER 5

TOWARDS A COMPLETE CENSUS OF GALAXIES AT $Z \sim 3$

5.1 Introduction

The Hubble Sequence, or at least the diversity of galaxy morphology and its connection to galaxy properties, has been observed up to $z \sim 2$. But the cosmic time of its first appearance is still in debate. In order to investigate the origin of the Hubble Sequence, a complete census of galaxy populations at $z \gtrsim 2$ is required.

High-redshift galaxies can be effectively selected from deep sky surveys through their broad band colors. Star-forming galaxies (SFGs) at $z \sim 3$ and above are prevalently selected with the dropout method by locating the position of the Lyman Break from their rest-frame UV colors (e.g., Giavalisco, 2002; Steidel et al., 2003; Giavalisco et al., 2004). This technique has been proved to be very successful because galaxies selected in this way, namely Lyman Break Galaxies (LBG, see Giavalisco, 2002, for a review), are spectroscopically confirmed as SFGs at high redshift (Steidel et al., 1996a,b, 1999, 2003) with little contamination. Recently, this technique has been extended to select galaxies at $1.4 < z < 2.5$ (BX/BM galaxies, Adelberger et al., 2004; Steidel et al., 2004). However, the Lyman break technique misses one interesting galaxy population, namely dusty SFGs. How much this population contributes to the cosmic SFRD and number density of galaxies at $z \sim 3$ is still controversial. Studies using far-IR or sub-millimeter emission from cold dust show that some dusty galaxies, for example sub-mm galaxies (e.g., Blain et al., 2002; Chapman et al., 2003, 2005; Swinbank et al., 2006), have SFRs up to $\sim 1000 M_{\odot}/\text{yr}$. The high SFRs of dusty

galaxies imply that the contribution of this population to the cosmic SFRD at $z \sim 3$ should not be ignored. To avoid underestimating the SFRD due to the exclusion of this population, a new color selection method is required to select SFGs independent of dust reddening.

Besides dusty SFGs, passively evolving galaxies (PEGs) at high redshift are also missed by the Lyman Break technique. Although PEGs contribute little to the SFRD, they are directly related to the ceasing of star formation in galaxies and to the history of stellar mass assembly in the universe. To search for this population, several color selection criteria have been proposed. Among them, the most commonly used two are the Extremely Red Objects (EROs, Thompson et al., 1999; Daddi et al., 2000; Roche et al., 2002, 2003; McCarthy, 2004) and Distant Red Galaxies (DRGs, Franx et al., 2003; van Dokkum et al., 2003, 2004, 2006; Papovich et al., 2006). EROs are selected with very red optical to near-IR color, typically $(R - K)_{Vega} > 5$, while DRGs have a red near-IR color with $(J - K)_{Vega} > 2.3$. Both methods use the red color as an indicator of the large amount of old stars in galaxies. However, due to the strong degeneracy between age and dust reddening, the red color of a galaxy could be caused by either old stars or high dust extinctions. As a result, samples selected by both methods contain both massive PEGs and dusty SFGs with similar fractions, as showed by spectroscopic observations (Cimatti et al., 2002, 2003; Förster Schreiber et al., 2004; Yan et al., 2004). To exclude the contamination of SFGs, a more efficient way of selecting PEGs at $z \sim 3$ is needed.

A selection method that satisfies the above requirements already exists for galaxies at $z \sim 2$. Proposed by Daddi et al. (2004a), this method uses the B-, z-, and K-band photometry to select both SFGs and PEGs at $z \sim 2$. Samples selected through the BzK method are now widely used to investigate several aspects of galaxies at $z \sim 2$, from physical properties (e.g., Daddi et al., 2004a, 2005; Reddy et al., 2005; Daddi et al., 2007b,a; Blanc et al., 2008), abundance (Kong et al., 2006; Lane et al., 2007;

Blanc et al., 2008), stellar mass function (Grazian et al., 2007), to clustering (Kong et al., 2006; Blanc et al., 2008).

In this chapter, we try to design an analogous method that selects and classifies simultaneously both SFGs (with different dust extinctions) and PEGs at $2.3 < z < 3.5$. For this purpose, we extend the successful BzK method from $z \sim 2$ to $z \sim 3$ by replacing the selection bands with the V-, J-, and IRAC $3.6\mu\text{m}$ band (hereafter L-band), according to the relative shift of galaxy spectra between the two redshifts. Our selection method (hereafter VJL) uses the same rest-frame colors as the BzK method so that galaxies selected by both methods have same spectral types. However, due to the different depth and sensitivities of the bands used in each method, the VJL selected sample may have different incompleteness and contamination from the BzK selected sample.

Nowadays, photometric redshift (photo- z) can be fairly accurately measured with relative error of only a few percent (e.g., Ilbert et al., 2009; Dahlen et al., 2010) and is hence widely used to select galaxies within a certain redshift range. However, the bias of photo- z selection is not explicit. It is common to characterize photo- z errors with a redshift probability distribution function. The accuracy of the distribution function strongly depends on the assumed mix of galaxy templates in the spectral energy distribution (SED) library. Unfortunately, our knowledge on the true SED types is limited and the commonly used SED libraries are often not good representatives of real galaxies. Let alone the mystery of dust extinction curve, initial mass function (IMF), metallicity of high- z galaxies, one major uncertainty of fitting high- z galaxies is the unknown star formation history (SFH). The commonly used exponentially declined SFH (τ -model) may be a suitable approximation for low- z galaxies, but is not a realistic model for high- z galaxies. Recently postulated hypotheses on SFH of high- z galaxies include exponentially increasing (Maraston et al., 2010) or roughly

linearly increasing (Lee et al., 2010) SFH. Using an unrealistic SFH would eventually result in a mis-interpretation of the bias of photo-z selection.

On the other side, the bias of color selection can be fairly explicitly determined. One easy way to do so is applying the color criterion to simulated galaxies that have a certain range of redshift, SFHs and extinctions and calculating the success and failure rate of the selection. Thus, one can robustly measure the expected redshift distribution as well as the incompleteness of the selection as a function of several variables, such as magnitude, size, and color of galaxies. Moreover, color selection is easier to reproduce. Unlike photo-z selections, results of which may vary from people to people, depending on the used SED-fitting codes or SED libraries, color selection results are robust and make the comparison of different works easy for the whole community. The success of color selection method has been proved by the prevalence of Lyman Break technique (see the review of Giavalisco, 2002).

In this chapter, we apply our VJL selection method to the HST/WFC3 Early Release Science (ERS, Windhorst et al., 2010) observations in the south field of the Great Observatories Origins Deep Survey (GOODS, Giavalisco et al., 2004) South field (GOODS-S). Serving as an ideal test field of our selection method, ERS brings three advantages for us to calibrate and optimize our method. First, its deep (~ 27 AB mag) J-band allows us to select galaxies that are faint in their rest-frame optical bands. These galaxies could be dusty SFGs and the ability to detect and correctly classify them is a key of our method. Second, embedded within GOODS South field, ERS is augmented by several existing data sets, from X-ray, optical to mid-Infrared band and sub-mm band. The multi-wavelength data enable us to accurately understand the nature of our selected galaxies. Third, ERS has similar depth on J- and H-band as the upcoming CANDELS observation (Grogin et al., 2011; Koekemoer et al., 2011) so that our method calibrated in ERS can be easily adapted to apply to CANDELS data.

5.2 Color Selection Criteria

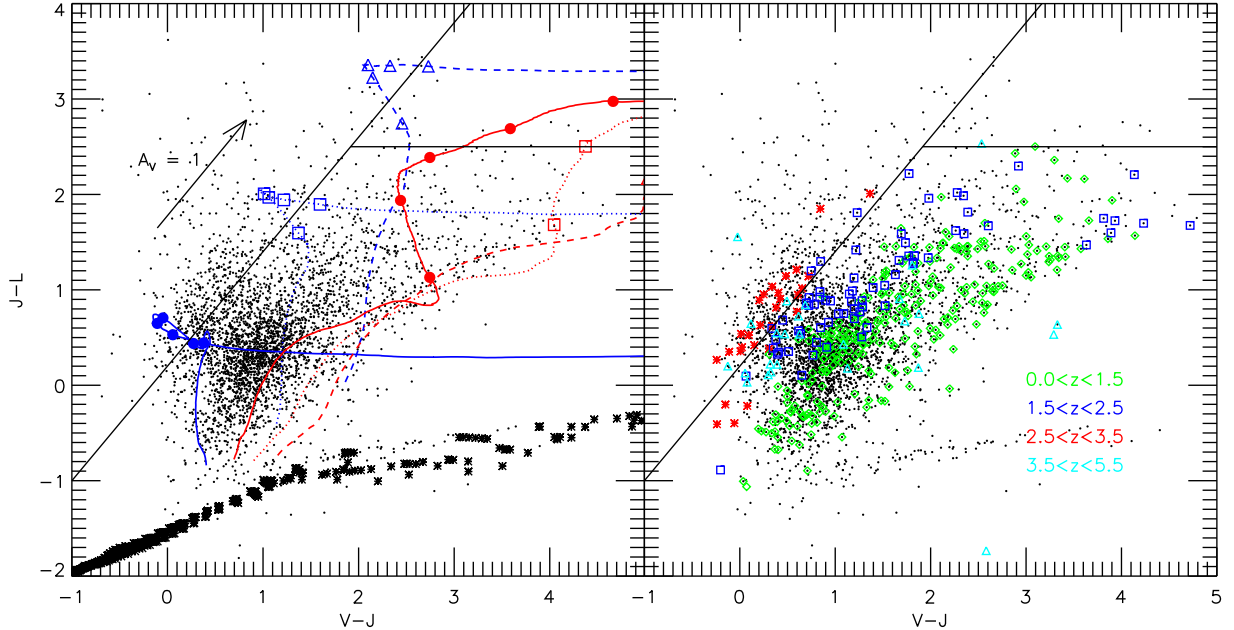


Figure 5.1 Galaxy models and observed ERS galaxies in the (J-L) vs. (V-J) two-color diagram. *Left*: tracks of galaxy models placed at different redshifts in the (J-L) vs. (V-J) two-color diagram. Symbols in each track are for redshift $z=2, 2.5, 3, 3.5$ and 4 . Blue tracks are models with a constant star formation rate (CSF), age of 0.5 Gyr and various dust reddenings (solid with filled points: $E(B-V)=0.0$; dotted with squares: $E(B-V)=0.3$; dashed with triangles: $E(B-V)=0.6$). Red lines show the tracks of dust-free SSP models with ages of 0.5 (solid with filled points), 1 (dotted with squares), and 2 Gyr (dashed with triangles). Black stars show the locus of stars of Lejeune et al. (1997). *Right*: ERS galaxies with spec- z in the (J-L) vs. (V-J) two-color diagram. Galaxies at different redshift ranges are color coded as labels show. The two solid black lines in each panel show our designed selection windows (upper left for sVJL and upper right for pVJL). In each panel, over-plotted small dots show all ERS galaxies with $S/N \geq 5$ in J- and L-band.

In order to simultaneously select both SFGs and PEGs at $z \sim 3$, we extend the BzK method at $z \sim 2$ (Daddi et al., 2004a) to $z \sim 3$ by replacing the B-z and z-K color in the BzK criteria with the V-J and J-L color, as the rest-frame wavelengths observed by the BzK bands for a galaxy at $z \sim 2$ are redshifted to the observation windows of the VJL bands at $z \sim 3$. Because ratios of central wavelengths of the VJL bands to the BzK bands are not a constant, we also adjust the coefficient in the original

BzK criteria so that the dust reddening vector is parallel to our selection window, which would ideally make our selection criteria independent of dust reddening. We determine the intersection terms of each selection equation through the distributions of galaxies with different redshifts in the J-L vs. V-J color diagram (the right panel of Fig. 5.1). Since the slope of the star-forming VJL criterion (Eq. 5.1) is fixed based on the dust reddening vector, we shift the criterion line (the diagonal line in Fig. 5.1) to get the term (+0.2) in Eq. 5.1 that optimally separates galaxies at $1.5 < z < 2.5$ (blue squares in the right panel of Fig. 5.1) from those at $2.5 < z < 3.5$ (red stars in the same panel). For the intersection term (2.5) in Eq. 5.2, since we do not have passive galaxies at $2.5 < z < 3.5$ that have been spectroscopically observed in our sample to help calibrate the selection window, we choose to use this term to exclude low-redshift interlopers as much as possible and meanwhile to keep the single stellar population model of galaxies with age of 1 Gyr (the red dotted line with squares in the left panel of Fig. 5.1 at $z=2.5$ within the selection window). Thus, our VJL criteria are

$$J - L \geq 1.2 \times (V - J) + 0.2 \quad (5.1)$$

for selecting SFGs and

$$J - L \geq 2.5 \wedge J - L < 1.2 \times (V - J) + 0.2 \quad (5.2)$$

for selecting PEGs, where \wedge means the logical *and*. Our method, similar to the BzK method, uses the strength and slope of the Balmer break, which is between the J and L band for galaxies around $z \sim 3$, to select SFGs and distinguish them from PEGs. For simplicity, in this thesis, we call galaxies selected or selection window defined by Equation 5.1 as sVJLs, while those by Equation 5.2 as pVJLs.

An extension of the BzK method to higher redshift has been already proposed by Daddi et al. (2004a), who suggested to use R-, J-, and L-band colors to select

galaxies at $z > 2.5$. Daddi et al. (2004a) tested the validity of the selection criterion in their K20 sample. They ended up with few detections at $z > 2.5$, as the K20 sample does not cover the redshift range $z > 2.5$. They also claimed that using GOODS ACS+ISAAC+*Spitzer* data set would be deep enough in all of the RJL bands to detect galaxies at $z > 2.5$. The RJL method is quite similar to our VJL, however, we use all space-based bands in our selection to ensure a deep sensitivity. Another color selection aiming toward selecting galaxies at $1.5 < z < 3.5$ by using rest-frame UV/optical colors has been proposed by Cameron et al. (2011). They use *HST* Y-H vs. V-z colors to identify and characterize $1.5 < z < 3.5$ galaxies in the HUDF and ERS field. While their criteria have the advantage of having similar resolutions in all bands that are used for selection, our criteria cover a much longer wavelength baseline. And our reddest band (the L-band), a close proxy of stellar mass in the interested redshift range, enables our selected to be easily compared with a stellar mass selected sample.

We test the validity of our VJL selection criteria in two ways. First, we study the evolutionary track of stellar population synthesis models along redshift in the (J-L) vs. (V-J) two-color diagram. Second, we study the distribution of real galaxies from the ERS field with spectroscopic redshift (spec-z) in the two-color diagram.

The left panel of Figure 5.1 shows tracks of shifting galaxy models along redshift (from $z=0$ to $z=7$) in the (J-L) vs. (V-J) two-color diagram. Symbols in each track stand for models at (starting from the lowest one) $z=2, 2.5, 3, 3.5,$ and 4 . Galaxy models are retrieved from an updated version (CB09) of the stellar population synthesis library of Bruzual & Charlot (2003, BC03) with the Salpeter IMF (Salpeter, 1955) and solar metallicity. The Calzetti law (Calzetti et al., 1997, 2000) and the recipe of Madau (1995) are applied to each model to account for the dust reddening and the opacity of intergalactic medium (IGM) in the universe. Our selection windows corresponding to Equation 5.1 (the upper left region) and 5.2 (the upper right region) are outlined by black lines.

Blue tracks stand for models with a constant star formation rate (CSF), age of 0.5 Gyr and various dust reddenings (solid: $E(B-V)=0.0$; dotted: $E(B-V)=0.3$; dashed: $E(B-V)=0.6$). These tracks show two facts: (1) all CSF models enter our sVJL selection window in the redshift range of $2.3 \leq z \leq 3.5$ and (2) the reddening vector (the black arrow in the panel) is almost parallel to our sVJL selection window (the diagonal black line). We also test our criteria with models with older ages (2 Gyr) as well as models with an exponentially declining SFH (τ -model, where τ , the characteristic time scale of star formation, is fixed to 1.0 Gyr). Both types of models have similar tracks as that of the CSF model with $t=0.5$ Gyr. These results demonstrate that our sVJL criterion can select SFGs with various SFH, age and SFR independent of dust reddening.

However, the CSF model with $E(B-V)=0.6$ enters our pVJL selection window twice, at $1.5 \lesssim z \lesssim 2.5$ and $z \geq 4.0$. Models with different SFH but same age and dust reddening also enter the pVJL selection window at similar redshifts. The behavior of these models suggests that our pVJL galaxies may be contaminated by highly obscured SFGs from both lower ($z \leq 2.0$) and higher ($z \geq 4.0$) redshift, regardless of their exact SFH.

Red tracks shows the evolutionary track of dust-free single stellar population (SSP) models with ages of 0.5, 1, and 2 Gyr. All three SSP models enter our pVJL selecting window, but at different redshifts: ~ 3.5 , ~ 3.0 , and ~ 2.5 for models with age of 0.5 Gyr (blue), 1.0 Gyr (green), and 2.0 Gyr (red). Overall, our pVJL criteria are able to select PEGs around $z=2.5$ and above.

The right panel of Figure 5.1 shows our second test, that is the position of galaxies with different spec-zs in the (J-L) and (V-J) diagram. This test with real galaxies supplements the first one in two ways: (1) it helps in understanding the effect of photometry uncertainty and (2) it shows how our method works for galaxies with

unknown and perhaps more complex SFH. Galaxies with spec- z in the ERS are divided into different redshift ranges and shown by colors and labels.

In this panel, the edge of our sVJL selection window effectively separates galaxies at $2.3 \leq z \leq 3.5$ from others, satisfying our expectation. However, several galaxies with lower redshift and a few with higher ones also enter our sVJL window. We suspect that photometry uncertainty is the main reason that scatters them into our sVJL window, although we cannot rule out the effect of a complex SFH. Few galaxies with (J-L) color redder than 2.5 are found in our spec- z sample. The lack of red galaxies is caused by the fact that spectroscopic observations are biased against dusty SFGs and PEGs because of their faint and featureless rest-frame optical spectra. It is also possible that red galaxies are really rare in the high- z universe. We notice that a few galaxies from lower redshift ($z < 2.5$) and higher redshift ($z > 4.5$) enter the pVJL selection window. The existence of these types of contamination is consistent with our above analysis with theoretical models (see the *left* panel). We will discuss how to eliminate contamination in both selection methods later.

AGN sources could also contaminate our VJL selected sample. As shown in Civano et al. (2011), about 30% of AGN at $z \gtrsim 3$ show an typical optical spectrum of a SFG, but have X-ray luminosity $> 10^{44} \text{ergs}^{-1}$, a typical value of quasars. In order to evaluate their contamination, we study the redshift tracks of AGN templates of Polletta et al. (2007) in the (J-L) vs. (V-J) plot. Template of type 2 QSO (QSO2), type 1 QSO with the lowest optical-to-IR ratio (BQSO1) and type 1 QSO with the highest optical-to-IR ratio (TQSO1) are all within our sVJL selection window at $z=0$. However, QSO2 leaves the window quickly before $z=0.5$, and BQSO1 also leaves the window around $z=1$. Given the small cosmic volume that our surveys observe at $z < 1$, we argue that these two types of AGN would not severely contaminate our sample. The only template that stays in our sVJL selection window up to $z > 3.5$ is TQSO1. We also examine the track of AGN + star-burst template of I19254 of

Polletta et al. (2007). The template enters our sVJL selection window at $z > 2$ and evolves to redder (J-L) direction within the window as redshift increases. It suggests that our red (J-L > 2.5) dusty SFG sample could be contaminated by Seyfert 2 galaxy. We will discuss the possible contamination in detail later in Sec. 5.3.3. We also note that no QSO template enters our pVJL selection window, which indicates that our selected PEG sample is in principle immune from AGN contamination.

As a summary, using both theoretical models (CSF, τ -model, and SSP) and spectroscopically observed galaxies, we show that our sVJL selection window (defined by Equation 5.1) can select SFGs with various levels of star formation rate independent of dust reddening at $2.3 \leq z \leq 3.5$. And our pVJL selection window (defined by Equation 5.2) can select PEGs around $z=2.5$ and above, although such a selected sample may be contaminated by dusty SFGs at $z \leq 2.0$ and $z \geq 4.0$. Also, no template at $z \leq 1.5$ or galaxies with spec- $z < 1.5$ enters either of our selection windows, suggesting that our criteria are effective at excluding low redshift galaxies.

5.3 Star-forming VJL Galaxies

We apply our sVJL criterion, defined by Eq. 5.1, to the multi-wavelength catalog of the ERS field, which is based on the WFC3 H-band detection, as discussed in §2.2, to select SFGs at $z \sim 3$. To ensure an accurate measure of galaxy colors, we require all selected galaxies to have $S/N > 10$ in J- and L-band. We also construct a samples with $S/N > 20$ in the two bands. Comparison between the two samples would show us how photometric uncertainty affects our selection results. For V-band photometry, if $S/N < 1$, we use the 1σ photometric uncertainty as the upper limit of flux. The two samples contain 354 and 146 galaxies, respectively.

We note that the BzK color criterion of Daddi et al. (2004a) was constructed to be applied to K-selected samples. Similarly, one would expect the VJL criterion to be applied to L-band limited samples. Without an L-band detection, thus with

an upper limit (at best) on the J-L color, no VJL galaxy can be unambiguously selected. Moreover, Using L-band also ensures the closest proxy for mass selection of the sample. In this chapter, we choose to apply the S/N cut on both bands instead of on only the L-band so that we could have accurate J-L color. This is not contradictory with selecting an L-band limited sample. Instead, it asks for more strict constraint on the J-L color to exclude interlopers. This is well fitting the purpose of this paper to demonstrate the validity of the selection criterion. We also acknowledge that the use of S/N cut on two bands would bring a more complicated selection effect on the completeness of sample, because now the completeness is not only dependent on the proxy of mass, but also on the color. However, we will argue later (in §5.3.4 and §5.4.3) that the induced selection effect would not significantly change the quantitative results of comparing our VJL samples with other samples.

5.3.1 Redshift Distribution

The redshift distributions of our sVJL samples with $S/N > 10$ and 20 are shown in Figure 5.2. Both distributions highly peak around $z \sim 2.7$ and extend to $z > 3.5$, demonstrating that, as we expected, our sVJL criterion is effective at selecting galaxies between $2.3 \leq z \leq 3.5$. The $S/N > 10$ sample has a secondary peak around $z = 1.8$, which implying that the main contamination of our sVJL selection is coming from galaxies at $z \sim 2$. Fortunately, this secondary peak is largely diminished in the $S/N > 20$ sample. The number ratio between galaxies at $z \sim 1.8$ and at $z \sim 2.8$ decreases from 0.27 in the $S/N > 10$ sample to 0.17 in the $S/N > 20$ one. It suggests that the low- z contamination in our sVJL sample is induced by photometric uncertainty rather than the deficit of our method and hence can be removed by increasing the S/N cuts in J- and L-band. In later study, to balance the fraction of contamination and the number of statistics, we use the $S/N > 10$ sample as our fiducial sample.

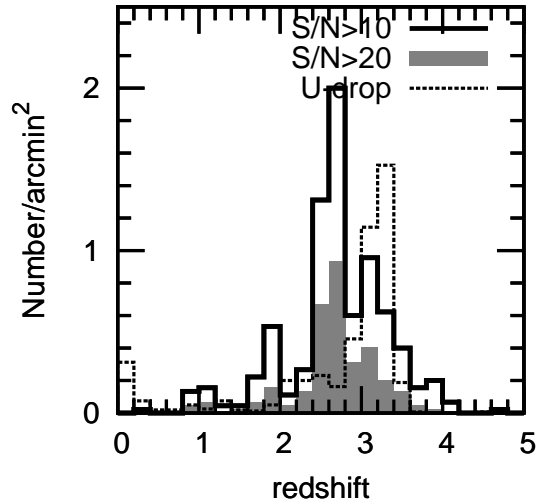


Figure 5.2 Redshift distributions of star-forming VJL galaxies. Solid line stands for the sample with $S/N > 10$ in J- and L-band, while filled grey histogram for the sample with $S/N > 20$ in the two bands. For comparison, the distribution of U-band dropouts selected in GOODS-N is plotted with dotted line.

5.3.2 Comparison with LBGs

Nowadays, high redshift SFGs are commonly selected through the Lyman Break technique. In order to avoid the contamination zone of elliptical galaxies, this technique compromises to only select galaxies with a bright and blue rest-frame UV continuum, namely SFGs with low or no dust extinction. Dusty SFGs, whose rest-frame UV color mimics that of elliptical galaxies, are missed by this technique. Because of this bias, the existence and contribution of dusty SFGs to the cosmic SFRD at $z \sim 3$ has been the topic of considerable debate. To shed a light on the above question, we compare galaxies selected through our sVJL method, which is designed to select both low-dust and dusty SFGs, with LBGs at $z \sim 3$.

The U-band dropout method is used to select LBGs at $z \sim 3$, because the Lyman Break of a SFG is redshifted to between the U-band and the B-band. A sample of 1161 U-band dropouts is selected from GOODS North (878) and South (283) fields with the following criteria:

$$\begin{aligned}
U - B &\geq 0.75 + 0.5 \times (B - z), & (5.3) \\
U - B &\geq 0.9, \\
B - z &\leq 4.0, \\
S/N_B &\geq 3 \quad \text{and} \quad S/N_z \geq 3.
\end{aligned}$$

We notice that the number of U-band dropouts in GOODS-S is significantly less than that in GOODS-N, because the CTIO U-band image in GOODS-S is 1.5 mag shallower than the KPNO U-band image in GOODS-N. The physical properties of the U-band dropouts are measured in the same way used for the sVJL galaxies.

In Figure 5.2, we over-plot the redshift distribution of the U-band dropout sample (dotted line) selected from GOODS-N. The distribution peaks around $z \sim 3$, being consistent with the expectation of LBGs, but significantly deviates from the peak of our sVJL sample. Since the offset between the peaks of the two samples is larger than 2σ deviation of our photo- z measurement ($\Delta z / (1+z) = 0.037$), it is an intrinsic difference between the two methods rather than due to photo- z uncertainty. However, since the cosmic time interval between the two redshift peaks (250 Myr) is about ten times less than the age of the universe at $z \sim 3$ (~ 2.2 Gyr), we assume that the evolution of galaxies between the two redshifts is negligible. Under this assumption, any difference between the two samples is considered due to the fact that the two methods select galaxies with different physical properties rather than select galaxies with different redshifts. Also, in order to eliminate the effect of possible contamination, we only compare galaxies within the range of $2.3 < z < 3.5$ in the two methods.

A direct and illustrative way to compare both methods is to study the location of the U-band dropouts in the (J-L) vs. (V-J) plot. We match the U-band dropouts that are selected from GOODS-S TFIT catalog to the ERS TFIT catalog to measure their (J-L) and (V-J) colors. Figure 5.3 shows the positions of 41 matched U-band dropouts (circles and squares) with $S/N > 10$ in J- and L-band in the (J-L) vs. (V-J) diagram,

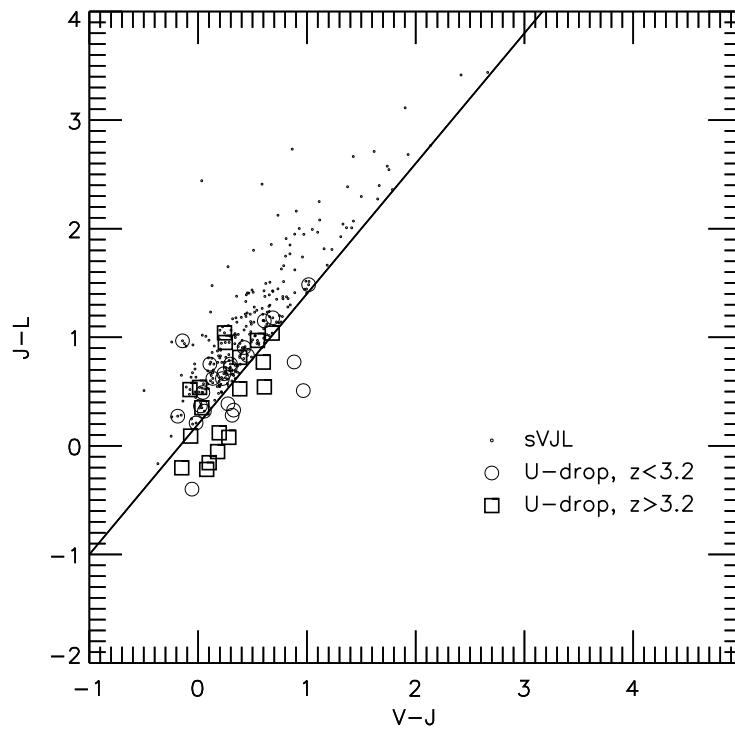


Figure 5.3 Star-forming VJLs (points) and U-band dropouts (circles: $z < 3.2$; squares: $z > 3.2$) in the $(J-L)$ vs. $(V-J)$ color-color diagram. Only U-band dropouts that fall into the ERS field are plotted. Both sVJL and U-band dropout samples have $S/N > 10$ in J- and L-band.

together with sVJLs (points). We notice that the U-band dropouts are scattered along the edge of our sVJL selection window. Among 41 U-band dropouts, 16 fall outside our sVJL selection window. Although photometric uncertainty could contribute to the scatter, we suspect that the primary reason is due to the different redshift distribution between sVJLs and U-band dropouts. As shown in Figure 5.2, the U-band dropouts have systematically higher redshift than sVJLs and is hence easier for them to be scattered out of the selection window. To examine our suspicion, we divide the U-band dropouts sample into two sub-samples: $z < 3.2$ (circles) and $z > 3.2$ (squares). 10 out of 16 (63%) U-band dropouts outside the sVJL selection window have $z > 3.2$, suggesting that redshift is the main reason for these galaxies not being selected by our sVJL method.

The other feature of U-band dropouts is more prominent and physical: no U-band dropout has J-L color redder than 2.0 mag. As shown in the *left* panel of Figure 5.1, CSF galaxies with $E(B-V) > 0.3$ would have J-L color redder than 2.0 mag. Therefore, $(J-L) > 2.0$ mag can be treated as a rough division for weakly and strongly obscured galaxies. The lack of red U-band dropouts confirms conclusions of previous studies that LBGs miss highly obscured galaxies (e.g., Bouwens et al., 2009; Ly et al., 2011; Riguccini et al., 2011). On the other side, our sVJL method selects galaxies up to J-L around 3.0 mag, suggesting its ability to select highly obscured SFGs.

The difference of the $E(B-V)$ distributions of samples selected by the two methods can be clearly seen from Figure 5.4, where $E(B-V)$ is measured from the slope of rest-frame UV continuum and plotted as a function of stellar mass of galaxies. Both samples have similar $E(B-V)$ distribution in the stellar mass range of $9 < \log(M/M_\odot) < 10$. But in the range of $10 < \log(M/M_\odot) < 11$, their $E(B-V)$ distributions differ: the distribution of U-band dropouts ends around $E(B-V)=0.4$, while that of sVJLs in the $S/N > 10$ sample extends beyond $E(B-V)=0.6$.

The two upper panels of Figure 5.5 show the cumulative fraction of number of galaxies as a function of $E(B-V)$ in both stellar mass ranges for sVJLs and U-band dropouts. In the range of $9 < \log(M/M_{\odot}) < 10$, both sVJL and U-band dropout samples have similar cumulative fraction curve and only contain galaxies with $E(B-V) < 0.4$. In the range of $10 < \log(M/M_{\odot}) < 11$, the U-band dropout sample still only contains $E(B-V) < 0.4$ galaxies, while about 20% of sVJLs (in the $S/N > 10$ sample) have $E(B-V) > 0.4$. The $E(B-V)$ distribution of massive ($10 < \log(M/M_{\odot}) < 11$) sVJLs drops quickly beyond $E(B-V) = 0.6$ in the $S/N > 10$ sample (only 5% have $E(B-V) > 0.6$). This could be attributed to two factors: (1) the real lack of very dusty SFGs at $z \sim 3$ or (2) the sensitivity of the catalog detection band image of ERS (H-band) is not deep enough to detect these galaxies. Either way, we can still conclude that, compared to U-band dropout method, our sVJL selection method can select moderate dusty ($E(B-V) \leq 0.6$) SFGs at $2.3 < z < 3.5$.

We also notice that the distribution of sVJLs in the $S/N > 20$ sample is similar to that of U-band dropouts, even in the range of $10 < \log(M/M_{\odot}) < 11$. This reflects that an over-cut on J-band S/N would reduce our ability to detect dusty SFGs at $z \sim 2.8$. The $S/N > 20$ sVJL sample also contains fewer low-mass (around $10^9 M_{\odot}$) galaxies than the $S/N > 10$ sVJL sample. This can also be attributed to the over-cut on L-band S/N in the latter.

5.3.3 Dusty Star-forming Galaxies

Although red ($J-L > 2.0$) sVJLs are likely to be dusty SFGs at $z \sim 2.7$, a more careful census is needed to distinguish them from possible contamination. Specifically, PEGs at similar redshift have similar red rest-frame UV colors and hence can easily enter our sVJL sample due to photometric uncertainty. In order to clean our dusty sVJL sample, we have to break the age–dust degeneracy, which, however, cannot be broken by simply using rest-frame UV and optical data. Fortunately, at $z \sim 2.7$, the rest-frame

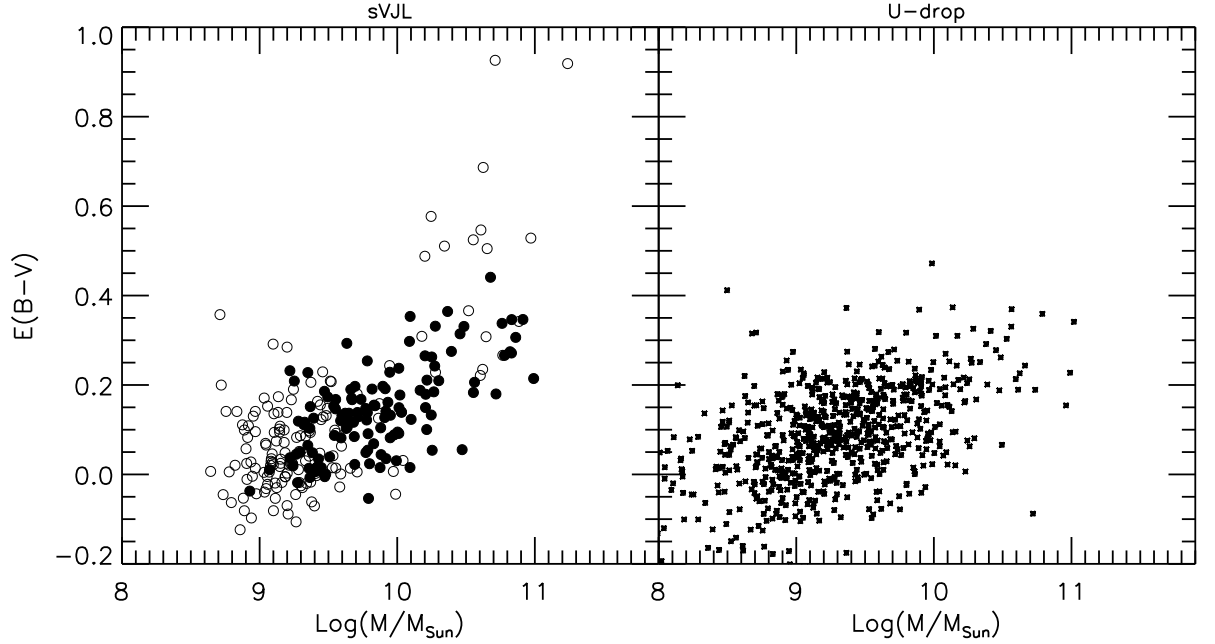


Figure 5.4 $E(B-V)$ distribution as a function of stellar mass for star-forming VJL galaxies (*left*) and U-band dropouts (*right*). Empty and solid circles in the *left* panels show sVJLs in the $S/N > 10$ and $S/N > 20$ sample, respectively.

6-micron emission from Polycyclic Aromatic Hydrocarbons (PAHs), a feature of dusty SFGs, falls into the MIPS 24-micron bandpass, and can help to separate dusty SFGs from PEGs. Any 24 μm fluxes that are significantly brighter than the prediction of pure stellar emission should be dominantly contributed by dust emission and hence indicate a high amount of dust in the galaxies.

We match our sVJLs to GOODS-S MIPS 24 μm catalog (see the description in Sec. 2.2), with a matching radius of $1.0''$. Galaxies without MIPS 24 μm counterparts are assigned a flux upper limit of 3 μJy , which is the upper envelope of the S/N -flux relation at $S/N=1$ in our MIPS 24 μm catalog (However, we note that we do not use 24 μm sources with flux level of 3 μJy for any scientific purpose. Sources with detection lower than 3σ should be treated with caution.). A potential issue of measuring MIPS 24 μm flux of galaxies is the uncertainty raised by confusion and crowding. Our 24 μm catalog over the GOODS-S field contains about 22000 sources, deducing an average

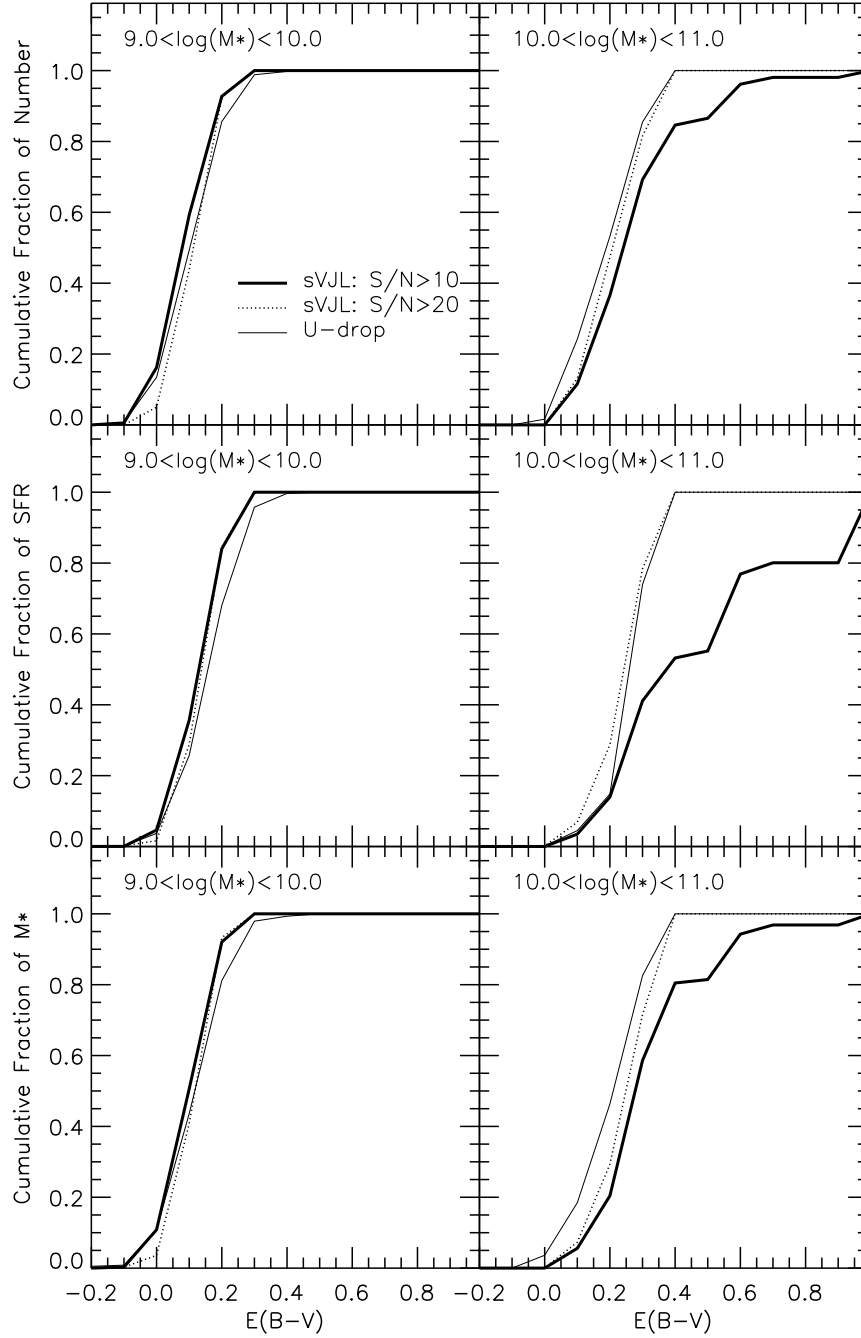


Figure 5.5 *Top*: Cumulative fraction of number of galaxies as a function of $E(B-V)$ for sVJLs (thick solid for $S/N > 10$ and dotted for $S/N > 20$) and U-band dropouts (thin solid) in two stellar mass ranges. *Middle*: Cumulative fraction of SFR for sVJLs and U-band dropouts. *Bottom*: Cumulative fraction of stellar mass for sVJLs and U-band dropouts. SVJLs and U-band dropouts in two stellar mass bins: $9.0 < \log(M_{\text{star}}/M_{\odot}) < 10.0$ (left) and $10.0 < \log(M_{\text{star}}/M_{\odot}) < 11.0$ (right) are plotted.

number density of 1.2 (4.8) sources in each circle with radius of 3'' (6''), which is 0.5 (1.0) times the FWHM of MIPS 24 μm PSF. This implies that 60% of light of a source is overlapping with the light of other sources. The PSF-fitting technique that we use to construct the catalog ideally reduces the influence to the lowest level by fitting nearby sources simultaneously. In this method, however, a slight over-subtraction (under-subtraction) of a bright source would result in a significant under-estimation (over-estimation) of fluxes of nearby sources.

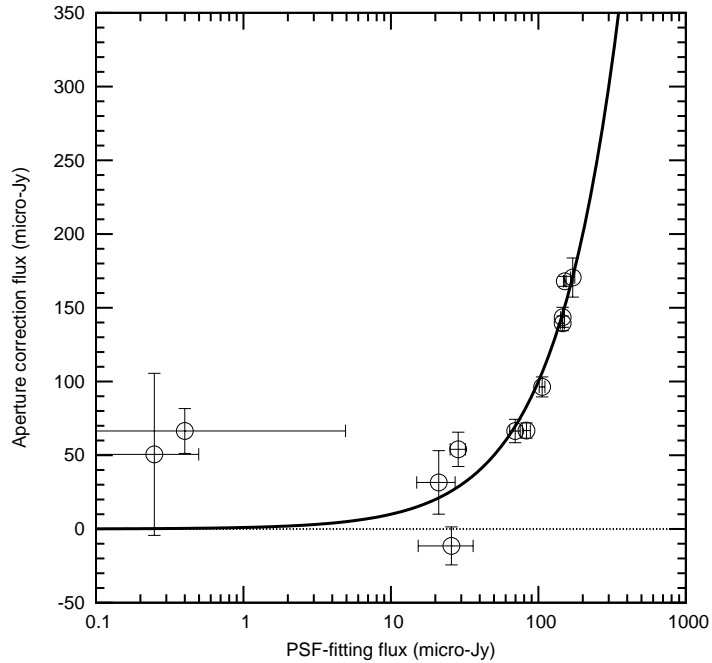


Figure 5.6 Comparison of MIPS 24 μm fluxes derived through PSF-fitting and aperture correction for sVJLs with $E(B-V) \geq 0.4$. The solid line shows one-to-one correspondence, while dotted line shows zero aperture corrected fluxes. Since a few sources have negative aperture corrected fluxes, we only use logarithmic scale for PSF-fitting fluxes.

In order to evaluate whether MIPS 24 μm fluxes are correctly measured, we compare our PSF-fitting fluxes to fluxes that are derived through aperture correction. In a crowding environment, aperture correction on the flux measured through the central region (e.g., within an aperture with size of 1 FWHM of PSF) of a faint object tends to overestimate its flux, since the central region of the object could be polluted by the light of its nearby sources. In this case, the aperture corrected flux can be

used as an upper limit. To obtain a conservative estimation of the contribution of dusty SFGs to the cosmic SFRD, we care more about sources whose fluxes are over-estimated by PSF-fitting than those whose fluxes are under-estimated, as the former could be PEGs but mis-classified as dusty SFGs. Such mis-classification would result in a severe over-estimation of their SFR and hence their contribution to the SFRD. For this purpose, any sources whose PSF-fitting fluxes are significantly larger than their aperture corrected fluxes are thought to have incorrect PSF-fitting fluxes, and aperture corrected fluxes will be used for them.

Figure 5.6 shows the comparison between aperture corrected fluxes and PSF-fitting fluxes for sVJLs with $E(B-V) \geq 0.4$. For sources with PSF-fitting fluxes larger than $40 \mu\text{Jy}$, fluxes derived by both methods are in good agreement. This is not surprising though, as both methods are robust for bright sources. For source with PSF-fitting fluxes less than $10 \mu\text{Jy}$, aperture correction over-estimates their fluxes due to the issue of confusion and crowding, as these sources are faint sources around bright sources. We use the PSF-fitting fluxes for these sources, as they are the best solution we can have for them. For sources with PSF-fitting fluxes between $10 \mu\text{Jy}$ and $40 \mu\text{Jy}$, particularly of our attention is one source whose aperture correction flux is less than zero but whose PSF-fitting flux is larger than $10 \mu\text{Jy}$. As we discuss above, the incorrectly high PSF-fitting flux of this source is due to the under-subtraction of its nearby bright sources. We will mark this problematic source in later analysis.

Figure 5.7 shows the $24 \mu\text{m}$ fluxes of our sVJLs as a function of stellar mass. For simplicity, we only plot sVJLs with $E(B-V) > 0.4$ and $2.3 < z < 3.5$. Over-plotted (black lines) in the figure are the predictions of the $24 \mu\text{m}$ flux–stellar mass relation for dust-free SSP models at $z \sim 2.7$, with age of 0.5, 1.0 and 2.0 Gyr (from top to bottom). Galaxies with $24 \mu\text{m}$ fluxes significantly brighter than the prediction of SSP models are thought to be dusty SFGs, because their $24 \mu\text{m}$ fluxes cannot be explained by pure stellar emission and hence should be contributed by PAH emission.

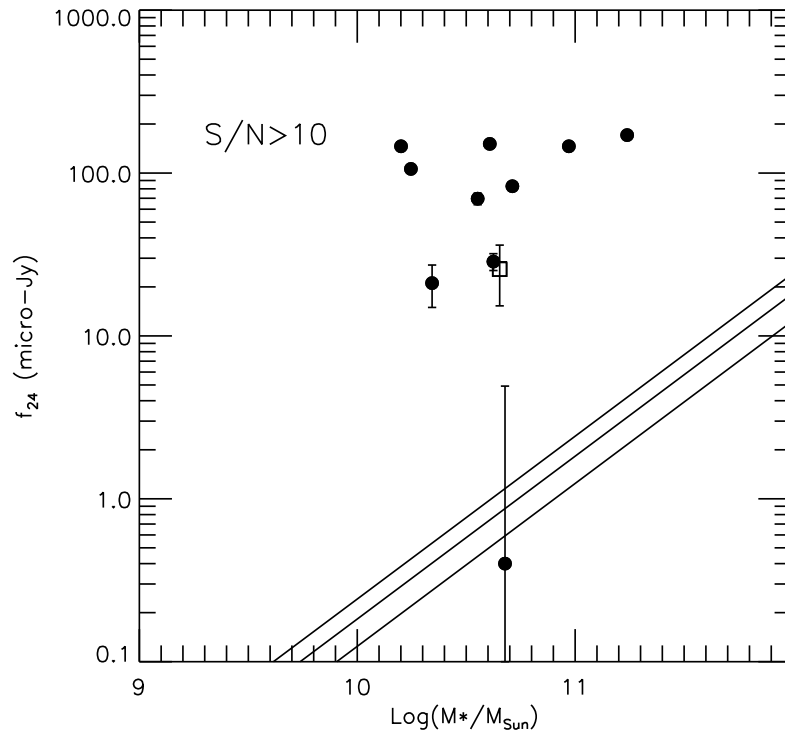


Figure 5.7 MIPS 24 μm fluxes of dusty sVJLs ($S/N > 10$) as a function of stellar mass. Here we only show galaxies with $E(B-V) \geq 0.4$ and $2.3 < z < 3.5$. Error bars show the photometric uncertainties. Three solid lines show the prediction of $z \sim 2.7$ PEGs with age of 0.5, 1.0, and 2.0 Gyr. The square shows the source with possibly problematic PSF-fitting flux.

On the other hand, galaxies whose 24 μm fluxes are consistent with the predictions of SSP models are thought as contamination. We also mark the the galaxy with problematic PSF-fitting flux with squares in the figure. If the the problematic galaxy is treated as a PEG, the fraction of contamination is about 18% (2 out of 11). This result is encouraging, as it shows our sVJL method can select dusty SFGs with a low level of contamination.

Another possible source of contamination in our dusty SFGs is from AGN host galaxies. The warm dust around AGN can absorb and reprocess the energetic photons of AGN into IR emission that can be observed in the MIPS 24 μm channel. We use the Chandra deep 4Ms X-ray image of CDFS¹ to study the possible AGN contamination. None of our 9 dusty SFGs is individually detected in the 4Ms Chandra catalog of Xue et al. (2011). The stacked hard X-ray image of them also reports a detection comparable to the noise level. However, the stacked soft X-ray image has a detection of 3.5σ . The soft detection may indicate that our dusty SFG sample is contaminated by AGN host galaxies. However, using the stacked image, we measured a hardness ratio of ~ -1 , which is softer than the predicted hardness ratio of even the least absorbed AGN model (column density $N_{\text{H}} = 10^{21} \text{cm}^{-2}$) at $z \sim 3$ in Wang et al. (2004). The ultra-soft spectrum of the stacked image implies that our dusty SFG sample is not heavily contaminated by AGN. We also calculate an average luminosity from the stacked soft-band X-ray images, using a mean redshift of 2.7. The mean luminosity is $1.2 \times 10^{42} \text{erg/s}$, with the lower and upper limit from the Poisson uncertainty on net counts of $8.3 \times 10^{41} \text{erg/s}$ and $1.5 \times 10^{42} \text{erg/s}$. If we use the SFR–X-ray relation of Ranalli et al. (2003): $L_{\text{X}}/\text{SFR} \sim 10^{40} \text{erg/s}/(\text{M}_{\odot}/\text{yr})$, we get an average SFR of about $100 \text{M}_{\odot}\text{yr}^{-1}$. This value is consistent with the SFR measure though the rest-frame UV continuum of these galaxies. These galaxies are heavily obscured and occupy the

¹<http://exc.harvard.edu/cda/Contrib/CDFS.html>

high SFR end of the whole star-forming VJL sample. Therefore, we conclude that they are compatible with being star-forming.

5.3.4 Contributions of Dusty Star-forming Galaxies

One of our motivations of selecting dusty SFGs around $z \sim 3$ is to evaluate their contribution to the number density, stellar mass density and SFRD of SFGs. A precise measurement of the absolute contributions of dusty SFGs relies on the accurate correction of the incompleteness of the sample, which is a function of the redshift, surface brightness, color and spectral types of galaxies. The best way to measure the incompleteness is simulating the detection ability of galaxies with different physical properties and multi-wavelength photometry. We leave such simulations to a future paper. Instead, in this thesis, we try to estimate the relative contributions (compared with those of low-dust galaxies) of dusty SFGs to the above quantities to the first order accuracy.

In our sVJL method, both low-dust and dusty galaxies are selected with the same color criterion from the same catalog. They are also aiming to the same redshift range. As a result, the two main factors that determine the selection incompleteness, namely redshift and surface brightness limit of the survey, are roughly same for both low-dust and dusty sub-samples. We can assume that, to the first order, incompleteness is roughly same for both sub-samples. Therefore, the ratio of total numbers, SFRs and stellar masses of both sub-samples should be immune to the incompleteness and accurate to the first order even no correction on incompleteness is applied. We acknowledge that the redder color and fainter rest-frame UV photometry of dusty galaxies may vary the selection incompleteness. However, both factors tend to increase the incompleteness of dusty SFGs so that our derived ratio is a conservative estimation of the contributions of dusty SFGs.

Based on above discussion, a simple way to measure the relative contributions of low-dust and dusty sub-samples is to study the cumulative number, SFR and stellar mass as functions of dust extinction $E(B-V)$. Since $E(B-V)$ has a loose relation with stellar mass (see Figure 5.4), we study sVJLs in two stellar mass ranges separately: $9 < \log(M/M_{\odot}) < 10$ and $10 < \log(M/M_{\odot}) < 11$. We plot the cumulative curves of number (top panel), SFR (middle) and stellar mass (bottom) of our $S/N > 10$ and $S/N > 20$ sVJL samples in Figure 5.5, together with the curves of the U-band dropout sample as a reference. For galaxies with $9 < \log(M/M_{\odot}) < 10$ (left column), sVJLs (in both $S/N > 10$ and $S/N > 20$ sample) have similar cumulative curves with U-band dropouts, simply because there are almost no dusty ($E(B-V) \geq 0.4$) galaxies detected in this mass range, as shown by the left panel of Figure 5.4. The situation is same for $S/N > 20$ sVJLs in the $10 < \log(M/M_{\odot}) < 11$ range (right column), as the overcut on J-band S/N reduces our ability to detect dusty galaxies. The significant difference comes from the $S/N > 10$ sVJLs, whose cumulative SFR curve obviously deviates from that of other samples in the $10 < \log(M/M_{\odot}) < 11$ range. About 50% of SFR is contributed by galaxies with $E(B-V) \geq 0.4$, although these dusty galaxies only contribute about 20% to number and 20% to stellar mass of galaxies in the mass range, as shown by the top right and bottom right panel of this figure.

An alternative way to evaluate the importance of dusty SFGs that are selected by our sVJL method is to compare their contributions (on number, SFR and stellar mass densities) to those of U-band dropouts. The comparison again relies on the accurate measurements of the incompleteness of the two selection methods, but can be compromised through the following way. We choose a certain population of galaxies that is highly completely selected by both methods so that its three densities measured with both samples should be same even when no correction on incompleteness is applied to this population. We then normalized the densities of other populations in both samples to those of this population. The normalized density distributions hence

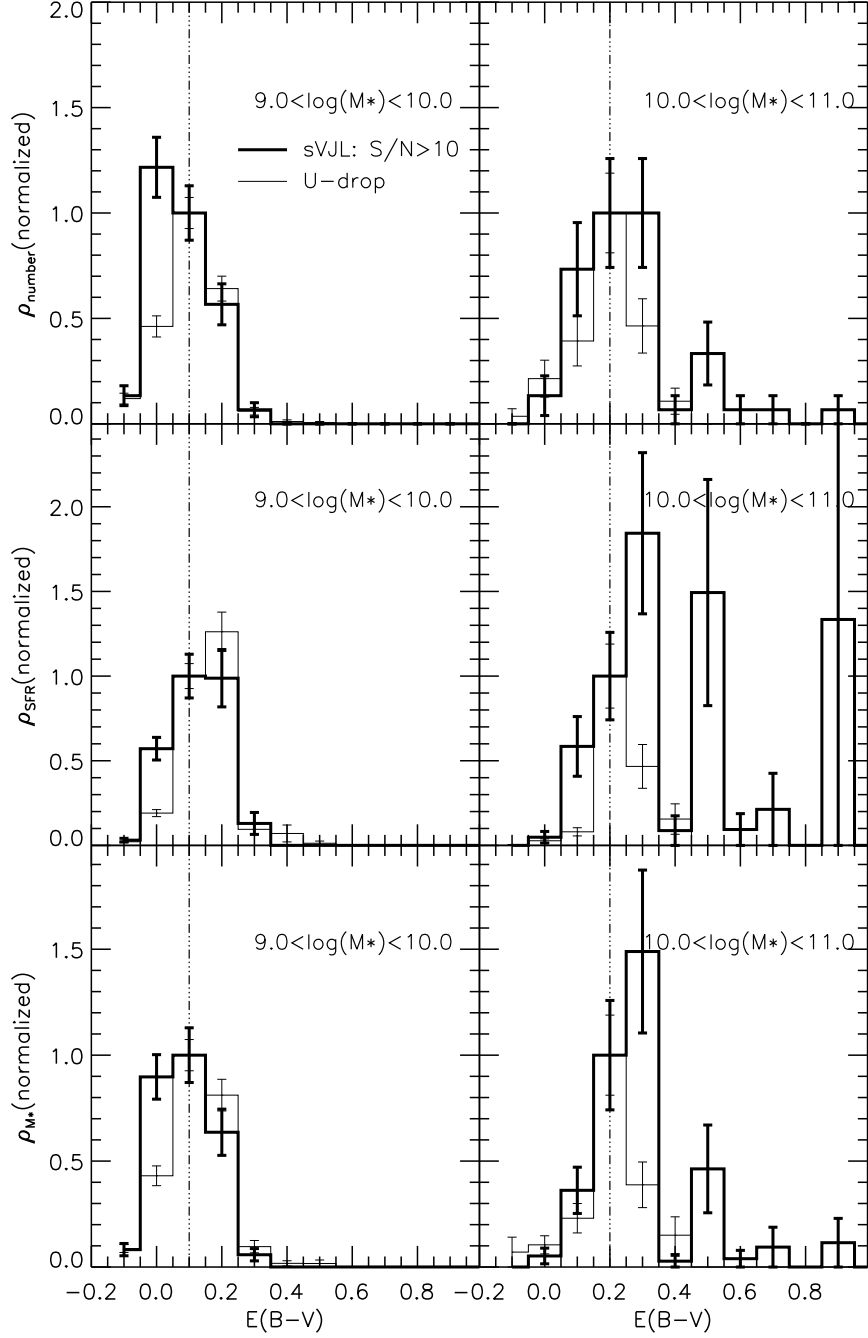


Figure 5.8 *Top*: Comparison of normalized number density (*top*), SFRD (*middle*) and stellar mass density (*bottom*) of U-band dropouts (thin lines) and S/N>10 sVJLs (thick lines), as a function of E(B-V). All densities are normalized to E(B-V)=0.1 for the stellar mass bin of $9.0 < \log(M_{\text{star}}/M_{\odot}) < 10.0$ and to E(B-V)=0.2 for $10.0 < \log(M_{\text{star}}/M_{\odot}) < 11.0$ (dotted-dashed lines). Error bars in top panels show the Poisson errors, while those in other panels show how the Poisson error propagates into each quantity by assuming an average stellar mass and SFR for each galaxy.

show the relative contributions of each different populations in the two samples. We choose galaxies whose $E(B-V)$ s are within ± 0.05 of the median $E(B-V)$ of each sample as the "complete" sub-sample. In the stellar mass bin of $9.0 < \log(M_{\text{star}}/M_{\odot}) < 10.0$, this sub-sample consists of galaxies with $0.05 < E(B - V) < 0.15$ for both U-band dropouts and sVJLs, while in the $10.0 < \log(M_{\text{star}}/M_{\odot}) < 11.0$ bin, galaxies with $0.15 < E(B - V) < 0.25$.

The comparisons of normalized number density (*top*), SFRD (*middle*) and stellar mass density (*bottom*) of U-band dropouts (thin lines) and $S/N > 10$ sVJLs (thick lines) as a function of $E(B-V)$ are shown in Figure 5.8. The same information of Figure 5.5, that about 20% to 30% of number density and about 50% of stellar mass and SFR densities in sVJLs at high mass end ($10.0 < \log(M_{\text{star}}/M_{\odot}) < 11.0$) are contributed by galaxies with $E(B-V) > 0.3$, can be inferred from this figure. However, an important point of Figure 5.8 is that the densities of low-dust ($E(B-V) < 0.3$) galaxies in the two samples are quite similar in both stellar mass bins, with an only $\sim 10\%$ excess from the sVJL sample, which demonstrates that although the cumulative distributions are different in the high-mass end of the two samples, our sVJL method has the same ability to select low-dust galaxies as the U-band dropout method, in terms of the three densities. The $\sim 50\%$ of contributions to stellar mass and SFR densities of dusty SFGs in our sVJL sample are "net" contributions, instead of due to the possibility that low-dust galaxies are largely missed in our sVJL sample.

Our results, along with some recent studies, highlight the importance of counting SFR from dusty galaxies, which occupy the high SFR (and massive) end in the SFR–stellar mass plane, when calculating the cosmic SFRD. These galaxies are usually faint or even undetected in observed UV band at $z \sim 3$ and could be missed by UV only selection (e.g. Lyman Break technique). Ly et al. (2011) carried out a census of SFGs at $z = 1-3$ in the Subaru Deep Field, where good statistics and accurate measurements of photo- z and physical properties are enabled by a large sample (~ 53000 galaxies)

and 20-band (1500\AA - $2.2\mu\text{m}$) photometry. They compared the selection results of BzK, LBG, and BX/BM, and found that among $z=1-2.5$ galaxies in their census, 81–90% of them can be selected by combining the BzK selection with one of the UV techniques ($z\sim 2$ LBG or BX and BM). What’s more important, they found that for galaxies brighter than $K>24$ AB (roughly corresponding to $\log(M/M_{\odot}) > 10$ for SFGs at $z\sim 2$), 65% of the star formation in them are contributed by galaxies with $E(B-V)>0.25$, even though they are only one-fourth of the census by number. Their results are in very good agreement with ours, although aiming to lower redshift. Yun et al. (2011, submitted) studied the rest-frame UV and optical properties of sources detected by the deep 1.1 mm-wavelength imaging of the GOODS-S by AzTEC/ASTE (Scott et al., 2010). They claimed that although not all sub-mm galaxies are faint and red in their rest-frame UV and optical bands, the majority of the AzTEC GOODS sources, which have a median redshift of 2.6 and 80% of which are at $z>2.6$, are too faint and red to have been identified in previous surveys of SFGs and are likely be entirely missed in the current measurements of the cosmic SFRD.

5.4 Passively-Evolving VJL Galaxies

In this section, we apply Eq. 5.2 to the ERS field to select PEGs at $z\sim 3$. With a concern that a high S/N threshold in rest-frame optical band would exclude real PEGs from our sample, we tune down the threshold to $S/N>5$ in both J- and L-band. However, we still construct samples with $S/N>10$ and 20 to provide a reference on how photometric uncertainty affects our selection results. We find 32, 27 and 13 galaxies falling into our pVJL selection window for $S/N>5$, 10 and 20. However, as shown in Figure 5.1, both low- z and high- z dusty SFGs also enter our pVJL selection window so that a fraction of our pVJL selected galaxies may not be real passive and old galaxies, but rather dusty SFGs. We will estimate the fraction of contamination in our pVJL sample and discuss how to clean the sample.

5.4.1 Clean Sample

As similar as in §5.3.3, we use MIPS 24 μm flux to help identify contamination in our pVJL sample. Galaxies whose observed 24 μm fluxes are 3σ higher than the prediction of a dust-free passively-evolving model (SSP with age of 2 Gyr) with the same redshift and stellar mass are considered as contaminating dusty galaxies, because their 24 μm fluxes cannot be explained by pure stellar emission and hence are dominated by dust emission. The same issue we face here is again the confusion and crowding of MIPS 24 μm image. We repeat the same test in Sec. 5.3.3 to compare PSF-fitting and aperture corrected fluxes. We use the aperture corrected fluxes for sources whose PSF-fitting fluxes are larger than the 1σ confidence level of their aperture corrected fluxes, and use the PSF-fitting fluxes for other sources.

Comparing the observed 24 μm fluxes of our pVJLs with stellar models, we find the contamination fraction of 59%, 59% and 77% for samples with S/N cuts of 5, 10 and 20. The fraction does not decrease with the increase of S/N thresholds, suggesting that simply increasing the S/N cuts cannot help clean our pVJL sample. This is because such contamination is due to the intrinsic deficit of our selection method (as shown by the left panel of Figure 5.1, where a few tracks of dusty SFGs also enter our pVJL selection window) rather than due to photometric uncertainty. Moreover, the fraction of contamination is very high in all samples. This is not surprising though, because the number density of PEGs is expected to be low at such high redshift so that a small absolute number of contamination can occupy a relatively large fraction of the sample.

An additional condition must be applied to remove contamination from our pVJL sample. Although observations at longer wavelength, such as MIPS and Herschel data, can readily help identify the contamination of dusty galaxies, we attempt to restrict our selection criterion to using only V-, J- and L-band information so that the method can be easily applied to large surveys where deep observations at longer

wavelengths may not be available. What is more important is that using only the three-band information enables a relatively easy multi-wavelength Monte-Carlo simulation, which is essential to understand the systematics and bias of our selections. In this study, longer wavelength observations are only used to help calibrate and optimize our selection method.

A possible way to clean the sample is to examine the rest-frame optical size of galaxies. Cassata et al. (2011) show that the fraction of compact galaxies in PEG samples increases with redshift. At $z \sim 2$, about 70% of PEGs are compact. Extrapolating their relation to $z \sim 3$, we expect more than 90% of PEGs to have small size. If this expectation is true, galaxies with no 24 μm detection is low should tend to have small radius, and vice versa.

Figure 5.9 confirms our speculation by showing the relation between the significance of 24 μm flux and J-band Kron radius. In the $S/N > 5$ sample, 85% of galaxies whose MIPS 24 μm fluxes are within 3σ deviation of a pure passive stellar emission have J-band Kron radius less than $1''$. On the other side, 84% of galaxies with significant 24 μm fluxes, an indicator of dust emission, are larger than $1''$ in terms of Kron radius. This interesting finding of the relation between MIPS 24 μm fluxes and galaxy sizes is a reflection of the size–star formation relation of massive galaxies at $z \gtrsim 2$ (e.g., Zirm et al., 2007; Toft et al., 2009) and suggests that using size can effectively distinguish real PEGs from dusty SFGs. Moreover, in the small size ($r_{\text{Kron}} < 1''$) sample with $S/N > 5$, only 2 out of 14 galaxies have significant 24 μm fluxes. Therefore, based on the high efficiency and low contamination of using small size to select PEGs, we add the condition $r_{\text{Kron},J} < 1''$ to our pVJL criterion (Eq. 5.2). After this extra condition being applied, our samples now contain 14, 10 and 2 galaxies with S/N cuts of 5, 10 and 20. And the contamination level is reduced to 14%, 10% and 0% in the three samples.

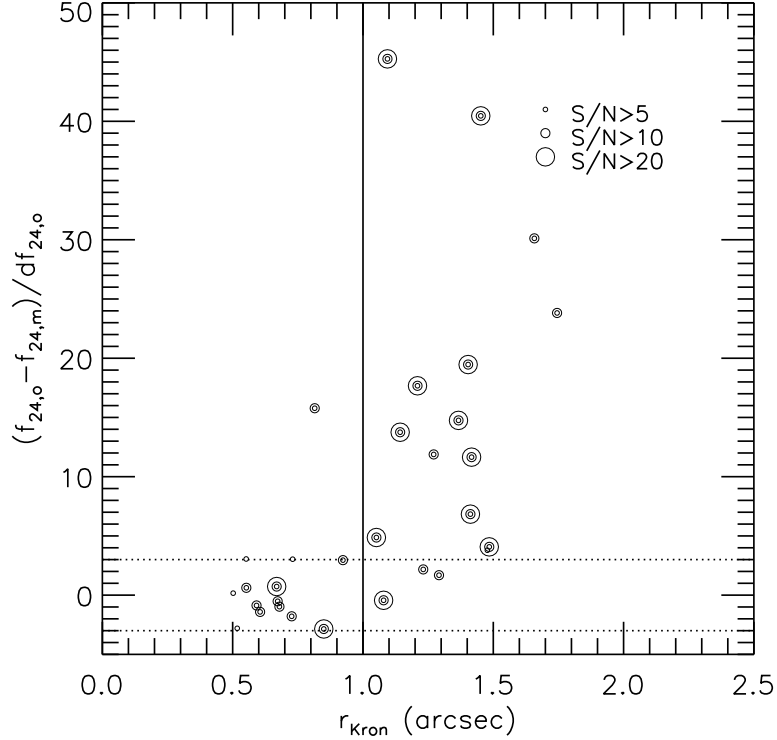


Figure 5.9 Deviation of MIPS 24 μm fluxes of pVJLs from the prediction of pure stellar emission as a function of Kron radius. Galaxies with different S/N cuts are shown with different point sizes, as labels show. The dotted lines show $\pm 3\sigma$ deviation from the prediction, and the solid line shows the extra criterion ($r_{\text{Kron},J} < 1''$) that we add to our pVJL selection method.

Table 5.1 Passively Evolving Candidates at $z > 3$

ID	RA J2000	DEC J2000	photo-z	E(B-V)	Z	Age Gyr	τ Gyr	M_{star} $\text{Log}(M^*/M_{\odot})$	SFR M_{\odot}/yr
2318	53.07387680	-27.72217050	3.43	0.00	0.004	1.00	0.1	10.54	0.04
2414	52.99881320	-27.72097790	3.08	0.00	0.020	0.80	0.1	10.56	0.27
2454	53.06628720	-27.72043590	3.35	0.00	0.020	0.80	0.1	10.28	0.14
3222	53.10302370	-27.71234920	4.52	0.65	0.004	0.02	99.99	10.55	1.87E+03
5218	53.17444360	-27.69261340	4.56	0.05	0.050	0.50	0.1	10.46	4.33
8124 ^a	53.14818030	-27.71810980	4.81	0.00	0.050	0.50	0.1	10.21	2.44

^aThe K-band image of this source is very faint so that TFIT likely has difficulty to measure reliable photometry for it. TFIT measures a negative flux with a large error bar. We carried out an aperture photometry with the aperture size of $1.0''$ and got a flux of $0.23 \pm 0.11 \mu\text{Jy}$. This is broadly consistent with the prediction of the best-fit SED (solid line in Fig. 5.11). We note that we did not include the K-band in the SED-fitting because of the negative TFIT flux. We also note that the marginal (1.3 sigma) detection of the source in K-band is somehow due to the lower sensitivity of the K-band image in this tile. The 5-sigma limiting magnitude of this tile is 24.28 AB, while its 1-sigma limiting magnitude is 26.03 AB. Our aperture photometry ($0.23 \mu\text{Jy}$, namely 25.50 AB) is broadly consistent with an about 2-sigma detection.

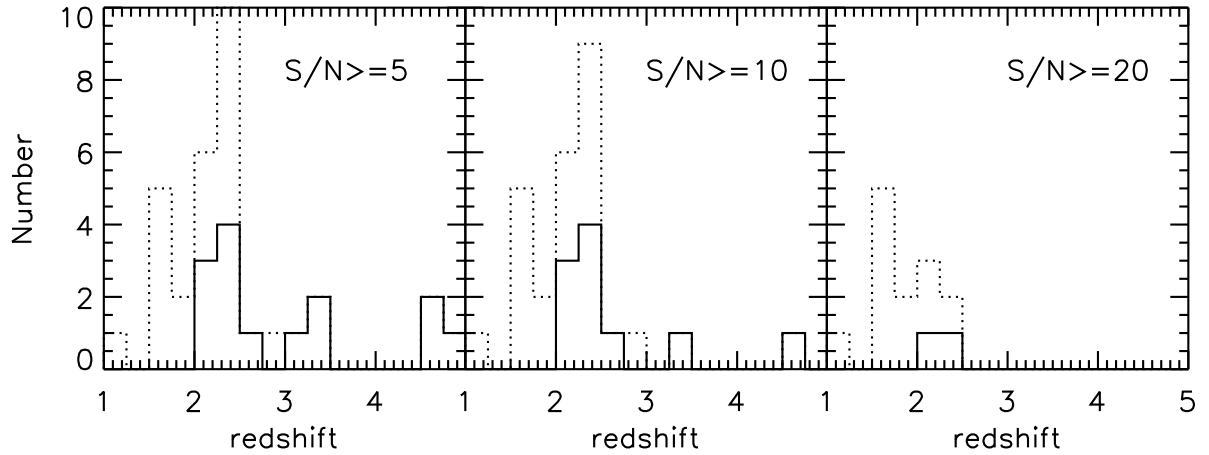


Figure 5.10 Redshift distributions of pVJL selected galaxies. Different panels show cases with different S/N cuts, as labels show. Dotted lines show the distributions of galaxies selected only through Eq. 5.2, while solid lines show the distribution of galaxies that satisfy both Eq. 5.2 and the size criterion ($r_{\text{Kron}} < 1''$).

The redshift distributions of galaxies in our final pVJL samples (solid lines) are shown in Figure 5.10. Comparison between samples with (solid lines) or without (dotted lines) the size criterion shows the efficiency of the additional size criterion on removing contamination from low redshift ($z < 2.0$). The redshift distribution of our final sample peaks around $z \sim 2.5$ regardless the applied S/N cut. This distribution is a little lower than our expectation ($z \sim 3.0$) but consistent with our previous analysis based on the color of stellar population synthetic models. As shown by the dotted line with squares in the left panel of Figure 5.1, the track of SSP galaxy with $t = 1.0$ Gyr begins to enter our pVJL selection window at $z \sim 2$. Although the track stays in our pVJL selection window at higher redshift, the number density of PEGs is expected to decline with redshift. As a result, it is not surprising that the redshift distribution peaks at a point where the number density of galaxies is still high and the photometric uncertainty cannot easily scatter galaxies out of the selection window.

5.4.2 Passively Evolving Galaxies at $z>3$?

Recently, PEGs are occasionally found at $z>3$ (e.g., Mancini et al., 2009; Marchesini et al., 2010). These galaxies contain important information of when and how galaxies stopped their star formation activity. Their number density, or even their existence itself, can set strong constraints on current theories of galaxy formation and evolution. Six galaxies in our $S/N>5$ sample are at $z>3$. Although they do not enter our $S/N>20$ sample because of the low S/N of their rest-frame optical photometry, it is still intriguing to study their physical properties and examine if they are real PEGs at $z>3$.

Table 5.1 summarizes the best-fit parameters of the six high- z PEG candidates. The ages of five galaxies are significantly (at least 5 times) older than their characteristic star-formation time scale (τ), suggesting that they have already passed their star-formation peaks and become quiescent. Only one galaxy (ID 3222) is fitted as a dusty star-burst galaxy with $SFR > 1000 M_{\odot}/yr$. Although the best-fit parameters support the passive natures of the majority of our candidates, the SED-fitting procedure, which only uses the rest-frame UV to NIR data, suffers from the age–dust degeneracy and is hence not capable of perfectly distinguishing dusty star-forming and old populations. If we assume that these galaxies are forming stars and that their red rest-frame UV colors are caused by dust obscuration rather than old stellar populations, their $E(B-V)$ s and obscuration corrected SFRs measured from their rest-frame UV continuum slopes would be much higher than the SED-fitting derived values, with all $E(B-V)s > 0.3$ and SFR on average a few hundred times higher than the best SED-fitting values. Such high $E(B-V)$ s and SFRs together suggest that these galaxies should have significant dust emission exists in longer wavelength (e.g., rest-frame IR and sub-mm), where dust emission dominates the radiative spectrum, if their dusty star-forming nature is true.

Figure 5.11 shows the best-fit stellar population SEDs (solid line) of the six galaxies. For comparison, we also plot templates of the SFGs (dotted line) retrieved from the templates of Chary & Elbaz (2001). The star-forming templates are not chosen by fitting to rest-frame UV and optical data to models. Instead, we calculate the obscured SFR (total SFR minus unobscured SFR) of these galaxies from their rest-frame UV continuum, assuming they are dusty SFGs. Then, for each galaxy, we convert the obscured SFR to the bolometric IR luminosity and choose the template whose bolometric IR luminosity best matches the luminosity of the galaxy. It is interesting to find from the plot that although we do not fit the templates to the rest-frame UV and optical data, the templates match the data fairly well (except Galaxy 3222). The best chosen template gives us an estimate of the fluxes from dust emission, which, if existing, can be observed by our current MIPS 24 μm , GOODS-*Herschel* (PI Elbaz) 100 and 160 μm , and AzTEC 1.1 mm observations (Scott et al., 2010).

At such high redshift, dust emission within the MIPS 24 μm bandpass is still comparable to the stellar emission, as the stellar emission peak is just a little blueward of the MIPS bandpass. As seen from the plot, in four out of six galaxies, the MIPS 24 μm fluxes cannot help distinguish old and dusty populations at all. In two galaxies (2414 and 2454), the observed 24 μm fluxes lean toward the prediction of dust emission, however, the prediction of pure stellar emission is still within the 3σ level of the observation and cannot be fully ruled out.

In principle, GOODS-*Herschel* and AzTEC data can be effective at distinguishing PEGs from dusty SFGs by sampling the blackbody radiation of cold dust. Unfortunately, the detection thresholds of these surveys are so high that the fluxes of dusty templates in Figure 5.11 are almost all under their 1σ detection limits. Indeed, flux measurements of individual galaxies in the AzTEC image suffer from a very low S/N, $\lesssim 1\sigma$, being comparable to the noise level. Due to the high detection thresholds, we cannot conclude that if the non-detections in the AzTEC image provide a tight

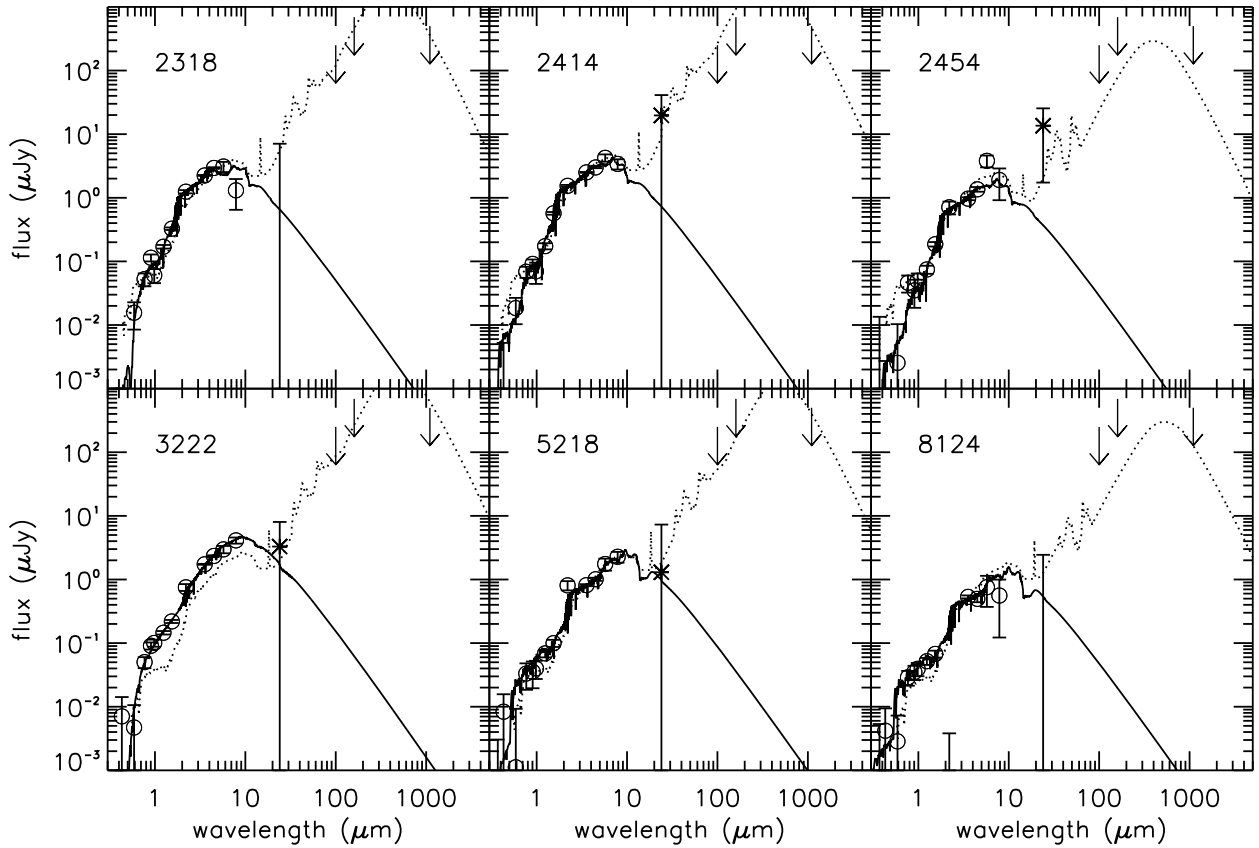


Figure 5.11 Observed and best-fit SEDs for six galaxies at $z > 3$ in our $S/N > 5$ pVJL sample. Open circles with error bars are fluxes and their uncertainties that are used for SED-fitting. Stars with error bars show the MIPS $24 \mu\text{m}$ fluxes and 3σ uncertainties. Arrows show the 1σ detection limits of GOODS-*Herschel* (PI Elbaz) 100 and $160 \mu\text{m}$ and AzTEC 1.1 mm images (Scott et al., 2010). MIPS, *Herschel* and AzTEC points are not used for SED-fitting. The best-fit models are shown by solid lines. Dotted lines are reference model of SFGs of Chary & Elbaz (2001).

constraint on the nature of our candidates. However, as shown in the figure, the predicted dust emission from three or four dusty star-forming templates is touching the 1σ detection limit of these long-wavelength bands. We expect an at least a 2σ detection in the stacked images if *all* our galaxies are dusty SFGs. In the stacked AzTEC image, we detect a signal with $S/N=1.1$ in the central pixels (with size of $3''$), still comparable to noise. Such low S/N in the stacked AzTEC image suggests that at least some of our candidates are not dusty SFGs but real PEGs at $z>3$. It also rule out our suspicion that Galaxy 3233 has SFR over $1000 M_{\odot}/\text{yr}$, as its best SED-fitting shows in Table 5.1. Such huge SFR should have been easily detected in the AzTEC image.

We also use the Chandra deep 4Ms X-ray image of CDFS to examine if AGN host galaxies contaminate our PEG candidates at $z>3$. None of our candidates is individually detected in the 4Ms Chandra catalog of Xue et al. (2011). The stacked images in both soft and hard bands show signals comparable to noises, with a S/N of 1.75 and 1.17 respectively. We conclude that our PEG candidates at $z>3$ are not contaminated by AGN host galaxies.

We notice that the two galaxies with the highest redshifts (5218 and 8124) have the largest SFRs. Their best-fit SFRs are comparable to that of our Milky Way, while their stellar masses are lower than that of Milky Way. The SSFR of these galaxies are higher than $10^{-11}/\text{yr}$, the usual value used to distinguish SFGs and PEGs. We suspect that it is possible that although these galaxies have passed their peaks of star-formation, their star formation activity has not yet been fully ceased. They could be in a transition stage from star-forming to fully quiescent, since their rest-frame UV and optical light is already dominated by old stellar populations. At lower redshift ($z<3.5$), galaxies all have SSFR less than $10^{-11}/\text{yr}$, very well fit to the usual criterion of PEGs. We speculate that galaxies in the universe begin to transit from star-forming to quiescent stages at $z\sim 4.5$ and become fully ceased PEGs at $z\sim 3.5$. However, the

fact of increasing SFR with redshift could also be due to a selection effect of a flux-limited sample, because SFR increases with luminosity so that galaxies with higher SFRs can be observed out to higher redshift. Deep and large NIR band survey, such as CANDELS, is required to observe galaxies down to a fainter luminosity (hence lower SFR) level to provide a more accurate SED-fitting results to reveal the secret of when galaxies began to cease their star-formation.

5.4.3 The Evolution of Integrated Stellar Mass Density of Passively-Evolving Galaxies

The integrated stellar mass density (ISMD) of PEGs is a key parameter for understanding the formation and evolution of the galaxies. It quantifies how many stars have been locked in passive systems at a given cosmic epoch. Currently, most studies on the evolution of stellar mass function and stellar mass density focus on all (both star-forming and passively-evolving) massive galaxies at $z > 2$ (e.g., Fontana et al., 2006; Marchesini et al., 2009, 2010). Only few works (Mancini et al., 2009; Ilbert et al., 2010; Brammer et al., 2011; Cassata et al., 2011) have been devoted to the study of the evolution of PEGs (or quiescent galaxies) only, partly due to the difficulty of identifying these galaxies at high redshift. However, the evolution of the passive population only is as important as that of all populations together, because it records when and how stars migrate from the star-forming population to passive population, which are critical for us to understand the physics that governs the ongoing and ceasing of star formation activity in the universe.

In this section, we estimate the ISMD at $2 < z < 3$ using our clean pVJL samples. The precise measurement of the function should be obtained by integrating the stellar mass function, either the analytic Schechter form or the stepwise one. However, our small number samples (only 14 pVJLs even in the $S/N > 5$ sample) limit our ability to obtain an accurate measurement of the stellar mass function at $2 < z < 3$. We leave

such an accurate measurement to an forthcoming paper (Guo et al. in prep.) that employs the advantage of the large survey area of the upcoming CANDELS. In this thesis, instead, we simply carry out a shortcut measurement of the ISMD to its first order accuracy.

We calculate the ISMD as follow:

$$\rho^* = \frac{\int \int MN_{obs}(M, z)C(M, z)dzdM}{\int \frac{dV}{dz}dz}, \quad (5.4)$$

where M is the stellar mass, $N_{obs}(M, z)$ the observed number of galaxies with stellar mass M and redshift z , $\frac{dV}{dz}$ the differential cosmic volume at z . The lower and upper limit of the integral over z are 2 and 3, while the lower limit of the integral over M is $10^{10}M_{\odot}$. $C(M, z)$ is a factor to correct the incompleteness caused by observation and selection for galaxies with M and z . As referred from Figure 5.10, the redshift distributions of our pVJL samples are very well peaked around $z \sim 2.5$ and have a narrow scatter. Therefore, it is safe to assume that $C(M, z)$ is primarily dominated by M and only has a weak relation on z in our sample. We choose $z=2.5$ for calculation $C(M, z)$ for all pVJLs. The uncertainty induced by such an assumption is less than that induced by the measurement of stellar mass of galaxies. Under this assumption, we place a SSP model with age of 1 Gyr and stellar mass M at $z=2.5$ and perturb its V-, J- and L-band photometry using Gaussian random deviation with the variance set equal to a photometric error that is randomly drawn from the distribution of observed photometric uncertainties for a given magnitude of a given band in our multi-wavelength catalog. The perturbation is repeated 1000 times and for each time we justify whether the perturbed galaxy can be selected as a pVJL according to our criterion, Equation 5.2, and different S/N cuts. The factor $C(M, z)$ is defined the reciprocal of the rate of successful selections.

The ISMD of our pVJLs at $2 < z < 3$ is shown in Figure 5.12, together with measurements for lower redshift from other studies (Bell et al., 2003; Borch et al., 2006).

We measure the ISMD for each of our three samples with different S/N cut and plot the mean and standard deviation of the three samples. As shown by the filled point with error bars at $z\sim 2.5$, the 1σ deviation of the three samples is about 0.2 dex, comparable to the typical stellar mass uncertainty obtained through SED-fitting at such redshift. The small deviation also demonstrates that the incompleteness is fairly accurately estimated for our samples so that the ISMDs of samples with different mass limits that are induced by different S/N cuts are in very good agreement.

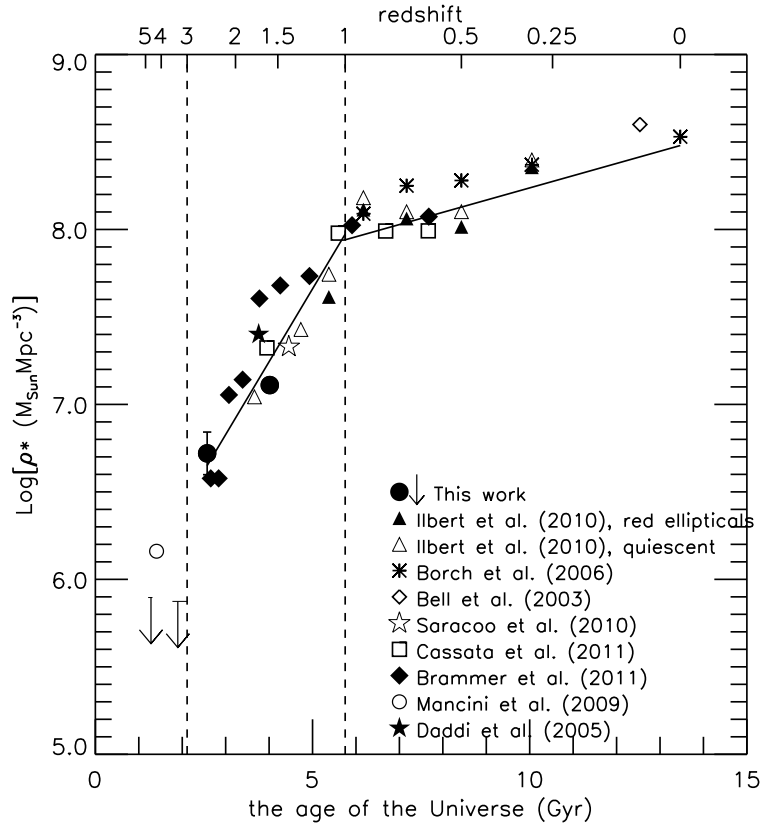


Figure 5.12 Evolution of ISMD for PEGs with $M_{\text{star}} > 10^{10}M_{\odot}$. Results of different works are shown by different symbols. The evolution can be schematically divided into three stages, as indicated by the two vertical dashed lines. The two solid lines are the best fit to the evolution of ISMDs of $1 < z < 3$ and $z < 1$.

To further test the reliability of our measurement of the ISMD, we apply our method to galaxies that are selected from GOODS-S using the passively-evolving criterion of the BzK method (pBzK, Daddi et al., 2004a). The redshift distribution of pBzKs peaks at $z\sim 1.5$, where a number of measurements of the ISMD (Ilbert et al.,

2010; Saracco et al., 2010; Brammer et al., 2011; Cassata et al., 2011) can be used as references to test the accuracy of our measurement. For pBzKs, we choose a SSP model with age of 2 Gyr at $z=1.5$, perturb its B-, z- and K-band photometry according to photometric uncertainties, and calculate the ISMD with the same formula as we use for pVJLs. We also calculate the ISMD using three pBzK samples with different S/N thresholds at z- and K-band ($S/N > 5, 10, \text{ and } 20$). Thanks to the relatively large number of galaxies in each sample, the ISMD of different pBzK samples agree with each other better than that of different pVJL samples, with the standard deviation less than 0.1 dex.

Figure 5.12 illustrates the evolution of the ISMD of PEGs from $z > 3$ to $z = 0$. We compile measurements of several previous studies and compare them with our results. In particular, we take the best-fit Schechter parameters by Bell et al. (2003); Borch et al. (2006); Ilbert et al. (2010) and integrate their Schechter functions down to mass limit $M_* > 10^{10} M_\odot$. We also take the ISMD listed in the tables of Saracco et al. (2010) and Brammer et al. (2011). The ISMD of PEGs at $1.3 < z < 2.0$ in HUDF measured by Daddi et al. (2005) and the measurement from one of our companion paper (Cassata et al., 2011) are also plotted. All adopted measurements are scaled to match our Salpeter IMF with the following relations: $\log(M_{\text{Salpeter}}) = \log(M_{\text{Chabrier}}) + 0.24$ (Salimbeni et al., 2009b) and $\log(M_{\text{Salpeter}}) = \log(M_{\text{Kroupa}}) + 0.20$ (Marchesini et al., 2009). Salimbeni et al. (2009b) also compared stellar masses measured with different stellar synthesis libraries, i.e., BC03, CB09 and Maraston (2005, M05) and found the following relations: $\log(M_{\text{CB09}}) = \log(M_{\text{M05}})$ at all redshift; $\log(M_{\text{CB09}}) = \log(M_{\text{BC03}}) + 0.20$ at $z < 1.5$ and $\log(M_{\text{CB09}}) = \log(M_{\text{BC03}}) + 0.10$ at $1.5 < z < 4$. We use these relations to scale stellar masses in other works to CB09.

Our ISMD at $z \sim 1.5$ (pBzK) agrees well with that of quiescent galaxies of Ilbert et al. (2010), with difference less than 0.1 dex. However, our ISMD deviates from other studies at $z \sim 1.5$ by a few tenth dex. Cassata et al. (2011) constructed a fairly

complete and clean sample by using not only SSFR but also morphology and MIPS 24 μm flux. Their ISMD should suffer the least from incompleteness and contamination. However, their field, namely the ERS field, is occupied by an over-dense large-scale structure at $z\sim 1.6$ (Salimbeni et al., 2009a), which might boost the ISMD upward. Daddi et al. (2005) used only a small sample (6 galaxies) over the 12.2 arcmin² HUDF area so that their result may suffer from both small number statistics and large cosmic variance. The scheme of separating quiescent and dusty star-forming galaxies by two rest-frame colors of Brammer et al. (2011) may induce into their quiescent sample a fraction of dusty contamination, which could partly explain the largest ISMD at $z\sim 1.5$ measured by them. Despite the discrepancy, ISMDs at $z\sim 1.5$ measured by different authors scatter around the best fit of the evolution of ISMD of PEGs at $1 < z < 3$ (solid line in the plot) within ~ 0.3 dex, which is just slightly larger than the typical uncertainty of deriving stellar mass through SED-fitting at this redshift (~ 0.2 dex). This suggests that the uncertainty of stellar mass is the dominant source of ISMD uncertainty, and that our simplified incompleteness correction is accurate to the first order.

Only our work and Brammer et al. (2011) measure the ISMD of PEGs at $z\sim 2.5$. The ISMD of Brammer et al. (2011) is 0.2 dex lower than that of ours, again within the typical uncertainty of stellar mass. Besides the stellar mass uncertainty, the discrepancy could also be due to the fact that Brammer et al. (2011) only integrate their stellar mass function at $z > 2.0$ down to $M_* > 10^{11} M_\odot$, whereas the stellar mass function of PEGs is dominated by galaxies around M^* , typically $M_* = 10^{10.6} M_\odot$ (Ilbert et al., 2010; Peng et al., 2010).

We even extend our measurement to $z > 3$, where we only have a few PEG candidates though. We measure the ISMD for three candidates at $3 < z < 3.5$ using a SSP model of 1 Gyr at $z=3.3$ and the ISMD for the other three candidates at $z > 4$ using a SSP model of 0.5 Gyr at $z=4.5$. Since there might be contamination of dusty SFGs

among our candidates (as discussed in §5.4.2), the ISMDs at $z>3$ can be only treated as an upper limit. The upper limit of ISMD at $z>3$ was also measured by Mancini et al. (2009), who found 21 $z>3.5$ quiescent candidates which are selected at IRAC 4.5 μm channel but have no MIPS 24 μm detection in GOODS-N. As argued by them as well as indicated by Figure 5.11, the lack of 24 μm emission is a necessary but insufficient condition for determining a galaxy to be quiescent. Our upper limit of ISDM at $z>3$ is about 0.3 dex lower than that of theirs (also shown in Figure 5.12), but still within the error bars of their upper limit. In this sense, the two measurements are not inconsistent.

5.4.4 Stellar Mass Locked in Passively-Evolving Galaxies

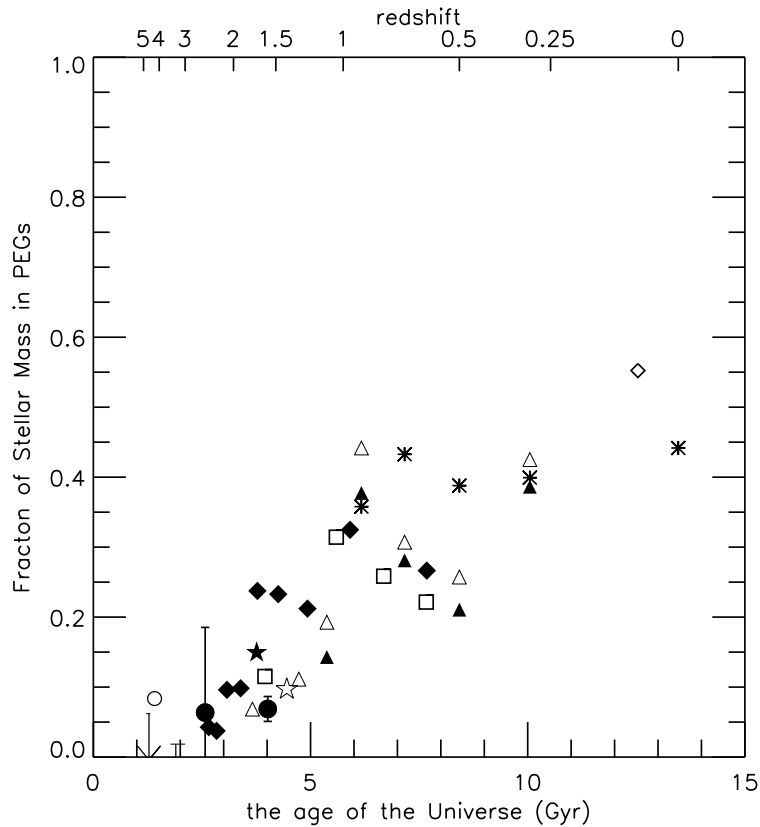


Figure 5.13 Fraction of stellar mass locked in PEGs as a function of redshift. Results of different works are shown by different symbols. See labels in Figure 5.12 for the meanings of symbols.

The evolution of ISMD of PEGs can be easily converted into the evolution of fraction of stellar mass in PEGs, if an underlying global stellar mass density (GSMD) is measured for all types of galaxies. We obtain such a measurement by fitting a linear relation to the evolution of GSMD ($\log(\text{GSMD})$ vs. redshift) of Figure 12 of Marchesini et al. (2009), which compiles measurements of GSMD from several previous studies. We then divide the ISMD of PEGs by the GSMD at a given redshift to obtain the fraction of stellar mass in PEGs.

The evolution of the mass fraction is shown in Figure 5.13. At $z > 3$, the mass fraction of PEGs is less than 5%. This fraction then increase from 5% to about 40% from $z=3$ to $z=1$. However, there is large discrepancy among measurements of the fraction at $z \sim 2$, from 5% of our study and Ilbert et al. (2010) to 25% of Brammer et al. (2011). The reason of such large discrepancy, as discussed above in the measurement of ISMD, is complicated, possibly due to sample selection, stellar mass density measurement method, and/or cosmic variance. A more accurate measure is needed in future to constrain this fraction and hence the mechanisms that are responsible for quenching the star formation activity during the peak of the cosmic SFRD. It is also should be noted that there is about 0.2 dex deviation for the GSMD at $z \sim 2$ measured by different authors (see Figure 12 of Marchesini et al. (2009)). Therefore the accurate measurement of stellar mass fraction in PEGs requires an improvement on measuring the stellar mass densities of both PEGs and all types of galaxies. Our work does not provide measurement on the mass fraction at $z < 1$, but we still plot the measurements of other authors for readers to obtain a sight of the evolution trend in lower redshift.

5.4.5 Discussion

The evolution of ISMD of PEGs can be schematically divided into three stages, as indicated by the vertical dashed lines in Figure 5.13. The physical mechanisms that govern the formation and evolution of PEGs in each stage may be different.

The first stage ($z > 3$) could be called as the formation (or present) stage. The existence of PEGs in the stage is still controversial (Mancini et al., 2009; Marchesini et al., 2010). In our study, we find six candidates at $z > 3$. Individual and stack analysis of the sub-mm AzTEC images show that at least some of them could be really passive. We cannot, however, draw a firm conclusion on which one is real passive. If we treat the ISMD that we measured at $z > 3$ as an upper limit, the ISMD grows by a factor of 10, or even larger in 1 Gyr from $z \sim 4$ to $z \sim 2.5$. The existence of PEGs of age of 1 Gyr at $z \sim 3.5$ suggests that these galaxies begin to form their stars at $z \gtrsim 5$ or 6. Due to the small sample and limited information, we cannot discuss the formation mechanism of these galaxies. Future studies in the following two aspects would shed a light on this question: (1) confirming or excluding the passive properties of our candidates by using other facilities and (2) exploiting larger and deeper NIR survey (e.g., CANDELS) to construct a large sample with a good statistics.

The second stage ($1 < z < 3$) is the rapid growth stage, during which the ISMD of PEGs grows by a factor of 10 in 3.5 Gyr. Stars are extensively formed in or migrated into passive systems in this period. This stage is coincident with the broad peak of the cosmic SFRD (e.g., Hopkins, 2004; Hopkins & Beacom, 2006; Pérez-González et al., 2008; Chary & Pope, 2010), suggesting that the formation of stars and the migration of stars from star-forming systems to passive systems are happening simultaneously during this epoch. Cassata et al. (2011) studied the size distribution of PEGs during this stage and found $\sim 80\%$ of PEGs at $z \sim 1.5$ are compact. The mechanisms that are responsible for the rapid mass growth of PEGs (e.g., gas-rich major merger, collapse

of unstable disks and monolithic collapse) also tend to produce passive remnants that are compact and small with respect to local early-type galaxies.

The third stage ($z < 1$) is the slow growth stage, during which the ISMD only increases by a factor of ~ 3 in ~ 7 Gyr. This suggests that the majority of PEGs has already been formed before this stage. This stage happens when the cosmic SFRD begin to rapidly decline from its peak (e.g., Hopkins, 2004; Hopkins & Beacom, 2006; Pérez-González et al., 2008; Chary & Pope, 2010), indicating that newly formed stars may not be enough for explaining the steady growth of the passive systems from $z=1$ to $z=0$. It requires stars that already formed in other systems to migrate into the passive systems. A joint analysis of stellar mass density, number density and size distribution of PEGs in this stage by Cassata et al. (2011) found that the number density increases by a factor of 1.5 from $z=1$ to $z=0.5$, while the ISMD keeps almost constant at the same time. And the average size of PEGs increases by a factor of about 2.5 in the same epoch. These findings imply that the mechanisms that increase PEGs' sizes during this redshift range would not significantly increase their stellar masses, most likely being minor merges and slow accretion (Hopkins et al., 2008; van Dokkum et al., 2010). Also, the newly formed PEGs that increase the number density at this time would have small stellar masses and larger sizes than those formed at $z < 1$, indicating a different formation mechanism.

5.5 Summary and Conclusions

In this chapter, we introduce a new method of selecting both SFGs and PEGs at $2.3 \lesssim z \lesssim 3.5$ using rest-frame UV-optical (V-J vs. J-L) colors. We apply our VJL criteria to select galaxies in the WFC3 ERS field and study the physical properties of the selected galaxies. We also discuss the implications of our selected galaxies on galaxy formation and evolution, especially the contribution of dusty SFGs to the

cosmic SFRD at $z \sim 3$ and the evolution of ISMD of PEGs. The chapter is summarized below.

Our VJL criteria are thoroughly tested with theoretical stellar population synthesis models and real galaxies with spectroscopic redshifts. The tests show that our criteria for SFGs (Equation 5.1, sVJL) is able to select galaxies with constant or exponentially declining SFH independently of their dust reddening. Our criteria for PEGs (Equation 5.2, pVJL) can select galaxies with properties similar to single stellar population models around $z \sim 2.5$ and above. The tests also show that, however, (1) the main source of contamination in our sVJL sample is the SFGs at $z \sim 2$ and $z \gtrsim 3.5$ and (2) contamination in our pVJL sample is mainly from dusty SFGs at $z \sim 2$.

We apply our sVJL criterion to the WFC3 ERS field to select 354 and 146 galaxies with J- and L-band S/N cuts greater than 10 and 20. The redshift distribution of our sVJL sample peaks at $z \sim 2.7$. However, it also has a secondary peak around $z \sim 1.8$. This secondary peak is induced by the color uncertainty, as the power of the secondary peak decreases with the increase of the S/N threshold.

We compare our sVJLs with Lyman Break Galaxies at $z \sim 3$ (U-band dropouts), assuming that the slight difference in the peak redshifts ($\langle z \rangle \sim 2.7$ for sVJLs and $\langle z \rangle \sim 3.0$ for U-band dropouts) would not result in any significant difference of properties of the two samples. In the ERS field, 39% of U-band dropouts are outside our sVJL selection window. Among the outsiders, 63% of them have redshift greater than 3.2, where our sVJL selection ability drops sharply.

Unlike the Lyman Break Technique, our sVJL method can select galaxies whose (J-L) color redder than 2.0, which implies high dust extinction in these galaxies. The measurement of $E(B-V)$ s from the rest-frame UV continuum shows that U-band dropouts all have $E(B-V) < 0.4$, while the distribution of $E(B-V)$ s of sVJLs extended to $E(B-V) \sim 1.0$.

We evaluate the fraction of contamination from old galaxies in our sample of dusty SFGs ($E(B-V) > 0.3$) by comparing their observed 24 μm fluxes to that predicted by a single stellar population model. We find that 18% of our galaxies have 24 μm fluxes that match the prediction of pure stellar emission. The low fraction of contamination indicates that our sVJL method is effective at selecting dusty galaxies around $z \sim 3$.

The dusty ($E(B-V) > 0.4$) galaxies selected by sVJLs reside in the massive end ($M_{\text{star}} > 10^{10} M_{\odot}$) of the mass distribution of sVJLs. Although they only counts for $\sim 20\%$ of the number density in the mass bin $10^{10} M_{\odot} < M_{\text{star}} < 10^{11} M_{\odot}$, they contribute about half of the star formation in this mass range. In the low-mass end $10^9 M_{\odot} < M_{\text{star}} < 10^{10} M_{\odot}$, sVJLs and LBGs have no obvious difference on their color, $E(B-V)$, and SFR.

We also apply our criteria to the WFC3 ERS field to select PEGs at $z \sim 3$. Through a similar comparison between the observed and predicted MIPS 24 μm fluxes, however, we find that our pVJL samples are heavily contaminated by dusty SFGs. An additional condition is needed to clean the samples. Inspired by the fact that the majority of PEGs at $z > 2$ is compact, we require galaxies to have a small radius (J-band Kron radius less than $1.0''$) to enter our pVJL sample. This extra criterion is proved to be able to effectively separate passive and dusty galaxies in our samples.

The redshift distribution of our clean pVJL samples peaks at $z \sim 2.5$ and extends to $z \sim 3$, and even to $z > 4$ when low S/N cuts are employed. We carry out case studies to examine the physical properties of our PEG candidates at $z > 3$. Most of these galaxies have very low SFRs derived through SED-fitting but high SFRs derived from their rest-frame UV continuum. We try to use observations at longer wavelengths (MIPS, Herschel and AzTEC) to break the age–dust degeneracy and understand the nature of these galaxies. Unfortunately, the detection limits of these long-wavelength observations are too high to help achieve a firm conclusion. However, we find no significant detection even in the stacked image of AzTEC, suggesting that

some our candidates are real PEGs at $z > 3$. We speculate that galaxies with very low SFR, possibly a transition stage from star-forming to passive, begin to exist at $z > 4$ and PEGs begin to exist at $z > 3$.

We estimate the ISMD of PEGs at $z \sim 2.5$ by using our clean pVJL sample. We evaluate the incompleteness of observation and selection in a simplified way, which is proved to be accurate to the first order by comparing our results with other studies as well as by comparing results of samples with different S/N cuts. We also extend our measurement to $z > 3$ and obtain a constraint on the ISMD at $z > 3$. Combining this with low redshift observations from previous studies, we find that the evolution of the ISMD can be divided into three stages: (1) formation stage ($z > 3$), when PEGs begin to form and their ISMD grows by at least a factor of 10 in 1 Gyr; (2) rapid growth stage ($1 < z < 3$), when the ISMD of PEGs grows by another factor of 10 in 3.5 Gyr; and (3) slow growth stage ($z < 1$), when the ISMD of PEGs grows by a factor of 3 in 7 Gyr. We discuss the possible mechanisms that drive the growth in each stage.

We conclude that our new color selection criteria are effective at selecting SFGs independent of dust reddening as well as PEGs at $z \sim 3$. This method is less model-dependent and easier to reproduce than methods based on SED-fitting so that it can be quickly applied to upcoming large optical and NIR surveys, such as CANDELS, where large samples obtained through wide survey areas would set stronger constraints and shed new light on our understanding of galaxy formation and evolution.

CHAPTER 6

SUMMARY AND FUTURE DEVELOPMENT

6.1 Summary

In this thesis, we study two important features of galaxies at $z \sim 2$, the clumpy structures of star-forming galaxies and color gradient of passively evolving galaxies, to answer the core question of galaxy formation and evolution: **how today’s Hubble Sequence has been formed**. We further design a set of color selection criteria to search for dusty star-forming galaxies and passively evolving galaxies at $z \sim 3$ to explore the question: **when today’s Hubble Sequence has begun to appear**.

First, we study the properties of kiloparsec-scale clumps in star-forming galaxies (SFGs) at $z \sim 2$ through multi-wavelength broad band photometry. A sample of 40 clumps is identified from HST/ACS z -band images through auto-detection and visual inspection from 10 galaxies with $1.5 < z < 2.5$ in HUDF, where deep and high-resolution HST/WFC3 and ACS images enable us to resolve structures of $z \sim 2$ galaxies down to kiloparsec (kpc) scale in the rest-frame UV and optical bands. Although the SFR–stellar mass relation of galaxies is dominated by the diffuse components, clumps emerge as regions with enhanced specific star formation rates (SSFRs), contributing individually $\sim 10\%$ and together $\sim 50\%$ of the star formation rate (SFR) of the host galaxies. However, the contributions of clumps to the rest-frame UV/optical luminosity and stellar mass are smaller, typically a few percent individually and $\sim 20\%$ together. On average, clumps are younger by 0.2 dex and denser by a factor of 8 than diffuse components. Clump properties have obvious radial variations in the sense that central clumps are redder, older, more extinguished, denser, and less active

on forming stars than outskirts clumps. Our results are broadly consistent with a widely held view that clumps are formed through gravitational instability in gas-rich turbulent disks and would eventually migrate toward galactic centers and coalesce into bulges. Roughly 40% of the galaxies in our sample contain a massive clump that could be identified as a proto-bulge, which seems qualitatively consistent with such a bulge-formation scenario.

Second, we report the detection of color gradients in six massive (stellar mass ($M_{\text{star}} > 10^{10} M_{\odot}$) passively-evolving galaxies (PEGs) with specific star formation rate (SSFR) $< 10^{-11} \text{yr}^{-1}$ at redshift $1.3 < z < 2.5$ identified in HUDF, using ultra-deep *HST* ACS and WFC3/IR images. We find that the inner regions of these galaxies have redder rest-frame UV-optical colors (U-V, U-B and B-V) than the outer parts. The slopes of the color gradient mildly depend on the overall dust obscuration ($E(B-V)$) and rest-frame (U-V) color, with more obscured or redder galaxies having steeper color gradients. The $z \sim 2$ color gradients are also steeper than those of local early-type ones. The origin of the color gradient is still unknown. The gradient of a single parameter (age, extinction or metallicity) cannot fully explain the observed color gradients. We find that the dust gradient might partly contributes to the observed color gradients, but the magnitude depends on the assumed extinction law. Due to the age-metallicity degeneracy, the derived age gradient depends on the assumptions for the metallicity gradient. Nonetheless, we find that the evolution of the mass-size relationship from $z \sim 2$ to the present cannot be driven by in-situ extended star formation, which implies that accretion or merger is mostly responsible for the growth of their stellar mass and size. The lack of a correlation between the strength of the color gradient and the stellar mass argues against the metallicity gradient predicted by the monolithic collapse scenario, which would require significant major mergers to evolve into the one observed at the present.

Last, we design a new set of color selection criteria (VJL) analogous with the BzK method to select both SFGs and PEGs at $2.3 \lesssim z \lesssim 3.5$ by using rest-frame UV–optical (V–J vs. J–L) colors. We apply the criteria to the HST/WFC3 Early Release Science field and study the physical properties of selected galaxies. The redshift distribution of selected SFGs peaks at $z \sim 2.7$, slightly lower than that of Lyman Break Galaxies at $z \sim 3$. We find that our VJL method is effective at selecting massive dusty SFGs that are missed by the Lyman Break Technique. About half of the star formation in massive ($M_{\text{star}} > 10^{10} M_{\odot}$) galaxies at $2.3 \lesssim z \lesssim 3.5$ is contributed by dusty (extinction $E(B-V) > 0.4$) SFGs, which however, only account for $\sim 20\%$ of the number density of massive SFGs. We also use the mid-infrared fluxes to clean our PEG sample, and find that galaxy size can be used as a secondary criterion to effectively eliminate the contamination of dusty SFGs. The redshift distribution of the cleaned PEG sample peaks at $z \sim 2.5$. We even find 6 PEG candidates at $z > 3$ and discuss possible methods to distinguish them from dusty contamination. We conclude that at least part of our candidates are real PEGs at $z \sim 3$, implying that this type of galaxies began to form their stars at $z \gtrsim 5$. We measure the integrated stellar mass density of PEGs at $z \sim 2.5$ and set constraints on it at $z > 3$. We find that the integrated stellar mass density grows by at least about factor of 10 in 1 Gyr at $3 < z < 5$ and by another factor of 10 in next 3.5 Gyr ($1 < z < 3$).

6.2 Future Development

Although this thesis uses the best available data to date to carry out a pilot study on the sub-structures of galaxies at $z \sim 2$ and sheds a light on the formation of the Hubble Sequence, it has a few limitations. These limitations should be overcome in future development toward a complete understanding of the physics of the formation of the Hubble Sequence.

1. Robust statistics: Our samples at $z \sim 2$ contain only several galaxies (10 for studying clumpy SFGs and 6 for color gradient of PEGs) and thus are subject to small number statistics incompleteness. Also, due to our sample selection criteria, our results on clumps apply strictly to galaxies with relatively large UV luminosity, while that on PEGs only to extremely massive and dead galaxies. In order to obtain a robust statistical characterization of the properties of sub-structures of galaxies at $z \sim 2$, a much larger sample covering a wider range of both luminosity and stellar mass is needed. The ongoing CANDELS (Grogin et al., 2011; Koekemoer et al., 2011) is beginning to obtain deep images over a larger sky area, ≈ 0.5 square degree, and will eventually provide robust answers to the questions that are discussed in this thesis. Moreover, the deep NIR observation of CANDELS will significantly improve the accuracy of the photometric redshift measurements at $z \sim 2$, enabling us to construct deeper samples not limited by spec-zs.

2. Galaxy components beyond stars: In this thesis, we mainly use the SEDs from broad-band images to derive the physical properties of the stellar component of galaxies. However, the formation of the Hubble Sequence is a result of interactions of multiple galaxy components: stars, gases, and dust. Therefore, we should investigate the behaviors of not only stars but also other components of galaxies. Such investigations would ask for observations more than deep broad-band imagings. For example, a fundamental question on clump formation is whether the clumpy galaxies are gas-rich turbulent disks, as required by current theoretical models. In order to answer this question, the gas distribution and kinematics of clumpy galaxies should be observed in the spatial resolution of ~ 1 kpc. Multiple CO rotational J transition lines provide powerful tools to diagnose the distribution and kinematics of gas in $z \sim 2$ galaxies. However, CO line observations with current instruments (e.g., PdBI) only provide constraints on total gas reservoir, but cannot resolve into the kpc scale at $z \sim 2$. The breakthrough will come in 2013 when ALMA is fully operated. The

unprecedented spatial resolution, $0.1''$, would allow us to measure the content and kinematics of gas at the scale of individual clumps.

3. One more player – environment: Galaxies are not formed and grown isolatedly. Instead, they reside in various environments, and their properties are correlated with their environments – at least in the low-redshift universe, where the role that galaxy environment plays on galaxy formation has been well studied. However, the study of galaxy environment and its influence at $z > 2$ is still lacking. (Proto-)Clusters have been detected up to $z \sim 1.6$ by many authors, [salimbenilss,papovich10](#) but only a small number of them have been serendipitously discovered at $z > 2$, mainly during the course of high-redshift galaxy spectroscopic surveys ([Steidel et al. 1998, 2005](#)). As a result, the existence, let alone the influence, of (proto-)clusters at $z > 2$ is still in doubt. However, if they exist, their roles on the formation of the Hubble Sequence should be carefully examined. One interesting topic is if the environment of clumpy SFGs is different from that of non-clumpy SFGs. The deep potential well of clusters may prompt the cold accretion of gas to form clumps, but on the other side, the high probability of interacting with other cluster members may destroy the unstable host disks. Also, the living environment of PEGs should be consistent with the explanations of their formation and subsequent evolution, e.g., major merger, minor merger, or inside-out.

All above future developments require extensive observations on galaxies in various environments with multiple upcoming or already ongoing facilities, including IFUs and multi-object near-IR spectrographs on 8–10-meter class telescopes, ALMA, JWST, and the extremely large ground-based telescopes of the next decade. Observations with these facilities, together with the progress on high-resolution simulations and semi-analytic models, will provide unprecedented tools to probe the diversity of galaxies at all redshifts, and hence display us a grand picture of the evolution of galaxies in the universe.

BIBLIOGRAPHY

- Abraham, R. G., Ellis, R. S., Fabian, A. C., Tanvir, N. R., & Glazebrook, K. 1999, *MNRAS*, 303, 641
- Adelberger, K. L., Steidel, C. C., Shapley, A. E., Hunt, M. P., Erb, D. K., Reddy, N. A., & Pettini, M. 2004, *ApJ*, 607, 226
- Arnouts, S., Walcher, C. J., Le Fèvre, O., Zamorani, G., Ilbert, O., Le Brun, V., Pozzetti, L., Bardelli, S., Tresse, L., Zucca, E., Charlot, S., Lamareille, F., McCracken, H. J., Bolzonella, M., Iovino, A., Lonsdale, C., Polletta, M., Surace, J., Bottini, D., Garilli, B., Maccagni, D., Picat, J. P., Scaramella, R., Scodreggio, M., Vettolani, G., Zanichelli, A., Adami, C., Cappi, A., Ciliegi, P., Contini, T., de la Torre, S., Foucaud, S., Franzetti, P., Gavignaud, I., Guzzo, L., Marano, B., Marinoni, C., Mazure, A., Meneux, B., Merighi, R., Paltani, S., Pellò, R., Pollo, A., Radovich, M., Temporin, S., & Vergani, D. 2007, *A&A*, 476, 137
- Baldry, I. K., Glazebrook, K., Brinkmann, J., Ivezić, Ž., Lupton, R. H., Nichol, R. C., & Szalay, A. S. 2004, *ApJ*, 600, 681
- Beckwith, S. V. W., Stiavelli, M., Koekemoer, A. M., Caldwell, J. A. R., Ferguson, H. C., Hook, R., Lucas, R. A., Bergeron, L. E., Corbin, M., Jogee, S., Panagia, N., Robberto, M., Royle, P., Somerville, R. S., & Sosey, M. 2006, *AJ*, 132, 1729
- Bell, E. F., McIntosh, D. H., Katz, N., & Weinberg, M. D. 2003, *ApJS*, 149, 289
- Bell, E. F., Wolf, C., Meisenheimer, K., Rix, H.-W., Borch, A., Dye, S., Kleinheinrich, M., Wisotzki, L., & McIntosh, D. H. 2004, *ApJ*, 608, 752
- Benson, A. J., Bower, R. G., Frenk, C. S., Lacey, C. G., Baugh, C. M., & Cole, S. 2003, *ApJ*, 599, 38
- Blain, A. W., Smail, I., Ivison, R. J., Kneib, J.-P., & Frayer, D. T. 2002, *Phys. Rep.*, 369, 111
- Blanc, G. A., Lira, P., Barrientos, L. F., Aguirre, P., Francke, H., Taylor, E. N., Quadri, R., Marchesini, D., Infante, L., Gawiser, E., Hall, P. B., Willis, J. P., Herrera, D., & Maza, J. 2008, *ApJ*, 681, 1099

- Blanton, M. R., Dalcanton, J., Eisenstein, D., Loveday, J., Strauss, M. A., SubbaRao, M., Weinberg, D. H., Anderson, Jr., J. E., Annis, J., Bahcall, N. A., Bernardi, M., Brinkmann, J., Brunner, R. J., Burles, S., Carey, L., Castander, F. J., Connolly, A. J., Csabai, I., Doi, M., Finkbeiner, D., Friedman, S., Frieman, J. A., Fukugita, M., Gunn, J. E., Hennessy, G. S., Hindsley, R. B., Hogg, D. W., Ichikawa, T., Ivezić, Ž., Kent, S., Knapp, G. R., Lamb, D. Q., Leger, R. F., Long, D. C., Lupton, R. H., McKay, T. A., Meiksin, A., Merelli, A., Munn, J. A., Narayanan, V., Newcomb, M., Nichol, R. C., Okamura, S., Owen, R., Pier, J. R., Pope, A., Postman, M., Quinn, T., Rockosi, C. M., Schlegel, D. J., Schneider, D. P., Shimasaku, K., Siegmund, W. A., Smee, S., Snir, Y., Stoughton, C., Stubbs, C., Szalay, A. S., Szokoly, G. P., Thakar, A. R., Tremonti, C., Tucker, D. L., Uomoto, A., Vanden Berk, D., Vogeley, M. S., Waddell, P., Yanny, B., Yasuda, N., & York, D. G. 2001, *AJ*, 121, 2358
- Blanton, M. R., Eisenstein, D., Hogg, D. W., Schlegel, D. J., & Brinkmann, J. 2005a, *ApJ*, 629, 143
- Blanton, M. R., Hogg, D. W., Bahcall, N. A., Baldry, I. K., Brinkmann, J., Csabai, I., Eisenstein, D., Fukugita, M., Gunn, J. E., Ivezić, Ž., Lamb, D. Q., Lupton, R. H., Loveday, J., Munn, J. A., Nichol, R. C., Okamura, S., Schlegel, D. J., Shimasaku, K., Strauss, M. A., Vogeley, M. S., & Weinberg, D. H. 2003a, *ApJ*, 594, 186
- Blanton, M. R., Hogg, D. W., Bahcall, N. A., Brinkmann, J., Britton, M., Connolly, A. J., Csabai, I., Fukugita, M., Loveday, J., Meiksin, A., Munn, J. A., Nichol, R. C., Okamura, S., Quinn, T., Schneider, D. P., Shimasaku, K., Strauss, M. A., Tegmark, M., Vogeley, M. S., & Weinberg, D. H. 2003b, *ApJ*, 592, 819
- Blanton, M. R., Lupton, R. H., Schlegel, D. J., Strauss, M. A., Brinkmann, J., Fukugita, M., & Loveday, J. 2005b, *ApJ*, 631, 208
- Blanton, M. R. & Moustakas, J. 2009, *ARA&A*, 47, 159
- Borch, A., Meisenheimer, K., Bell, E. F., Rix, H.-W., Wolf, C., Dye, S., Kleinheinrich, M., Kovacs, Z., & Wisotzki, L. 2006, *A&A*, 453, 869
- Bournaud, F., Daddi, E., Elmegreen, B. G., Elmegreen, D. M., Nesvadba, N., Vanzella, E., Di Matteo, P., Le Tiran, L., Lehnert, M., & Elbaz, D. 2008, *A&A*, 486, 741
- Bournaud, F., Dekel, A., Teyssier, R., Cacciato, M., Daddi, E., Juneau, S., & Shankar, F. 2011, *ApJ*, 741, L33
- Bournaud, F., Elmegreen, B. G., & Elmegreen, D. M. 2007, *ApJ*, 670, 237
- Bournaud, F., Elmegreen, B. G., & Martig, M. 2009, *ApJ*, 707, L1
- Bouwens, R. J., Illingworth, G. D., Franx, M., Chary, R.-R., Meurer, G. R., Conselice, C. J., Ford, H., Giavalisco, M., & van Dokkum, P. 2009, *ApJ*, 705, 936
- Bouwens, R. J., Illingworth, G. D., Franx, M., & Ford, H. 2007, *ApJ*, 670, 928

- Bouwens, R. J., Illingworth, G. D., Oesch, P. A., Labbé, I., Trenti, M., van Dokkum, P., Franx, M., Stiavelli, M., Carollo, C. M., Magee, D., & Gonzalez, V. 2011, *ApJ*, 737, 90
- Bouwens, R. J., Illingworth, G. D., Oesch, P. A., Stiavelli, M., van Dokkum, P., Trenti, M., Magee, D., Labbé, I., Franx, M., Carollo, C. M., & Gonzalez, V. 2010, *ApJ*, 709, L133
- Bower, R. G., Benson, A. J., Malbon, R., Helly, J. C., Frenk, C. S., Baugh, C. M., Cole, S., & Lacey, C. G. 2006, *MNRAS*, 370, 645
- Brammer, G. B., Whitaker, K. E., van Dokkum, P. G., Marchesini, D., Franx, M., Kriek, M., Labbe, I., Lee, K.-S., Muzzin, A., Quadri, R. F., Rudnick, G., & Williams, R. 2011, *ArXiv e-prints*
- Brammer, G. B., Whitaker, K. E., van Dokkum, P. G., Marchesini, D., Labbé, I., Franx, M., Kriek, M., Quadri, R. F., Illingworth, G., Lee, K.-S., Muzzin, A., & Rudnick, G. 2009, *ApJ*, 706, L173
- Brinchmann, J. & Ellis, R. S. 2000, *ApJ*, 536, L77
- Bruzual, G. & Charlot, S. 2003, *MNRAS*, 344, 1000
- Buitrago, F., Trujillo, I., Conselice, C. J., Bouwens, R. J., Dickinson, M., & Yan, H. 2008, *ApJ*, 687, L61
- Calzetti, D., Armus, L., Bohlin, R. C., Kinney, A. L., Koornneef, J., & Storchi-Bergmann, T. 2000, *ApJ*, 533, 682
- Calzetti, D., Kinney, A. L., & Storchi-Bergmann, T. 1994, *ApJ*, 429, 582
- Calzetti, D., Meurer, G. R., Bohlin, R. C., Garnett, D. R., Kinney, A. L., Leitherer, C., & Storchi-Bergmann, T. 1997, *AJ*, 114, 1834
- Cameron, E., Carollo, C. M., Oesch, P. A., Bouwens, R. J., Illingworth, G. D., Trenti, M., Labbé, I., & Magee, D. 2011, *ApJ*, 743, 146
- Caon, N., Macchetto, D., & Pastoriza, M. 2000, *ApJS*, 127, 39
- Cardelli, J. A., Clayton, G. C., & Mathis, J. S. 1989, *ApJ*, 345, 245
- Cardiel, N., Gorgas, J., Sánchez-Blázquez, P., Cenarro, A. J., Pedraz, S., Bruzual, G., & Klement, J. 2003, *A&A*, 409, 511
- Carlberg, R. G. 1984, *ApJ*, 286, 416
- Cassata, P., Cimatti, A., Kurk, J., Rodighiero, G., Pozzetti, L., Bolzonella, M., Daddi, E., Mignoli, M., Berta, S., Dickinson, M., Franceschini, A., Halliday, C., Renzini, A., Rosati, P., & Zamorani, G. 2008, *A&A*, 483, L39

- Cassata, P., Giavalisco, M., Guo, Y., Ferguson, H., Koekemoer, A. M., Renzini, A., Fontana, A., Salimbeni, S., Dickinson, M., Casertano, S., Conselice, C. J., Grogin, N., Lotz, J. M., Papovich, C., Lucas, R. A., Straughn, A., Gardner, J. P., & Moustakas, L. 2010, *ApJ*, 714, L79
- Cassata, P., Giavalisco, M., Guo, Y., Renzini, A., Ferguson, H., Koekemoer, A. M., Salimbeni, S., Scarlata, C., Grogin, N. A., Conselice, C. J., Dahlen, T., Lotz, J. M., Dickinson, M., & Lin, L. 2011, *ArXiv e-prints*
- Ceverino, D., Dekel, A., & Bournaud, F. 2010, *MNRAS*, 404, 2151
- Ceverino, D., Dekel, A., Mandelker, N., Bournaud, F., Burkert, A., Genzel, R., & Primack, J. 2012, *MNRAS*, 420, 3490
- Chabrier, G. 2003, *PASP*, 115, 763
- Chapman, S. C., Blain, A. W., Ivison, R. J., & Smail, I. R. 2003, *Nature*, 422, 695
- Chapman, S. C., Blain, A. W., Smail, I., & Ivison, R. J. 2005, *ApJ*, 622, 772
- Chary, R. & Elbaz, D. 2001, *ApJ*, 556, 562
- Chary, R.-R. & Pope, A. 2010, *ArXiv e-prints*
- Cimatti, A., Cassata, P., Pozzetti, L., Kurk, J., Mignoli, M., Renzini, A., Daddi, E., Bolzonella, M., Brusa, M., Rodighiero, G., Dickinson, M., Franceschini, A., Zamorani, G., Berta, S., Rosati, P., & Halliday, C. 2008, *A&A*, 482, 21
- Cimatti, A., Daddi, E., Cassata, P., Pignatelli, E., Fasano, G., Vernet, J., Fomalont, E., Kellermann, K., Zamorani, G., Mignoli, M., Pozzetti, L., Renzini, A., di Serego Alighieri, S., Franceschini, A., Giallongo, E., & Fontana, A. 2003, *A&A*, 412, L1
- Cimatti, A., Daddi, E., Mignoli, M., Pozzetti, L., Renzini, A., Zamorani, G., Broadhurst, T., Fontana, A., Saracco, P., Poli, F., Cristiani, S., D'Odorico, S., Giallongo, E., Gilmozzi, R., & Menci, N. 2002, *A&A*, 381, L68
- Civano, F., Brusa, M., Comastri, A., Elvis, M., Salvato, M., Zamorani, G., Capak, P., Fiore, F., Gilli, R., Hao, H., Ikeda, H., Kakazu, Y., Kartaltepe, J. S., Masters, D., Miyaji, T., Mignoli, M., Puccetti, S., Shankar, F., Silverman, J., Vignali, C., Zezas, A., & Koekemoer, A. M. 2011, *ApJ*, 741, 91
- Conselice, C. J., Grogin, N. A., Jogee, S., Lucas, R. A., Dahlen, T., de Mello, D., Gardner, J. P., Mobasher, B., & Ravindranath, S. 2004, *ApJ*, 600, L139
- Conselice, C. J., Rajgor, S., & Myers, R. 2008, *MNRAS*, 386, 909
- Cresci, G., Mannucci, F., Maiolino, R., Marconi, A., Gnerucci, A., & Magrini, L. 2010, *Nature*, 467, 811

- Croton, D. J., Springel, V., White, S. D. M., De Lucia, G., Frenk, C. S., Gao, L., Jenkins, A., Kauffmann, G., Navarro, J. F., & Yoshida, N. 2006, *MNRAS*, 365, 11
- Daddi, E., Alexander, D. M., Dickinson, M., Gilli, R., Renzini, A., Elbaz, D., Cimatti, A., Chary, R., Frayer, D., Bauer, F. E., Brandt, W. N., Giavalisco, M., Grogin, N. A., Huynh, M., Kurk, J., Mignoli, M., Morrison, G., Pope, A., & Ravindranath, S. 2007a, *ApJ*, 670, 173
- Daddi, E., Bournaud, F., Walter, F., Dannerbauer, H., Carilli, C. L., Dickinson, M., Elbaz, D., Morrison, G. E., Riechers, D., Onodera, M., Salmi, F., Krips, M., & Stern, D. 2010, *ApJ*, 713, 686
- Daddi, E., Cimatti, A., Pozzetti, L., Hoekstra, H., Röttgering, H. J. A., Renzini, A., Zamorani, G., & Mannucci, F. 2000, *A&A*, 361, 535
- Daddi, E., Cimatti, A., Renzini, A., Fontana, A., Mignoli, M., Pozzetti, L., Tozzi, P., & Zamorani, G. 2004a, *ApJ*, 617, 746
- Daddi, E., Cimatti, A., Renzini, A., Vernet, J., Conselice, C., Pozzetti, L., Mignoli, M., Tozzi, P., Broadhurst, T., di Serego Alighieri, S., Fontana, A., Nonino, M., Rosati, P., & Zamorani, G. 2004b, *ApJ*, 600, L127
- Daddi, E., Dickinson, M., Morrison, G., Chary, R., Cimatti, A., Elbaz, D., Frayer, D., Renzini, A., Pope, A., Alexander, D. M., Bauer, F. E., Giavalisco, M., Huynh, M., Kurk, J., & Mignoli, M. 2007b, *ApJ*, 670, 156
- Daddi, E., Renzini, A., Pirzkal, N., Cimatti, A., Malhotra, S., Stiavelli, M., Xu, C., Pasquali, A., Rhoads, J. E., Brusa, M., di Serego Alighieri, S., Ferguson, H. C., Koekemoer, A. M., Moustakas, L. A., Panagia, N., & Windhorst, R. A. 2005, *ApJ*, 626, 680
- Dahlen, T., Mobasher, B., Dickinson, M., Ferguson, H. C., Giavalisco, M., Grogin, N. A., Guo, Y., Koekemoer, A., Lee, K.-S., Lee, S.-K., Nonino, M., Riess, A. G., & Salimbeni, S. 2010, *ApJ*, 724, 425
- Dahlen, T., Mobasher, B., Somerville, R. S., Moustakas, L. A., Dickinson, M., Ferguson, H. C., & Giavalisco, M. 2005, *ApJ*, 631, 126
- de Jong, R. S. 1996, *A&A*, 313, 377
- De Lucia, G., Springel, V., White, S. D. M., Croton, D., & Kauffmann, G. 2006, *MNRAS*, 366, 499
- Dekel, A., Birnboim, Y., Engel, G., Freundlich, J., Goerdt, T., Mumcuoglu, M., Neistein, E., Pichon, C., Teyssier, R., & Zinger, E. 2009a, *Nature*, 457, 451
- Dekel, A., Sari, R., & Ceverino, D. 2009b, *ApJ*, 703, 785

- Draine, B. T. 2009, in *Astronomical Society of the Pacific Conference Series*, Vol. 414, *Astronomical Society of the Pacific Conference Series*, ed. T. Henning, E. Grün, & J. Steinacker, 453–+
- Driver, S. P., Allen, P. D., Graham, A. W., Cameron, E., Liske, J., Ellis, S. C., Cross, N. J. G., De Propriis, R., Phillipps, S., & Couch, W. J. 2006, *MNRAS*, 368, 414
- Dunlop, J. S., Cirasuolo, M., & McLure, R. J. 2007, *MNRAS*, 376, 1054
- Elmegreen, B. G., Bournaud, F., & Elmegreen, D. M. 2008, *ApJ*, 688, 67
- Elmegreen, B. G. & Elmegreen, D. M. 2005, *ApJ*, 627, 632
- Elmegreen, B. G., Elmegreen, D. M., Fernandez, M. X., & Lemonias, J. J. 2009a, *ApJ*, 692, 12
- Elmegreen, D. M., Elmegreen, B. G., Marcus, M. T., Shahinyan, K., Yau, A., & Petersen, M. 2009b, *ApJ*, 701, 306
- Elmegreen, D. M., Elmegreen, B. G., Ravindranath, S., & Coe, D. A. 2007, *ApJ*, 658, 763
- Erb, D. K., Steidel, C. C., Shapley, A. E., Pettini, M., Reddy, N. A., & Adelberger, K. L. 2006, *ApJ*, 646, 107
- Escala, A. & Larson, R. B. 2008, *ApJ*, 685, L31
- Faber, S. M. 1972, in *Bulletin of the American Astronomical Society*, Vol. 4, *Bulletin of the American Astronomical Society*, 224–+
- Fan, L., Lapi, A., De Zotti, G., & Danese, L. 2008, *ApJ*, 689, L101
- Fioc, M. & Rocca-Volmerange, B. 1997, *A&A*, 326, 950
- Fitzpatrick, E. L. 1986, *AJ*, 92, 1068
- Fontana, A., Pozzetti, L., Donnarumma, I., Renzini, A., Cimatti, A., Zamorani, G., Menci, N., Daddi, E., Giallongo, E., Mignoli, M., Perna, C., Salimbeni, S., Saracco, P., Broadhurst, T., Cristiani, S., D’Odorico, S., & Gilmozzi, R. 2004, *A&A*, 424, 23
- Fontana, A., Salimbeni, S., Grazian, A., Giallongo, E., Pentericci, L., Nonino, M., Fontanot, F., Menci, N., Monaco, P., Cristiani, S., Vanzella, E., de Santis, C., & Gallozzi, S. 2006, *A&A*, 459, 745
- Fontana, A., Santini, P., Grazian, A., Pentericci, L., Fiore, F., Castellano, M., Giallongo, E., Menci, N., Salimbeni, S., Cristiani, S., Nonino, M., & Vanzella, E. 2009, *A&A*, 501, 15

- Förster Schreiber, N. M., Genzel, R., Bouché, N., Cresci, G., Davies, R., Buschkamp, P., Shapiro, K., Tacconi, L. J., Hicks, E. K. S., Genel, S., Shapley, A. E., Erb, D. K., Steidel, C. C., Lutz, D., Eisenhauer, F., Gillessen, S., Sternberg, A., Renzini, A., Cimatti, A., Daddi, E., Kurk, J., Lilly, S., Kong, X., Lehnert, M. D., Nesvadba, N., Verma, A., McCracken, H., Arimoto, N., Mignoli, M., & Onodera, M. 2009, *ApJ*, 706, 1364
- Förster Schreiber, N. M., Shapley, A. E., Genzel, R., Bouché, N., Cresci, G., Davies, R., Erb, D. K., Genel, S., Lutz, D., Newman, S., Shapiro, K. L., Steidel, C. C., Sternberg, A., & Tacconi, L. J. 2011, *ApJ*, 739, 45
- Förster Schreiber, N. M., van Dokkum, P. G., Franx, M., Labbé, I., Rudnick, G., Daddi, E., Illingworth, G. D., Kriek, M., Moorwood, A. F. M., Rix, H.-W., Röttgering, H., Trujillo, I., van der Werf, P., van Starckenburg, L., & Wuyts, S. 2004, *ApJ*, 616, 40
- Franx, M., Labbé, I., Rudnick, G., van Dokkum, P. G., Daddi, E., Förster Schreiber, N. M., Moorwood, A., Rix, H.-W., Röttgering, H., van de Wel, A., van der Werf, P., & van Starckenburg, L. 2003, *ApJ*, 587, L79
- Franx, M., van Dokkum, P. G., Schreiber, N. M. F., Wuyts, S., Labbé, I., & Toft, S. 2008, *ApJ*, 688, 770
- Gargiulo, A., Saracco, P., & Longhetti, M. 2011, *MNRAS*, 67
- Genel, S., Naab, T., Genzel, R., Förster Schreiber, N. M., Sternberg, A., Oser, L., Johansson, P. H., Davé, R., Oppenheimer, B. D., & Burkert, A. 2012, *ApJ*, 745, 11
- Genzel, R., Burkert, A., Bouché, N., Cresci, G., Förster Schreiber, N. M., Shapley, A., Shapiro, K., Tacconi, L. J., Buschkamp, P., Cimatti, A., Daddi, E., Davies, R., Eisenhauer, F., Erb, D. K., Genel, S., Gerhard, O., Hicks, E., Lutz, D., Naab, T., Ott, T., Rabien, S., Renzini, A., Steidel, C. C., Sternberg, A., & Lilly, S. J. 2008, *ApJ*, 687, 59
- Genzel, R., Newman, S., Jones, T., Förster Schreiber, N. M., Shapiro, K., Genel, S., Lilly, S. J., Renzini, A., Tacconi, L. J., Bouché, N., Burkert, A., Cresci, G., Buschkamp, P., Carollo, C. M., Ceverino, D., Davies, R., Dekel, A., Eisenhauer, F., Hicks, E., Kurk, J., Lutz, D., Mancini, C., Naab, T., Peng, Y., Sternberg, A., Vergani, D., & Zamorani, G. 2011, *ApJ*, 733, 101
- Giavalisco, M. 2002, *ARA&A*, 40, 579
- Giavalisco, M., Dickinson, M., Ferguson, H. C., Ravindranath, S., Kretchmer, C., Moustakas, L. A., Madau, P., Fall, S. M., Gardner, J. P., Livio, M., Papovich, C., Renzini, A., Spinrad, H., Stern, D., & Riess, A. 2004, *ApJ*, 600, L103
- Giavalisco, M., Steidel, C. C., & Macchetto, F. D. 1996, *ApJ*, 470, 189

- Giavalisco, M., Vanzella, E., Salimbeni, S., Tripp, T. M., Dickinson, M., Cassata, P., Renzini, A., Guo, Y., Ferguson, H. C., Nonino, M., Cimatti, A., Kurk, J., Mignoli, M., & Tang, Y. 2011, *ApJ*, 743, 95
- Glazebrook, K., Abraham, R. G., McCarthy, P. J., Savaglio, S., Chen, H.-W., Cramp-ton, D., Murowinski, R., Jørgensen, I., Roth, K., Hook, I., Marzke, R. O., & Carl-berg, R. G. 2004, *Nature*, 430, 181
- Gonzalez-Perez, V., Castander, F. J., & Kauffmann, G. 2011, *MNRAS*, 411, 1151
- Goudfrooij, P. & de Jong, T. 1995, *A&A*, 298, 784
- Graham, A. W. & Driver, S. P. 2005, *PASA*, 22, 118
- Grazian, A., Salimbeni, S., Pentericci, L., Fontana, A., Nonino, M., Vanzella, E., Cristiani, S., de Santis, C., Gallozzi, S., Giallongo, E., & Santini, P. 2007, *A&A*, 465, 393
- Grogin, N. A., Kocevski, D. D., Faber, S. M., Ferguson, H. C., Koekemoer, A. M., Riess, A. G., Acquaviva, V., Alexander, D. M., Almaini, O., Ashby, M. L. N., Barden, M., Bell, E. F., Bournaud, F., Brown, T. M., Caputi, K. I., Casertano, S., Cassata, P., Castellano, M., Challis, P., Chary, R.-R., Cheung, E., Cirasuolo, M., Conselice, C. J., Roshan Cooray, A., Croton, D. J., Daddi, E., Dahlen, T., Davé, R., de Mello, D. F., Dekel, A., Dickinson, M., Dolch, T., Donley, J. L., Dunlop, J. S., Dutton, A. A., Elbaz, D., Fazio, G. G., Filippenko, A. V., Finkelstein, S. L., Fontana, A., Gardner, J. P., Garnavich, P. M., Gawiser, E., Giavalisco, M., Grazian, A., Guo, Y., Hathi, N. P., Häussler, B., Hopkins, P. F., Huang, J.-S., Huang, K.-H., Jha, S. W., Kartaltepe, J. S., Kirshner, R. P., Koo, D. C., Lai, K., Lee, K.-S., Li, W., Lotz, J. M., Lucas, R. A., Madau, P., McCarthy, P. J., McGrath, E. J., McIntosh, D. H., McLure, R. J., Mobasher, B., Moustakas, L. A., Mozena, M., Nandra, K., Newman, J. A., Niemi, S.-M., Noeske, K. G., Papovich, C. J., Pentericci, L., Pope, A., Primack, J. R., Rajan, A., Ravindranath, S., Reddy, N. A., Renzini, A., Rix, H.-W., Robaina, A. R., Rodney, S. A., Rosario, D. J., Rosati, P., Salimbeni, S., Scarlata, C., Siana, B., Simard, L., Smidt, J., Somerville, R. S., Spinrad, H., Straughn, A. N., Strolger, L.-G., Telford, O., Teplitz, H. I., Trump, J. R., van der Wel, A., Villforth, C., Wechsler, R. H., Weiner, B. J., Wiklind, T., Wild, V., Wilson, G., Wuyts, S., Yan, H.-J., & Yun, M. S. 2011, *ApJS*, 197, 35
- Guo, Y., Giavalisco, M., Cassata, P., Ferguson, H. C., Dickinson, M., Renzini, A., Koekemoer, A., Grogin, N. A., Papovich, C., Tundo, E., Fontana, A., Lotz, J. M., & Salimbeni, S. 2011, *ApJ*, 735, 18
- Guo, Y., Giavalisco, M., Cassata, P., Ferguson, H. C., Williams, C. C., Dickinson, M., Koekemoer, A., Grogin, N. A., Chary, R.-R., Messias, H., Tundo, E., Lin, L., Lee, S.-K., Salimbeni, S., Fontana, A., Grazian, A., Kocevski, D., Lee, K.-S., Villanueva, E., & van der Wel, A. 2012, *ApJ*, 749, 149

- Guo, Y., McIntosh, D. H., Mo, H. J., Katz, N., van den Bosch, F. C., Weinberg, M., Weinmann, S. M., Pasquali, A., & Yang, X. 2009, *MNRAS*, 398, 1129
- Hogg, D. W., Blanton, M., Strateva, I., Bahcall, N. A., Brinkmann, J., Csabai, I., Doi, M., Fukugita, M., Hennessy, G., Ivezić, Ž., Knapp, G. R., Lamb, D. Q., Lupton, R., Munn, J. A., Nichol, R., Schlegel, D. J., Schneider, D. P., & York, D. G. 2002, *AJ*, 124, 646
- Hopkins, A. M. 2004, *ApJ*, 615, 209
- Hopkins, A. M. & Beacom, J. F. 2006, *ApJ*, 651, 142
- Hopkins, P. F., Bundy, K., Hernquist, L., Wuyts, S., & Cox, T. J. 2010, *MNRAS*, 401, 1099
- Hopkins, P. F., Bundy, K., Murray, N., Quataert, E., Lauer, T. R., & Ma, C. 2009a, *MNRAS*, 398, 898
- Hopkins, P. F., Cox, T. J., Kereš, D., & Hernquist, L. 2008, *ApJS*, 175, 390
- Hopkins, P. F., Lauer, T. R., Cox, T. J., Hernquist, L., & Kormendy, J. 2009b, *ApJS*, 181, 486
- Iidart, T. P., Michard, R., & de Freitas Pacheco, J. A. 2003, *A&A*, 398, 949
- Ilbert, O., Capak, P., Salvato, M., Aussel, H., McCracken, H. J., Sanders, D. B., Scoville, N., Kartaltepe, J., Arnouts, S., Le Floch, E., Mobasher, B., Taniguchi, Y., Lamareille, F., Leauthaud, A., Sasaki, S., Thompson, D., Zamojski, M., Zamorani, G., Bardelli, S., Bolzonella, M., Bongiorno, A., Brusa, M., Caputi, K. I., Carollo, C. M., Contini, T., Cook, R., Coppa, G., Cucciati, O., de la Torre, S., de Ravel, L., Franzetti, P., Garilli, B., Hasinger, G., Iovino, A., Kampczyk, P., Kneib, J.-P., Knobel, C., Kovac, K., Le Borgne, J. F., Le Brun, V., Fèvre, O. L., Lilly, S., Looper, D., Maier, C., Mainieri, V., Mellier, Y., Mignoli, M., Murayama, T., Pellò, R., Peng, Y., Pérez-Montero, E., Renzini, A., Ricciardelli, E., Schiminovich, D., Scodreggio, M., Shioya, Y., Silverman, J., Surace, J., Tanaka, M., Tasca, L., Tresse, L., Vergani, D., & Zucca, E. 2009, *ApJ*, 690, 1236
- Ilbert, O., Salvato, M., Le Floch, E., Aussel, H., Capak, P., McCracken, H. J., Mobasher, B., Kartaltepe, J., Scoville, N., Sanders, D. B., Arnouts, S., Bundy, K., Cassata, P., Kneib, J.-P., Koekemoer, A., Le Fèvre, O., Lilly, S., Surace, J., Taniguchi, Y., Tasca, L., Thompson, D., Tresse, L., Zamojski, M., Zamorani, G., & Zucca, E. 2010, *ApJ*, 709, 644
- Immeli, A., Samland, M., Gerhard, O., & Westera, P. 2004a, *A&A*, 413, 547
- Immeli, A., Samland, M., Westera, P., & Gerhard, O. 2004b, *ApJ*, 611, 20
- Jones, T. A., Swinbank, A. M., Ellis, R. S., Richard, J., & Stark, D. P. 2010, *MNRAS*, 404, 1247

- Kauffmann, G., Heckman, T. M., White, S. D. M., Charlot, S., Tremonti, C., Brinchmann, J., Bruzual, G., Peng, E. W., Seibert, M., Bernardi, M., Blanton, M., Brinkmann, J., Castander, F., Csábai, I., Fukugita, M., Ivezić, Z., Munn, J. A., Nichol, R. C., Padmanabhan, N., Thakar, A. R., Weinberg, D. H., & York, D. 2003a, *MNRAS*, 341, 33
- Kauffmann, G., Heckman, T. M., White, S. D. M., Charlot, S., Tremonti, C., Peng, E. W., Seibert, M., Brinkmann, J., Nichol, R. C., SubbaRao, M., & York, D. 2003b, *MNRAS*, 341, 54
- Kellermann, K. I., Fomalont, E. B., Mainieri, V., Padovani, P., Rosati, P., Shaver, P., Tozzi, P., & Miller, N. 2008, *ApJS*, 179, 71
- Kennicutt, Jr., R. C. 1998, *ARA&A*, 36, 189
- Kereš, D., Katz, N., Weinberg, D. H., & Davé, R. 2005, *MNRAS*, 363, 2
- Kobayashi, C. 2004, *MNRAS*, 347, 740
- Koekemoer, A. M., Faber, S. M., Ferguson, H. C., Grogin, N. A., Kocevski, D. D., Koo, D. C., Lai, K., Lotz, J. M., Lucas, R. A., McGrath, E. J., Ogaz, S., Rajan, A., Riess, A. G., Rodney, S. A., Strolger, L., Casertano, S., Castellano, M., Dahlen, T., Dickinson, M., Dolch, T., Fontana, A., Giavalisco, M., Grazian, A., Guo, Y., Hathi, N. P., Huang, K.-H., van der Wel, A., Yan, H.-J., Acquaviva, V., Alexander, D. M., Almaini, O., Ashby, M. L. N., Barden, M., Bell, E. F., Bournaud, F., Brown, T. M., Caputi, K. I., Cassata, P., Challis, P. J., Chary, R.-R., Cheung, E., Cirasuolo, M., Conselice, C. J., Roshan Cooray, A., Croton, D. J., Daddi, E., Davé, R., de Mello, D. F., de Ravel, L., Dekel, A., Donley, J. L., Dunlop, J. S., Dutton, A. A., Elbaz, D., Fazio, G. G., Filippenko, A. V., Finkelstein, S. L., Frazer, C., Gardner, J. P., Garnavich, P. M., Gawiser, E., Gruetzbauch, R., Hartley, W. G., Häussler, B., Herrington, J., Hopkins, P. F., Huang, J.-S., Jha, S. W., Johnson, A., Kartaltepe, J. S., Khostovan, A. A., Kirshner, R. P., Lani, C., Lee, K.-S., Li, W., Madau, P., McCarthy, P. J., McIntosh, D. H., McLure, R. J., McPartland, C., Mobasher, B., Moreira, H., Mortlock, A., Moustakas, L. A., Mozena, M., Nandra, K., Newman, J. A., Nielsen, J. L., Niemi, S., Noeske, K. G., Papovich, C. J., Pentericci, L., Pope, A., Primack, J. R., Ravindranath, S., Reddy, N. A., Renzini, A., Rix, H.-W., Robaina, A. R., Rosario, D. J., Rosati, P., Salimbeni, S., Scarlata, C., Siana, B., Simard, L., Smidt, J., Snyder, D., Somerville, R. S., Spinrad, H., Straughn, A. N., Telford, O., Teplitz, H. I., Trump, J. R., Vargas, C., Villforth, C., Wagner, C. R., Wandro, P., Wechsler, R. H., Weiner, B. J., Wiklind, T., Wild, V., Wilson, G., Wuyts, S., & Yun, M. S. 2011, *ApJS*, 197, 36
- Komatsu, E., Smith, K. M., Dunkley, J., Bennett, C. L., Gold, B., Hinshaw, G., Jarosik, N., Larson, D., Nolta, M. R., Page, L., Spergel, D. N., Halpern, M., Hill, R. S., Kogut, A., Limon, M., Meyer, S. S., Odegard, N., Tucker, G. S., Weiland, J. L., Wollack, E., & Wright, E. L. 2011, *ApJS*, 192, 18

- Kong, X., Daddi, E., Arimoto, N., Renzini, A., Broadhurst, T., Cimatti, A., Ikuta, C., Ohta, K., da Costa, L., Olsen, L. F., Onodera, M., & Tamura, N. 2006, *ApJ*, 638, 72
- Kriek, M., van der Wel, A., van Dokkum, P. G., Franx, M., & Illingworth, G. D. 2008, *ApJ*, 682, 896
- Kriek, M., van Dokkum, P. G., Franx, M., Förster Schreiber, N. M., Gawiser, E., Illingworth, G. D., Labbé, I., Marchesini, D., Quadri, R., Rix, H.-W., Rudnick, G., Toft, S., van der Werf, P., & Wuyts, S. 2006a, *ApJ*, 645, 44
- Kriek, M., van Dokkum, P. G., Franx, M., Illingworth, G. D., & Magee, D. K. 2009, *ApJ*, 705, L71
- Kriek, M., van Dokkum, P. G., Franx, M., Quadri, R., Gawiser, E., Herrera, D., Illingworth, G. D., Labbé, I., Lira, P., Marchesini, D., Rix, H.-W., Rudnick, G., Taylor, E. N., Toft, S., Urry, C. M., & Wuyts, S. 2006b, *ApJ*, 649, L71
- La Barbera, F. & de Carvalho, R. R. 2009, *ApJ*, 699, L76
- La Barbera, F., de Carvalho, R. R., Gal, R. R., Busarello, G., Merluzzi, P., Capaccioli, M., & Djorgovski, S. G. 2005, *ApJ*, 626, L19
- Laidler, V. G., Papovich, C., Grogin, N. A., Idzi, R., Dickinson, M., Ferguson, H. C., Hilbert, B., Clubb, K., & Ravindranath, S. 2007, *PASP*, 119, 1325
- Lane, K. P., Almaini, O., Foucaud, S., Simpson, C., Smail, I., McLure, R. J., Con-
selice, C. J., Cirasuolo, M., Page, M. J., Dunlop, J. S., Hirst, P., Watson, M. G.,
& Sekiguchi, K. 2007, *MNRAS*, 379, L25
- Larson, R. B. 1974, *MNRAS*, 166, 585
- Lauer, T. R., Faber, S. M., Gebhardt, K., Richstone, D., Tremaine, S., Ajhar, E. A.,
Aller, M. C., Bender, R., Dressler, A., Filippenko, A. V., Green, R., Grillmair,
C. J., Ho, L. C., Kormendy, J., Magorrian, J., Pinkney, J., & Siopis, C. 2005, *AJ*,
129, 2138
- Le Fèvre, O., Abraham, R., Lilly, S. J., Ellis, R. S., Brinchmann, J., Schade, D.,
Tresse, L., Colless, M., Crampton, D., Glazebrook, K., Hammer, F., & Broadhurst,
T. 2000, *MNRAS*, 311, 565
- Lee, K.-S., Ferguson, H. C., Wiklind, T., Dahlen, T., Dickinson, M. E., Giavalisco,
M., Grogin, N., Papovich, C., Messias, H., Guo, Y., & Lin, L. 2012, *ApJ*, 752, 66
- Lee, S., Ferguson, H. C., Somerville, R. S., Wiklind, T., & Giavalisco, M. 2010, *ApJ*,
725, 1644
- Lee, S.-K., Idzi, R., Ferguson, H. C., Somerville, R. S., Wiklind, T., & Giavalisco, M.
2009, *ApJS*, 184, 100

- Lejeune, T., Cuisinier, F., & Buser, R. 1997, *A&AS*, 125, 229
- Lotz, J. M., Madau, P., Giavalisco, M., Primack, J., & Ferguson, H. C. 2006, *ApJ*, 636, 592
- Luo, B., Bauer, F. E., Brandt, W. N., Alexander, D. M., Lehmer, B. D., Schneider, D. P., Brusa, M., Comastri, A., Fabian, A. C., Finoguenov, A., Gilli, R., Hasinger, G., Hornschemeier, A. E., Koekemoer, A., Mainieri, V., Paolillo, M., Rosati, P., Shemmer, O., Silverman, J. D., Smail, I., Steffen, A. T., & Vignali, C. 2008, *ApJS*, 179, 19
- Ly, C., Malkan, M. A., Hayashi, M., Motohara, K., Kashikawa, N., Shimasaku, K., Nagao, T., & Grady, C. 2011, *ApJ*, 735, 91
- MacArthur, L. A., Courteau, S., Bell, E., & Holtzman, J. A. 2004, *ApJS*, 152, 175
- Madau, P. 1995, *ApJ*, 441, 18
- Madau, P., Ferguson, H. C., Dickinson, M. E., Giavalisco, M., Steidel, C. C., & Fruchter, A. 1996, *MNRAS*, 283, 1388
- Magnelli, B., Elbaz, D., Chary, R. R., Dickinson, M., Le Borgne, D., Frayer, D. T., & Willmer, C. N. A. 2011, *A&A*, 528, A35+
- Mancini, C., Daddi, E., Renzini, A., Salmi, F., McCracken, H. J., Cimatti, A., Onodera, M., Salvato, M., Koekemoer, A. M., Aussel, H., Le Floc'h, E., Willott, C., & Capak, P. 2010, *MNRAS*, 401, 933
- Mancini, C., Matute, I., Cimatti, A., Daddi, E., Dickinson, M., Rodighiero, G., Bolzonella, M., & Pozzetti, L. 2009, *A&A*, 500, 705
- Maraston, C. 2005, *MNRAS*, 362, 799
- Maraston, C., Pforr, J., Renzini, A., Daddi, E., Dickinson, M., Cimatti, A., & Tonini, C. 2010, *MNRAS*, 407, 830
- Marchesini, D., van Dokkum, P. G., Förster Schreiber, N. M., Franx, M., Labbé, I., & Wuyts, S. 2009, *ApJ*, 701, 1765
- Marchesini, D., Whitaker, K. E., Brammer, G., van Dokkum, P. G., Labbé, I., Muzzin, A., Quadri, R. F., Kriek, M., Lee, K.-S., Rudnick, G., Franx, M., Illingworth, G. D., & Wake, D. 2010, *ApJ*, 725, 1277
- Martinelli, A., Matteucci, F., & Colafrancesco, S. 1998, *MNRAS*, 298, 42
- Mathews, W. G. & Brighenti, F. 2003, *ARA&A*, 41, 191
- McCarthy, P. J. 2004, *ARA&A*, 42, 477

- Menanteau, F., Abraham, R. G., & Ellis, R. S. 2001a, *MNRAS*, 322, 1
- . 2001b, *MNRAS*, 322, 1
- Menanteau, F., Ford, H. C., Illingworth, G. D., Sirianni, M., Blakeslee, J. P., Meurer, G. R., Martel, A. R., Benítez, N., Postman, M., Franx, M., Ardila, D. R., Bartko, F., Bouwens, R. J., Broadhurst, T. J., Brown, R. A., Burrows, C. J., Cheng, E. S., Clampin, M., Cross, N. J. G., Feldman, P. D., Golimowski, D. A., Gronwall, C., Hartig, G. F., Infante, L., Kimble, R. A., Krist, J. E., Lesser, M. P., Miley, G. K., Rosati, P., Sparks, W. B., Tran, H. D., Tsvetanov, Z. I., White, R. L., & Zheng, W. 2004, *ApJ*, 612, 202
- Menanteau, F., Jimenez, R., & Matteucci, F. 2001c, *ApJ*, 562, L23
- Mendez, A. J., Coil, A. L., Lotz, J., Salim, S., Moustakas, J., & Simard, L. 2011, *ApJ*, 736, 110
- Miller, N. A., Fomalont, E. B., Kellermann, K. I., Mainieri, V., Norman, C., Padovani, P., Rosati, P., & Tozzi, P. 2008, *ApJS*, 179, 114
- Mobasher, B., Dickinson, M., Ferguson, H. C., Giavalisco, M., Wiklind, T., Stark, D., Ellis, R. S., Fall, S. M., Grogin, N. A., Moustakas, L. A., Panagia, N., Sosey, M., Stiavelli, M., Bergeron, E., Casertano, S., Ingraham, P., Koekemoer, A., Labbé, I., Livio, M., Rodgers, B., Scarlata, C., Vernet, J., Renzini, A., Rosati, P., Kuntschner, H., Kümmel, M., Walsh, J. R., Chary, R., Eisenhardt, P., Pirzkal, N., & Stern, D. 2005, *ApJ*, 635, 832
- Murray, N., Quataert, E., & Thompson, T. A. 2010, *ApJ*, 709, 191
- Naab, T., Johansson, P. H., & Ostriker, J. P. 2009, *ApJ*, 699, L178
- Naab, T., Johansson, P. H., Ostriker, J. P., & Efstathiou, G. 2007, *ApJ*, 658, 710
- Naab, T. & Ostriker, J. P. 2009, *ApJ*, 690, 1452
- Navarro, J. F., Frenk, C. S., & White, S. D. M. 1996, *ApJ*, 462, 563
- . 1997, *ApJ*, 490, 493
- Noguchi, M. 1999, *ApJ*, 514, 77
- Nonino, M., Dickinson, M., Rosati, P., Grazian, A., Reddy, N., Cristiani, S., Giavalisco, M., Kuntschner, H., Vanzella, E., Daddi, E., Fosbury, R. A. E., & Cesarsky, C. 2009, *ApJS*, 183, 244
- Norberg, P., Cole, S., Baugh, C. M., Frenk, C. S., Baldry, I., Bland-Hawthorn, J., Bridges, T., Cannon, R., Colless, M., Collins, C., Couch, W., Cross, N. J. G., Dalton, G., De Propris, R., Driver, S. P., Efstathiou, G., Ellis, R. S., Glazebrook, K., Jackson, C., Lahav, O., Lewis, I., Lumsden, S., Maddox, S., Madgwick, D., Peacock, J. A., Peterson, B. A., Sutherland, W., & Taylor, K. 2002, *MNRAS*, 336, 907

- Oesch, P. A., Bouwens, R. J., Illingworth, G. D., Carollo, C. M., Franx, M., Labbé, I., Magee, D., Stiavelli, M., Trenti, M., & van Dokkum, P. G. 2010, *ApJ*, 709, L16
- Oesch, P. A., Stiavelli, M., Carollo, C. M., Bergeron, L. E., Koekemoer, A. M., Lucas, R. A., Pavlovsky, C. M., Trenti, M., Lilly, S. J., Beckwith, S. V. W., Dahlen, T., Ferguson, H. C., Gardner, J. P., Lacey, C., Mobasher, B., Panagia, N., & Rix, H. 2007, *ApJ*, 671, 1212
- Oke, J. B. 1974, *ApJS*, 27, 21
- Onodera, M., Daddi, E., Gobat, R., Cappellari, M., Arimoto, N., Renzini, A., Yamada, Y., McCracken, H. J., Mancini, C., Capak, P., Carollo, M., Cimatti, A., Giavalisco, M., Ilbert, O., Kong, X., Lilly, S., Motohara, K., Ohta, K., Sanders, D. B., Scoville, N., Tamura, N., & Taniguchi, Y. 2010, *ApJ*, 715, L6
- Pahre, M. A., Ashby, M. L. N., Fazio, G. G., & Willner, S. P. 2004, *ApJS*, 154, 229
- Papovich, C., Dickinson, M., & Ferguson, H. C. 2001, *ApJ*, 559, 620
- Papovich, C., Finkelstein, S. L., Ferguson, H. C., Lotz, J. M., & Giavalisco, M. 2011, *MNRAS*, 412, 1123
- Papovich, C., Momcheva, I., Willmer, C. N. A., Finkelstein, K. D., Finkelstein, S. L., Tran, K.-V., Brodwin, M., Dunlop, J. S., Farrah, D., Khan, S. A., Lotz, J., McCarthy, P., McLure, R. J., Rieke, M., Rudnick, G., Sivanandam, S., Pacaud, F., & Pierre, M. 2010, *ApJ*, 716, 1503
- Papovich, C., Moustakas, L. A., Dickinson, M., Le Floch, E., Rieke, G. H., Daddi, E., Alexander, D. M., Bauer, F., Brandt, W. N., Dahlen, T., Egami, E., Eisenhardt, P., Elbaz, D., Ferguson, H. C., Giavalisco, M., Lucas, R. A., Mobasher, B., Pérez-González, P. G., Stutz, A., Rieke, M. J., & Yan, H. 2006, *ApJ*, 640, 92
- Peletier, R. F., Davies, R. L., Illingworth, G. D., Davis, L. E., & Cawson, M. 1990a, *AJ*, 100, 1091
- Peletier, R. F., Valentijn, E. A., & Jameson, R. F. 1990b, *A&A*, 233, 62
- Peng, Y., Lilly, S. J., Kovač, K., Bolzonella, M., Pozzetti, L., Renzini, A., Zamorani, G., Ilbert, O., Knobel, C., Iovino, A., Maier, C., Cucciati, O., Tasca, L., Carollo, C. M., Silverman, J., Kampczyk, P., de Ravel, L., Sanders, D., Scoville, N., Contini, T., Mainieri, V., Scodreggio, M., Kneib, J., Le Fèvre, O., Bardelli, S., Bongiorno, A., Caputi, K., Coppa, G., de la Torre, S., Franzetti, P., Garilli, B., Lamareille, F., Le Borgne, J., Le Brun, V., Mignoli, M., Perez Montero, E., Pello, R., Ricciardelli, E., Tanaka, M., Tresse, L., Vergani, D., Welikala, N., Zucca, E., Oesch, P., Abbas, U., Barnes, L., Bordoloi, R., Bottini, D., Cappi, A., Cassata, P., Cimatti, A., Fumana, M., Hasinger, G., Koekemoer, A., Leauthaud, A., Maccagni, D., Marinoni, C., McCracken, H., Memeo, P., Meneux, B., Nair, P., Porciani, C., Presotto, V., & Scaramella, R. 2010, *ApJ*, 721, 193

- Percival, W. J., Cole, S., Eisenstein, D. J., Nichol, R. C., Peacock, J. A., Pope, A. C., & Szalay, A. S. 2007, *MNRAS*, 381, 1053
- Percival, W. J., Reid, B. A., Eisenstein, D. J., Bahcall, N. A., Budavari, T., Frieman, J. A., Fukugita, M., Gunn, J. E., Ivezić, Ž., Knapp, G. R., Kron, R. G., Loveday, J., Lupton, R. H., McKay, T. A., Meiksin, A., Nichol, R. C., Pope, A. C., Schlegel, D. J., Schneider, D. P., Spergel, D. N., Stoughton, C., Strauss, M. A., Szalay, A. S., Tegmark, M., Vogeley, M. S., Weinberg, D. H., York, D. G., & Zehavi, I. 2010, *MNRAS*, 401, 2148
- Pérez-González, P. G., Rieke, G. H., Villar, V., Barro, G., Blaylock, M., Egami, E., Gallego, J., Gil de Paz, A., Pascual, S., Zamorano, J., & Donley, J. L. 2008, *ApJ*, 675, 234
- Pipino, A., D’Ercole, A., Chiappini, C., & Matteucci, F. 2010, *MNRAS*, 407, 1347
- Polletta, M., Tajer, M., Maraschi, L., Trinchieri, G., Lonsdale, C. J., Chiappetti, L., Andreon, S., Pierre, M., Le Fèvre, O., Zamorani, G., Maccagni, D., Garcet, O., Surdej, J., Franceschini, A., Alloin, D., Shupe, D. L., Surace, J. A., Fang, F., Rowan-Robinson, M., Smith, H. E., & Tresse, L. 2007, *ApJ*, 663, 81
- Prevot, M. L., Lequeux, J., Prevot, L., Maurice, E., & Rocca-Volmerange, B. 1984, *A&A*, 132, 389
- Ranalli, P., Comastri, A., & Setti, G. 2003, *A&A*, 399, 39
- Rauch, M., Haehnelt, M., Bunker, A., Becker, G., Marleau, F., Graham, J., Cristiani, S., Jarvis, M., Lacey, C., Morris, S., Peroux, C., Röttgering, H., & Theuns, T. 2008, *ApJ*, 681, 856
- Ravindranath, S., Giavalisco, M., Ferguson, H. C., Conselice, C., Katz, N., Weinberg, M., Lotz, J., Dickinson, M., Fall, S. M., Mobasher, B., & Papovich, C. 2006, *ApJ*, 652, 963
- Reddy, N. A., Erb, D. K., Steidel, C. C., Shapley, A. E., Adelberger, K. L., & Pettini, M. 2005, *ApJ*, 633, 748
- Reddy, N. A., Steidel, C. C., Pettini, M., Adelberger, K. L., Shapley, A. E., Erb, D. K., & Dickinson, M. 2008, *ApJS*, 175, 48
- Rest, A., van den Bosch, F. C., Jaffe, W., Tran, H., Tsvetanov, Z., Ford, H. C., Davies, J., & Schafer, J. 2001, *AJ*, 121, 2431
- Retzlaff, J., Rosati, P., Dickinson, M., Vandame, B., Rité, C., Nonino, M., Cesarsky, C., & GOODS Team. 2010, *A&A*, 511, A50+
- Riess, A. G., Filippenko, A. V., Challis, P., Clocchiatti, A., Diercks, A., Garnavich, P. M., Gilliland, R. L., Hogan, C. J., Jha, S., Kirshner, R. P., Leibundgut, B., Phillips, M. M., Reiss, D., Schmidt, B. P., Schommer, R. A., Smith, R. C., Spyromilio, J., Stubbs, C., Suntzeff, N. B., & Tonry, J. 1998, *AJ*, 116, 1009

- Riess, A. G., Macri, L., Casertano, S., Sosey, M., Lampeitl, H., Ferguson, H. C., Filippenko, A. V., Jha, S. W., Li, W., Chornock, R., & Sarkar, D. 2009, *ApJ*, 699, 539
- Riguccini, L., Le Floch, E., Ilbert, O., Aussel, H., Salvato, M., Capak, P., McCracken, H., Kartaltepe, J., Sanders, D., & Scoville, N. 2011, *ArXiv e-prints*
- Roche, N. D., Almaini, O., Dunlop, J., Ivison, R. J., & Willott, C. J. 2002, *MNRAS*, 337, 1282
- Roche, N. D., Dunlop, J., & Almaini, O. 2003, *MNRAS*, 346, 803
- Rodighiero, G., Cimatti, A., Franceschini, A., Brusa, M., Fritz, J., & Bolzonella, M. 2007, *A&A*, 470, 21
- Rodighiero, G., Daddi, E., Baronchelli, I., Cimatti, A., Renzini, A., Aussel, H., Popesso, P., Lutz, D., Andreani, P., Berta, S., Cava, A., Elbaz, D., Feltre, A., Fontana, A., Förster Schreiber, N. M., Franceschini, A., Genzel, R., Grazian, A., Gruppioni, C., Ilbert, O., Le Floch, E., Magdis, G., Magliocchetti, M., Magnelli, B., Maiolino, R., McCracken, H., Nordon, R., Poglitsch, A., Santini, P., Pozzi, F., Riguccini, L., Tacconi, L. J., Wuyts, S., & Zamorani, G. 2011, *ApJ*, 739, L40
- Salimbeni, S., Castellano, M., Pentericci, L., Trevese, D., Fiore, F., Grazian, A., Fontana, A., Giallongo, E., Boutsia, K., Cristiani, S., de Santis, C., Gallozzi, S., Menci, N., Nonino, M., Paris, D., Santini, P., & Vanzella, E. 2009a, *A&A*, 501, 865
- Salimbeni, S., Fontana, A., Giallongo, E., Grazian, A., Menci, N., Pentericci, L., & Santini, P. 2009b, in *American Institute of Physics Conference Series*, Vol. 1111, American Institute of Physics Conference Series, ed. G. Giobbi, A. Tornambe, G. Raimondo, M. Limongi, L. A. Antonelli, N. Menci, & E. Brocato, 207–211
- Salpeter, E. E. 1955, *ApJ*, 121, 161
- Saracco, P., Longhetti, M., & Gargiulo, A. 2010, *MNRAS*, L115+
- Saracco, P., Longhetti, M., Severgnini, P., Della Ceca, R., Braitto, V., Mannucci, F., Bender, R., Drory, N., Feulner, G., Hopp, U., & Maraston, C. 2005, *MNRAS*, 357, L40
- Scott, K. S., Yun, M. S., Wilson, G. W., Austermann, J. E., Aguilar, E., Aretxaga, I., Ezawa, H., Ferrusca, D., Hatsukade, B., Hughes, D. H., Iono, D., Giavalisco, M., Kawabe, R., Kohno, K., Mauskopf, P. D., Oshima, T., Perera, T. A., Rand, J., Tamura, Y., Tosaki, T., Velazquez, M., Williams, C. C., & Zeballos, M. 2010, *MNRAS*, 405, 2260
- Sérsic, J. L. 1963, *Boletín de la Asociación Argentina de Astronomía La Plata Argentina*, 6, 41

- Shapley, A. E., Steidel, C. C., Adelberger, K. L., Dickinson, M., Giavalisco, M., & Pettini, M. 2001, *ApJ*, 562, 95
- Somerville, R. S., Barden, M., Rix, H.-W., Bell, E. F., Beckwith, S. V. W., Borch, A., Caldwell, J. A. R., Häußler, B., Heymans, C., Jahnke, K., Jogee, S., McIntosh, D. H., Meisenheimer, K., Peng, C. Y., Sánchez, S. F., Wisotzki, L., & Wolf, C. 2008, *ApJ*, 672, 776
- Spergel, D. N., Verde, L., Peiris, H. V., Komatsu, E., Nolta, M. R., Bennett, C. L., Halpern, M., Hinshaw, G., Jarosik, N., Kogut, A., Limon, M., Meyer, S. S., Page, L., Tucker, G. S., Weiland, J. L., Wollack, E., & Wright, E. L. 2003, *ApJS*, 148, 175
- Springel, V., White, S. D. M., Jenkins, A., Frenk, C. S., Yoshida, N., Gao, L., Navarro, J., Thacker, R., Croton, D., Helly, J., Peacock, J. A., Cole, S., Thomas, P., Couchman, H., Evrard, A., Colberg, J., & Pearce, F. 2005, *Nature*, 435, 629
- Steidel, C. C., Adelberger, K. L., Dickinson, M., Giavalisco, M., Pettini, M., & Kellogg, M. 1998, *ApJ*, 492, 428
- Steidel, C. C., Adelberger, K. L., Giavalisco, M., Dickinson, M., & Pettini, M. 1999, *ApJ*, 519, 1
- Steidel, C. C., Adelberger, K. L., Shapley, A. E., Erb, D. K., Reddy, N. A., & Pettini, M. 2005, *ApJ*, 626, 44
- Steidel, C. C., Adelberger, K. L., Shapley, A. E., Pettini, M., Dickinson, M., & Giavalisco, M. 2003, *ApJ*, 592, 728
- Steidel, C. C., Erb, D. K., Shapley, A. E., Pettini, M., Reddy, N., Bogosavljević, M., Rudie, G. C., & Rakic, O. 2010, *ApJ*, 717, 289
- Steidel, C. C., Giavalisco, M., Dickinson, M., & Adelberger, K. L. 1996a, *AJ*, 112, 352
- Steidel, C. C., Giavalisco, M., Pettini, M., Dickinson, M., & Adelberger, K. L. 1996b, *ApJ*, 462, L17+
- Steidel, C. C., Shapley, A. E., Pettini, M., Adelberger, K. L., Erb, D. K., Reddy, N. A., & Hunt, M. P. 2004, *ApJ*, 604, 534
- Strateva, I., Ivezić, Ž., Knapp, G. R., Narayanan, V. K., Strauss, M. A., Gunn, J. E., Lupton, R. H., Schlegel, D., Bahcall, N. A., Brinkmann, J., Brunner, R. J., Budavári, T., Csabai, I., Castander, F. J., Doi, M., Fukugita, M., Győry, Z., Hamabe, M., Hennessy, G., Ichikawa, T., Kunszt, P. Z., Lamb, D. Q., McKay, T. A., Okamura, S., Racusin, J., Sekiguchi, M., Schneider, D. P., Shimasaku, K., & York, D. 2001, *AJ*, 122, 1861

- Swinbank, A. M., Chapman, S. C., Smail, I., Lindner, C., Borys, C., Blain, A. W., Ivison, R. J., & Lewis, G. F. 2006, *MNRAS*, 371, 465
- Swinbank, A. M., Smail, I., Longmore, S., Harris, A. I., Baker, A. J., De Breuck, C., Richard, J., Edge, A. C., Ivison, R. J., Blundell, R., Coppin, K. E. K., Cox, P., Gurwell, M., Hainline, L. J., Krips, M., Lundgren, A., Neri, R., Siana, B., Siringo, G., Stark, D. P., Wilner, D., & Younger, J. D. 2010, *Nature*, 464, 733
- Szomoru, D., Franx, M., Bouwens, R. J., van Dokkum, P. G., Labbé, I., Illingworth, G. D., & Trenti, M. 2011, *ApJ*, 735, L22+
- Tacconi, L. J., Genzel, R., Neri, R., Cox, P., Cooper, M. C., Shapiro, K., Bolatto, A., Bouché, N., Bournaud, F., Burkert, A., Combes, F., Comerford, J., Davis, M., Schreiber, N. M. F., Garcia-Burillo, S., Gracia-Carpio, J., Lutz, D., Naab, T., Omont, A., Shapley, A., Sternberg, A., & Weiner, B. 2010, *Nature*, 463, 781
- Tacconi, L. J., Genzel, R., Smail, I., Neri, R., Chapman, S. C., Ivison, R. J., Blain, A., Cox, P., Omont, A., Bertoldi, F., Greve, T., Förster Schreiber, N. M., Genel, S., Lutz, D., Swinbank, A. M., Shapley, A. E., Erb, D. K., Cimatti, A., Daddi, E., & Baker, A. J. 2008, *ApJ*, 680, 246
- Tamura, N., Kobayashi, C., Arimoto, N., Kodama, T., & Ohta, K. 2000, *AJ*, 119, 2134
- Tamura, N. & Ohta, K. 2003, *AJ*, 126, 596
- . 2004, *MNRAS*, 355, 617
- Temi, P., Brighenti, F., & Mathews, W. G. 2007, *ApJ*, 660, 1215
- Thompson, D., Beckwith, S. V. W., Fockenbrock, R., Fried, J., Hippelein, H., Huang, J.-S., von Kuhlmann, B., Leinert, C., Meisenheimer, K., Phleps, S., Röser, H.-J., Thommes, E., & Wolf, C. 1999, *ApJ*, 523, 100
- Toft, S., Franx, M., van Dokkum, P., Förster Schreiber, N. M., Labbe, I., Wuyts, S., & Marchesini, D. 2009, *ApJ*, 705, 255
- Tortora, C., Napolitano, N. R., Cardone, V. F., Capaccioli, M., Jetzer, P., & Molinaro, R. 2010, *MNRAS*, 407, 144
- Tran, H. D., Tsvetanov, Z., Ford, H. C., Davies, J., Jaffe, W., van den Bosch, F. C., & Rest, A. 2001, *AJ*, 121, 2928
- Trujillo, I., Conselice, C. J., Bundy, K., Cooper, M. C., Eisenhardt, P., & Ellis, R. S. 2007, *MNRAS*, 382, 109
- Trujillo, I., Feulner, G., Goranova, Y., Hopp, U., Longhetti, M., Saracco, P., Bender, R., Braito, V., Della Ceca, R., Drory, N., Mannucci, F., & Severgnini, P. 2006, *MNRAS*, 373, L36

- van den Bergh, S., Cohen, J. G., Hogg, D. W., & Blandford, R. 2000, *AJ*, 120, 2190
- van der Wel, A., Bell, E. F., van den Bosch, F. C., Gallazzi, A., & Rix, H. 2009, *ApJ*, 698, 1232
- van Dokkum, P. G., Förster Schreiber, N. M., Franx, M., Daddi, E., Illingworth, G. D., Labbé, I., Moorwood, A., Rix, H.-W., Röttgering, H., Rudnick, G., van der Wel, A., van der Werf, P., & van Starckenburg, L. 2003, *ApJ*, 587, L83
- van Dokkum, P. G. & Franx, M. 1995, *AJ*, 110, 2027
- van Dokkum, P. G., Franx, M., Förster Schreiber, N. M., Illingworth, G. D., Daddi, E., Knudsen, K. K., Labbé, I., Moorwood, A., Rix, H.-W., Röttgering, H., Rudnick, G., Trujillo, I., van der Werf, P., van der Wel, A., van Starckenburg, L., & Wuyts, S. 2004, *ApJ*, 611, 703
- van Dokkum, P. G., Franx, M., Kriek, M., Holden, B., Illingworth, G. D., Magee, D., Bouwens, R., Marchesini, D., Quadri, R., Rudnick, G., Taylor, E. N., & Toft, S. 2008, *ApJ*, 677, L5
- van Dokkum, P. G., Quadri, R., Marchesini, D., Rudnick, G., Franx, M., Gawiser, E., Herrera, D., Wuyts, S., Lira, P., Labbé, I., Maza, J., Illingworth, G. D., Förster Schreiber, N. M., Kriek, M., Rix, H.-W., Taylor, E. N., Toft, S., Webb, T., & Yi, S. K. 2006, *ApJ*, 638, L59
- van Dokkum, P. G., Whitaker, K. E., Brammer, G., Franx, M., Kriek, M., Labbé, I., Marchesini, D., Quadri, R., Bezanson, R., Illingworth, G. D., Muzzin, A., Rudnick, G., Tal, T., & Wake, D. 2010, *ApJ*, 709, 1018
- Vanzella, E., Cristiani, S., Dickinson, M., Giavalisco, M., Kuntschner, H., Haase, J., Nonino, M., Rosati, P., Cesarsky, C., Ferguson, H. C., Fosbury, R. A. E., Grazian, A., Moustakas, L. A., Rettura, A., Popesso, P., Renzini, A., Stern, D., & The GOODS Team. 2008, *A&A*, 478, 83
- Wang, J. X., Malhotra, S., Rhoads, J. E., & Norman, C. A. 2004, *ApJ*, 612, L109
- Wang, W.-H., Cowie, L. L., Barger, A. J., Keenan, R. C., & Ting, H.-C. 2010, *ApJS*, 187, 251
- Wechsler, R. H., Bullock, J. S., Primack, J. R., Kravtsov, A. V., & Dekel, A. 2002, *ApJ*, 568, 52
- White, S. D. M. & Rees, M. J. 1978, *MNRAS*, 183, 341
- Wiklind, T., Dickinson, M., Ferguson, H. C., Giavalisco, M., Mobasher, B., Grogin, N. A., & Panagia, N. 2008, *ApJ*, 676, 781
- Williams, R. J., Quadri, R. F., Franx, M., van Dokkum, P., & Labbé, I. 2009, *ApJ*, 691, 1879

- Windhorst, R. A., Cohen, S. H., Hathi, N. P., McCarthy, P. J., Ryan, R. E., Jr., Yan, H., Baldry, I. K., Driver, S. P., Frogel, J. A., Hill, D. T., Kelvin, L. S., Koekemoer, A. M., Mechtley, M., O'Connell, R. W., Robotham, A. S. G., Rutkowski, M. J., Seibert, M., Tuffs, R. J., Balick, B., Bond, H. E., Bushouse, H., Calzetti, D., Crockett, M., Disney, M. J., Dopita, M. A., Hall, D. N. B., Holtzman, J. A., Kaviraj, S., Kimble, R. A., MacKenty, J. W., Mutchler, M., Paresce, F., Saha, A., Silk, J. I., Trauger, J., Walker, A. R., Whitmore, B. C., & Young, E. 2010, ArXiv e-prints
- Wise, M. W. & Silva, D. R. 1996, ApJ, 461, 155
- Wu, H., Shao, Z., Mo, H. J., Xia, X., & Deng, Z. 2005, ApJ, 622, 244
- Wuyts, S., Cox, T. J., Hayward, C. C., Franx, M., Hernquist, L., Hopkins, P. F., Jonsson, P., & van Dokkum, P. G. 2010, ApJ, 722, 1666
- Wuyts, S., Förster Schreiber, N. M., Genzel, R., Guo, Y., Barro, G., Bell, E. F., Dekel, A., Faber, S. M., Ferguson, H. C., Giavalisco, M., Grogin, N. A., Hathi, N. P., Huang, K.-H., Kocevski, D. D., Koekemoer, A. M., Koo, D. C., Lotz, J., Lutz, D., McGrath, E., Newman, J. A., Rosario, D., Saintonge, A., Tacconi, L. J., Weiner, B. J., & van der Wel, A. 2012, ArXiv e-prints
- Wuyts, S., Förster Schreiber, N. M., van der Wel, A., Magnelli, B., Guo, Y., Genzel, R., Lutz, D., Aussel, H., Barro, G., Berta, S., Cava, A., Graciá-Carpio, J., Hathi, N. P., Huang, K.-H., Kocevski, D. D., Koekemoer, A. M., Lee, K.-S., Le Floc'h, E., McGrath, E. J., Nordon, R., Popesso, P., Pozzi, F., Riguccini, L., Rodighiero, G., Saintonge, A., & Tacconi, L. 2011, ApJ, 742, 96
- Xue, Y. Q., Luo, B., Brandt, W. N., Bauer, F. E., Lehmer, B. D., Broos, P. S., Schneider, D. P., Alexander, D. M., Brusa, M., Comastri, A., Fabian, A. C., Gilli, R., Hasinger, G., Hornschemeier, A. E., Koekemoer, A., Liu, T., Mainieri, V., Paolillo, M., Rafferty, D. A., Rosati, P., Shemmer, O., Silverman, J. D., Smail, I., Tozzi, P., & Vignali, C. 2011, ApJS, 195, 10
- Yan, L., Thompson, D., & Soifer, B. T. 2004, AJ, 127, 1274
- Zirm, A. W., van der Wel, A., Franx, M., Labbé, I., Trujillo, I., van Dokkum, P., Toft, S., Daddi, E., Rudnick, G., Rix, H.-W., Röttgering, H. J. A., & van der Werf, P. 2007, ApJ, 656, 66